Technical Report Documentation Page

1. Report No.	2. Government Accession No.	3. Recipient's Catalog No.
FHWA/TX-97/1335-3F		

4. Title and Subtitle	5. Report Date
DEVELOPMENT OF A PROCEDURE FOR THE STRUCTURAL EVALUATION OF SUPERHEAVY LOAD ROUTES	November 1995
	6. Performing Organization Code
7. Author(s)	8. Performing Organization Report No.
Fritz J. Jooste and Emmanuel G. Fernando	Research Report 1335-3F
9. Performing Organization Name and Address	10. Work Unit No. (TRAIS)
Texas Transportation Institute The Texas A&M University System College Station, Texas 77843-3135	11. Contract or Grant No. Study No. 0-1335
12. Sponsoring Agency Name and Address	13. Type of Report and Period Covered
Texas Department of Transportation Research and Technology Transfer Office P. O. Box 5080 Austin, Texas 78763-5080	Final: January 1993 - August 1995
	14. Sponsoring Agency Code

15. Supplementary Notes

Research performed in cooperation with the Texas Department of Transportation and the U.S. Department of Transportation, Federal Highway Administration.

Research Study Title: Movement of Superheavy Loads over the State Highway System

16. Abstract

The Texas Department of Transportation (TXDOT) receives about 75 to 100 permit requests for superheavy load moves annually. Most of the moves take place in the southeast region of the state due to the proximity to the Gulf of Mexico and the presence of navigational inland waterways. Gross vehicle weights associated with these moves range from 1112 kN to over 8896 kN and include loads like dragline components, off-shore pipe-laying equipment, oil pressure vessels, and electric transformers. The number of superheavy load permit applications has increased over the years. Before a permit can be issued, TxDOT needs to determine whether the proposed route is structurally adequate to sustain the superheavy load. The analysis of damage potential under superheavy loads concerns the likelihood of a rapid, load-induced shear failure as opposed to the long-term accumulation of permanent deformation and fatigue due to repeated load applications. In this project, researchers developed a procedure for evaluating the potential for pavement damage prior to a superheavy load move based on the Mohr-Coulomb yield criterion. In developing this procedure, researchers investigated the sensitivity of the Mohr-Coulomb yield criterion to changes in the predicted stress state and material strength parameters; compared different models for evaluating pavement response under vehicle loading; and investigated the effect of different load configurations on the predicted pavement response and yield function value. Using the results from these investigations, researchers developed a two-stage procedure for the structural assessment of superheavy load routes which utilizes existing capabilities within TxDOT. Flexibility is provided to conduct structural evaluations with varying degrees of complexity depending on the quantity and quality of information available on the proposed superheavy load route. In the first stage, structural adequacy is evaluated by means of charts with minimal requirements for materials characterization. Relationships are provided for estimating resilient and strength parameters of base and subgrade materials from results of simple soil tests. Should the initial results indicate that the structure is inadequate to accommodate the expected superheavy load, then the second stage analysis should be conducted which requires a more detailed characterization of the proposed route. In this stage, the evaluation uses an incremental, non-linear layered elastic computer program. This report documents the development of the methodology for permitting superheavy load moves.

17. Key Words	18. Distribution Statement
Superheavy Loads, Pavement Evaluation, Pavement Response Modeling, Nonlinear Material Behavior, Mohr-Coulomb Yield Criterion	No restrictions. This document is available to the public through NTIS: National Technical Information Service 5285 Port Royal Road Springfield, Virginia 22161

19. Security Classif.(of this report)	20. Security Classif.(of this page)	21. No. of Pages	22. Price
Unclassified	Unclassified	282	

Form DOT F 1700.7 (8-72) Reproduction of completed page authorized

DEVELOPMENT OF A PROCEDURE FOR THE STRUCTURAL EVALUATION OF SUPERHEAVY LOAD ROUTES

by

Fritz J. Jooste
Graduate Research Assistant
Texas Transportation Institute

and

Emmanuel G. Fernando
Assistant Research Engineer
Texas Transportation Institute

Research Report 1335-3F
Research Study Number 0-1335
Research Study Title: Movement of Superheavy Loads over the State Highway System

Sponsored by the
Texas Department of Transportation
In Cooperation with
U. S. Department of Transportation
Federal Highway Administration

November 1995

TEXAS TRANSPORTATION INSTITUTE
The Texas A&M University System
College Station, Texas 77843-3135

IMPLEMENTATION STATEMENT

This study has developed a methodology for evaluating the structural adequacy of routes for permitting superheavy load moves. Researchers recommend that the Texas Department of Transportation (TxDOT) implement the procedure. Texas Transportation Institute (TTI) can assist in this implementation effort, particularly in training TxDOT engineers in the proper use of the structural evaluation procedure. The study has also shown the need for additional research in the following areas to facilitate the evaluation of failure potential under superheavy loads:

1) The accuracy of the structural evaluation depends strongly on the estimates of the cohesion of the pavement materials at the time of the superheavy load move. Methods do exist to estimate the cohesion of pavement materials through non-destructive testing techniques such as ground penetrating radar, coupled with data on the moisture-suction curves of the pavement materials in question. Indeed, research efforts made in this project have led to the development of an alternative method for estimating cohesion in the absence of triaxial test data. It is recommended that additional research be conducted to test and calibrate the method developed in this study using a more extensive database of material strength parameters. This research should also investigate relationships between cohesion and material stiffness.
2) The present study has shown that, of the three non-linear material parameters (K_1, K_2, and K_3), the Mohr-Coulomb yield function is most significantly affected by K_1. This factor varies not only with the material type but also with the prevailing environmental conditions. It is recommended that further research be conducted to investigate the possibility of determining K_1 through non-destructive testing such as FWD testing.

DISCLAIMER

The contents of this report reflect the views of the authors who are responsible for the facts and the accuracy of the data presented herein. The contents do not necessarily reflect the official views or policies of the Texas Department of Transportation (TxDOT) or the Federal Highway Administration (FHWA). This report does not constitute a standard, specification, or regulation, nor is it intended for construction, bidding, or permit purposes. The engineer in charge of the project was Dr. Emmanuel G. Fernando, P.E. # 69614.

ACKNOWLEDGMENTS

The work reported herein was conducted as part of a research study sponsored by TxDOT, and the Federal Highway Administration, U.S. Department of Transportation. The objective of the study was to develop a procedure for evaluating the structural adequacy of pavement sections along a proposed superheavy load route. The support and guidance of the project director, Mr. Michael Murphy, is gratefully acknowledged. A sincere note of appreciation is extended to the following Districts who assisted the researchers in the collection of data on superheavy load routes: Atlanta, Austin, Beaumont, Houston, Tyler, and Yoakum Districts.

TABLE OF CONTENTS

LIST OF FIGURES

FIGURE Page

FIGURE Page

FIGURE Page

FIGURE Page

FIGURE Page

FIGURE Page

FIGURE Page

LIST OF TABLES

TABLE Page

SUMMARY

Recent years have seen an increasing number of superheavy load moves over the Texas State Highway system. Prior to this research project, TxDOT did not have a procedure for evaluating the damage potential under superheavy loads. The analysis of pavement response under superheavy loads concerns the potential for rapid, load-induced failure rather than long-term failure induced by fatigue. In this study, researchers developed a procedure to evaluate the pavement response under superheavy loads and the potential for pavement damage using the Mohr-Coulomb failure criterion.

Researchers developed a non-linear finite element model to study the sensitivity of the Mohr-Coulomb yield function to changes in the non-linear material parameters K_1, K_2, and K_3, as well as to changes in the strength parameters. Of the non-linear parameters, K_1 was found to have the most pronounced influence on the yield function. Of the strength parameters, cohesion was found to have a consistent and pronounced effect on the yield function. Two simplified response models were compared with the finite element model. These models were a traditional linear layered elastic program and a non-linear layered elastic version of the finite element program. The latter model was found to provide reasonable comparisons with the more complex finite element model. The effects of different load configurations on the yield function were studied using the non-linear layered elastic program. It was found that simplified wheel load configurations lead to yield function values that are very similar to more complex load configurations.

Based on the results of the above investigations, researchers developed a two-staged procedure for routine evaluation of the potential for pavement damage under superheavy loads. The first stage analysis makes use of charts that provide the user with the maximum wheel load that can be sustained by a given pavement. The second stage analysis is more accurate and makes use of a computer program in which more detailed information such as backcalculated moduli can be used. This report documents the development of the procedure for permitting superheavy load moves.

CHAPTER I
INTRODUCTION

GENERAL

An increasing number of superheavy loads are being moved over the Texas State Highway System. By definition, these loads have gross vehicle weights in excess of 1112 kN. In the past, loads in excess of 8900 kN have been moved. Most superheavy load transport vehicles are equipped with multiple axles to increase load distribution. However, the total load on a single axle is often close to or more than 500 kN.

The analysis of damage potential under superheavy loads differs from routine pavement design methods, mainly in the way that failure is defined. To prevent structural failure under normal loading conditions, the designer is primarily concerned with preventing long term accumulated strains and fatigue, which manifest themselves in the form of rutting and cracking (1,2,3). However, in the analysis of pavements under superheavy loads, the concern is with the magnitude of the wheel loads rather than with the number of load repetitions. Load repetitions in the case of superheavy load vehicles are not likely to exceed 30 or 40, even when two vehicles are moved in short succession. Thus, the expected mode of failure is a more rapid load-induced failure resulting from a shear stress which exceeds the shear strength afforded by the material's internal frictional resistance and cohesion (4).

The problem of predicting the likelihood of failure under a superheavy load can be solved by determining the maximum allowable wheel load that can be sustained by a given pavement structure. To do this, the stresses invoked by the applied load as well as the material strength parameters need to be known. Laboratory testing normally determines material parameters, while a mechanistic model of the pavement structure and the applied load determines stresses (5,6,7,8). In order to compare the stress invoked by the applied load to the material strength, a yield criterion, such as the well known Mohr-Coulomb criterion, is typically used (9,10).

Apart from requiring a different method of analysis to determine failure potential, superheavy load vehicles are equipped with multiple wheels. On some superheavy load transport vehicles, 20 axles, each with as many as 12 wheels, are used. The three distinguishing features of a superheavy load analysis can, therefore, be summarized as: (1) a damage potential analysis method that differs from that used in routine pavement design; (2) abnormally high axle loads; and (3) the need to account for complex load configurations that make use of multiple wheel and axle assemblies, and specially designed tires with tire pressures approaching 966 kPa.

PROBLEM STATEMENT

During the early to middle 1990s, the Texas Department of Transportation (TxDOT) received between 75 to 100 superheavy load permit applications per year. Such an application is typically accompanied by diagrams of the proposed route as well as of the load configuration. Before a permit can be issued, TxDOT needs to determine whether the proposed route is structurally adequate to sustain the superheavy load. Prior to this research project, TxDOT did not have a procedure for assessing the potential for pavement damage prior to a superheavy load move. A definite need, therefore, existed to develop a methodology which could determine the structural adequacy of proposed superheavy load routes on a routine basis.

It is immediately evident from the relatively large number of load permit applications received every year that any procedure for analyzing the structural adequacy of superheavy load routes has to be as simple and easy to implement as possible. This requirement of simplicity and ease of implementation stands in direct contrast to the relatively complex behavior of pavement materials and the unusual load configurations imposed by superheavy load vehicles. While pavement response can be modeled fairly accurately through the use of finite element models that take account material non-linearity, such programs may be difficult to implement owing to their relatively complex formulation (1,7,8). Despite its shortcomings, the multilayered elastic approach has been used with success in predicting pavement response under normal traffic conditions (11,12,13). This approach has also been implemented in conjunction with nondestructive testing apparatus to backcalculate

pavement layer properties, a factor that makes it eminently suitable for routine applications (14,15). However, the validity of linear layered elastic programs in predicting pavement response under superheavy loads needs to be determined. Researchers hypothesize that the effects of non-linear behavior are likely to be amplified under the heavy axle loads. Should traditional linear layered elastic procedures prove to be inaccurate, then a different methodology needs to be developed based on more accurate modeling procedures, such as the finite element method.

A problem also exists in routinely predicting pavement response under multiple wheel assemblies such as those used by superheavy load vehicles. Modeling multiple wheel assemblies on a routine basis is likely to be a complex and time consuming process. The possibility of simplifying complex load assemblies in the modeling process needs to be investigated. The effect of such simplification on the predicted pavement response is not known and needs to be determined.

RESEARCH OBJECTIVES

The general objective of this research is to develop a methodology whereby pavement engineers can assess potential damage prior to a superheavy load being moved over a pavement. It is vital that the methodology utilize those resources that are already available to the Texas Department of Transportation. Specific objectives of the research are as follows:

1) to investigate the factors affecting the bearing capacity of pavement materials under loading;
2) to investigate the sensitivity of the chosen yield criterion to changes in the predicted stress state and material strength parameters;
3) to investigate and compare different models used for evaluating the response of pavement structures under loading;
4) to investigate the effect of different load configurations on the predicted pavement response; and
5) to develop an evaluation procedure whereby the adequacy of a given pavement structure for sustaining a superheavy load can be determined prior to the move.

SCOPE OF RESEARCH REPORT

The research conducted in this TxDOT project is documented in eight chapters. Chapter I is the introductory chapter. Chapter II presents the research approach followed in developing the pavement structural evaluation procedure for permitting superheavy load moves. Chapter III describes the development of the finite element response model and its verification through the use of laboratory data. This finite element model was used in subsequent analysis as a benchmark against which simpler response models were compared. All important aspects of the finite element model are discussed, including the stress dependent resilient modulus formulation and the stress dependent Poisson's ratio formulation. Two different methods of modeling a stress dependent Poisson's ratio are discussed. Laboratory results are presented and discussed together with results calculated by means of the finite element response model. Comparisons are made between the measured and calculated results.

Chapter IV documents the results of a sensitivity analysis of the Mohr-Coulomb yield criterion. In this analysis, all the elements needed to predict the point of yield were varied to determine the effect each has on the predicted yield point, and to determine which stress and material parameters have the most pronounced effect on the predicted yield point.

In Chapter V, three different response models are compared. Because the purpose of this study is primarily concerned with the prediction of yield under superheavy loads, the parameter used to compare and evaluate the different response models was the Mohr-Coulomb yield function value. The three response models compared were: (1) the finite element response model described in Chapter III; (2) a traditional linear layered elastic model; and (3) a non-linear version of a layered elastic program developed specifically for the purposes of this research.

Chapter VI documents the results of the analysis to determine the effect load configuration has on predicted pavement response. As before, the parameter of interest was the Mohr-Coulomb yield function value. The consequences of using a simplified load configuration as opposed to a more complex and realistic load configuration are studied, and the results are documented. Three different load configurations are compared, and the

effect each has on different pavement structures are studied. An attempt is made to explain the differences in the predicted yield function values by studying the stress tensor at a point as predicted by each load configuration.

In Chapter VII, the findings of the sensitivity analyses are synthesized into a methodology for assessing the structural adequacy of superheavy load routes on a routine basis. This methodology is developed with due consideration to the practical guidelines established for this study, identified in Chapter II. Alternative methods for determining whether a proposed route can carry a given load are proposed. The methods differ with respect to the quantity and quality of information required to perform the analysis and, therefore, some methods are of necessity more conservative than others in their predictions. Chapter VIII provides a summary with conclusions.

In addition to the eight chapters outlined above, there are six appendices. Appendix A summarizes the results of a literature survey on different constitutive models and yield criteria that are applicable for superheavy load analysis. The survey of constitutive models focuses on the theoretical premises underlying each model and discusses the advantages and disadvantages of each model. Appendix B provides a derivation of the relationship between the Poisson's ratio and the stress state. Appendix C contains photographs of the laboratory testing performed to verify the response model described in Chapter III, and Appendix D documents some of the results of the sensitivity analysis discussed in Chapter IV. Since the concept of stress is important to understanding yield criteria and the application of the Mohr-Coulomb yield function to the problem of evaluating superheavy load routes, a review of stress concepts is presented in Appendix E. Principal stresses and stress invariants are explained to provide the necessary background for using the Mohr-Coulomb yield criterion to establish the potential for pavement damage under superheavy loads. Finally, a glossary of selected technical terms used in this report is presented in Appendix F. Many of the technical terms are defined in sufficient detail to provide a handy reference to users of the superheavy load analysis procedure documented in this report.

CHAPTER II
RESEARCH APPROACH

RESEARCHERS' PERSPECTIVE OF THE PROBLEM

When viewed from a general perspective, the movement of a superheavy load is no different from most geotechnical engineering problems in that it can be reduced to an applied load as well as the response of the structure to that load. The load in this case is a superheavy load moving vehicle, and the pavement response depends on the properties of the pavement structure in question. Almost all geotechnical engineering problems require a determination of the stresses and strains that develop under a given set of loading conditions, as well as a prediction of the reaction of the structure to those stresses. Chen and Baladi (16) point out that such a problem is typically one that requires a two stage solution: first, the forces that act on the structure have to be defined, and second, the reactions of the structure to the imposed loads have to be evaluated. In many engineering applications, the suitability of a structure for operating under predetermined loading conditions is based primarily on whether its response falls within an acceptable range. Both steps noted above fall within the realm of continuum mechanics (16).

Typically, the determination of the force that acts on the structure will require a consideration of the basic laws of mechanics, such as the conservation of mass, energy, and momentum (17). However, it is clear that even structures with the same geometry to which the same external forces are applied will respond differently if their internal properties are not the same. Therefore, in addition to considering the laws of mechanics, it is necessary to consider the internal properties of the materials used in the structure before the response of that material to a given loading condition can be predicted.

The response of a material to a fixed loading condition is defined by the constitutive equations, or laws, that apply to that material. Desai and Siriwardane (17) called constitutive laws the relationship between cause and effect for a specific material.

Figure 2.1 illustrates the use of constitutive equations in continuum mechanics. It also represents the researchers' perspective on how the analysis of superheavy loads can be

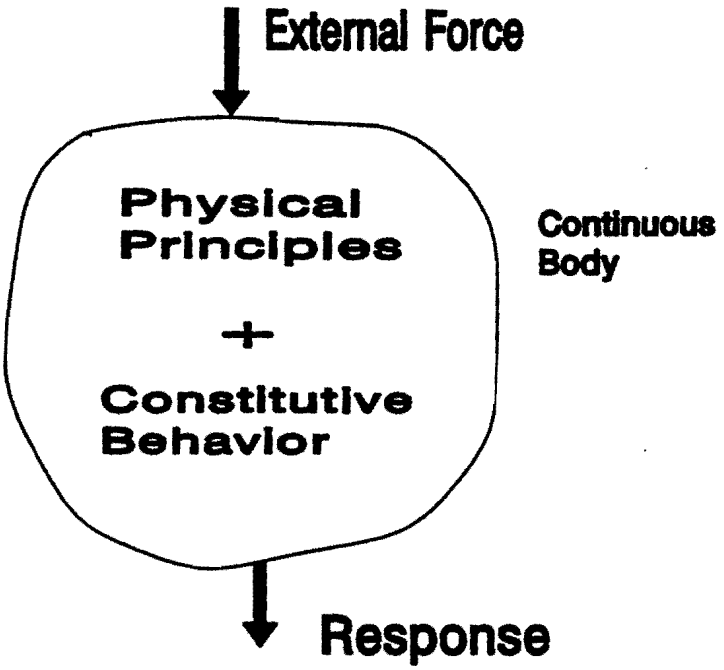

Figure 2.1. The Role of Constitutive Laws in Determining Material Response (From (17)).

accomplished. The continuous body in the figure represents a given pavement which is subjected to an external force (the superheavy load). The induced pavement response to the external force will determine whether the given pavement structure is adequate to sustain the imposed load. It is obvious, therefore, that a model for predicting pavement response under superheavy loads is needed. In this regard, several models have been used to predict the behavior of geotechnical materials. Appendix A presents a literature survey of available constitutive models and yield criteria that may be used to predict pavement response under vehicle loads. The interested reader is encouraged to go over the literature survey for a detailed discussion of the applicable models. Some of the more important observations from the literature review are:

1. The basic constitutive models such as the Cauchy linear elastic model and the more complex non-linear elastic models differ in their ability to accurately model the response of granular materials. While the more complex models offer greater accuracy in terms of predicted response, they are difficult to implement owing to the large number of constants needed in the constitutive model.
2. The response of a material to a load can be divided into two phases or domains, namely an elastic and a plastic phase. The boundary between these zones is not always clearly defined. This is particularly true in the case of loose granular materials. A yield criterion can be used to predict when the response will be elastic and when it is likely to become plastic.
3. Several yield criteria have been proposed. The oldest and most well known of these is the Mohr-Coulomb criterion. The other criteria reviewed are more suited to applications where plastic response is important. However, all of these theories in one way or another relate to the basic premise of the Mohr-Coulomb criterion that resistance to failure depends on interparticle friction and internal cohesion.

In developing the superheavy load analysis procedure, the findings from the literature review were considered in identifying and selecting the constitutive models and yield criterion to use for evaluating pavement response under superheavy loads. Additionally, researchers were guided by the following practical considerations:

1. The structural evaluation procedure must accommodate the relatively large number of permit requests received by TxDOT annually. In addition to the requirement for accuracy in the response predictions, the procedure must be implementable to be useful.
2. The objective in the permitting process is to prevent pavement damage. In those cases where the structural assessment indicates potential pavement damage under a specified superheavy load, alternative routes should be investigated, the vehicle configuration modified, or temporary strengthening measures applied on the weak portions of the proposed superheavy load route.

3. Where applicable, the structural evaluation procedure should utilize existing capabilities within TxDOT.

For the first guideline noted above, researchers took the approach that an accurate procedure for modeling the complex behavior of pavement materials is necessary during the initial stage of development. This will provide a reference with which to evaluate simpler models or to identify suitable simplifications that can be made based on the sensitivity of predicted pavement response to the material input parameters of the reference model.

The second guideline was used by researchers to define the scope of the pavement response modeling. Since the objective of the permitting process is to prevent pavement damage, the response modeling is limited to the elastic domain, and the primary concern is to predict the occurrence of first yield, i.e., the stress level at which plastic deformations will take place. From this standpoint, the response modeling is simplified since the post-yield behavior is not of interest.

With respect to the third guideline, researchers developed a methodology which accommodates the use of existing TxDOT capabilities in the structural evaluation procedure. These include nondestructive testing using the Falling Weight Deflectometer (FWD) to estimate insitu layer stiffnesses, and Ground Penetrating Radar (GPR) to estimate layer thicknesses and moisture contents of the base and subgrade. In addition, the Mohr-Coulomb yield criterion was selected for assessing the potential for pavement damage during a given superheavy load move. This criterion is the basis of the Texas Triaxial Class which TxDOT engineers are familiar with. In fact, there is a standard test method for determining the Mohr-Coulomb failure envelopes of granular and fine grained soils from laboratory tests on molded soil specimens. Consequently, for reasons of achieving consistency with current TxDOT practice and its applicability to pavement materials, the Mohr-Coulomb criterion has been implemented in the structural evaluation procedure for superheavy loads.

THE USE OF YIELD CRITERIA IN PAVEMENT ANALYSIS

The mechanistic design and analysis of pavements traditionally involves the determination of a number of stress and strain parameters which are compared to some empirically determined fatigue curve for the parameter under consideration (1,2). For the asphalt layer, the strain at the bottom of the layer is used to predict the likelihood of premature cracking or shallow rutting. This approach, widely referred to as the "mechanistic-empirical" approach, is concerned with preventing excessive strains, which, due to repeated loads over a long period of time, may lead to cracking and rutting. All of the traditional methods are fatigue related and are used to design pavements on which hundreds of thousands of standard axle loads are expected within the pavements' lifetime. Ullidtz defines the bearing capacity of a pavement as (18): "The number of wheel passages of a specified type that the pavement can support before it reaches an unacceptable level of functional or structural distress."

The analysis of superheavy loads differs from conventional pavement analysis methods in that a limited number of wheel loads are expected. Even when more than one superheavy load is moved in short succession over the same pavement, the number of wheel loads that are expected is unlikely to be more than forty. Table 2.1 shows some statistics that were measured during the course of the study. In Table 2.1, the number of units refer to the maximum number of units that were moved in short succession, i.e., within the space of one day.

It is evident, by looking at the total number of axle applications shown in Table 2.1, that the analysis of superheavy loads does not involve long term fatigue, but rather a rapid succession of higher than normal wheel loads. It should also be noted that, although some of the maximum loads shown in Table 2.1 do not seem abnormally high, there can be as many as twelve of these loads on any one axle.

It is thus clear that the analysis of superheavy loads is concerned with a rapid load-induced deformation rather than a long term settlement under repeated loads. As such, the analysis of superheavy loads is related to the more traditional geotechnical analysis of yield in granular media which involves a yield criterion. Applications of this approach to

Table 2.1. Details of Ten Superheavy Loads Monitored During Study.

Date Moved	Location	Number of Units	Total Number of Axles	Maximum Wheel Load (kN)
12/08/92	Victoria, Texas	2*	13	28.0
12/10/92	Victoria, Texas	1	18	33.0
02/21/93	Beaumont, Texas	2*	23	38.1
03/14/93	Beaumont, Texas	2*	23	38.1
04/23/93	Beaumont, Texas	2	16	38.8
08/01/94	Freeport, Texas	2	22	47.4
08/22/94	Freeport, Texas	2*	15	38.1
04/05/93	Henderson, Texas	2*	9	21.4
04/16/93	Henderson, Texas	2*	9	27.0
04/21/93	Henderson, Texas	2*	15	28.1

* Tractor and trailer

the analysis of foundations and other geotechnical structures are easy to find in the literature (see, for example (17), (19), (20), and (21)). The use of such yield criteria in pavement analysis is less well reported due to the reasons stated above. The following presents a survey of some of the cases where failure or yield criteria were used to predict rapid deformation in pavement structures.

Previously Reported Uses of Failure Criteria in Pavement Analysis

Several researchers have used some form of yield criteria to predict whether rapid deformation of some pavement layers is likely to occur. Freeman and Carpenter (22) have shown that situations exist where permanent deformation can occur in asphalt pavements under a relatively small number of load repetitions. They used the ratio between the octahedral shear stress and shear strength developed under loading to predict rapid deformation in asphalt concrete layers. Ameri-Gaznon and Little (4,23) used the same

criterion to predict rapidly developing permanent deformation in asphalt concrete pavements.

The octahedral shear stress ratio, as used by Ameri-Gaznon and Little (4), is related to the Mohr-Coulomb yield theory in that a shear stress is compared to a shear strength which is dependent on the state of stress and the two material parameters, cohesion (c) and angle of friction (ϕ). The octahedral shear stress can be expressed as (21):

$$\tau_{oct} = \sqrt{\frac{2}{3} J_2} \tag{2.1}$$

where J_2 is the second deviatoric stress invariant, defined as:

$$J_2 = \frac{1}{6}\left[(\sigma_{11} - \sigma_{22})^2 + (\sigma_{22} - \sigma_{33})^3 + (\sigma_{33} - \sigma_{11})^2 \right] + \sigma_{12}^2 + \sigma_{23}^2 + \sigma_{13}^2 \tag{2.2}$$

and σ_{ij} are components of the stress tensor. The octahedral shear stress given by equation 2.1 is compared to the octahedral shear strength, which, for triaxial conditions ($\sigma_{22} = \sigma_{33}$), is calculated as (4):

$$\tau_{oct\text{-}strength} = \left[\frac{2\sqrt{2}}{3 - \sin(\phi)}\right][\sigma_{oct} \sin(\phi) + c \cos(\phi)] \tag{2.3}$$

Where ϕ = angle of internal friction,

c = cohesive strength, and

σ_{oct} = $(1/3)(\sigma_{11} + \sigma_{22} + \sigma_{33})$

The ratio of octahedral shear strength to theoretical (predicted) shear stress is thus used to predict whether rapid deformation of the asphalt layer is likely to take place. The closer the ratio of octahedral shear strength to octahedral shear stress is to one, the more likely the rapid development of plastic deformation. Perdomo and Button used the octahedral strength/stress ratio to calculate the likelihood of plastic deformation taking place for different pavement types and different wheel configurations (24). By making

contour plots of the octahedral shear strength to shear stress ratio, the critical stress points within the asphalt surface were determined.

Based on their study, Perdomo and Button drew the following conclusion (24): for all pavement and load conditions, there was a critical value of the resilient elastic modulus, above which the shear stress ratio changed very little. This was attributed to the high cohesive strength of the asphalt at higher moduli values. The likelihood of rapid plastic deformations taking place was much higher for the cases where a low modulus value was assigned to the asphalt.

Material Considerations

All of the researchers referred to above, in addition to investigating the stresses that develop under loading, concentrated a significant part of their research on determining which material characteristics are conducive to situations where rapid plastic deformations develop under loading. Although all of this work was devoted to asphalt concrete materials, it is important to note that, in many cases, the cause of failure (i.e., rapid plastic deformations) can be attributed not to an excessive load but to material characteristics. This observation also has significance with respect to the study of pavement response under superheavy loads. It is conceivable that a pavement structure may seem adequate to sustain a superheavy load if the material parameters used in the analysis are those which are typical for a well designed and stable material. However, if one or more of the pavement layer materials prove to be poorly designed or susceptible to rutting, then rapid plastic deformations may occur. For this reason, the material parameters are vital determinants in predicting the likelihood of failure under abnormal loading conditions.

Perdomo and Button noted that some of the situations which contribute substantially to plastic deformations in asphalt concrete pavements are (24): excessive asphalt cement content, excessive fine aggregate, and round shape and smooth texture in fine aggregate. Clearly, these factors cannot be controlled when planning and analyzing the movement of a superheavy load. However, it may be possible to investigate beforehand whether any of these characteristics, which are substantial contributors to plastic deformation, are present

in the pavement materials of the planned superheavy load route. The highway engineer should then take this into account in the subsequent analysis.

SUMMARY AND CONCLUSIONS

In summary, the expected mode of failure under superheavy loads is a rapid, load-induced shear failure as opposed to the long-term accumulation of permanent deformation and fatigue due to repeated load applications. Thus, the evaluation of structural adequacy under superheavy loads is concerned with the potential for material yielding. Very little work has been done in pavement engineering wherein yield criteria were used. Of the studies reviewed, the Mohr-Coulomb yield criterion was used to predict the potential for permanent deformation. In all cases, interest was centered around the asphalt concrete layer.

Consequently, there is a need to conduct a broader investigation in developing a procedure for permitting superheavy load moves based on a yield criterion. This research effort must accomplish the following:

1. Evaluate the sensitivity of the predicted yield function to material parameters;
2. Evaluate different pavement response models and the effects of differences between models on the predicted yield function;
3. Establish the effects of different load configurations on the predicted yield function considering the range in vehicle configurations used in superheavy load moves; and
4. Integrate the research findings into a procedure for permitting superheavy load moves that is both accurate and implementable.

CHAPTER III

DESCRIPTION AND VERIFICATION OF THE RESPONSE MODEL

BACKGROUND

The analysis and design of flexible pavements currently rely on two basic pavement modeling techniques. The first is the layered elastic approach, which is a closed form solution to the mathematical problem of determining a stress or displacement field within an elastic half-space. Several computer programs such as BISAR (5) and WESLEA (6) are popularly used by practitioners and researchers alike. The second approach is the finite element technique, which is a numerical solution to the determination of a displacement field within an elastic medium. The advantages and disadvantages associated with each approach have been described by several researchers. Huang (1) made a fairly detailed study of the results obtained by each method. In general, the layered elastic approach is an extremely useful and easily implemented method of calculating the design parameters in a pavement structure. The most important disadvantage of the layered elastic programs is their inability to account for the effects of material non-linearity.

The finite element approach, by virtue of its formulation, is well suited to modeling the nonlinear behavior of pavement materials. Several finite element programs, such as ILLIPAVE (8) and MICHPAVE (25), are able to account for material nonlinearity. Not many researchers have studied the effects the linearity assumption has on predictions of pavement life, but it is generally assumed that the finite element solution is more accurate in modeling pavement behavior. Most finite element programs are not well suited for routine applications and require knowledge of how to construct a finite element mesh, which boundary conditions to use, and other criteria.

The fundamental goal of this research is to develop a method by which road authorities can routinely analyze superheavy load routes and predict whether permanent deformation is likely to occur under the estimated load and material conditions. Naturally, this methodology would need to be easily implementable on a routine basis in field offices

with limited computer facilities. Recognizing that the finite element approach is more accurate with respect to material characterization, but taking into account the difficulties associated with its implementation, the following approach was adopted: first, a finite element program was developed which was capable of accurately characterizing nonlinear material behavior. The predictions made by using the finite element program were then compared to those made by the simpler layered elastic approach. This comparison was then used to investigate the effects that the assumption of linearity have on the calculated yield function. Finally, these findings were used to construct a methodology by which superheavy load moves can be analyzed on a routine basis.

Chapter V describes the comparison of the different modeling procedures in detail. In the following, a description of the finite element program developed for the purposes of this study will be given. Also described here is the verification of the finite element model by means of laboratory testing and simulation. Because the underlying theory of the finite element method is well documented (19, 26, 27), it will not be reiterated here. Instead, only those elements of the program that were specifically developed in the course of this study will be described.

The program used in this study is a modified version of the program described by Owen and Hinton (19). The program utilizes an axisymmetric formulation and makes use of 8-node serendipity quadrilateral elements which assume a quadratic variation of the displacement field within the element. The program described by Owen and Hinton was modified to account for the material nonlinearity by making use of stress dependent moduli and Poisson's ratios. The load is applied in an incremental fashion. For each load increment and each element, the stress dependent moduli and Poisson's ratios are calculated iteratively until convergence is achieved. This methodology is similar to that used by researchers such as Uzan and Scullion (28).

MODELING OF STRESS DEPENDENT RESILIENT MODULI

If a standard load is applied to a well designed pavement, the resulting strain should be nearly completely recoverable and proportional to the applied load. Although there is some plastic deformation involved in each load application, this strain is normally small and causes only long term deterioration of the pavement structure. Figure 3.1 shows the typical stress-strain pattern that results from a repeated load test. The resilient modulus (often denoted by M_r or E_r) is defined as the ratio of the repeated deviatoric stress to the recoverable part of the axial strain (1).

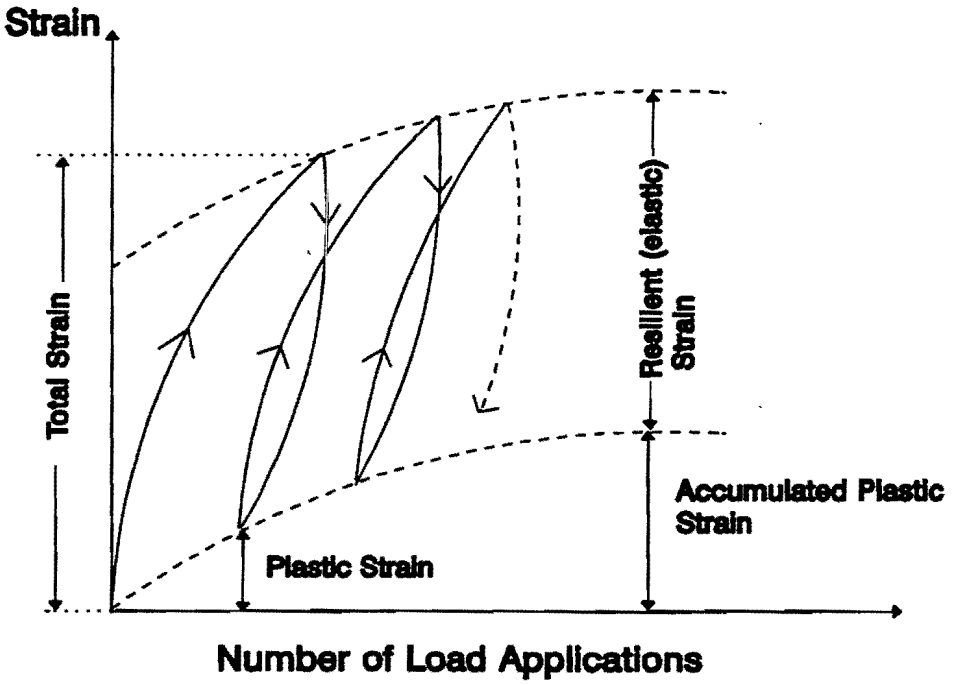

Figure 3.1. Typical Strains Resulting from a Repeated Load Test.

In response models that consider non-linear material behavior, the resilient modulus has often been expressed as a function of the state of stress (29,30,31,32). Hicks and Monismith (33) reported the resilient modulus - stress relationship to be of the following form:

$$E_r = k_1 \ (I_1)^{k_2} \tag{3.1}$$

Where Er is the resilient modulus; I_1 is the first stress invariant; and k_1 and k_2 are material constants. The ILLIPAVE (8) and MICHPAVE (25) programs are examples of finite element programs that include resilient moduli - stress relationship expressed by equation 3.1. Values for k_1 range between 1600 and 9000, while those of k_2 vary approximately between 0.3 and 0.6 (1,29,34,35).

A more complete description of the stress dependency of the resilient modulus is expressed by the following (32,36,37):

$$E_r = (k_1 \ Pa) \left(\frac{I_1}{Pa} \right)^{k_2} \left(\frac{\tau_{oct}}{Pa} \right)^{k_3} \tag{3.2}$$

Where I_1 is the first stress invariant, τ_{oct} is the octahedral shear stress, k_1 to k_3 are material constants, and Pa is the atmospheric pressure which is used to express the results in a nondimensionalized form. The relationship expressed by equation 3.2 is often referred to as the Universal Soil Model because it can be used to express the resilient characteristics of both fine and coarse grained materials. Because of its generality, and because of the relationship that it bears to the stress dependent Poisson's ratio, equation 3.2 was adopted to describe the stress dependent resilient modulus in the response model described here.

MODELING OF STRESS DEPENDENT POISSON'S RATIO

Analytical and Numerical Solutions for the Stress Condition - Poisson's Ratio Relationship

For an elastic isotropic material, the relationship between stress and strain can be described completely in terms of two independent constants, the elastic modulus and the Poisson's ratio. In the case of pavement materials, the laboratory determined stress dependent resilient modulus is normally used as an elastic modulus in modeling (1).

Until recently, only the elastic modulus was considered to be stress dependent, with a constant value being used for the Poisson's ratio. Various researchers have reported the stress dependent nature of the Poisson's ratio of particulate materials (38,39,40). The stress dependent nature of the Poisson's ratio can easily be surmised from Figure 3.2. Figure 3.2 shows that the volume change with increasing strain or stress will depend on the density of the material. The density or state of packing of the material will clearly be dependent on the volumetric stress component, or overall confinement. Figure 3.2 also shows that dense granular materials may also start to dilate at certain levels of stress or strain.

Because of the assumption of an isotropic, homogeneous material, traditional layered elastic programs can only accommodate materials with a Poisson's ratio below 0.5. For most granular pavement materials, a fixed value for Poisson's ratio is normally used. This value typically lies within the range of 0.30 to 0.40 (1). However, when a material dilates, Poisson's ratios can be as high as 1.2 or higher (38,39). This tendency to dilate is caused by the motion of particles that tend to roll over one another when a shearing stress is applied to the material.

In the past, the Poisson's ratio and the dilational behavior of dense granular materials has often been linked to the ratio of the major to minor principal stresses, also referred to as the principal stress ratio (28,38). Most researchers agree that dense granular materials start to dilate when the principal stress ratio exceeds a certain value. Frydman (40) has shown that dense sands start to dilate at a constant principal stress ratio of 3.5. Most of the relationships used to express the stress dependency of the Poisson's ratio are empirical in nature. Allen (34) expressed the relationship between the Poisson's ratio and the stress state in terms of the principal stress ratio, which was used in a polynomial form. In Allen's study, various Poisson's ratio-principal stress ratio relationships were derived for different qualities of granular materials. Figure 3.3 shows a plot of some of the relationships derived by Allen (34).

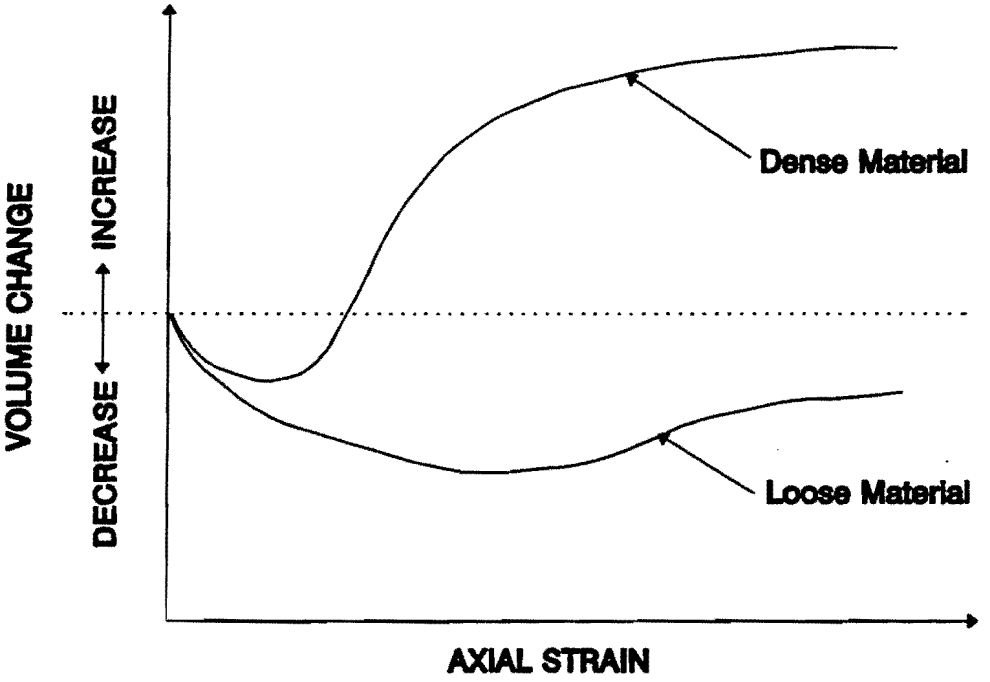

Figure 3.2. Volume Change Characteristics for Granular Materials (From (17)).

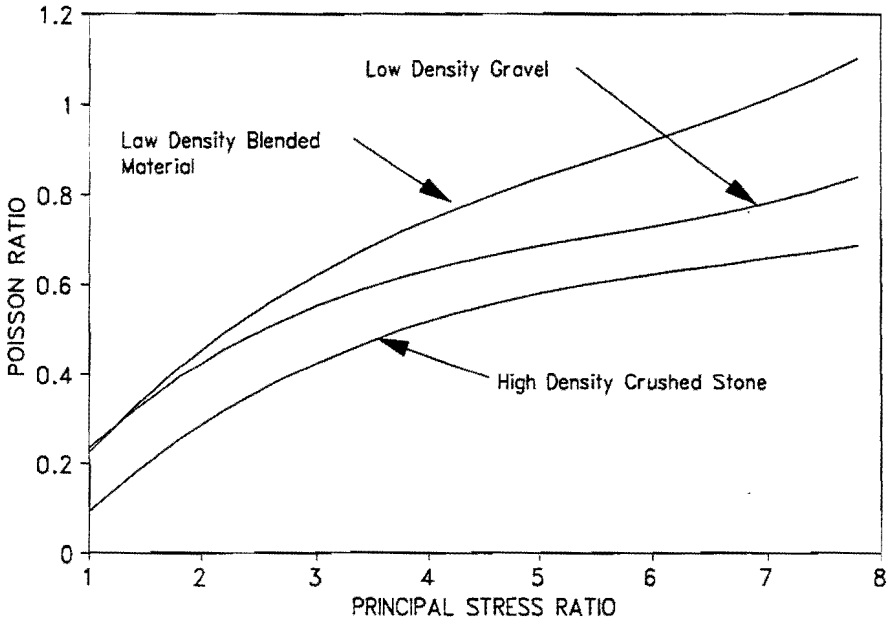

Figure 3.3. Empirically Based Relationships between Poisson's Ratio and Principal Stress Ratio (From (34)).

In recent years, some researchers have tried to determine a more theoretical basis for relating the Poisson's ratio to the stress state. Chen and Saleeb (41), and Lade and Nelson (42) derived a relationship between the Poisson's ratio and the resilient modulus based on a thermodynamic constraint. Uzan (39) used a relationship between the resilient modulus expression given by equation 3.2 and the thermodynamic constraints to derive an expression that relates the stress state and the rate of change of the Poisson's ratio with a changing stress state, to the Poisson's ratio. The derivation of this equation is based on the principle of the conservation of energy and the path independence of the energy density function, W. This procedure is described in some detail by Liu (43) and is repeated in Appendix B for completeness. Based on the above mentioned energy considerations, the following relationship between the Poisson's ratio and the stress state can be derived:

$$\frac{2}{3}\frac{\partial \nu}{\partial J_2} + \frac{1}{I_1}\frac{\partial \nu}{\partial I_1} = \nu\left(\frac{2}{3}\frac{k_3'}{J_2} + \frac{k_2}{I_1^2}\right) + \left(-\frac{1}{3}\frac{k_3'}{J_2} + \frac{k_2}{I_1^2}\right) \tag{3.3}$$

Where: ν = Poisson's ratio

k_3' = $k_3/2$

k_1, k_2, k_3 = material constants (the same as those used in equation 3.2)

I_1 = normalized first stress invariant

J_2 = normalized second invariant of the deviatoric stress tensor

Equation 3.3 is a quasi-linear partial differential equation of the first order which can be reduced to the solution of the following system of differential equations (39,44):

$$\frac{dI_1}{\frac{1}{I_1}} = \frac{dJ_2}{\frac{2}{3}} = \frac{d\nu}{\nu\left(\frac{k_2}{I_1^2} + \frac{2}{3}\frac{k_3'}{J_2}\right) + \left(\frac{k_2}{I_1^2} - \frac{1}{3}\frac{k_3'}{J_2}\right)} \tag{3.4}$$

The solutions of the above system of equations were obtained by Uzan (39). Two general solutions are:

$$u_1 = 3\ J_2 - I_1^2 \tag{3.5}$$

and

$$u_2 = \frac{v}{I_1^{k_2} J_2^{k_3'}} - \frac{3^{k_3'}}{2(I_1^2 - 3J_2)^{\frac{k_2}{2}+k_3'}} \left[-k_2 B_v \left(\frac{k_2}{2} + k_3',\ -k_3' + 1 \right) + k_3 B_v \left(\frac{k_2}{2} + k_3',\ -k_3' \right) \right] \tag{3.6}$$

Where $B_v(x,y)$ is the incomplete beta function, with $v = 1 - 3J_2/I_1^2$.
There are actually an infinite number of solutions for the system of equations given by equation 3.4. Based on experimental results, Uzan (39) showed that u_1 and u_2 can be related by means of two additional material constants k_4 and k_5:

$$u_2 = k_4(-u_1)^{k5} \tag{3.7}$$

The values of k_4 and k_5 need to be determined experimentally. Once k_4 and k_5 have been determined, the Poisson's ratio can be determined in terms of the stress state and the material constants, k_2 to k_3, by using equations 3.5 to 3.7.

The stress dependent Poisson's ratio determination described above has been successfully applied to a finite element program by Liu (43). However, it was found that the analytical solution described in the above can be indeterminate for certain combinations of I_1 to J_2. It was, therefore, decided to include a numerical solution to the stress dependent Poisson's ratio relationship given by the partial differential equation (3.3) in the response model. The numerical solution would also eliminate the need for determining the two additional material constants k_4 and k_5, provided that the user can supply suitable boundary conditions at the start of the solution process. The numerical solution to equation 3.3 is determined by simple substitution of the backward difference formula (45,46):

$$\frac{\partial v}{\partial J_2} = \frac{v_j^i - v_{j-1}^i}{k} \tag{3.8}$$

$$\frac{\partial \nu}{\partial I_1} = \frac{\nu_i^j - \nu_{i-1}^j}{l} \tag{3.9}$$

Where l,k = step sizes for increasing I_1 and J_2, respectively, and

i,j = counter for I_1 and J_2 respectively

Where $\nu_j^i - \nu_{j-1}^i$ denotes the difference between the Poisson's ratio for J_2 at j and j - 1 for a fixed value of I_1 represented by i. By setting equations 3.8 and 3.9 into equation 3.3 and after some algebraic manipulation, the iterative formula for determining the Poisson's ratio for a given stress condition can be written as:

$$\nu_j^i = \frac{\left[\left(\frac{2}{3k}\right) * \dot{\nu}_{j-1}^i + \left(\frac{1}{l*I_1}\right) * \nu_j^{j-1} - \frac{k_3'}{3J_2} + \frac{k_2}{I_1^2}\right]}{\left[\frac{2}{3k} + \frac{1}{l * I_1} - 2\frac{k_3'}{3J_2} - \frac{k_2}{I_1^2}\right]} \tag{3.10}$$

Equation 3.10 is solved by choosing a step size for increasing I_1 and J_2 and then increasing I_1 and J_2 from a fixed boundary condition for which the Poisson's ratio is known.

Sensitivity of the Numerical Solution to Different Boundary Conditions

The analytical solution given by equations 3.5 through 3.7 includes the boundary conditions needed for solving the partial differential equation 3.3. However, the numerical solution of equation 3.3 proceeds from a given boundary condition. Although this requires the user to estimate boundary conditions, it does provide some flexibility in choosing suitable boundary conditions for different applications. In the following, an analysis is described in which the purpose was to determine the sensitivity of the Poisson's ratio for different boundary conditions.

As a way of verifying the response model described in this chapter, laboratory tests were conducted on samples of crushed limestone and a uniformly graded sand. The test procedure was similar to that of a normal triaxial test, but the tests were conducted in an

air pressure chamber. Three axial and three lateral deformation measurements were taken at 120° offsets while the load on the sample was monotonically increased. For each material type, three tests were run, each at a different confining pressure. Confining pressures of 13.8, 34.5, and 69 kPa (2, 5, and 10 psi) were used.

By making use of the lateral and axial strains measured in the laboratory, the Poisson's ratio at different levels of stress could be determined. Figures 3.4 through 3.7 show the laboratory measured Poisson's ratio plotted versus the I_1 and J_2 (based on the stresses applied to the laboratory sample) for the different material types. It should be noted that some fluctuation of the Poisson's ratio was originally noted at the beginning of each test. At this stage of the loading procedure, the measured strains are very small compared to the strains measured at higher load levels. This means that a small variation in strain coupled with the error inherent in laboratory measuring procedures can lead to large fluctuations in the measured Poisson's ratio at low stress levels. These fluctuations, which were clearly visible in the measured data (especially in the case of the crushed limestone), are not considered to be representative of actual field conditions. For this reason, the first few data points were removed from the measured data. Naturally, this complicates any attempt to gain insight into the behavior of the Poisson's ratio at low stress levels, which could otherwise have provided a clear indication of boundary conditions. However, valuable insight can still be gained from the consideration of the nature of the relationship between stress and Poisson's ratio. For instance, Figures 3.5 and 3.7 clearly show that the Poisson's ratio tends to increase from an initial low value as J_2 increases. Figure 3.5 also shows that the Poisson's ratio tends to increase more rapidly at lower levels of confinement. This is expected since higher confining pressures would naturally tend to restrain lateral deformations. However, this was not observed in the case of the crushed limestone where somewhat erratic trends were observed, namely that the highest level of confinement showed a higher Poisson's ratio. The reason for this is not clear. A possible explanation may be that some particle rearrangement had taken place when the confining pressure was applied.

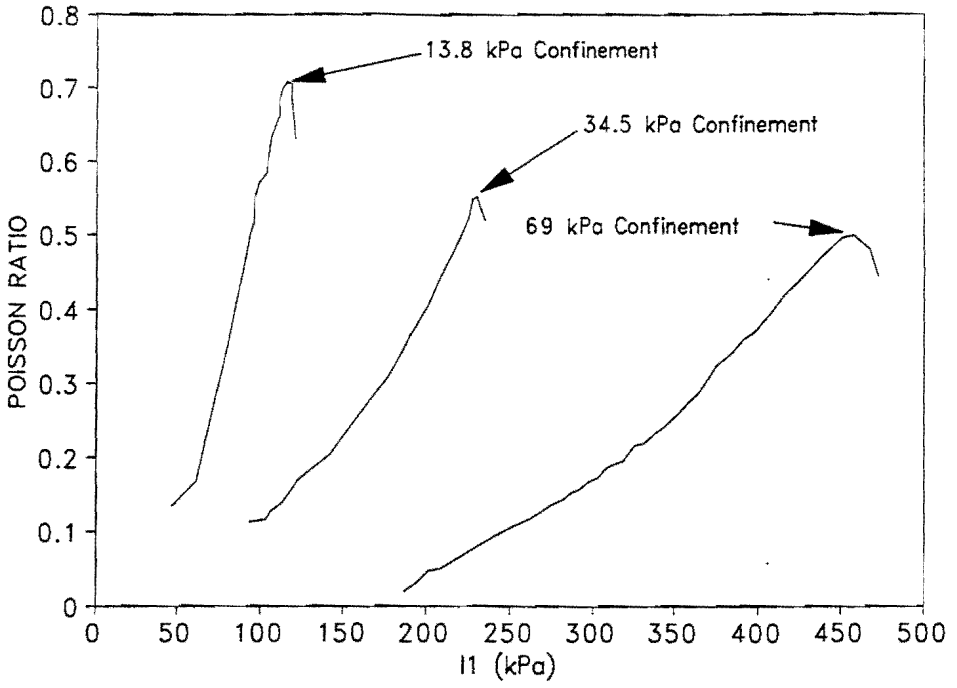

Figure 3.4. Measured Poisson's Ratio vs. I_1 for Sand.

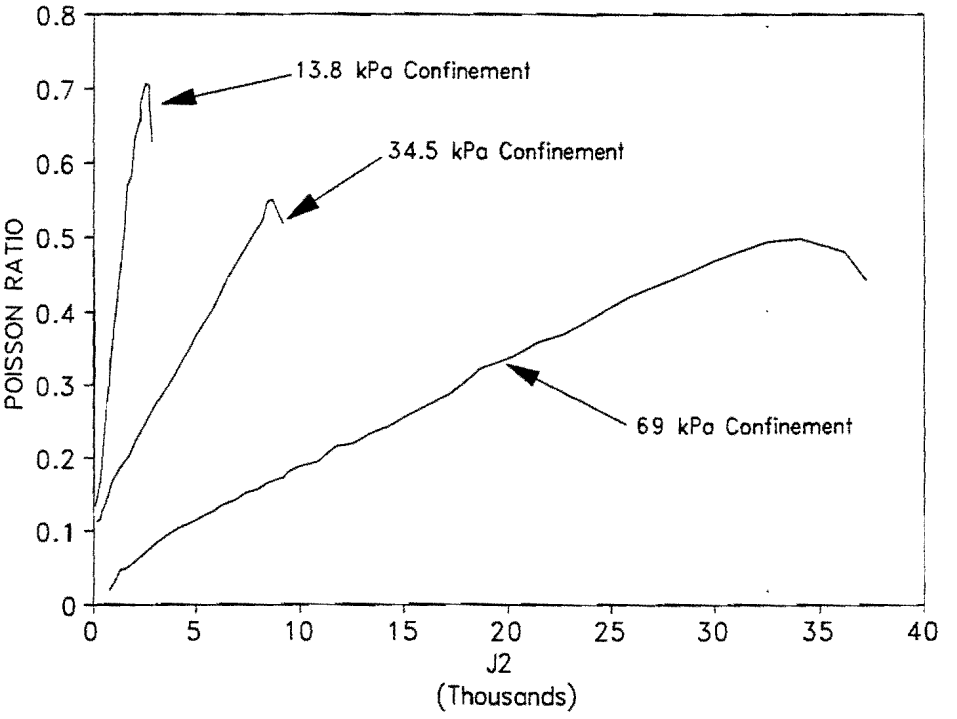

Figure 3.5. Measured Poisson's Ratio vs. J_2 for Sand.

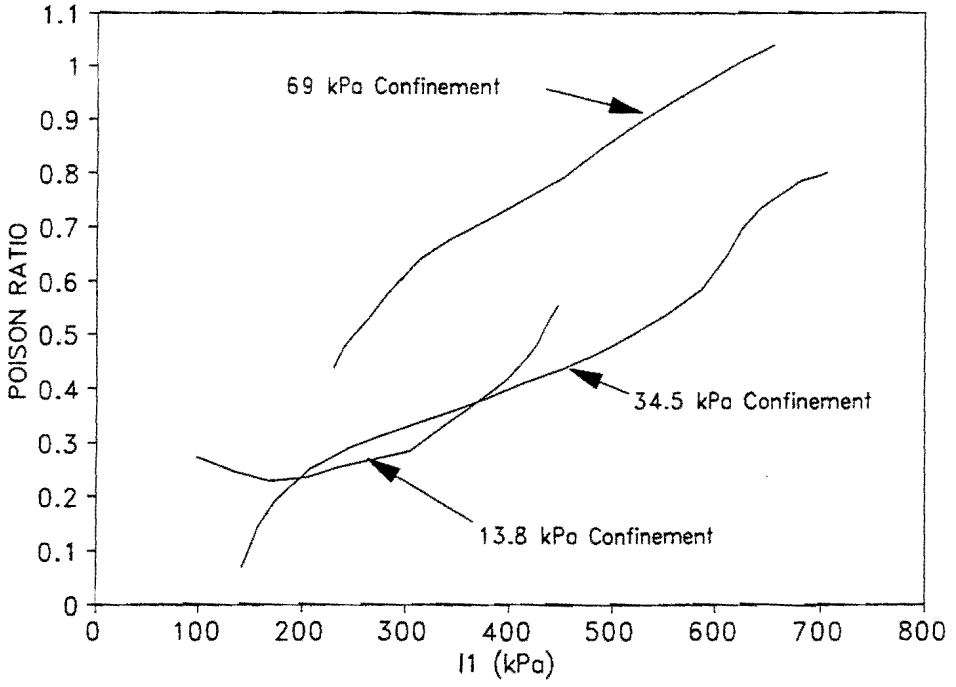

Figure 3.6. Measured Poisson's Ratio vs. I_1 for Crushed Limestone.

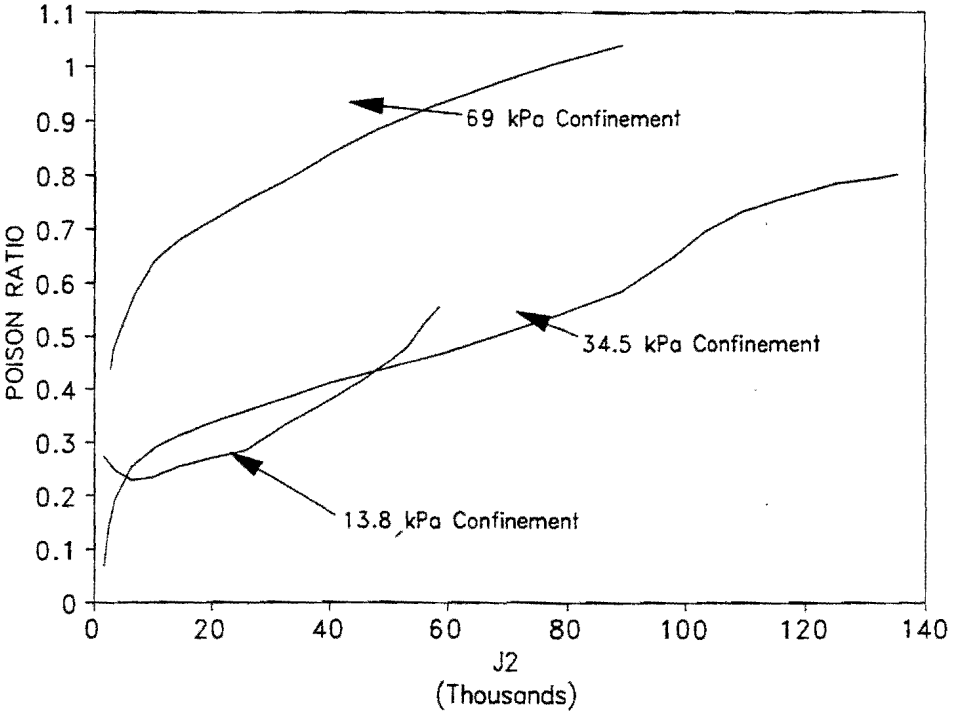

Figure 3.7. Measured Poisson's Ratio vs. J_2 for Crushed Limestone.

The large particle size of crushed limestone makes accurate point measurements somewhat difficult. It may be that a very different lateral deformation would be measured at points that are closely situated on the laboratory sample, which makes it difficult to generalize the behavior of the sample as a whole. This may be caused by slipping of the sensors attached to the sample or by movement of the particles themselves. Perhaps the trends observed in the case of the more finely grained sand material are more revealing in this regard. Figures 3.4 and 3.5 show that the Poisson's ratio at a low level of stress tends to assume low values between 0.0 and 0.2. Figure 3.5 shows that this initial Poisson's ratio tends to be lower for higher levels of confinement. The Poisson's ratio then increases as the shear component of the stress tensor (characterized by J_2) increases. The rate at which the Poisson's ratio tends to increase is dependent on the volumetric component of the stress state (characterized by I_1).

Figures 3.8 and 3.9 show the results of a simulation of the laboratory test conducted on sand as described above. In this simulation, the numerical solution procedure described by equation 3.10 was used for solving equation 3.3. The boundary conditions used were similar to those observed for sand, and are tabulated in Table 3.1.

The predicted Poisson's ratio is not only dependent on the stress state, but also on the material constants. The non-linearity constants (k_1 to k_3) for the sand have to be estimated and, as a result, there should be some differences between the absolute values of the Poisson's ratios shown in Figures 3.4 and 3.5, and those shown in Figures 3.8 and 3.9. However, it is clear from Figures 3.8 and 3.9 that the observed relationship between stress and the Poisson's ratio is captured reasonably well by equation 3.3.

The boundary conditions needed for the numerical solution should be supplied in a form similar to that shown in Table 3.1. That is, a minimum Poisson's ratio at an initial stress state needs to be supplied. As seen from Figures 3.4 through 3.7, the Poisson's ratio is normally small (below 0.3) in the low stress range. The Poisson's ratio then increases as J_2 increases. It can easily be visualized that the Poisson's ratio will be close to zero as long as the deviatoric component of the stress state is also close to zero. For

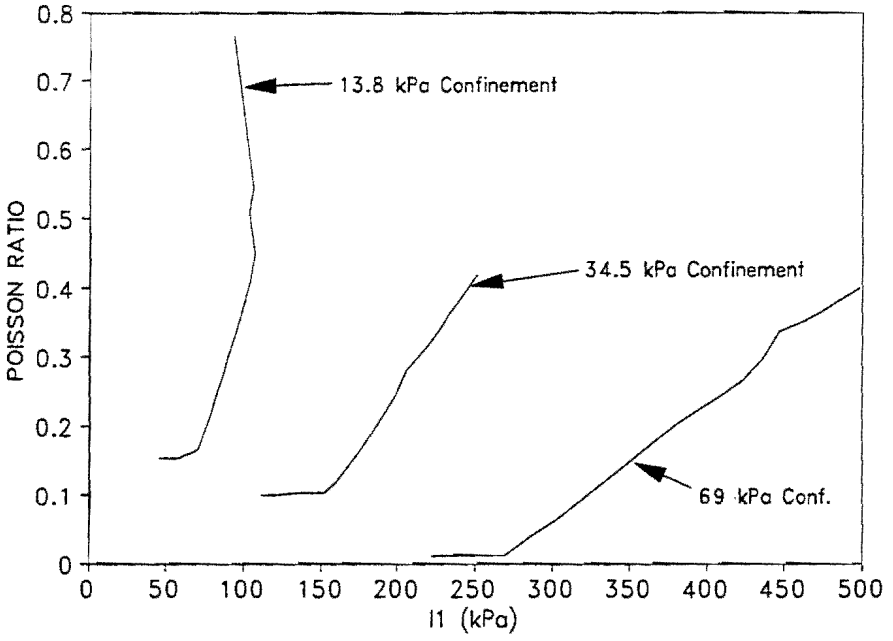

Figure 3.8. Calculated Poisson's Ratio vs. I_1 for Sand.

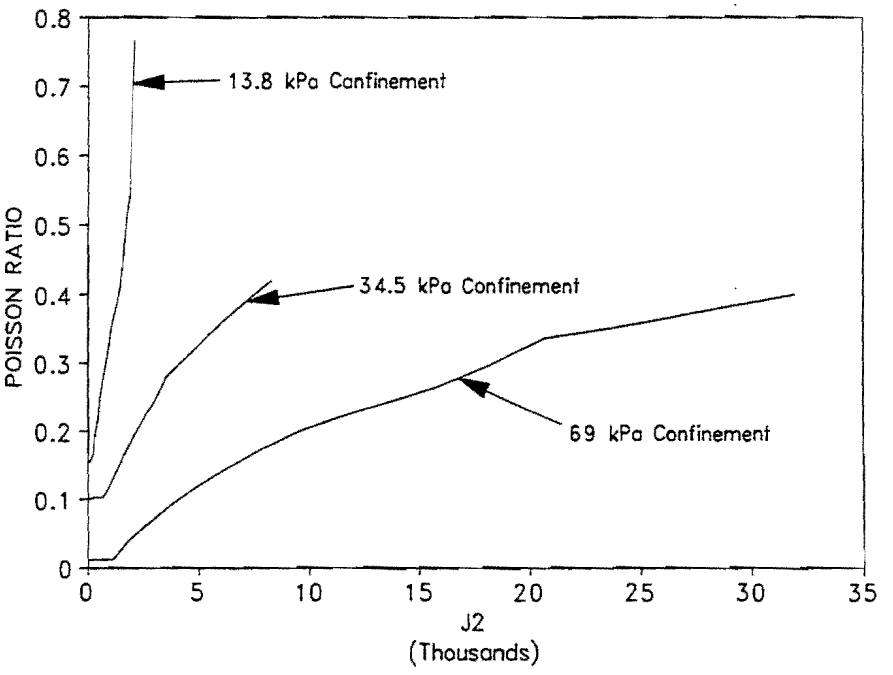

Figure 3.9. Calculated Poisson's Ratio vs. J_2 for Sand.

Table 3.1. Boundary Conditions Used in Simulated Laboratory Test.

Confining Pressure (kPa)	Initial Poisson's Ratio	Initial Stress Condition
13.8	0.15	$I_1, J_2 = 34.5$
34.5	0.10	$I_1, J_2 = 103.5$
69.0	0.01	$I_1, J_2 = 172.5$

applications in the analysis of pavement structures, therefore, a low initial Poisson's ratio can be expected in the absence of loads.

The sensitivity of the Poisson's ratio to various boundary conditions is shown in Figure 3.10. Figure 3.10 was obtained by using typical stress values that would result from the application of a 44.5 kN single wheel load to a medium thick pavement structure. Two sets of material coefficients, k_2 and k_3, were used to represent a coarse and fine grained material. Different boundary values for the Poisson's ratio were then assumed, and the corresponding Poisson's ratios were then determined by using the numerical solution procedure described by equation 3.10. The boundary conditions 1 to 3 referred to in Figure 3.10 are given in Table 3.2. Figure 3.10 shows that the predicted Poisson's ratio is fairly insensitive to changes in the initial condition, meaning that the Poisson's ratio does not fluctuate much with small changes in the boundary conditions. This was true for both the fine-grained and coarse-grained material coefficients.

Comparison Between Analytical and Numerical Solutions for the Poisson's Ratio Equation

In order to validate the more direct numerical approach to the solution of equation 3.3, a comparison between the analytical and numerical solution procedures was undertaken. In order to accomplish this comparison, a data base of 67 randomly generated values of I_1 and J_2, and their normalized values was developed. Values for k_2

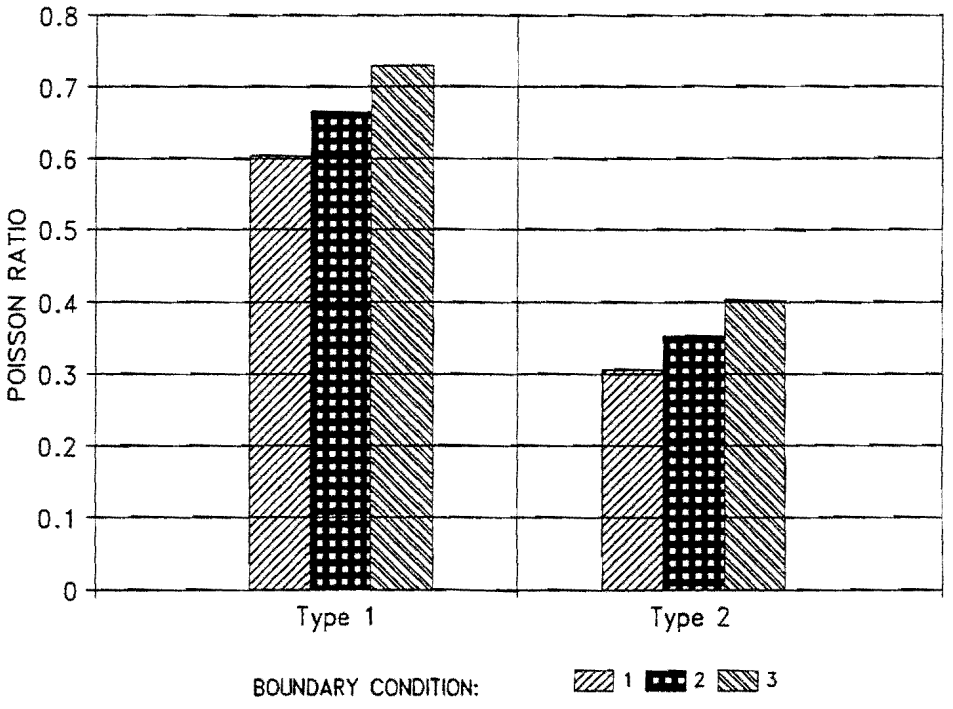

Figure 3.10. Sensitivity of Predicted Poisson's Ratio to Different Boundary Conditions (Note: Boundary Condition Number Refers to Table 3.2).

Table 3.2. Boundary Conditions Used in Sensitivity Analysis.

Boundary Condition Number	Initial Poisson's ratio	Initial Stress Condition
1	0.10	$I_1, J_2 = 13.8$
2	0.20	$I_1, J_2 = 13.8$
3	0.30	$I_1, J_2 = 13.8$

and k_3, as well as for the boundary conditions, were then chosen. The values for k_2 and k_3 were chosen to represent a coarse granular material. The numerical solution procedure described by equation 3.10 was then used to determine the Poisson's ratio corresponding to each of the generated values for I_1 and J_2.

The determination of the analytical solution values proceeded as follows: first the incomplete beta function values were calculated corresponding to the arguments dependent on k_3 and k_2, as shown in equation 3.6. Then, values for u_1 were determined from equation 3.5 using the data base of I_1 and J_2 values. The k_4 and k_5 values that correspond to the chosen set of boundary conditions were then determined. To do this, the first 20 of the 67 data points were used together with their numerical solutions for the Poisson's ratio. Using the numerically predicted Poisson's ratios, u_2 values corresponding to each of the 20 data points were determined. The u_2 and $-u_1$ values of these 20 points were then used in a log-log regression to determine the values of k_4 and k_5 ($-u_1$ and u_2 are related by equation 3.7). Once the k_4 and k_5 values were determined, the $-u_1$ values of the remaining points were used to predict u_2 values for each of the remaining points in the data base. The u_2 values were then used together with the normalized values of I_1, J_2, k_3, and k_2 in equation 3.6, which was then rearranged to solve for the Poisson's ratio.

Once the analytical Poisson's ratios for each of the remaining data points were calculated, a graphical comparison was made between the numerical and analytical predictions for the Poisson's ratio. Figure 3.11 shows the numerically predicted Poisson's ratios plotted versus the analytical predictions for the Poisson's ratio. Figure 3.12 shows the data points and regression line that were used to determine k_4 and k_5. Figure 3.11 shows a good correlation between the analytical and numerical solutions for the Poisson's ratio. There is a slight loss in accuracy for the numerical procedure at higher values of the Poisson's ratio. However, for the range of Poisson's ratios that can be expected under most conditions (i.e., 0.3 to 1.0), the comparison seems acceptable.

The above procedure was repeated for a different set of boundary conditions, with the same set of I_1 and J_2 values being used. This was done in order to ascertain whether

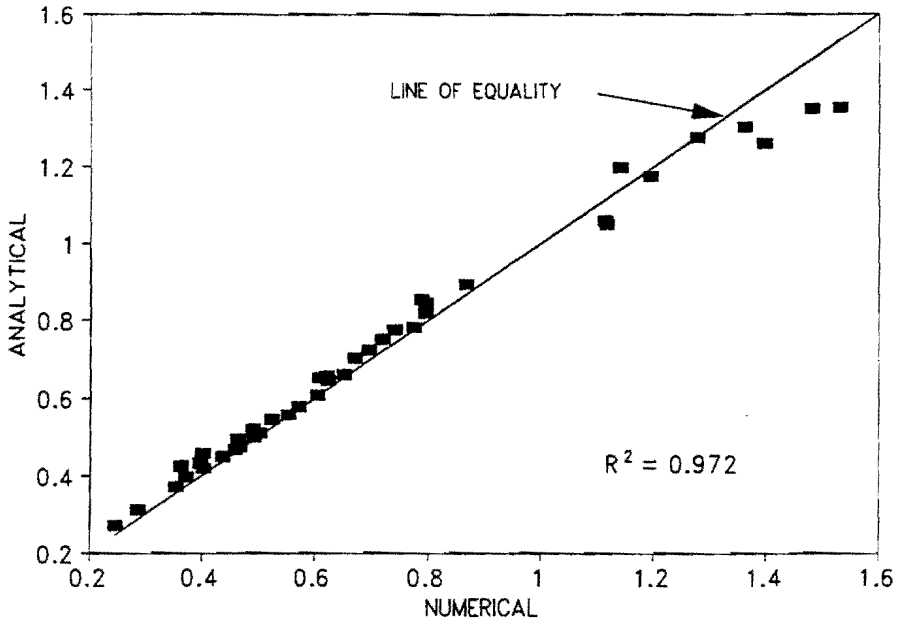

Figure 3.11. Comparison of Poisson's Ratio Predictions by Analytical and Numerical Methods (First Boundary Condition).

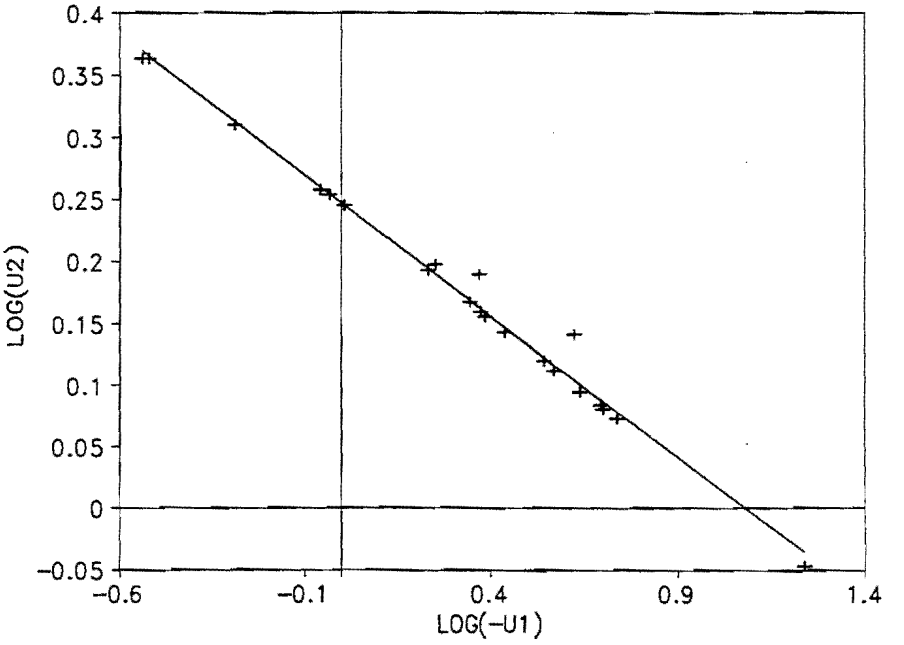

Figure 3.12. Determination of k_4 and k_5 Parameters (First Boundary Condition).

the choice of boundary conditions has an effect on the correlation between the numerical and analytical Poisson's ratio predictions. The new boundary conditions were again used to find k_4 and k_5 values that are compatible with the chosen boundary conditions. Table 3.3 summarizes the initial Poisson's ratio values as well as the k_4 and k_5 values found for the two boundary conditions used. In Table 3.3, boundary condition 1 refers to the boundary conditions used in obtaining Figures 3.11 and 3.12, while boundary condition 2 refers to the boundary condition used to obtain Figure 3.13.

Figure 3.13 indicates that the change in boundary conditions had a very small effect on the correlation between the analytical and numerical procedures. A very small change in R^2 values was observed with a change in boundary conditions. The comparison between the methods is still reasonably good. Table 3.3 shows that the change in boundary conditions had a relatively small effect on the regressed k_4 and k_5 values. This seems to support the earlier observation that the chosen boundary condition has a relatively small influence on the predicted Poisson's ratio.

Modeling of Resilient Dilation in Granular Materials

Perhaps the most significant example of material behavior that cannot be modeled by standard layered elastic programs is the dilation observed in particulate media in a dense state of packing. This effect is considered to be significant because not only layered elastic programs, but also non-linear finite element programs, frequently predict high tensile stresses at the bottom of granular layers on soft subgrades (1).

While it is conceivable that tensile stresses develop in cohesive materials, most granular materials, due to their low apparent cohesion, cannot develop high tensile stresses without failure or decompaction taking place. Furthermore, since the yield function is dependent on the shear stress that develops under loading, which in turn is related to the difference between the major and minor principal stresses, a compressive major principal stress acting together with a tensile minor principal stress results in a high shear stress. This results in the prediction of an overly conservative estimate of the potential for failure.

Table 3.3. Boundary Conditions Used in Comparison of Numerical and Analytical Procedures.

Boundary Condition	Initial Poisson's Ratio	Initial Stress State	Regressed k_4	Regressed k_5
1	0.20	I1, J2 = 34.5	1.766	-0.227
2	0.00	I1, J2 = 34.5	1.650	-0.218

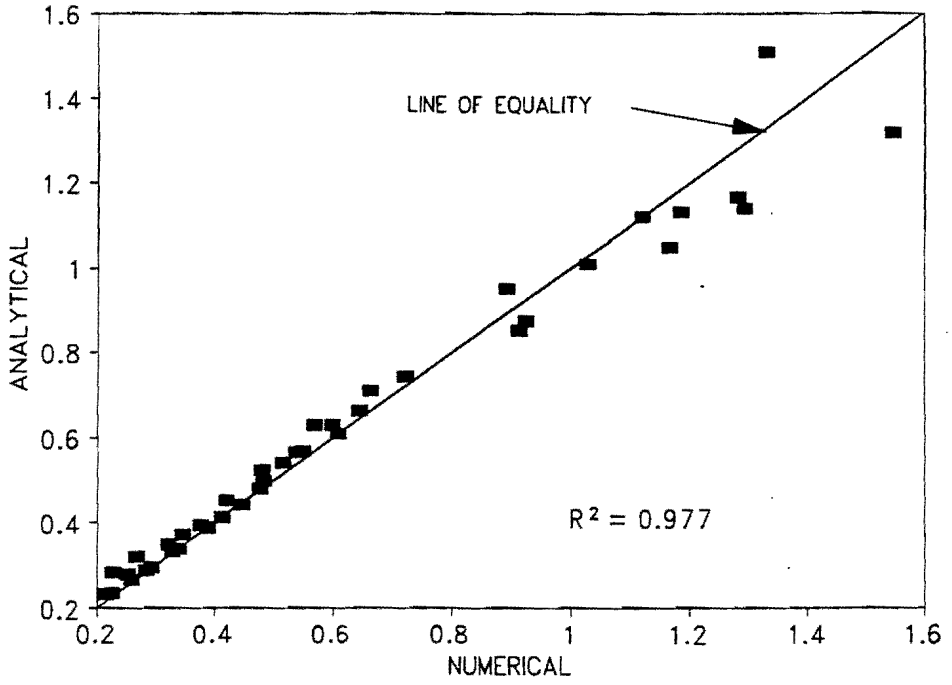

Figure 3.13. Comparison of Poisson's Ratio Predictions by Analytical and Numerical Methods (Second Boundary Condition).

Many researchers have addressed this problem by assuming a confining pressure of zero whenever tensile stresses are encountered in granular layers (1). While generally considered to be conservative, this procedure does not attempt to model the behavior of dense materials that tend to dilate. Also, it was suggested by Heulekom and Klomp that granular bases can sustain small tensile stresses without failing (47). However, the tensile stresses tend to cause local decompaction and a loss in resilient modulus value. For instance, Hicks found that an untreated granular material in an unconfined condition can have a minimum vertical modulus of 34,500 kPa or more (29). Neither the setting of the confining pressures to zero nor the use of a minimum or failure modulus takes account of actual dilation. This is because layered elastic theory is based on the assumption of a homogeneous, isotropic material for which a maximum Poisson's ratio of 0.5 has to be used.

Very little literature exists that describes dilational behavior of dense granular materials. However, most researchers agree that these types of materials start dilating when the principal stress ratio exceeds a certain value (28). The solutions for equation 3.3 suggest that the Poisson's ratio increases as J_2 increases. The rate at which it will increase depends on the volumetric stress component, I_1, and the material properties characterized by k_1 to k_3. The effect that dilatancy has on the stress state is not clear. Most researchers agree that the tendency to dilate results in the material experiencing confining stresses in addition to those induced by the load (28,48). The following statements will illustrate the point. Uzan and Scullion (28) stated:

> "The Witczak, Uzan study (32) indicated that granular material in flexible pavements are in general subjected to stress states with large major to minor stress ratios. Under these conditions, the material may dilate and develop additional confining pressures, (in addition to the pressure induced by compaction)."

Billam (48), commenting on the effects of crushing on the properties of granular materials, stated:

"The principal effective stress ratio at failure decreases with increasing confining pressure due to the suppression of dilatancy, but it does tend towards a lower constant value."

However, the question remains as to how much confining pressure is generated by the tendency to dilate and what factors control the material behavior during the dilating phase. Uzan and Scullion (28) have used the concept of the initial strain method of Zienkiewicz (26) to describe the dilation phenomenon in granular layers. In this method, the strain resulting from load application is decomposed into two parts. Thus,

$$\epsilon_z = \frac{1}{E}\left[\sigma_z - (\mu + \alpha)(\sigma_r + \sigma_\theta)\right] \tag{3.11}$$

or similarly

$$\epsilon_z = \frac{1}{E}\left[\sigma_z - \mu(\sigma_r + \sigma_\theta)\right] - \epsilon_{zo} \tag{3.12}$$

With $$\epsilon_{zo} = \frac{\alpha}{E}(\sigma_r + \sigma_\theta) \tag{3.13}$$

Where

	ϵ_{z0}	=	the initial strain resulting from dilation or excess of strain;
	ϵ_z	=	total vertical strain;
	$\sigma_z, \sigma_r, \sigma_\theta$	=	vertical, radial, and tangential stresses, respectively;
	μ	=	Poisson's ratio (a constant value);
	α	=	factor to describe the additional deformation; and
	E	=	Modulus of Elasticity.

In equation 3.11, the factor $(\mu + \alpha)$ represents the total Poisson's ratio. This consists of a constant part (μ) and a dilatory part (α). The value of the latter part depends on the amount of dilation that takes place.

Uzan and Scullion have applied this approach to the finite element method with success (28). However, this procedure requires that the actual Poisson's ratio be estimated with a high degree of accuracy. An analysis of the sensitivity of the above procedure to small changes in the overall Poisson's ratio ($\mu + \alpha$) has shown that, under typical stress conditions, using a Poisson's ratio of 0.6 instead of (say) 0.5 can lead to a large increase in the predicted confining pressure. Figure 3.14 shows a number of predicted versus measured Poisson's ratios (from reference 39). It is clear from the figure that, although the overall comparison between actual and predicted Poisson's ratios is very good, errors of 0.2 or larger may easily occur. This error may not have a significant effect on the predicted stress state when the applied load is small. However, in the case of superheavy loads where high stresses prevail, a small error in the predicted Poisson's ratio may lead to a significant over or underestimation of the confining stresses. While underpredicting the confining stresses will lead to a conservative estimate of the yield point, overestimating the

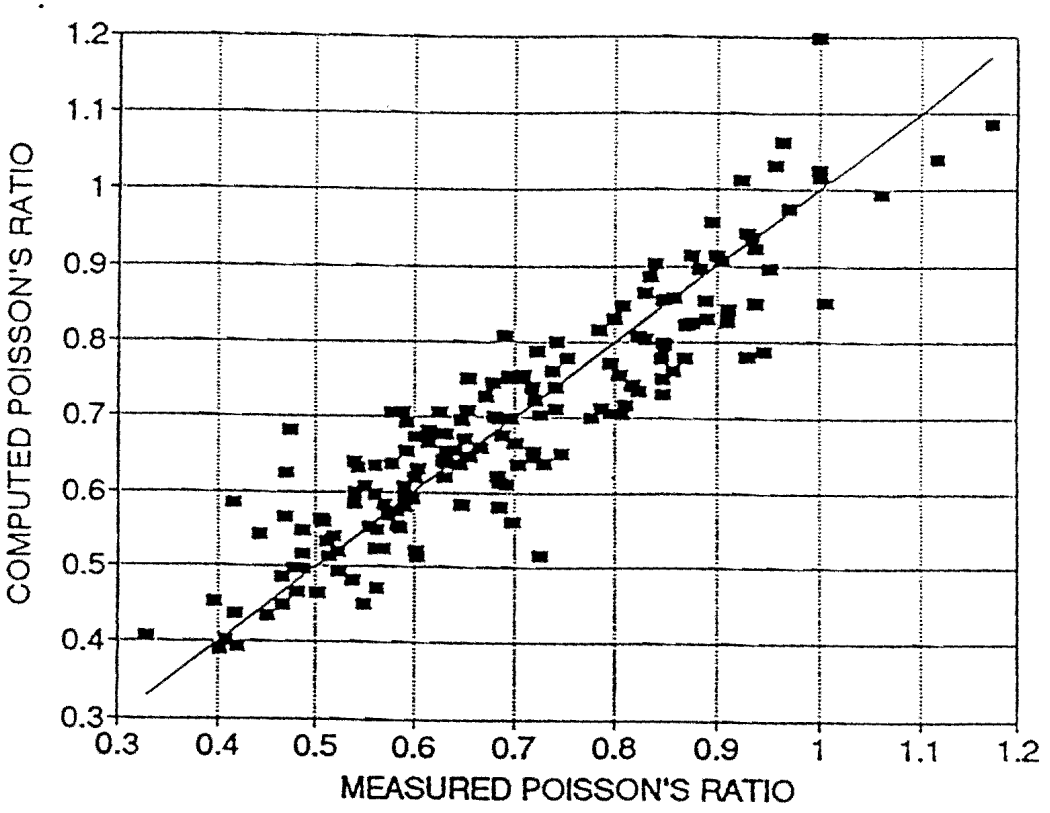

Figure 3.14. Measured and Predicted Poisson's Ratios (From (39)).

confining stresses may lead to a significant overestimation of the material's resistance to shear. The success of the above procedure will, therefore, be largely dependent on the ability of the response model to accurately predict the Poisson's ratio, especially when Poisson's ratios larger than 0.5 are predicted.

The above procedure for predicting stress states under resilient dilation was initially included in the response model. However, an attempt to verify the predicted radial strains by using laboratory data was unsuccessful (the following section discusses this verification procedure in detail). The large stresses predicted by the larger Poisson's ratios also caused severe fluctuations in the stress dependent moduli to take place, which, in turn, led to problems with the convergence of the iterative procedures used to determine stress sensitive moduli and Poisson's ratios. For these reasons, it was decided not to allow any Poisson's ratio larger than 0.48 to be included in the final response model. This means that in its final form, the response model will include a stress sensitive moduli and a stress sensitive Poisson's ratio, but only for Poisson's ratio values below 0.48. This simplification of actual material behavior is conservative, and will not lead to an overestimation of material strength.

VERIFICATION OF THE RESPONSE MODEL

In this section, the results of several laboratory tests will be shown together with the results predicted by the response model. The laboratory tests consisted of triaxial type tests which were conducted in an air pressure chamber. Details of the experimental set-up are shown in Appendix C. Two material types were used, a crushed limestone and a uniformly graded sand. All samples were compacted at optimum moisture content. For each material type, three tests were performed at different confining stress levels. Lateral and axial displacements were measured throughout the test until a significant loss in material strength was observed. A series of triaxial tests were also performed on the same materials at the same levels of compaction and moisture content. The purpose of these tests was to find the material strength parameters (cohesion and angle of friction) which are

needed to compute the yield function. Details of these tests and their results can be found in reference 49. The material strength parameters used to predict the yield point were:

for crushed limestone: cohesion = 48.0 kPa, friction angle = 52.5°

for sand: cohesion = 10.35 kPa, friction angle = 39.5°

After the laboratory tests were completed, a finite element mesh was constructed to simulate the geometry of the laboratory samples. The finite element response model was then run several times for each material type using different material coefficients to find a set of material constants that would allow the laboratory results to be predicted as accurately as possible by the response model. The stresses predicted by the finite element program were used to predict the strains according to equations 3.11 and 3.12. The total Poisson's ratio ($\mu + \alpha$) used was that predicted by the stress state and material constants at each load increment. However, in this procedure, no stress correction was made for Poisson's ratios greater than 0.5. This means that the stresses predicted by the elastic system (with no Poisson's ratios larger than 0.5) were used with the actual predicted Poisson's ratios to predict the strains that would develop under the given conditions of stress and Poisson's ratio. This approach was used because the actual confining pressures were fixed and did not rise or fall with material dilation and compression. The backcalculated material constants were as follows:

for crushed limestone: k1 = 700, k2 = 0.8, k3 = -0.3

for sand: k1 = 190, k2 = 0.8, k3 = -0.9

These results were for a single load application that was monotonically increased until failure. The backcalculated material constants from this test can therefore be expected to differ somewhat from those found by means of repeated load tests.

Figures 3.15 through 3.26 show the axial (vertical) and radial strains plotted versus the vertical pressure at different confining pressures and for different material types. The figures show that the axial stress-strain behavior was captured quite well by the response model. It should be noted that for each material type only one set of material constants

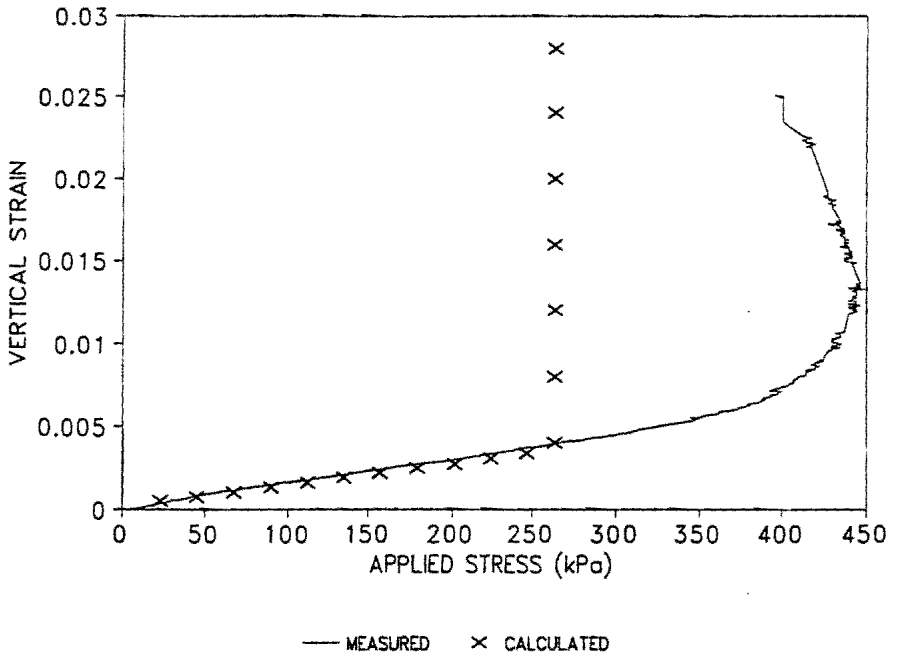

Figure 3.15. Measured vs. Calculated Results - Vertical Strains for Crushed Limestone at 13.8 kPa Confining Pressure.

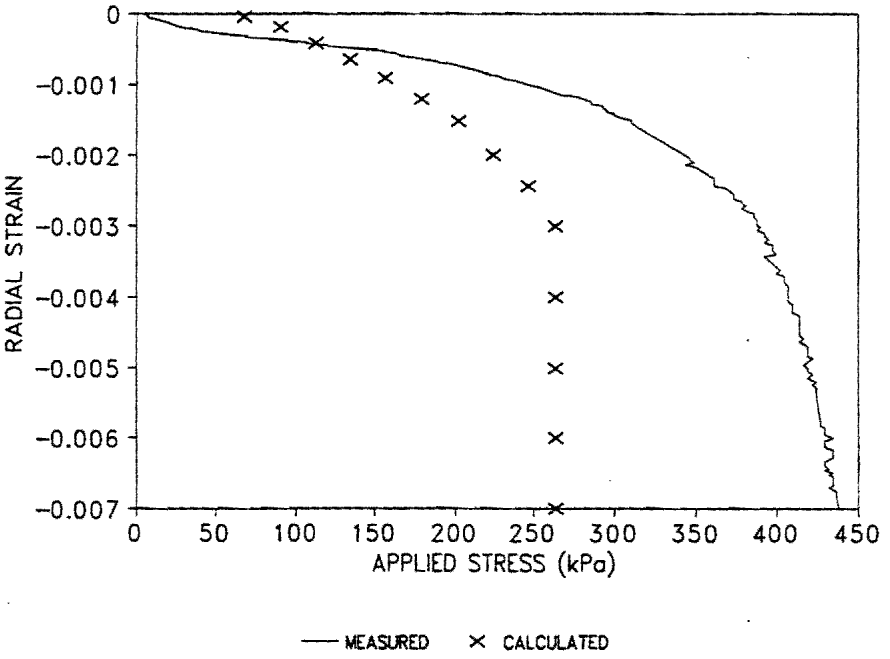

Figure 3.16. Measured vs. Calculated Results - Radial Strains for Crushed Limestone at 13.8 kPa Confining Pressure.

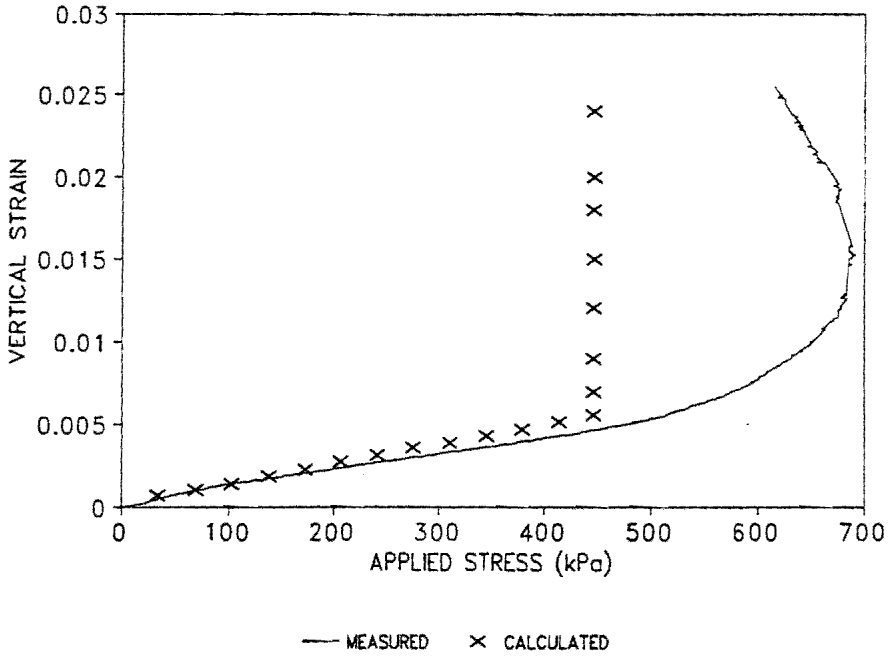

Figure 3.17. Measured vs. Calculated Results - Vertical Strains for Crushed Limestone at 34.5 kPa Confining Pressure.

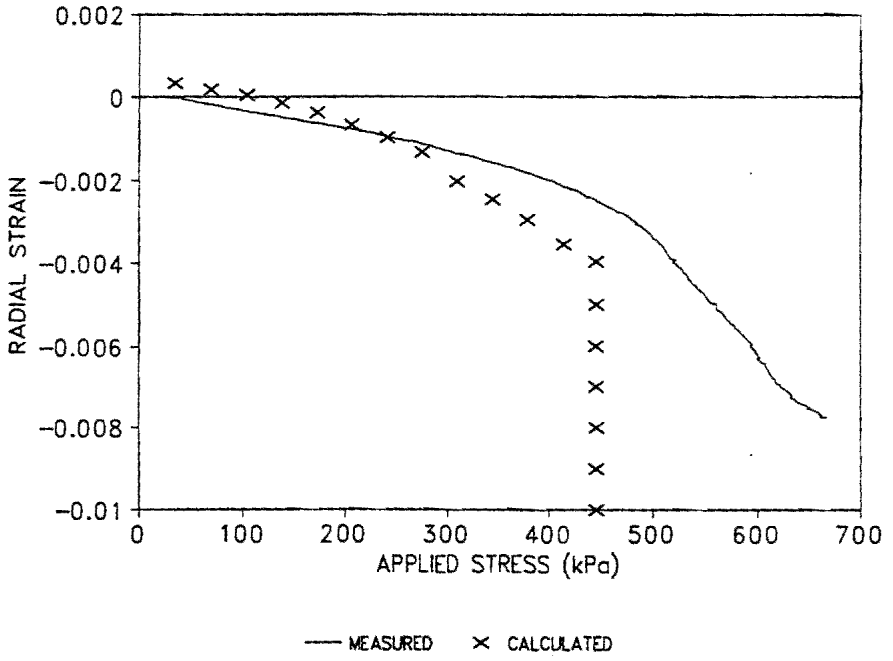

Figure 3.18. Measured vs. Calculated Results - Radial Strains for Crushed Limestone at 34.5 kPa Confining Pressure.

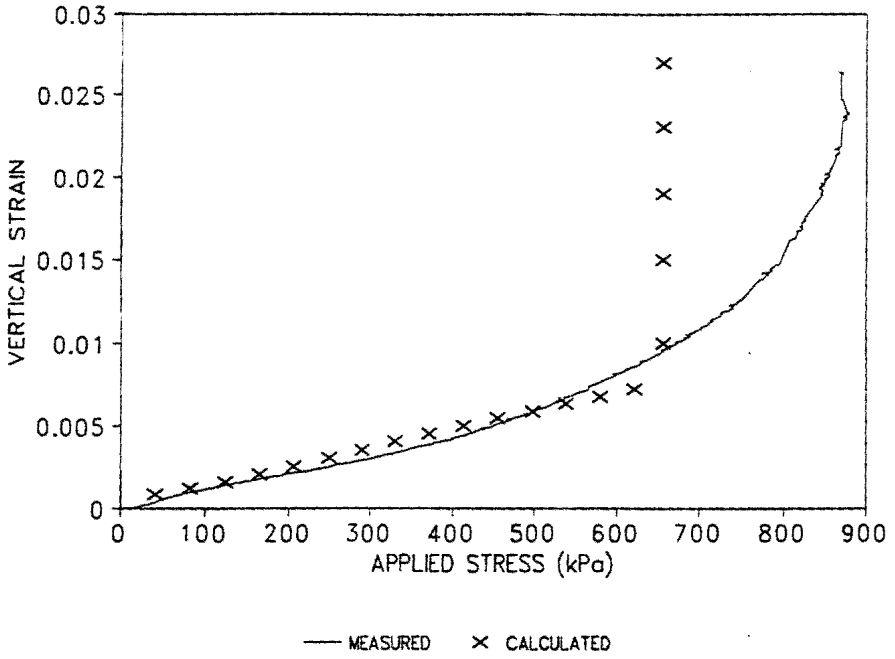

Figure 3.19. Measured vs. Calculated Results - Vertical Strains for Crushed Limestone at 69 kPa Confining Pressure.

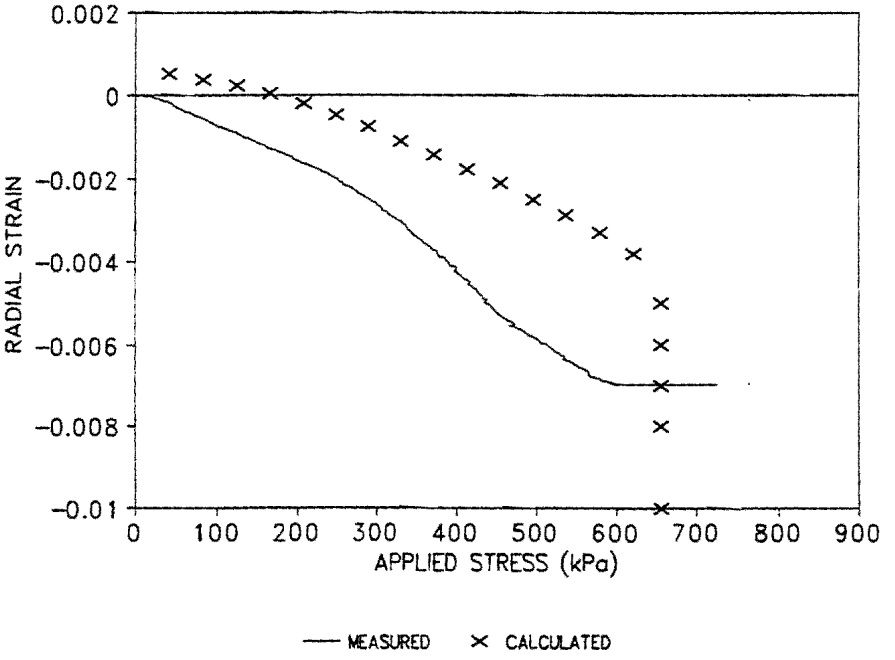

Figure 3.20. Measured vs. Calculated Results - Radial Strains for Crushed Limestone at 69 kPa Confining Pressure.

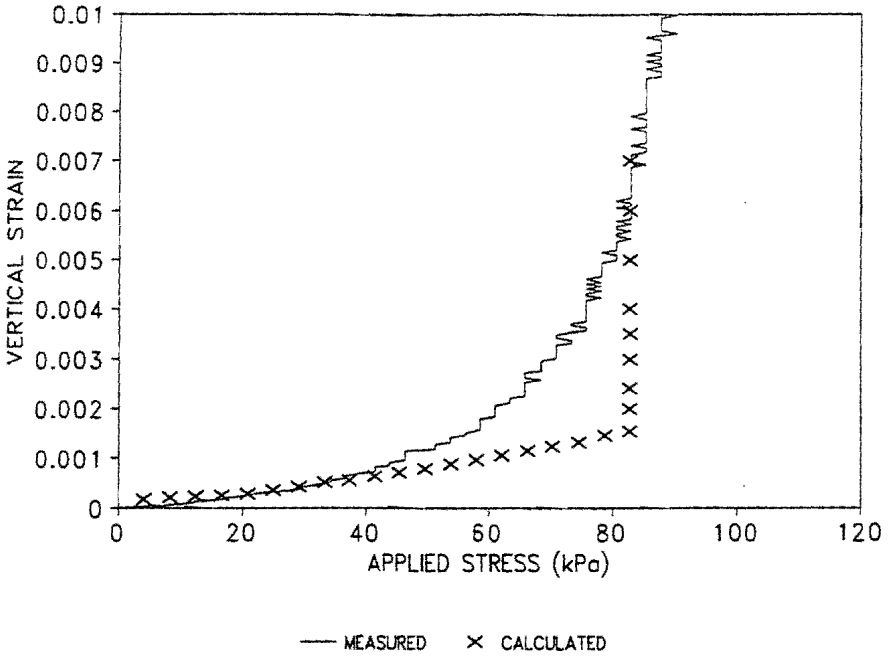

Figure 3.21. Measured vs. Calculated Results - Vertical Strains for Sand at 13.8 kPa Confining Pressure.

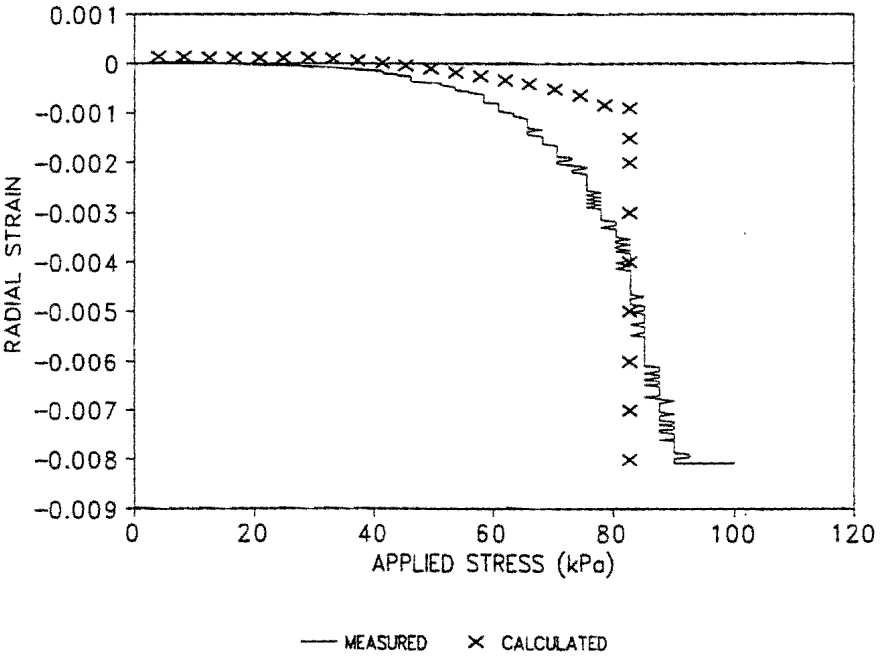

Figure 3.22. Measured vs. Calculated Results - Radial Strains for Sand at 13.8 kPa Confining Pressure.

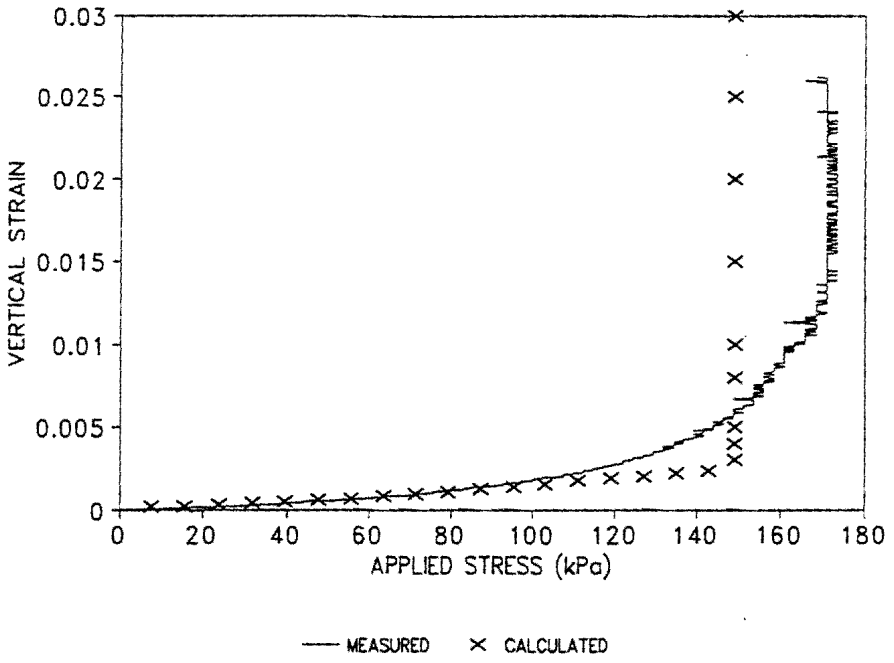

Figure 3.23. Measured vs. Calculated Results - Vertical Strains for Sand at 34.5 kPa Confining Pressure.

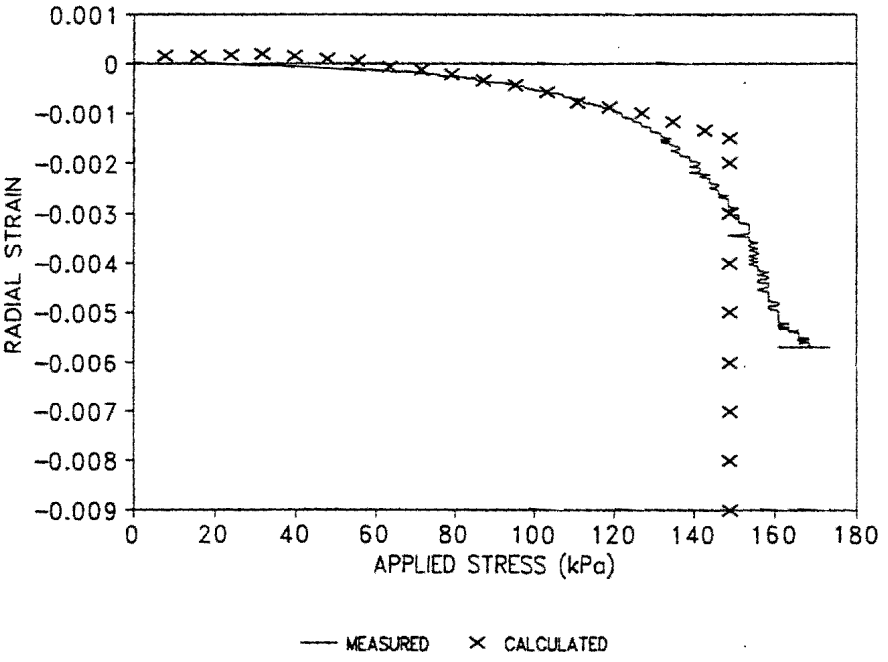

Figure 3.24. Measured vs. Calculated Results - Radial Strains for Sand at 34.5 kPa Confining Pressure.

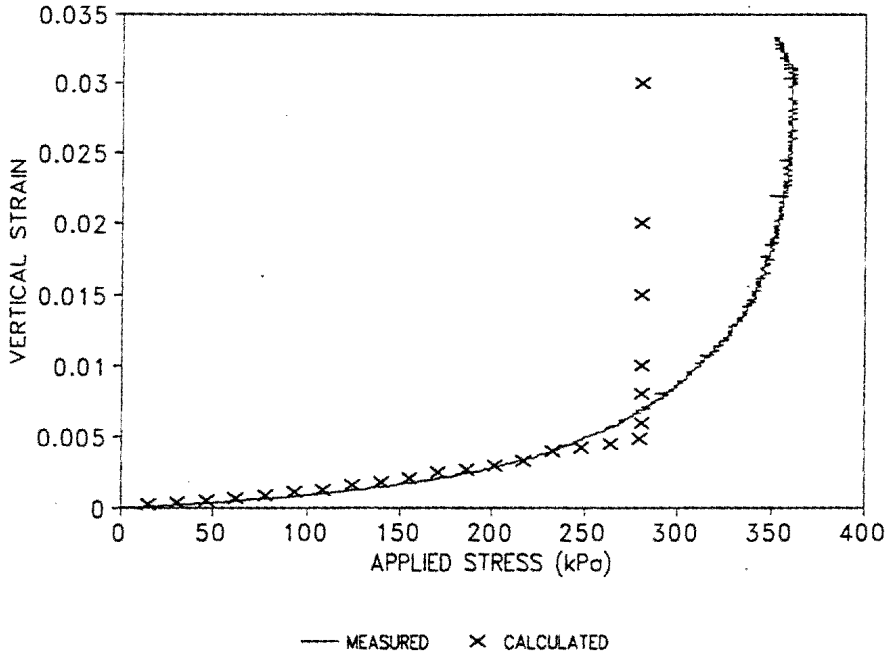

Figure 3.25. Measured vs. Calculated Results - Vertical Strains for Sand at 69 kPa Confining Pressure.

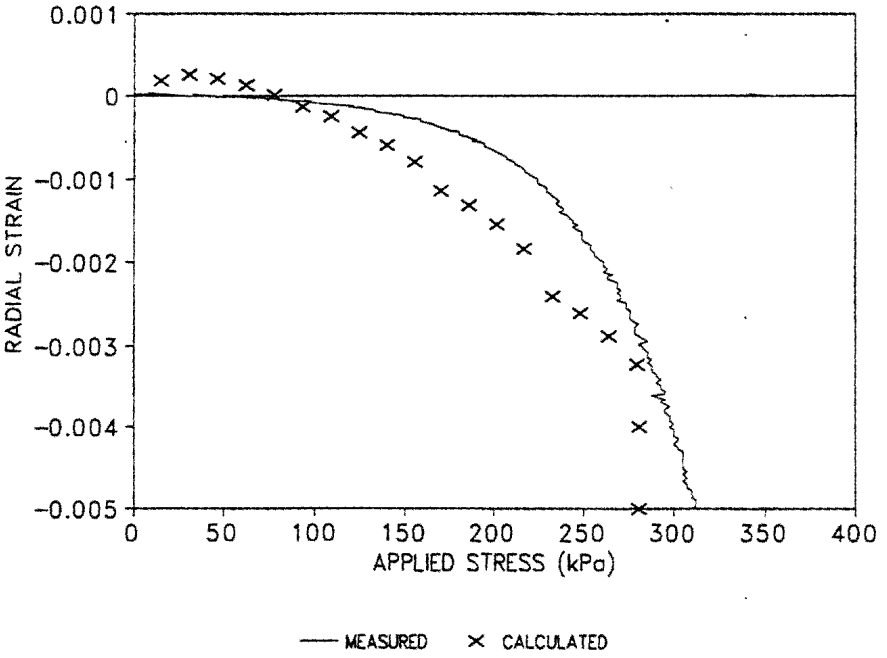

Figure 3.26. Measured vs. Calculated Results - Radial Strains for Sand at 69 kPa Confining Pressure.

were used. The figures, therefore, clearly show the model's ability to account for the effect that the increase in confinement has on the stiffness of each material. Unfortunately, the radial strain predictions compared less well with the measured strains. This was especially the case for the limestone material. A somewhat better agreement between the measured and calculated results was obtained in the case of the sand. The figures show that although the predicted radial strains follow the same general trend as the measured strains, there can be a significant over or underestimation of the radial strains. Figure 3.20, for instance, shows that the predicted strains at 400 kPa are nearly half of the measured strains.

Also shown in the figures are the points at which the Mohr-Coulomb criteria predicted yield. From this point onward, the response model assumed no further stress increase (corresponding to an elastic-perfectly plastic idealization). Most figures show that the predicted yield point was more conservative than the measured yield point. This means that the response model predicted that yield would occur at a lower stress than was actually the case. An exception to this was the sand at low confining pressures (Figures 3.21 and 3.22). It should be noted that the exact point of yield is not easily determined for soils with low confining pressures. It is quite possible for the material to yield and then experience some hardening in the plastic region.

As noted in the previous section, overestimation of the radial strains when the material is dilating can lead to the prediction of fairly large confining pressures even for small radial strains, which may be unconservative. This inability of the response model to accurately match the radial strains resulted in the exclusion of the dilation modeling procedure from the response model. It should, however, be noted that the inclusion of the stress sensitive Poisson's ratio did allow Poisson's ratios above 0.5 to be used and, therefore, resulted in a significantly better prediction of radial strains as compared to the normal elastic theory.

SUMMARY AND CONCLUSIONS

In this chapter, a finite element response model that includes procedures to model non-linear elastic moduli and Poisson's ratios has been described. Analytical and numerical procedures for obtaining stress sensitive Poisson's ratios were described. A comparison between the results obtained by each method was made. For the numerical procedure, an investigation into the relevancy of different boundary conditions was made based on the results obtained with the response model as well as the results obtained by laboratory testing. Laboratory testing consisted of triaxial type tests on sand and crushed limestone.

A procedure for modeling the resilient dilation observed in granular materials was also presented. Finally, a comparison between the predictions made by the response model with corresponding measurements from laboratory tests were conducted. Based on these investigations, the following conclusions are drawn:

1. The Poisson's ratio tends to increase from a fixed initial value as the load is increased. The rate at which this increase will take place depends on the material properties (as characterized by the constants k_1 to k_3), the rate at which the second invariant of the deviatoric stress tensor, J_2, increases, and the value of the first stress invariant, I_1. Generally, the rate at which the Poisson's ratio increases with increasing J_2 will be lower at higher values of I_1.
2. For the sand, it was found that the initial Poisson's ratio depends on I_1. The higher the value of I_1 at the start of the loading procedure, the lower the initial Poisson's ratio. For the crushed limestone, the changes in Poisson's ratio seemed to be more erratic, although the Poisson's ratio was still observed to increase with increasing J_2.
3. It was found that small changes in the boundary conditions needed for the numerical Poisson's ratio prediction procedure did not have a significant effect on the predicted Poisson's ratio.

4. The comparison between the analytical and numerical procedures for predicting the Poisson's ratio as a function of the stress state showed that results obtained with the numerical procedure compared well with the results obtained with the analytical procedure. At higher values of the Poisson's ratio, a slightly reduced correlation between the two procedures was observed.
5. A comparison between laboratory results and predictions made by the response model showed that the response model could predict the vertical strains that develop in a laboratory sample under triaxial loading conditions. The response model also predicted the observed trends in the lateral strains when the material was in a state of dilation. However, the absolute values of the lateral strains could not be predicted with accuracy. Because the proposed resilient dilation modeling procedure is sensitive to changes in the predicted Poisson's ratio (and thus lateral strains), more calibration of the Poisson's ratio prediction model would be needed before a resilient dilation procedure could be included in the response model. It was decided to include the stress sensitive Poisson's ratio procedure in the response model for Poisson's ratios that fall within the 0.0 to 0.48 range.

CHAPTER IV

SENSITIVITY ANALYSIS OF MOHR-COULOMB YIELD CRITERIA

INTRODUCTION

In order to make an accurate estimate of the yield point of a material under stress, several parameters need to be estimated. These parameters can generally be classified as either stress parameters or material parameters. In the case of the Mohr-Coulomb failure criterion, the stress parameters are those stresses that are required to calculate the first stress invariant as well as the second and third deviatoric stress invariants, as shown by the equation (16):

$$f = \frac{I_1}{3}\sin(\phi) + \sqrt{J_2}\sin\left(\Theta + \frac{\pi}{3}\right) + \frac{\sqrt{J_2}}{\sqrt{3}}\cos\left(\Theta + \frac{\pi}{3}\right)\sin(\phi) - c\cos(\phi) = 0 \tag{4.1}$$

where the Lode Angle, Θ, is defined by (16):

$$\theta = (1/3)\cos^{-1}\left(\frac{3\sqrt{3}}{2}\frac{J_3}{(J_2)^{(3/2)}}\right) \tag{4.2}$$

and I_1 is the first stress invariant, and J_2 and J_3 are the second and third deviatoric stress invariants, respectively. These stresses are modeled stresses and depend on the type of constitutive model used to predict them.

Equations 4.1 and 4.2 are reprinted from Appendix A, which gives a more detailed discussion of the Mohr-Coulomb yield criterion. Equation 4.1 is the invariant form of the Mohr-Coulomb yield criterion. In addition to knowing the state of stress, two other parameters are needed to predict failure. They are the cohesion (c) and the internal angle of friction (ϕ). Both these parameters can be determined through conventional triaxial laboratory testing.

The material parameters are independent of the chosen constitutive model. Both the stress and material parameters are estimates of the actual values that occur in the field. The accuracy of the yield point determination will depend on the degree to which the stress

and material parameters match the actual field values. However, not all parameters have an equal effect on the yield function. Some parameters, because of their magnitude or typical variation in the field, affect the yield criterion to a larger extent than others.

This chapter describes an analysis in which the purpose is to determine the sensitivity of the Mohr-Coulomb yield criterion to each of the different stress and material parameters. In this analysis, typical parameter values are assumed, after which individual parameters are varied one at a time, and the influence of this variation on the yield function is then studied. This chapter is divided into two main sections. The first section reports studies concerning the sensitivity of the yield function to the stress parameters and the parameters used in the constitutive model. The second section shows evaluation of the sensitivity of the yield function to the strength parameters.

YIELD FUNCTION VARIATION WITHIN PAVEMENT LAYERS

General

Before the sensitivity analysis of the Mohr-Coulomb yield function was undertaken, an analysis of the expected variation of the yield function values within different pavement layers was conducted. It was hoped that this investigation would assist in identifying those positions at which critical yield function values could be expected. In order to obtain yield function values, typical stress values were first generated by modeling the response of a pavement structure to a 35.6 kN load distributed over a 127 mm load radius. Figure 4.1 shows a schematic representation of the pavement structure, load, and material strength parameters used for this analysis. The modeling was completed using a non-linear version of the BISAR (5) layered elastic program. This program, which is described in more detail in Chapter V, incorporates stress dependent resilient moduli and Poisson's ratios, thereby allowing non-linear material behavior to be included in the response model. The reason for using this program instead of the more accurate finite element model was that the layered elastic approach allows more flexibility in choosing points at which to evaluate stresses.

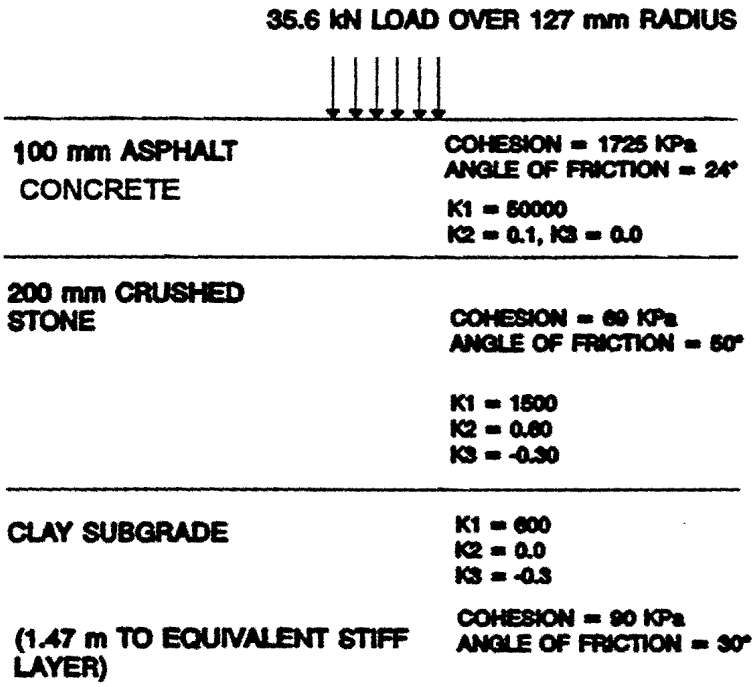

Figure 4.1. Load and Pavement Model Used to Investigate Yield Function Variation within Pavement Layers.

Asphalt Surfacing

Figure 4.2 shows the typical variation of Mohr-Coulomb yield function values within the asphalt layer of the structure shown in Figure 4.1. This figure shows that the yield function increases (i.e., becomes more critical) with increasing depth. However, it should be noted that, typically, high tensile stresses prevail in the lower part of the asphalt layer. This is shown in Figure 4.3 which shows the bulk stress values at various depths. As can be seen from Figure 4.3, the bulk stress becomes positive slightly below midpoint of the layer (positive stresses denote tension). This positive bulk stress indicates the material is in a state of tension, and frictional resistance is no longer mobilized. This means the material is now being pulled apart and the shearing strength of the asphalt is totally dependent on the cohesive strength of the material. Because of this, it was decided that for evaluation positions such as the bottom of the asphalt where the bulk stress is positive, a friction

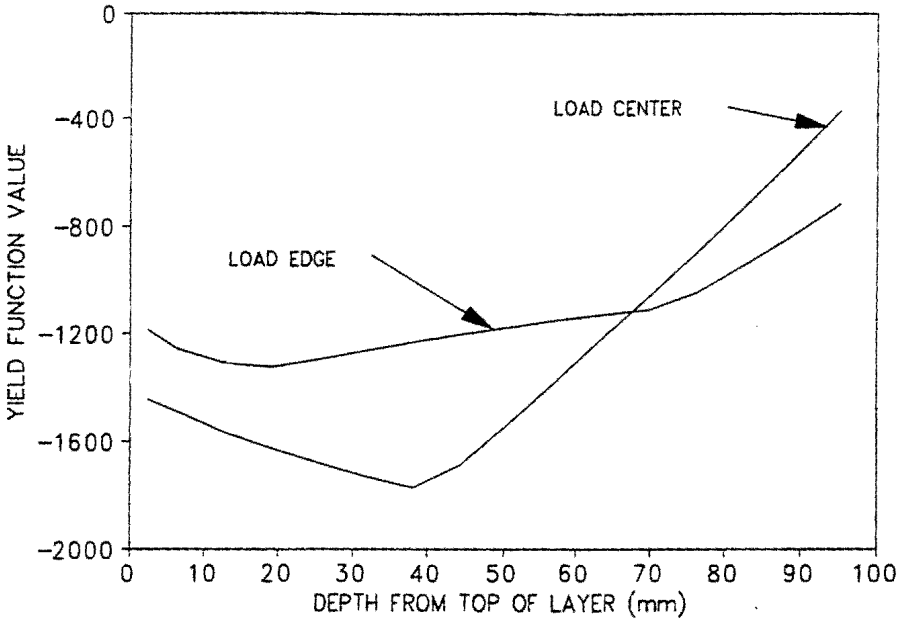

Figure 4.2. Variation of Mohr-Coulomb Yield Function Values within Asphalt Surface Layer.

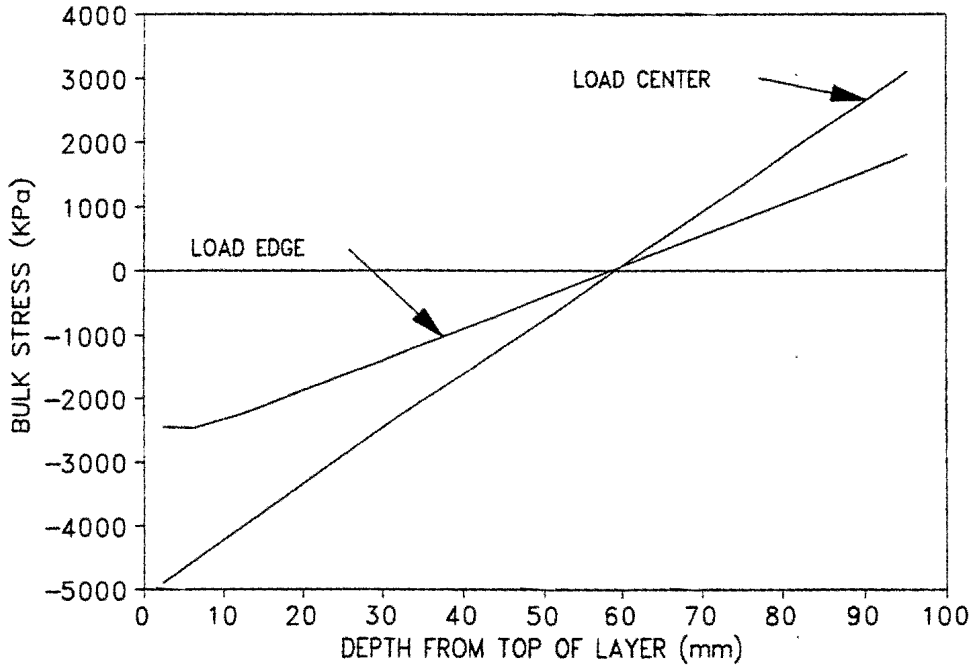

Figure 4.3. Bulk Stress Variation within Asphalt Surfacing.

angle of zero would be used. In effect, this means that a Tresca criterion is used to evaluate the failure potential of asphalt that is in tension. Since the lower part of the asphalt layer is the critical part, stresses will be evaluated in the lower part of the layer to calculate yield function values.

Base and Subgrade

Figures 4.4 and 4.5 show the expected variation of the Mohr-Coulomb yield function within the base layer and upper part of the subgrade. Figures 4.6 and 4.7 show the expected variation of the bulk stress within each of these layers. The variation of the yield function within the base follows a similar pattern as that of the asphalt layer. However, in the case of the base layer, a negative bulk stress is maintained throughout the entire layer (Figure 4.6), even though small tensile stresses may exist at the bottom of the base. The low bulk stress values at the lower part of the base indicate that only a small part of the frictional resistance is mobilized and the cohesive properties of the material play a significant role. For the purposes of this investigation, it was decided to monitor the yield function values at the bottom of the base layer.

Figure 4.5 clearly indicates that the yield function is most critical at the top of the subgrade. This is to be expected since the vertical stress component reduces with increasing depth while the horizontal stress components remain virtually unchanged. Therefore, the evaluation positions for the subgrade were chosen to be at the top of this layer. For all layers, evaluations were made at both the center and edge of the load.

SENSITIVITY OF THE MOHR-COULOMB YIELD FUNCTION TO STRESS PARAMETERS

As noted in the literature survey, choosing an appropriate constitutive model is vital to accurately model the stress and strain conditions that develop under loading. Furthermore, the effectiveness of a constitutive model depends on the accuracy of its coefficients. Even when these coefficients are accurately estimated by means of sampling and laboratory testing, the natural variation in the thickness, stiffness, and consistency of

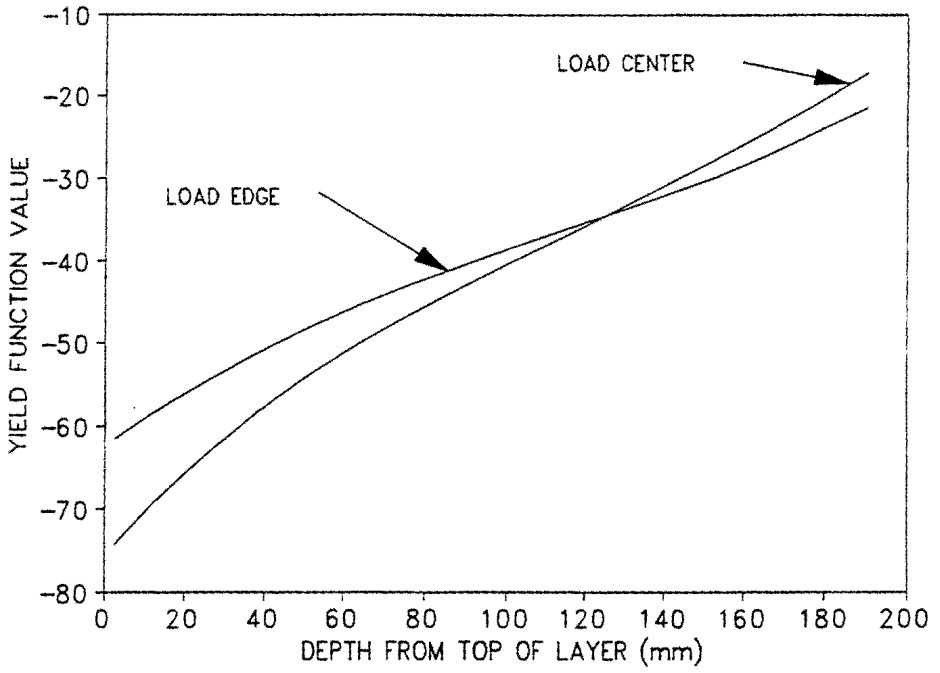

Figure 4.4. Mohr-Coulomb Yield Function Variation in Base Layer.

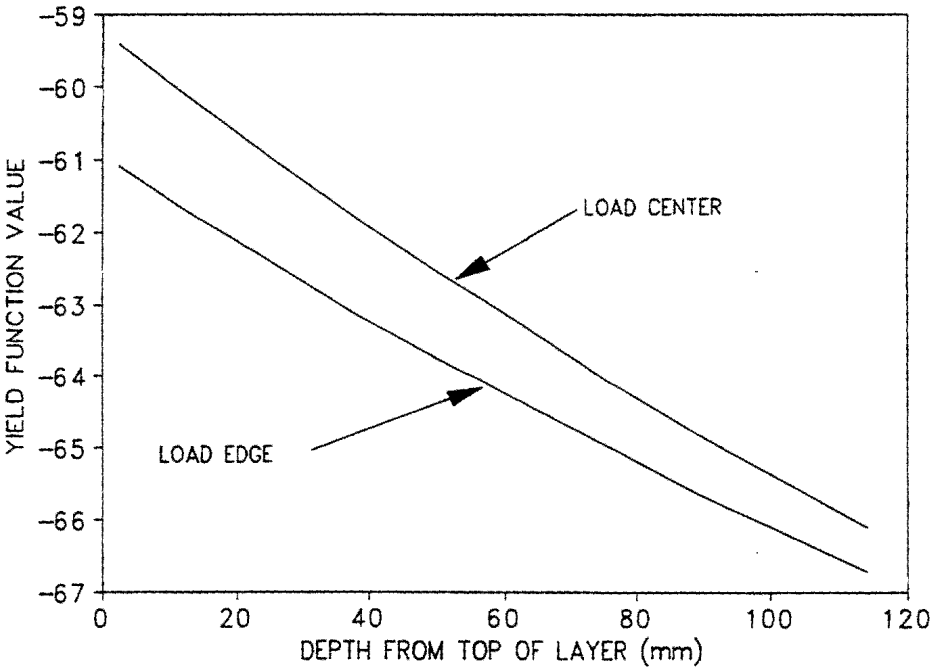

Figure 4.5. Mohr-Coulomb Yield Function Variation in the Subgrade.

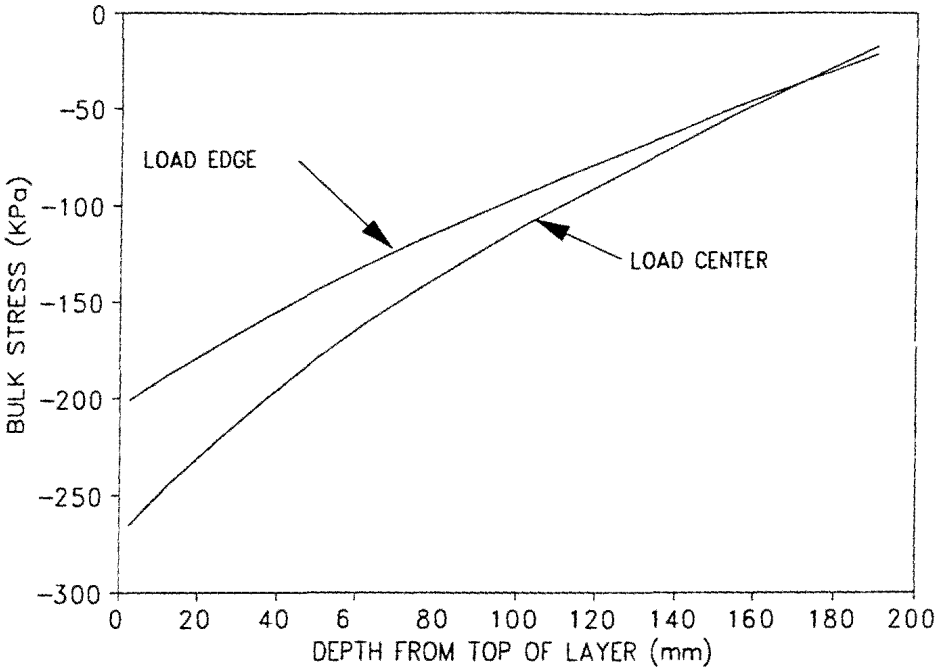

Figure 4.6. Bulk Stress Variation in Base Layer.

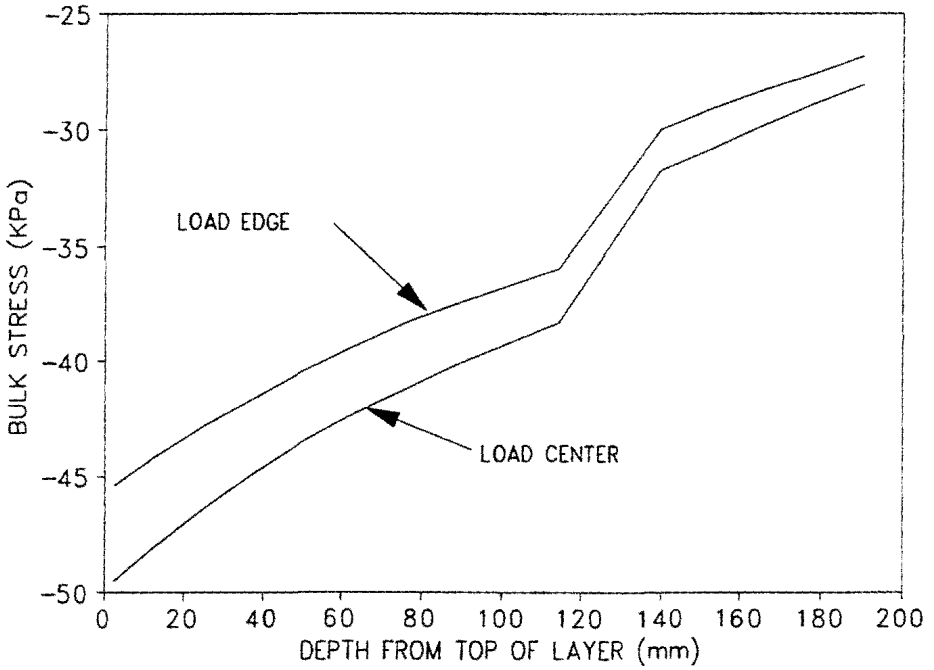

Figure 4.7. Bulk Stress Variation in the Subgrade.

pavement layers may lead to a loss of accuracy in the prediction of the stresses and strains that develop under loading. Several researchers have studied the sensitivity of stresses and strains to variations in layer thickness, resilient modulus, and Poisson's ratio (1,2,18). However, all of these studies were aimed at investigating the sensitivity of those parameters which are involved in predicting long term fatigue life, such as horizontal strain at the bottom of the asphalt layer, and vertical strain at the top of the subgrade. In this study, the effects of variations in the constitutive model parameters on the Mohr-Coulomb yield function are studied.

The sensitivity of the Mohr-Coulomb yield function to the stress parameters was studied using the finite element program described in Chapter III. Two different pavement types were used in this analysis, which are shown schematically in Figures 4.8 and 4.9. A single load of 31.1 kN was applied over a circular area with a radius of 100 mm, which corresponds to a surface pressure of 989 kPa. This load was chosen because it is similar to the load magnitudes that were encountered on a single wheel of a superheavy load moving vehicle (50). For each pavement type, the yield function was evaluated close to the centerline as well as close to the edge of the load, as shown in Figures 4.8 and 4.9. In the analysis, the sensitivity of the yield function to variations in the constants which determine the resilient modulus and Poisson's ratio was studied.

Variation of Resilient Modulus and Poisson's Ratio Coefficients

The three coefficients which determine the value of the resilient modulus and the Poisson's ratio were varied in this part of the analysis. The relationships between the stress condition and resilient modulus as well as Poisson's ratio were discussed in some detail in Chapter III, but are repeated here for completeness. For resilient modulus:

$$E = (k_1\, p_a)\left(\frac{\theta}{p_a}\right)^{k_2}\left(\frac{\tau_{oct}}{p_a}\right)^{k_3} \tag{4.3}$$

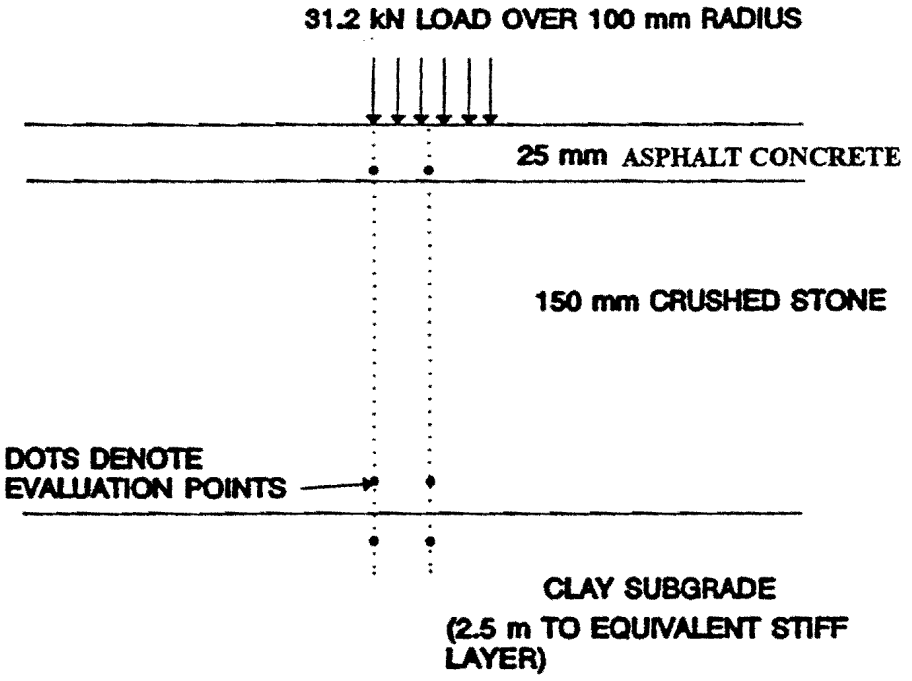

Figure 4.8. Thin Pavement Structure Used in Sensitivity Analysis.

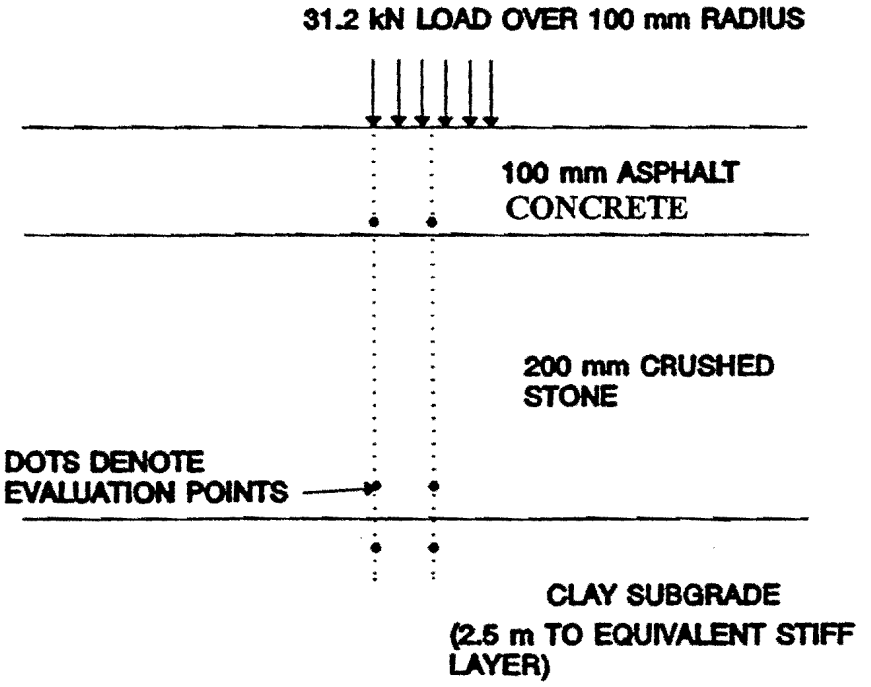

Figure 4.9. Thick Pavement Structure Used in Sensitivity Analysis.

Where: E = resilient modulus

p_a = atmospheric pressure

Θ = first stress invariant

τ_{oct} = octahedral shear stress

k_i = material constants (to be varied)

For the Poisson's ratio:

$$\frac{2}{3}\frac{\partial \nu}{\partial J_2} + \frac{1}{I_1}\frac{\partial \nu}{\partial I_1} = \nu\left(\frac{2}{3}\frac{k_3'}{J_2} + \frac{k_2}{I_1^2}\right) + \left(-\frac{1}{3}\frac{k_3'}{J_2} + \frac{k_2}{I_1^2}\right) \tag{4.4}$$

Where: ν = Poisson's ratio

k_i = the same material constants noted in equation 4.3.

I_1 = the first stress invariant, and

J_2 = the second invariant of the deviatoric stress tensor

The general approach was to assume average values for each of the material coefficients k_i. The yield function was then calculated at each of the evaluation points shown in Figures 4.8 and 4.9. These calculated values for the yield function were then assumed to be the average yield function values. After these values were calculated, the k_1 to k_3 values for each layer were varied thirty percent up and down. Only one parameter was changed at a time. All other parameters were kept constant so the influence of that parameter with respect to the yield function could be established. The average values assumed for each of the k_i values for each layer are noted in Table 4.1. The typical k_3 value used for the asphalt surfacing was zero, as was the k_2 value for the subgrade material, based on typical results and were not varied in the analysis. During the analysis, the cohesion and angle of friction values were kept constant. The values used for angle of friction and cohesion were average values for layer material types. Details of how these values were determined are given in a later section. However, for the sake of completeness, the cohesion and angle of friction values used for each of the layer types are summarized in Table 4.2.

Table 4.1. Average Coefficients Used in Sensitivity Analysis.

Layer	k_1	k_2	k_3
Asphalt Surface	50,000.0	0.1	0.0
Crushed Stone Base	700.0	0.6	-0.3
Clay Subgrade	400.0	0.0	-0.3

Table 4.2. Values Used for Cohesion and Angle of Friction.

Layer and Material Type	Cohesion (kPa)	Friction Angle (degrees)
Asphalt Surface	1720	0° or 24° *
Crushed Stone Base	68.9	50°
Clay Subgrade	89.6	30°

* A friction angle of 0° was used only where the material was in a state of tension. For other cases a friction angle of 24° was used.

Discussion of Results: Variation in Resilient Modulus and Poisson's Ratio Coefficients

The results from the variation in the resilient modulus and Poisson's ratio coefficients are shown graphically in Figures D.1 to D.12 in Appendix D. These graphs illustrate, in compact form, the general magnitude and direction of fluctuations in the yield function due to changes in the k_1 to k_3 coefficients. The main observations drawn from Figures D.1 to D.12 are noted in the following. The reader may wish to verify these observations by referring to the figures.

a) Thin Pavement

For both evaluation positions (i.e., center and edge of the load), the greatest change in yield function was brought about by changes in the k_1 factor. The greatest overall change in yield function was calculated in the base, along the edge of the load. This change was brought about by changing the k_1 factor for the base itself.

In almost all cases, the variations of the yield function value calculated in the asphalt surface and the base were far greater than that calculated in the subgrade. An exception to this was when the k_1 and k_3 factors for the subgrade itself were changed. However, when these factors were changed, the resulting changes in the yield function were still greater in the base than in the subgrade.

In general, the greatest fluctuations in the yield function were calculated in the base. This was observed even when the k_1 to k_3 factors of the surface and subgrade were changed. As already noted, the factors which relate to the nonlinearity of the material (i.e., k_2 and k_3) had smaller effect on the yield function than did the k_1 factor. The base was the only layer in which all three factors were greater than zero. For the base, k_2 had a greater impact on the yield function than did k_3, although this observation may simply be ascribed to the larger average value chosen for k_2.

b) Thick Pavement

The changes in the yield function which were calculated in the thicker pavement generally showed the same trends as the thin structure. However, in the case of the thicker pavement, changes in the k_1 to k_3 factors had a far lesser effect on the calculated yield function than was the case for the thin pavement. In the case of the thin structure, yield function variations in excess of 200 percent were noted. In the case of the thick structure, the greatest change in yield function was slightly higher than 25 percent. As before, the calculated yield function generally showed the most sensitivity to changes in the k_1 factor. An exception to this was the calculated yield function in the base (edge and center of load evaluation position). For this case, the yield function seemed to be more sensitive to changes in the k_2 than the k_1 factor.

As with the thin structure, the yield function values calculated in the base generally showed the most sensitivity to changes in the k_1 to k_3 parameters. There were, however, some exceptions to this observation, such as when the k_1 factor in the surface was varied. In this case, the yield function calculated in the surface showed the greatest fluctuation.

As before, the yield function calculated in the subgrade showed a low sensitivity to changes in most of the k_1 to k_3 factors. However, it did show a greater sensitivity to changes in the k_1 factor of the surface than did the yield function calculated in the base. This was observed at both the edge and center of load evaluation positions.

c) Observations Regarding Tendencies in the Yield Function

Although this analysis is concerned with the sensitivity of the yield function and not with the actually calculated yield function values, several tendencies were noted in the sensitivity analysis which warrant some discussion. These tendencies will briefly be outlined in the following.

For the chosen pavement configuration and load situation, no positive yield function was calculated in the case of the thick pavement at either the edge or the centerline of the load positions. This indicates that none of the layers of the thicker pavement would have experienced plastic deformation. However, for the thin pavement, a positive yield function was calculated in several instances. For both the thin and thick pavement, the most critical

(i.e., most positive) yield function was generally calculated in the base. For the base, the edge-of-the-load evaluation position proved to be more critical than the center-of-the-load position. In no case was plastic deformation predicted in the subgrade.

A tendency that may seem inconsistent with experience or intuition was that, for some cases, a higher modulus (as brought about by increasing the k_1 factor, for example) resulted in a more positive yield function being calculated for that layer. This seems to indicate that a stiffer layer will be more likely to fail than a softer layer. For instance, in the case of the changes in the k_1 factor for the asphalt surface, the yield function calculated at the higher k_1 value was much higher than that calculated in the case of the lower k_1 value. However, it should be borne in mind that the material parameters (cohesion and angle of friction) were kept constant throughout this analysis. In practice, an increase in the resilient modulus would normally be accompanied by an increase in either the cohesion or the angle of friction of the material, or both. This would increase the strength of the material and, thus, reduce the yield function an effect that was specifically not taken into account in the above analysis. Perdomo and Button (24), for instance, have found that there was a critical modulus value above which the octahedral shear stress to octahedral shear strength ratio showed very little change. They ascribed this observation to the high cohesion of the material at higher moduli values.

It may, therefore, be more illuminating to study the effect that changes in the k_1 to k_3 factors for one layer have on the yield function calculated in the other pavement layers. In general, the tendencies observed in this manner are similar to those encountered in typical mechanistic design of flexible pavements. For instance, increasing the modulus in the base reduces the potential for failure in the surface. Similarly, stiffening the subgrade reduces the potential for failure in the base and surface (caused by a reduced bending effect).

Observations Regarding Typical Stress Components Calculated Under High Wheel Loads

Table 4.3 provides a summary of the typical stress values. The stresses noted are those which were calculated when the average values for the k_1 to k_3 parameters were used (Table 4.1). In total, six stress tensors are considered for each pavement type (three layers, two evaluation points per layer). The stress components are given in terms of an axisymmetric coordinate system. In Table 4.3, a positive sign denotes compression. This summary is provided as a reference and because it can assist in explaining many of the tendencies that are to be expected in the Mohr-Coulomb yield function.

Several observations can be made from Table 4.3. As expected, the vertical stress calculated in the base and subgrade is much higher than the two horizontal stress components. This was especially true of the center-of-the load evaluation position. The situation is reversed in the case of the asphalt surface, where high tensile forces prevail at the bottom of the layer. As expected, the shear stress at the edge of the load is much higher than at the center of the load. With respect to the base and subgrade, the high ratio between the vertical and horizontal stress components is seen as important, as it indicates that the vertical stress is a major determinant in the yield function. For instance, due to the relative magnitudes of the vertical and horizontal stresses, it can be expected that a certain percentage of change (or error) in the vertical stress will have a higher influence on the yield function than will a similar percentage of change in the horizontal stress components. This observation is considered to be of some importance, as the vertical stress is the one stress parameter that can often be predicted consistently by different constitutive models (1,18). This may indicate that, due to the overwhelming influence of the vertical stress component, the yield function is not very sensitive to the type of constitutive model used to predict vertical stresses. This matter is pursued in detail in Chapter V.

Table 4.3 Summary of Calculated Stresses: Thin Pavement Structure*

Stress Component	Pavement Structure**	SURFACE Evaluation at		BASE COURSE Evaluation at		SUBGRADE Evaluation at	
		Center	Edge	Center	Edge	Center	Edge
Vertical	Thin	884.6	98.6	336.8	170.5	182.7	141.7
	Thick	333.2	134.6	64.2	52.4	53.4	48.0
Radial	Thin	-2207.5	-165.4	7.2	23.0	3.1	9.4
	Thick	-992.3	-531.6	5.3	5.0	-3.5	-2.0
Tangential	Thin	-2220.8	-1244.0	6.3	-4.4	2.78	-3.3
	Thick	-995.5	-763.9	5.2	7.3	-3.6	-3.8
Shear	Thin	24.4	502.6	17.6	92.3	6.6	47.2
	Thick	51.6	306.4	2.4	13.7	1.2	10.6

* All Stresses in kPa

** Pavement Structures refer to Figures 4.8 and 4.9

SENSITIVITY OF MOHR-COULOMB YIELD FUNCTION TO CHANGES IN THE MATERIAL PARAMETERS

As discussed in the literature study given in Appendix A, the shear strength of a particulate material such as soil or crushed stone consists of two main components, namely the cohesive and the frictional component. These two components contribute to the shear strength of the material in different ways for different materials. A wet clay, for instance, has low or zero frictional resistance, as the clay particles tend to slide over one another. In such a case, almost all of the shear strength is due to the cohesion that exists between individual particles. In the case of a coarse granular material under compression, almost all the shear strength is derived from the frictional component. This friction is brought about by the resistance that exists between particles which tend to slide or roll over one another when under loading.

Cohesive strength in the case of granular materials and clays is related to the moisture content of the material. In the case of asphaltic materials, cohesive strength is dependent on the properties of the mixture and temperature (37). The friction angle is dependent on the surface roughness, angularity, and degree of particle packing (51). The moisture content and density can vary considerably within a pavement layer over time and distance. It can, therefore, be expected that the cohesion and angle of friction, which are determined through sampling and testing at discrete locations along a pavement, may not accurately describe the shear strength of the pavement material over the entire length of the roadway. In the following, the sensitivity of the yield function to changes in the estimated cohesion and angle of friction will be studied. As in the preceding analysis, the approach was to assume average values for all variables in the yield function. The variable of interest (cohesion or angle of friction) was then varied, and the effect of this variation on the yield function was analyzed. The stresses which were used for this part of the analysis were those calculated for the average k_1 to k_3 values. For each material type, two different stress conditions were considered, one for each of the evaluation positions.

In this analysis, extensive use was made of the results from tests conducted by Titus-Glover and Fernando (49). These tests consisted of a series of Texas Triaxial Class tests (52) which were conducted on various base and subgrade type materials. The tests were also conducted at different moisture contents. Tables 4.4 and 4.5 note typical values for cohesion and angle of friction for typical subgrade and base course material types. For asphalt materials, the results reported by Lytton et al. (37) were used. These values are summarized in Table 4.6. In Table 4.4, a distinction was made between sandy and clayey subgrade materials when calculating averages.

The results of the yield function variations for different values of cohesion and angle of friction are shown in Figures D.13 to D.24 in Appendix D. In these figures, the same vertical axis scale was used for a specific material type so the influence of cohesion and angle of friction on the yield function for a given layer could be compared.

Discussion of Results: Thin Pavement

For all layers, the cohesion had a direct linear relationship with the yield function. This can, in fact, also be observed from the mathematical relationship between the cohesion and the yield function. The effect of changing the cohesion was the same for both the edge and center of the load stress conditions. In the case of the asphalt concrete surface and the subgrade, the cohesion had a more pronounced effect on the yield function than the angle of friction (Figures D.13 and D.14, and Figures D.17 and D.18). However, in the case of the base, the angle of friction had a major effect on the calculated yield function when the stresses were evaluated close to the centerline of the load. If the stresses used to calculate the yield function are those calculated at the edge of the load, then the effect of the angle of friction diminishes, and the yield function is more sensitive to changes in cohesion (Figures D.15 and D.16).

It should be noted that, in the case of the base course, the edge of the load is the most critical for almost the entire range of the angle of friction used. However, there is a specific angle of friction at which the critical evaluation point shifts from the edge of

Table 4.4. Typical Cohesion and Angle of Friction Values for Subgrade Materials (49).

Material Type	Cohesion at moisture content (kPa)			Angle of Friction at moisture content (Degrees)		
	below opt.	at opt.	above opt.	below opt.	at opt.	above opt.
Sand	7.6	10.3	4.8	42	40	41
Sandy Gravel	24.8	15.8	21.4	29	48	39
Lean Clay	108.9	113.0	51.7	44	38	38
Fat Clay	137.1	119.9	43.4	18	0	0
Silt	32.4	33.1	28.9	43	42	43
Averages for Sandy Materials	16.5	13.1	13.1	36	44	40
Standard Deviation for Sandy Materials	12.2	3.89	11.7	9.9	5.7	1.41
Averages for Clayey Materials	92.8	88.7	41.3	35	27	27
Standard Deviation for Clayey Materials	54.2	48.3	11.5	14.7	23.2	23.5

Table 4.5. Typical Cohesion and Angle of Friction Values for Base Materials (49).

Material Type	Cohesion at moisture content (kPa)			Angle of Friction (Degrees)		
	below opt.	at opt.	above opt.	below opt.	at opt.	above opt.
Caliche	90.8	77.3	46.9	43	48	49
Iron Ore Gravel	68.3	73.3	59.3	47	48	48
Shell Base	74.4	68.2	59.9	51	51	53
Limestone	29.5	48.9	54.4	55	53	52
Average	65.8	66.9	55.1	49.0	50.0	50.5
Std. Dev.	26.0	12.6	6.0	5.2	2.4	2.4

Table 4.6. Typical Cohesion and Angle of Friction Values for Asphalt Concrete (37).

Statistical Parameter	Cohesion at (kPa)			Angle of Friction at (Degrees)		
	4°C	20°C	39°C	4°C	20°C	39°C
Average	2386.9	1818.3	420.6	30	24	25
Maximum	3049.5	3631.0	829.6	60	34	34
Minimum	1793.5	458.9	108.0	20	20	20
Standard Deviation	374.2	660.8	185.3	12	5	4

the load to the center of the load position. The same observation can be made in the case of the subgrade.

As expected, the difference between the predicted yield function at the edge and center of the load evaluation positions diminishes with depth. This can clearly be seen in Figures D.17 and D.18, where the cohesion and angle of friction were varied for the subgrade. These figures show that almost identical yield function values were calculated over the entire range of cohesion and angle of friction values.

Discussion of Results: Thick Pavement

The results obtained by using the stresses calculated for the thick pavement generally show the same trends as those of the thin structure. In all cases, cohesion was found to have a slightly greater effect on the yield function than did the angle of friction. As before, the difference in yield function calculated at the center and the edge of the load diminished with depth, and virtually the same yield function values were calculated at both these positions in the case of the subgrade.

An observation that seems somewhat inconsistent with the general theory of shear strength is that the yield function becomes more positive (i.e., predicts a higher potential for failure) as the angle of friction increases. Normally, an increased angle of friction would mean an increased resistance to shear (as was found to be the case for the center of the load evaluation position in the base of the thin structure). This inconsistency can be explained by considering the different terms which constitute the Mohr-Coulomb yield function in three dimensions. If the material is in compression (assuming compression is negative), the first term in equation 4.1 would become more negative as the angle of friction increases. The second term is independent of the angle of friction and would, therefore, remain unchanged. The third term would tend to become more positive, as J_2 is always a positive quantity. The fourth term (the cohesion term) would diminish as the angle of friction increases, and, since this term is subtracted from the other terms, it would mean that as the angle of friction increases, the effect of the fourth term would be to make the yield function more positive.

The first term is, therefore, the only term that accounts for the increase in shear strength as the angle of friction increases. However, if the quantity I_1 in this term is small relative to the cohesion (c) and the second deviatoric stress invariant (J_2), then the overall effect of an increased angle of friction would be to increase the value of the yield function towards the positive side. Thus, it can be seen that when the material is in a state of tension, (as is the case at the bottom of the asphalt layer), or when the material is in a relatively low state of confinement (as is the case in the deeper layers of thicker pavements), the cohesive properties of the material exert a higher influence on the yield function than does the angle of friction.

SUMMARY AND CONCLUSIONS

In this chapter, an analysis was discussed in which the purpose was to study the sensitivity of the Mohr-Coulomb yield function to changes in the response parameters, k_1 to k_3, and material strength parameters, c and ϕ. Based on the results of this analysis, the following observations are made.

For the k_1 to k_3 factors:

1. The yield function is most sensitive to changes in the k_1 factor. This was found to be the case for both the thin and thick pavements. The base layer was the only layer in which both k_2 and k_3 were assigned absolute values greater than zero. For this layer, k_2 was found to have a greater influence in the yield function than k_3.
2. In general, the greatest fluctuations in yield function were calculated in the base. This was found to be true even in cases where the material parameters of the other layers were varied.
3. The subgrade generally showed the least sensitivity to changes in the k_1 to k_3 parameters.
4. Changes in the material parameters were found to have a far lesser influence on the yield function in the case of the thick pavement than it did in the case of the thin pavement. In the case of the thick pavement, a 30 percent change

in the material parameters affected the yield function by a maximum of 25 percent. In the case of the thin pavement, changes in excess of 200 percent were noted in some instances.

For the material strength parameters:

5. In all cases studied, cohesion was found to have a linear effect on the yield function. Cohesion greatly affects the yield function value, and it is, therefore, vital to estimate this parameter as accurately as possible. Cohesion was especially found to have a pronounced effect on the yield function values calculated in the asphalt and subgrade.
6. In the case of the base, the angle of friction was found to have a major effect on the calculated yield function. This influence was most pronounced at the center of the load and diminished toward the edge of the load.

The above observations prompt the following conclusions:

1. An accurate estimate of the material parameters, k_1 to k_3, is vital if an accurate assessment of the potential for failure needs to be made. The k_1 parameter, which defines the general stiffness of the material, plays the most important role. The parameters related to the non-linearity of the material (k_2 and k_3) are also important but play a lesser role. This is especially applicable in the case of thick pavements. Currently, the material parameters, k_1 to k_3, are determined through laboratory testing. The possibility should be investigated of determining k_1 by means of a simpler procedure such as through calibration of moduli determined through FWD testing.
2. Both of the material strength parameters play an important role in determining resistance to shear failure. The results indicate that for asphalt and subgrade materials, cohesion is the most important parameter to estimate. While the friction angle was also shown to have an influence on the predicted yield function value (especially in the case of the base), this parameter is not expected to vary as much as cohesion with changes in moisture content and

other seasonal influences. This can clearly be seen from Tables 4.4 through 4.6 which show that, for a given material, cohesion varies more than the angle of friction with changes in moisture content or temperature. Because of this, cohesion is likely to be site specific and, under ideal conditions, would have to be determined shortly in advance of a superheavy load move. In the case of subgrade and base materials, cohesion can be estimated by making use of suction and moisture content information. This procedure requires that the moisture content of the soil as well as the moisture content versus suction curve be known.

3. Most of the results indicate that the yield function is most likely to be critical in the base. The cohesion of the base is not likely to be as sensitive to seasonal variations as the subgrade. Accelerated deterioration, potholes that seemed to have originated in the base, pumping, and unsealed cracks in the surface accompanied by rainfall are all indicators that moisture may be trapped in the base. Visual indicators such as these should prompt a further investigation, possibly accompanied by laboratory tests.

CHAPTER V
COMPARISON OF DIFFERENT RESPONSE MODELS

INTRODUCTION

The pavement response model described in Chapter III is based on a non-linear finite element model that has the capability of using stress dependent moduli and Poisson's ratios. It was noted that this model would be used as a benchmark against which other, less accurate, models are to be evaluated. The reason for wanting to make use of less complex response models is related to the difficulties associated with the finite element method in general. The accuracy of the finite element method depends to a large extent on how well the mesh itself is constructed. Constructing a proper mesh requires some experience in the use of finite elements. Furthermore, modeling multiple wheel loads requires a mesh that is relatively large which may pose problems with the availability of computing power. Also, the positions at which stresses can be evaluated depends on the geometry of the mesh and cannot be chosen at will by the user.

Most of the problems noted above can be avoided when the layered elastic approach is used instead of the finite element method. However, this less complex approach is also less accurate in its characterization of material behavior. However, there are instances when this loss in accuracy may be tolerable, or, in some cases, even negligible. Huang (1) conducted a fairly detailed comparison of the results predicted by the different types of response models. However, Huang's analysis was restricted to comparisons between the traditional design parameters such as strain at the bottom of the asphalt layer and strain at the top of the subgrade.

This chapter compares three different types of response models. Because this research is concerned with the prediction of yield rather than long term deformation, the parameter chosen for comparison is the predicted yield function value. In addition to the comparison of the yield function values predicted by different types of response models, a comparison between the predicted stresses at different offsets from the load center is also

conducted. Finally, the three models are compared in a case study involving in situ field measurements.

RESPONSE MODELS AND PAVEMENT TYPES USED

Response Models Used

The response models considered in this comparison are the following:

a) non-linear finite element model with stress dependent moduli and Poisson's ratios (maximum Poisson's ratio allowed is 0.48);

b) traditional linear layered elastic model;

c) layered elastic model adapted to include stress dependent moduli and Poisson's ratios (maximum Poisson's ratio allowed is 0.48).

The finite element model is discussed in detail in Chapter III and will, therefore, not be discussed here. The linear layered elastic program used here is BISAR (5), which is a proven and easy to use program. The non-linear version of the layered elastic program is exactly the same as the original BISAR program. However, a driver program was developed so the main program can be run in an iterative fashion. After each iteration, the stresses are used to compute moduli and Poisson's ratios that are compatible with the state of stress. These new moduli and Poisson's ratios are then written to the (new) input file and the calculation is repeated. This procedure is repeated until the moduli converge (convergence is based on a user specified allowable error). This program requires that in addition to the layer thicknesses and elasticity constants, the material constants k_1 to k_3 also be provided at the start of the computation. With this program, each layer is also subdivided into several sublayers. The non-linear layered elastic program and the traditional layered elastic program (BISAR, in this case) use the same formulation and would calculate the same results given that the same number of sublayers and the same material parameters are used in the normal BISAR program.

Pavement Structures, Material Constants and Load Types Used

For this analysis, the same two pavement structures assumed in the sensitivity analysis (Chapter IV) are used. Figures 4.8 and 4.9 show schematic representations of these two pavement structures. The material parameters used for this analysis are given in Tables 5.1 and 5.2.

For the comparison of the stress states predicted by the different models, a single 44.5 kN load with a 127 mm load radius was used. For the comparison of the calculated yield functions, three load magnitudes were used, 22.3 kN, 33.4 kN, and 44.5 kN. A 127 mm load radius was used for all loads.

Table 5.1. Coefficients Used in Sensitivity Analysis.

Layer	k_1	k_2	k_3
Asphalt Surface	50,000.0	0.1	0.0
Crushed Stone Base	1500.0	0.6	-0.3
Clay Subgrade	600.0	0.0	-0.3

Table 5.2. Material Strength Parameters Used.

Layer and Material Type	Cohesion (kPa)	Friction Angle (degrees)
Asphalt Surface	1720	24
Crushed Stone Base	68.9	50
Clay Subgrade	89.6	30

COMPARISON OF PREDICTED STRESSES

If, in the non-linear layered elastic (N.L.E.) program, a pavement structure is modeled with the same number of sublayers as that of the finite element (F.E.) mesh, then the resulting moduli and Poisson's ratios close to the load center can be expected to be comparable to those of the finite element mesh. However, by virtue of its formulation, the non-linear layered elastic approach does not allow the elastic constants to be varied within a layer. This means that the modulus and Poisson's ratios can only be varied in the vertical direction. The finite element formulation allows the modulus values to be varied in both the radial and vertical directions. The purpose of this section is to study the effect this limitation has on the stresses predicted by the non-linear layered elastic program. Also, the traditional linear layered elastic approach is compared to the non-linear layered elastic and finite element programs in order to study the effect sublayering has on the predicted stress state.

In the finite element and non-linear layered elastic approach, the moduli and Poisson's ratio values are dependent on the state of stress. In the traditional linear layered elastic (L.L.E.) approach, the elastic constants are supplied by the user. Naturally, the stresses predicted by the linear layered elastic program will differ from those predicted by the non-linear layered elastic and finite element programs if the elastic constants of these programs are not at least similar. In order to provide elastic constants to the linear layered elastic program that are similar to those used by the two non-linear programs, the averages of the modulus values of the nonlinear layered elastic program were used. Figures 5.1 through 5.3 illustrate this concept. Figures 5.1 and 5.2 illustrate how the modulus and Poisson's ratio values were distributed in the thick pavement structure after a 44.5 kN load was applied to the surface. Each block in Figure 5.1 represents an element in the finite element mesh. Each block contains two numbers. The upper number represents the modulus in MPa, while the lower number represents the Poisson's ratio. Figure 5.3 shows the structure used in the traditional linear layered elastic approach. In Figure 5.3, the modulus and Poisson's ratio values used are the averages of the sublayers used in the non-linear layered elastic pavement model.

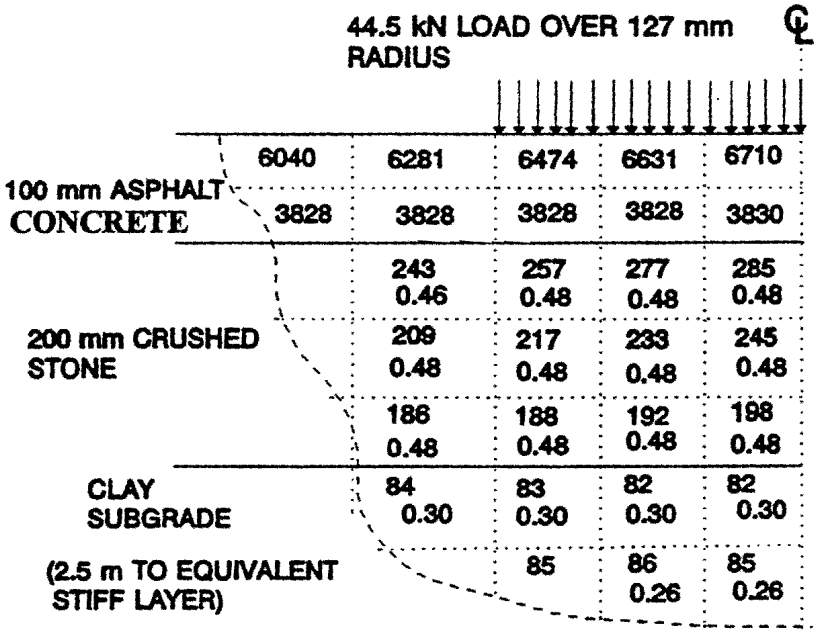

Figure 5.1. Pavement Structure Predicted by the Finite Element Model (Resilient Modulus Values are in MPa).

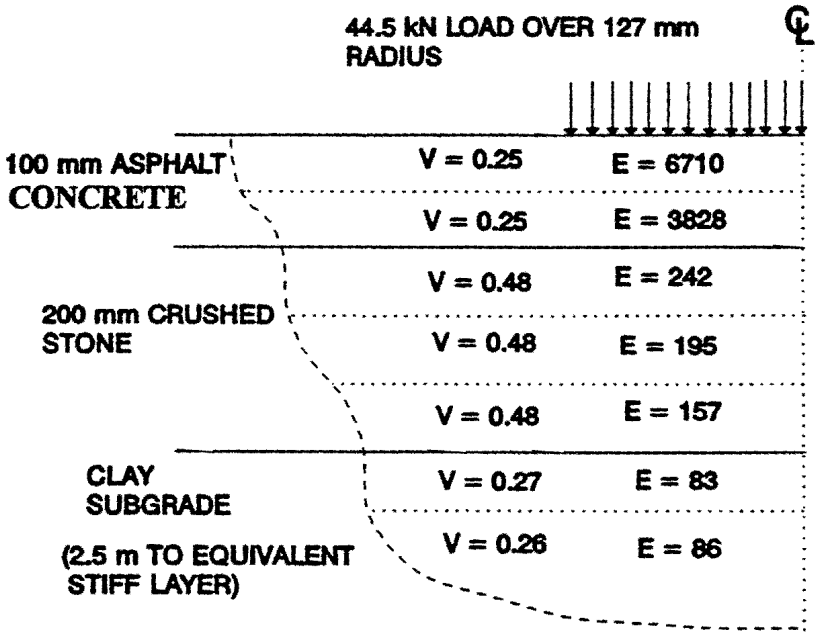

Figure 5.2. Pavement Structure Predicted by Non-Linear Layered Elastic Model (Resilient Modulus Values are in MPa).

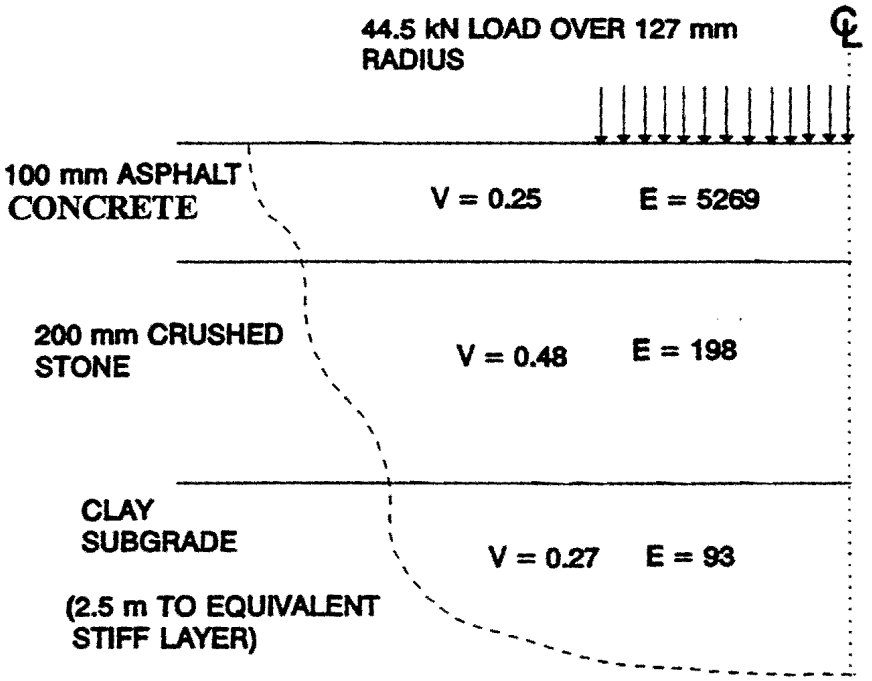

Figure 5.3. Pavement Structure Used in Linear Layered Elastic Model (Resilient Modulus Values are in MPa).

(It should be noted that not all the sublayers used in the non-linear layered elastic program are shown in Figure 5.2.)

Figures 5.1 through 5.3 highlight some of the fundamental differences between the different types of response models. These figures also provide useful insight into the way the different response models account (or neglect to account) for known material behavior. Figure 5.1 shows that the finite element characterization of the pavement incorporates most of the trends currently known to exist in pavement structures. For example, Figure 5.1 shows that the base, which is modeled as a stress-stiffening material, has a higher stiffness at the top of the layer. The stiffness of this layer then decreases as the confining stresses decrease and the octahedral shear stress increases towards the bottom of the layer. This same trend is observed in the case of the surface. Figure 5.1 shows that although the surface is modeled only as a slightly non-linear material ($k_2 = 0.1$, $k_3 = 0.0$), a significant decrease in modulus occurred towards the bottom of the layer. This can be explained by

the relatively high compressive stresses that exist close to the load. The Poisson's ratios in the surface layer also conform to expected trends. Close to the load, where the first stress invariant (I_1) has a high value compared to the second invariant of the deviatoric stress tensor (J_2), the Poisson's ratio did not increase much from the boundary condition but was suppressed by the high I_1 value. Towards the bottom of the layer, the Poisson's ratio did increase somewhat, although this increase was slight owing to the low k_2 and k_3 values assigned to this material type.

The Poisson's ratios in the base have all increased significantly so the maximum allowable Poisson's ratio of 0.48 was assigned to most elements in the base. The uppermost element in the base, at the extreme left in Figure 5.1, however, does show that the Poisson's ratio decreases at larger distances away from the load. As expected, the modulus values for the base also decrease at larger radial offsets from the center of the load. However, this decrease is not as pronounced as that which occurs in the vertical direction. Figure 5.1 shows that the subgrade, which is modeled as a stress-softening material, has an increased modulus at larger distances from the point of load application. The Poisson's ratio of the subgrade decreased with increasing offset from the load centerline.

Figure 5.2 shows that the non-linear layered elastic program also captured the stress-stiffening behavior of the surface and base as well as the stress-softening behavior of the subgrade. However, in the case of the non-linear layered elastic program, the elasticity constants could be varied only in the vertical direction. This limitation increases the beam-effect which leads to stresses that tend towards tension in the bottom part of each sublayer. These stresses, in turn, lead to a lower state of confinement which explains why the modulus values shown in Figure 5.2 are all lower than the modulus values in the corresponding sublayer in Figure 5.1. The ability of the finite element program to vary the modulus and Poisson's ratio values not only in the vertical but also in the horizontal direction diminishes the beam effect to a large extent. This is also a reason why the layered elastic programs frequently predict tensile stresses at the bottom of the base layers,

while the finite element program with the variable Poisson's ratios seldom predicts tension in any layer except the surface.

Figure 5.3 shows the pavement model used in the linear layered elastic program. As can be seen from Figure 5.3, the pavement structure used here consisted of only three layers without any sublayers. Each layer was characterized by a single set of elasticity constants, which means there was no variation in the modulus and Poisson's ratios within a given layer. In effect, this means the pavement structure is modeled somewhat like a beam on an elastic foundation. The increased beam-effect, in the case of the layered elastic response model, may lead to increased tension at the bottom of some of the pavement layers.

It can be gathered from the preceding discussion that each response model bases its computations on a different model of the pavement structure. The finite element model characterizes the pavement as distinct blocks, each with elasticity coefficients which are compatible with the state of stress that exists in that region. The two layered elastic programs characterize each layer (or sublayer) as a continuous medium with no change in properties in the horizontal direction. Figures 5.4 through 5.11 illustrate the effects these different structures have on the stress state. Figures 5.4 through 5.11 show the principal stresses at different depths and offsets from the load center. For each program, the stresses were calculated at three different depths: at the top of the base, at the bottom of the base, and at the top of the subgrade. Each figure shows two sets of three lines. The uppermost set represents the major principal stress, while the bottom set of lines represent the minor principal stresses calculated by each program. In the figures, a negative stress denotes compression, while a positive stress denotes tension. The minor principal stress acts approximately in the vertical direction, while the major principal stress (i.e., the least negative stress) acts approximately in the horizontal direction.

In the case of the thick pavement, all three programs predicted large tensile stresses at the edge of the load (lower part of the asphalt surface, Figure 5.4). While all three programs predicted a similar pattern of stress, it is obvious that the stresses attenuate

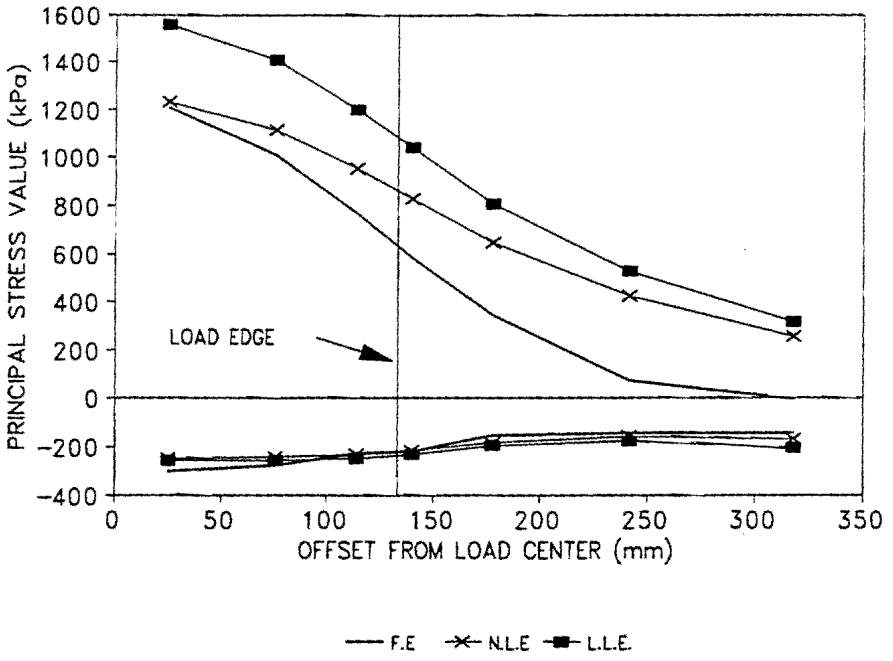

Figure 5.4. Comparison of Predicted Stresses - Thick Pavement, Lower Part of Asphalt Surface.

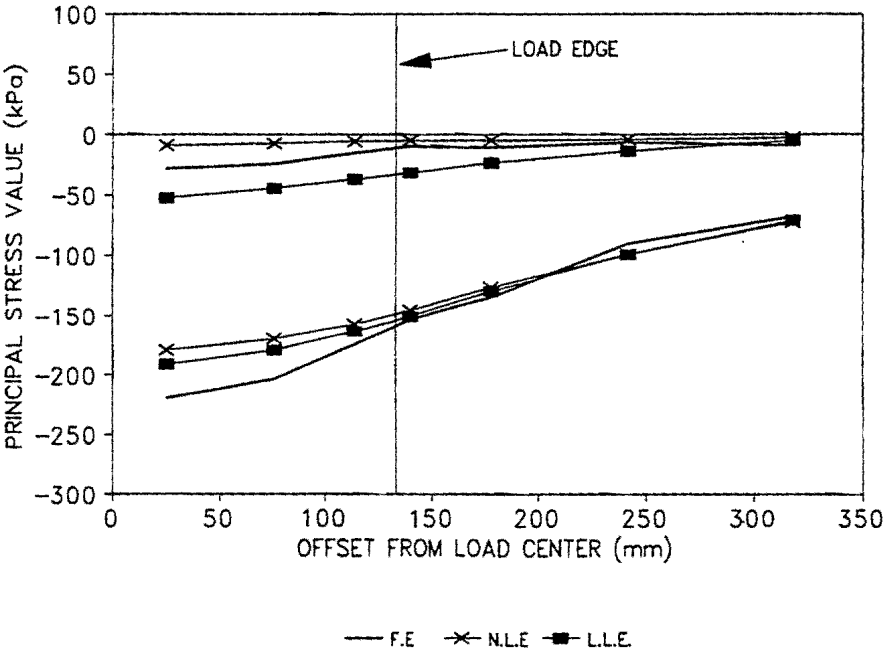

Figure 5.5. Comparison of Predicted Stresses - Thick Pavement, Top of Base.

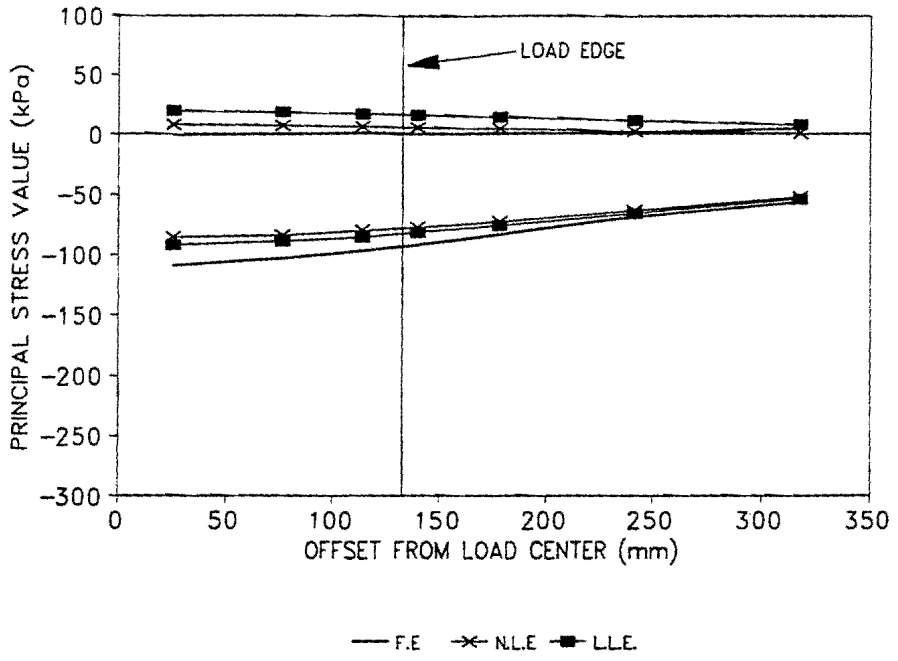

Figure 5.6. Comparison of Predicted Stresses - Thick Pavement, Bottom of Base.

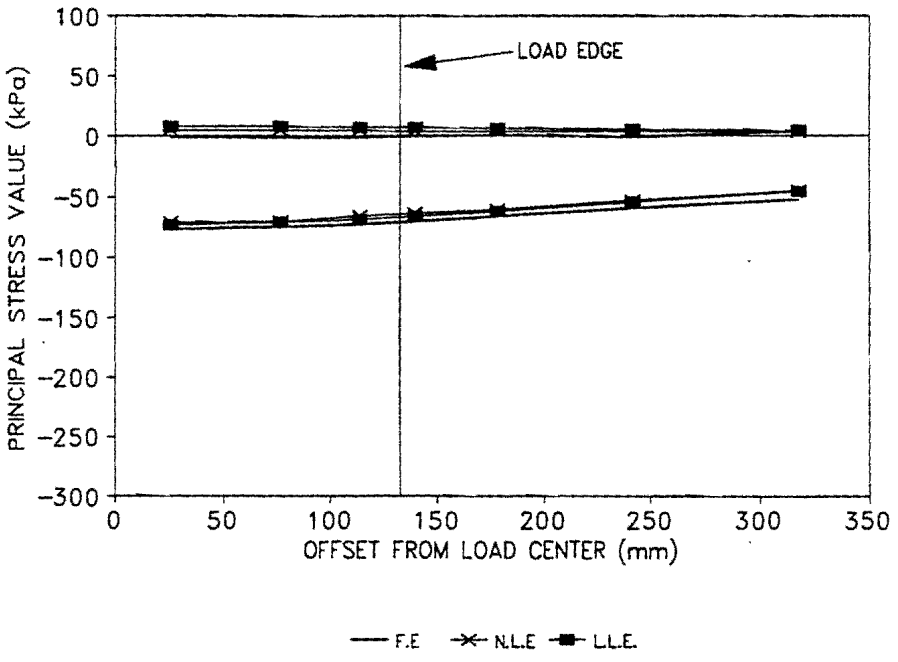

Figure 5.7. Comparison of Predicted Stresses - Thick Pavement, Top of Subgrade.

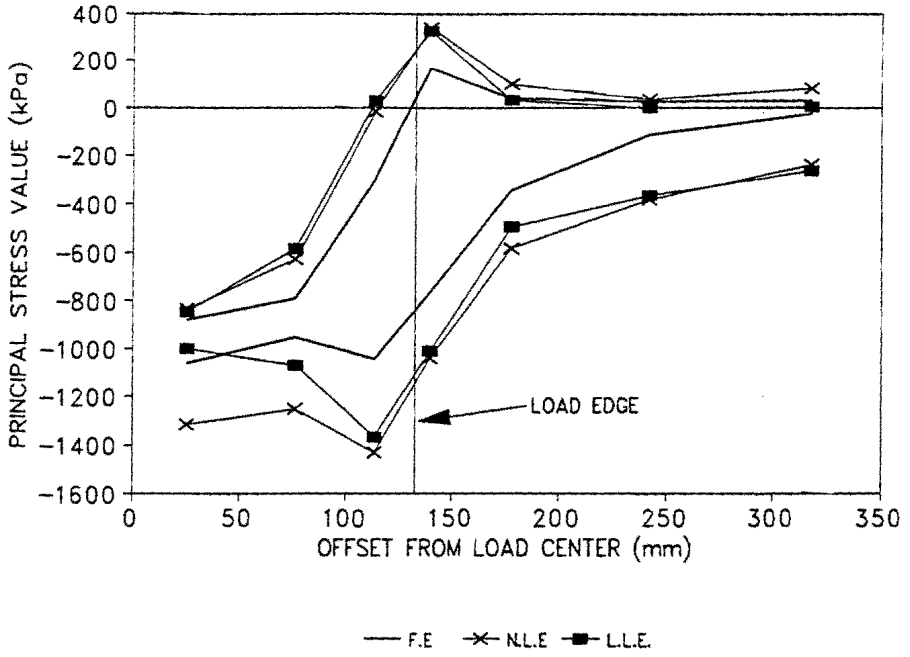

Figure 5.8. Comparison of Predicted Stresses - Thin Pavement, Center of Asphalt Surface.

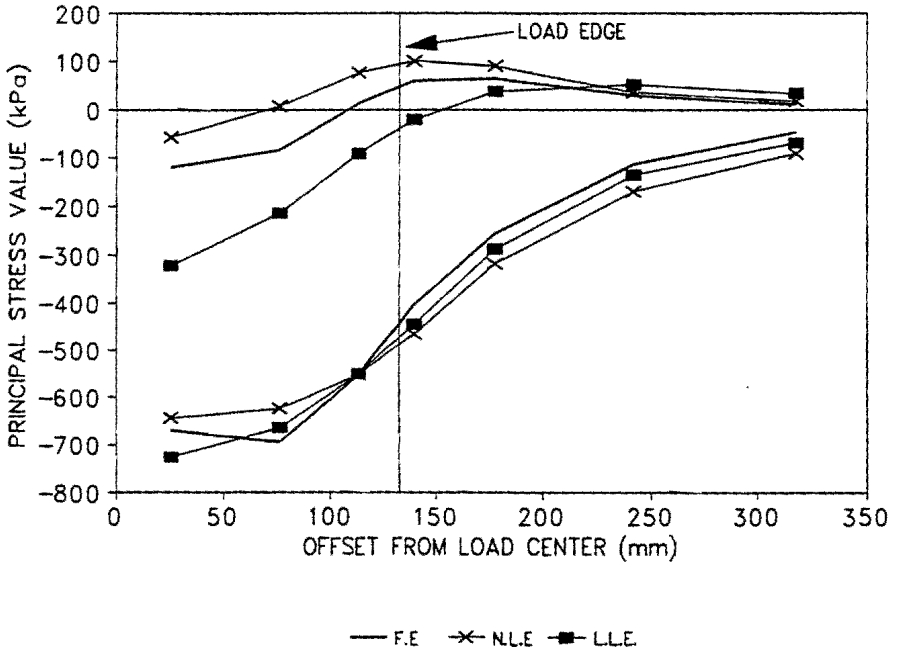

Figure 5.9. Comparison of Predicted Stresses - Thin Pavement, Top of Base.

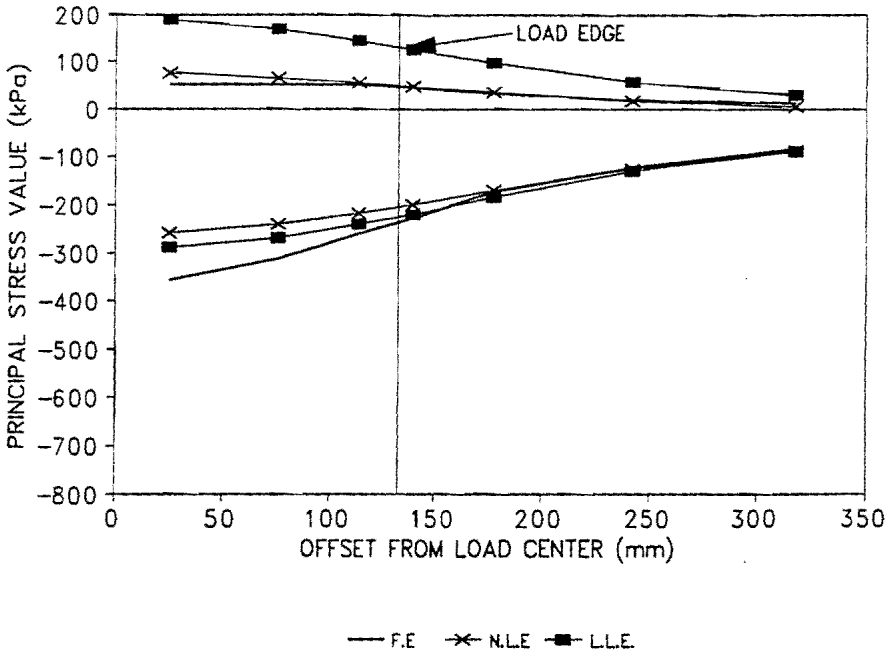

Figure 5.10. Comparison of Predicted Stresses - Thin Pavement, Bottom of Base.

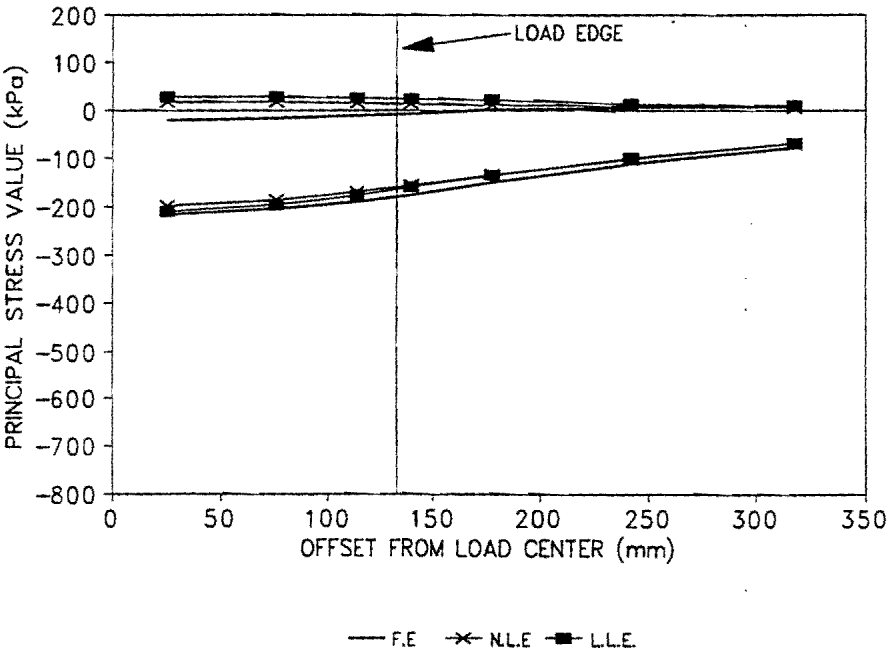

Figure 5.11. Comparison of Predicted Stresses - Thin Pavement, Top of Subgrade.

much faster in the case of the finite element program. Close to the center of the load, the linear layered elastic program predicted higher tensile stresses than the other two programs. The minor principal stresses predicted by the three programs were nearly identical, but the two layered elastic programs predicted higher major principal stresses than the finite element program. For the thick pavement, top of the base evaluation position (Figure 5.5), none of the three programs predicted tensile stresses. The linear layered elastic program predicted the most compressive (i.e., most negative) major principal stress. This can probably be attributed to the bending effect that is most pronounced in the case of the linear layered elastic program.

At the bottom of the base (Figure 5.6), the two layered elastic programs predicted tensile stresses, while the finite element program predicted only small tensile stresses at the larger offset positions. The non-linear layered elastic program predicted smaller tensile stresses than the conventional linear layered elastic program. This can probably be attributed to both the effect of sublayering and the smaller modulus of the sublayer at the bottom of the base. The evaluation close to the top of the subgrade (Figure 5.7) showed that all three programs predicted similar stresses. As before, the linear layered elastic program predicted the highest tensile stresses.

The same basic trends were observed for the thin pavement (Figures 5.8 through 5.11) as was observed for the thick pavement, although the differences in the predicted stress states were higher in the case of the thin pavement. It should be noted that the finite element method does not have the same accuracy at all points within a mesh. The stresses calculated close to the applied load will not be as accurate as those calculated some distance away from the load. Therefore, in the case of the extremely thin surfacing used for the thin pavement, the differences between the predictions shown in Figure 5.8 are possibly also due to a loss in accuracy of the finite element program. For the asphalt surfacing and top of the base evaluation position (Figures 5.8 and 5.9), all three programs predicted a tensile major principal stress. However, the effect of shear is incorporated in the principal stresses. Therefore the tensile stresses observed in the case of the thin pavement, top of the base evaluation position, are largely brought about by the high shear stresses that exist at the load edge.

The advantage of using a non-linear program that makes use of sublayers can clearly be seen in the case of Figure 5.10 which shows the results for the thin pavement, bottom of the base evaluation position. Here, the linear layered elastic program predicted a significantly higher tensile stress than the other two programs. The non-linear layered elastic and finite element programs predicted very similar major principal stresses. The finite element program predicted a higher minor principal stress. Similar trends are observed for the evaluation close to the top of the subgrade. Once again, the linear layered elastic program predicted slightly higher tensile stresses than the other two programs.

A trend that can be observed in all the figures is that the stresses predicted by the different programs tend to approach one another as the offset from the load axis increases. This is most likely due to the fact that the stresses, in general, tend to decrease away from the point of load application. This attenuation of stresses away from the load also seems to be more pronounced in the case of the finite element program.

COMPARISON OF PREDICTED YIELD FUNCTIONS

In the preceding section, the impacts the different response models have on the predicted stress state were discussed. In the following, the impacts these differences in the predicted stress state have on the yield function will be discussed. For this analysis, the same set of material constants and pavement structures as before are used. However, two other load levels are analyzed in addition to the 44.5 kN load used before. Tables 5.1 and 5.2 summarize the material constants used in this analysis. For each response model and pavement type, the yield function was calculated at the top and bottom of the base as well as at the top of the subgrade. This evaluation was done close to the load centerline as well as close to the edge of the load.

Figures 5.12 through 5.17 show the yield function predictions for each of the response models at different evaluation positions. The numbers on the abscissa indicate the evaluation position and are explained in Table 5.3. In these figures, a negative yield function value indicates that the stress state is such that failure is not expected. A positive yield function value indicates incipient failure. The trends observed in the yield

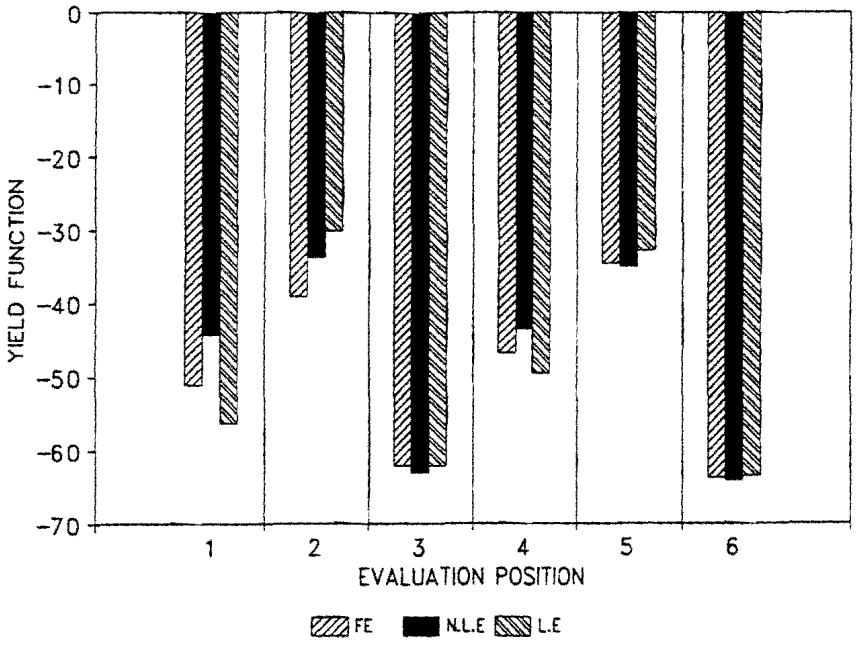

Figure 5.12. Comparison of Predicted Yield Functions - Thick Pavement, 22.25 kN Load.

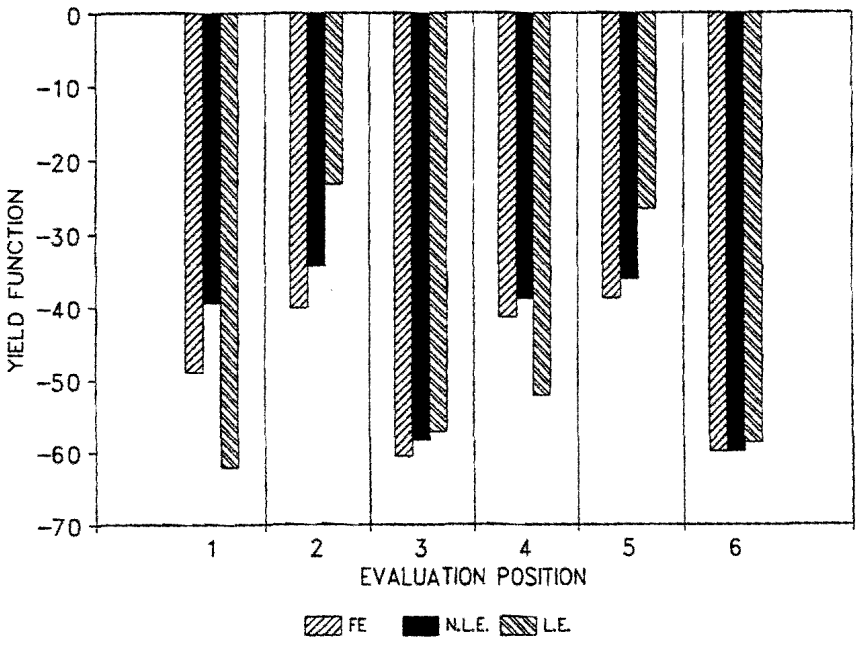

Figure 5.13. Comparison of Predicted Yield Functions - Thick Pavement, 33.38 kN Load.

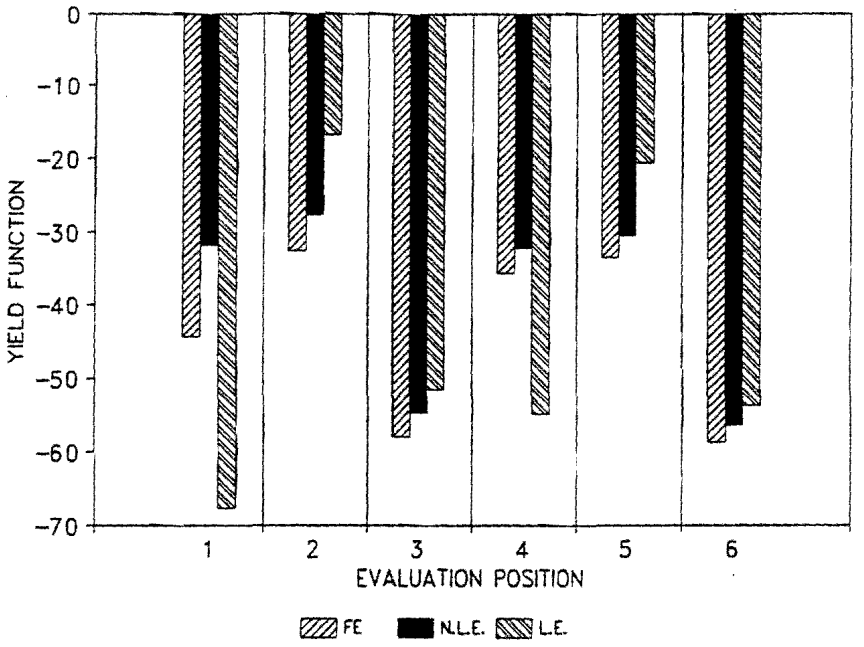

Figure 5.14. Comparison of Predicted Yield Functions - Thick Pavement, 44.50 kN Load.

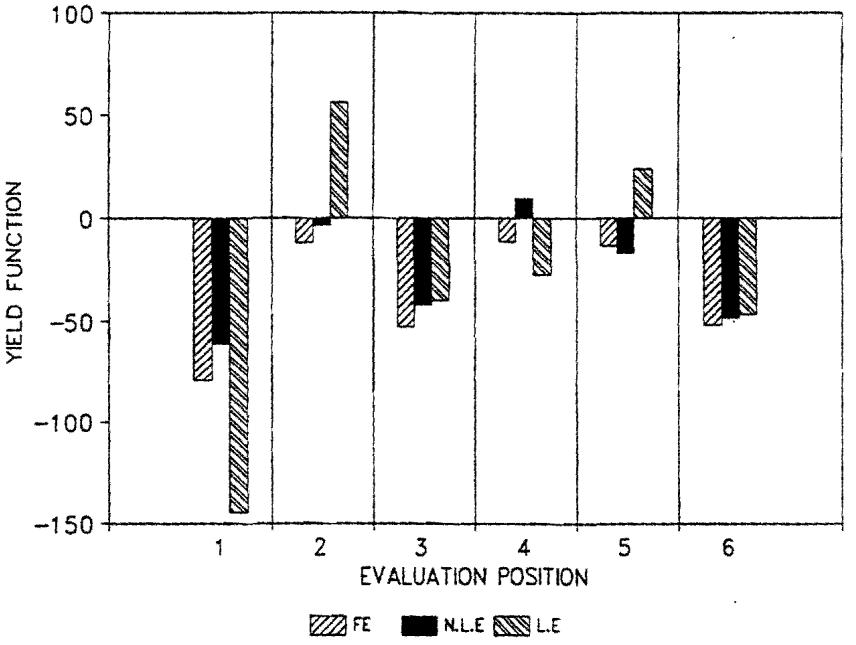

Figure 5.15. Comparison of Predicted Yield Functions - Thin Pavement, 22.25 kN Load.

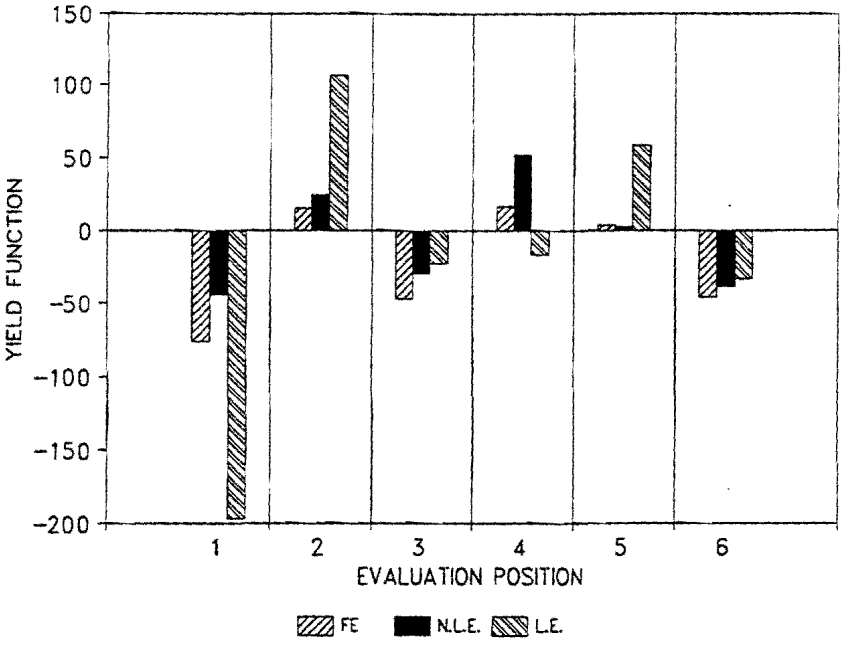

Figure 5.16. Comparison of Predicted Yield Functions - Thin Pavement, 33.38 kN Load.

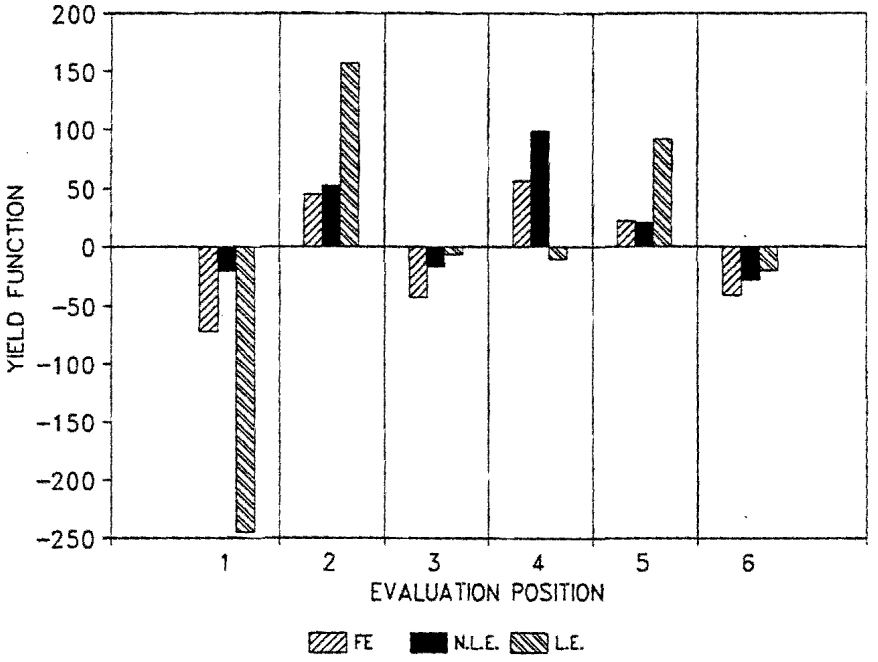

Figure 5.17. Comparison of Predicted Yield Functions - Thin Pavement, 44.50 kN Load.

Table 5.3. Key to Evaluation Position Numbers Used in Figures 5.12 through 5.17.

Number	Description of Evaluation Position
1	Top of base, close to load center
2	Bottom of base, close to load center
3	Top of subgrade, close to load center
4	Top of base, close to load edge
5	Bottom of base, close to load edge
6	Top of subgrade, close to load edge

function values calculated in the asphalt closely approximated those calculated in the base. However, these yield function values were less critical than any of those observed in the base. Furthermore, the large negative yield function values calculated in the asphalt layer tend to distort the scale and diminish patterns noted in yield function values calculated at other positions. For these reasons, the yield function values calculated in the surface are not shown in Figures 5.12 through 5.17.

Most of the trends observed in Figures 5.12 through 5.17 can be anticipated based on the comparison of stresses discussed in the preceding section. For instance, Figure 5.12 shows that, at the top of the base evaluation position, the linear layered elastic program predicted the most negative (i.e., least conservative) yield function value. This is due to the higher confining pressures predicted by the linear layered elastic program. Conversely, at the bottom of the base, the linear layered elastic program predicts higher tensile stresses than the other two programs and, therefore, also larger yield function values. A trend that can be observed in all the figures is that the non-linear layered elastic program seems to be a compromise between the finite element and conventional linear layered elastic program. In the case of the thick pavement, none of the response models predicted failure (i.e., all yield function values were negative).

The results for the thin pavement show the same trends as the thicker pavement. However, as before, the differences between the predictions are greater in the case of the

thin pavement. Also, at all load levels, there were some evaluation positions at which failure was predicted. The changes in yield function values with increasing loads were all as expected. That is, the yield function values all became larger as the load increased. An exception to this was the yield function value predicted by the linear layered elastic model, for the evaluation positions at the top of the base, center of the load (position 1). In this instance, the yield function decreased with increasing load. This can probably be attributed to the increased bending at higher loads which leads to higher confining pressures at the top of the base.

One case was observed where the linear layered elastic program predicted failure but the other two programs did not. However, there were two instances where the linear layered elastic program did not predict failure while the other two programs did. This seems to indicate that the linear layered elastic program can be unconservative, in some cases.

In all but one instance, the non-linear and finite element programs predicted the same outcome (i.e., failure versus no failure). The only instance where these two programs did not predict the same outcome was in the case of the thin pavement, 22.5 kN load, evaluation position number 4. In this case, the non-linear elastic program predicted failure while the finite element program did not, which indicates the non-linear layered elastic program is conservative. However, a closer inspection of the same evaluation position at higher stress levels will indicate that the finite element program also predicted failure at a higher stress. This indicates that the two programs do predict the same trends, but some difference in the magnitude of the predicted yield function does exist due to the differences in formulation of the two programs.

CASE STUDY

During 1993, three superheavy loads were moved over a relatively thin pavement section in Rusk County, Texas. As part of the research effort of this project, multidepth deflectometers (MDDs) (53,54) were installed at various depths in the pavement structure. The pavement response was then measured under several falling weight deflectometer (FWD) drops, as well as under some of the superheavy loads themselves. Figure 5.18 shows the pavement structure and MDD evaluation positions. An attempt was made to backcalculate the pavement moduli by using two different approaches. The first approach involved a conventional backcalculation (14,15) of elastic properties using surface deflections measured under the FWD and the MODULUS (55) backcalculation program. The second approach involved a backcalculation of non-linear material parameters using the finite element response model and the in-situ displacement measurements from the MDD positions. This approach is similar to that used by Uzan and Scullion (28), and De Beer et al. (56).

After the backcalculation of material parameters was completed, an attempt was made to predict the MDD displacements measured under different FWD drop heights by making use of the three response models. The backcalculated non-linear material constants were used in the two non-linear models, and the backcalculated linear moduli were used in the linear response model. Figures 5.19 through 5.21 show the measured and predicted displacements at the different FWD drop heights for each response model. These figures show that all three response models predicted the MDD displacements reasonably well. The pavement structure used in the linear layered elastic program was backcalculated from surface displacements measured under a single FWD drop height, while the two non-linear programs made use of MDD displacements to backcalculate material parameters. It follows that the predictions made by the linear layered elastic program required considerably less time and effort to obtain. The larger average error associated with these predictions (i.e., 12 percent as opposed to approximately 6 percent) is not considered to be significant when compared to typical errors encountered when performing backcalculation of layer moduli. Based on the above discussion, it would appear that all three programs

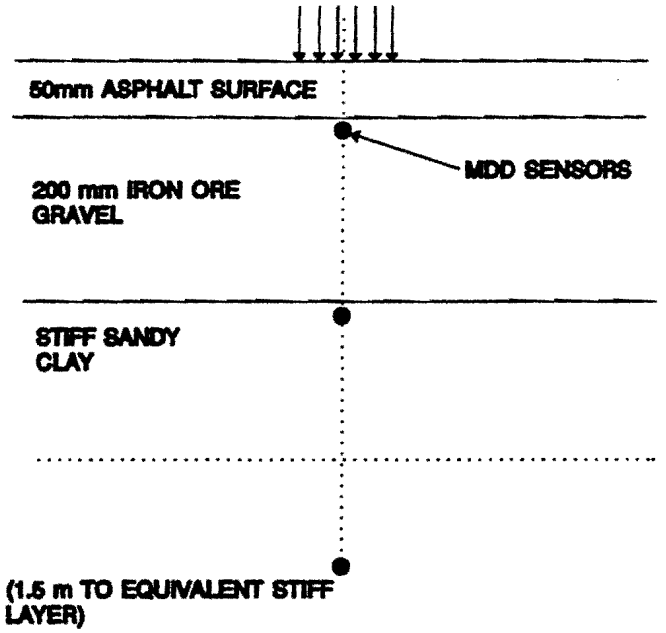

Figure 5.18. Pavement Structure and MDD Positions Used in Rusk County Case Study.

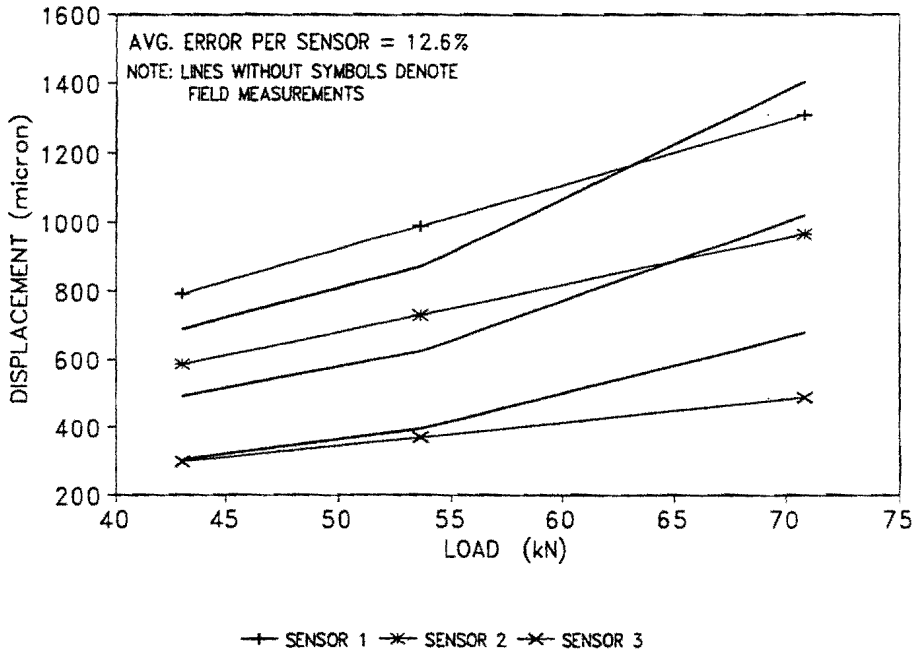

Figure 5.19. Measured and Predicted Displacements - Linear Layered Elastic Response Model.

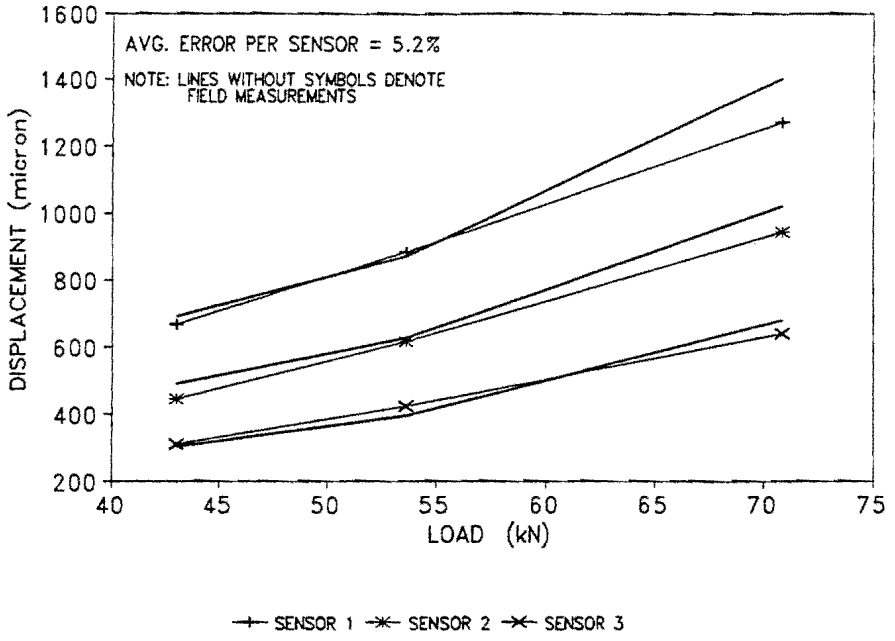

Figure 5.20. Measured and Predicted MDD Displacements - Non-Linear Layered Elastic Program.

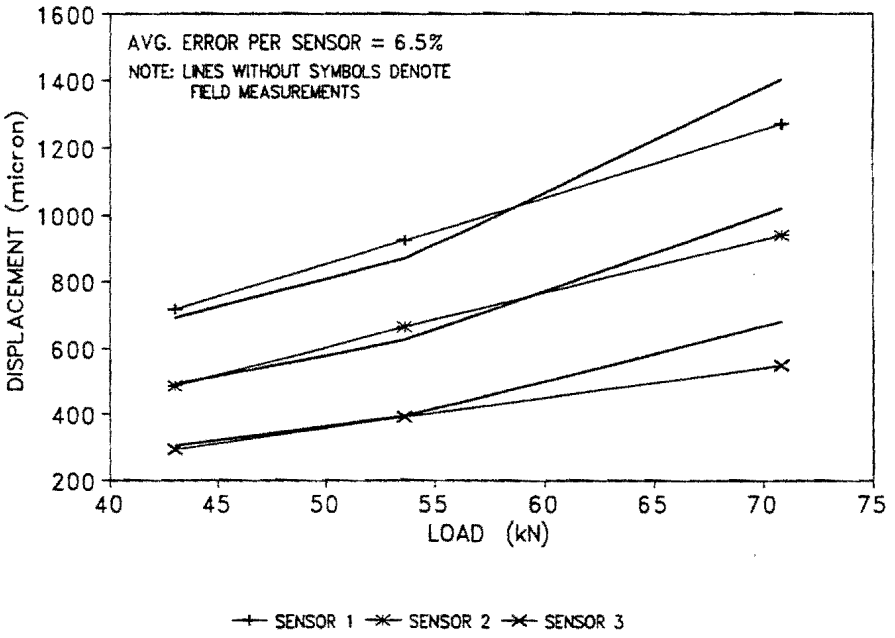

Figure 5.21. Measured and Calculated MDD Displacements - Finite Element Response Model.

predicted pavement response with reasonable accuracy. However, significant differences were observed when the same response models and material coefficients were used to calculate the yield function value. The maximum load applied to the pavement during the series of superheavy load vehicle passes was a 60.08 kN single wheel load. When this load was used to calculate the yield function value at different evaluation positions, the same trends highlighted in the preceding section were observed. Figure 5.22 shows the yield function values predicted by each of the response models at the edge of the load and at three different depths (for the chosen material strength parameters, the edge of the load evaluation position was found to be the most critical). Figure 5.22 seems to indicate that the different response models may, under certain circumstances, predict different yield functions even when the same programs predict very similar vertical displacements. This may indicate that vertical displacement alone is not an encompassing measure of the response model's ability to accurately model pavement behavior. It should also be noted that the predicted yield function values from the finite element and non-linear layered elastic program are consistent with the observation that no visible damage resulted from the superheavy load moves evaluated in this case study.

SUMMARY AND CONCLUSIONS

In this chapter, an analysis was described in which the results of three different response models were compared. The three models used were a finite element model, a non-linear version of a layered elastic program, and a conventional linear layered elastic program. The stresses and predicted yield function values calculated by each program were compared with one another. In this comparison, the finite element model was considered to be the most accurate with respect to its ability to model actual pavement behavior. The results of the finite element program were, therefore, used as a benchmark against which the two simplified response models were evaluated. The following observations can be made:

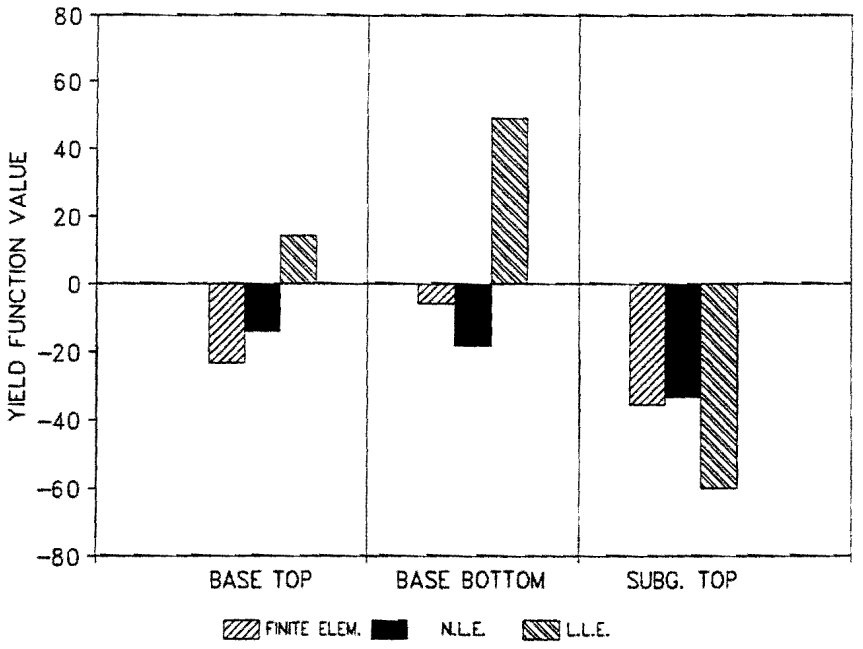

Figure 5.22. Yield Function Values Calculated by Different Response Models - Rusk County Case Study, Edge of Load Evaluation Position.

1. All three response models show the same basic patterns of stresses within a pavement. Differences in the magnitudes of predicted stresses are the results of failure of the simplified models to account for certain aspects of material behavior. Due to the pronounced bending effect that exists in the case of the linear elastic program, compressive stresses calculated at the top of the layer and tensile stresses calculated at the bottom of the layer tend to be higher than those calculated by the finite element program.
2. The effect of sublayering and using stress-dependent moduli and Poisson's ratios can greatly reduce the tensile stresses calculated for the bottom of the base layer. This can most probably be attributed to the reduction of the bending effect brought about by sublayering.

3. Stresses predicted by the three programs tend to approach one another as the offset from the load increases. While this may merely be due to the attenuation of stresses with increasing distance from the load, it does suggest that the inability of the non-linear layered elastic approach to vary moduli and Poisson's ratios in a lateral direction does not greatly affect the accuracy of predictions.
4. In the case of the thick pavement, the differences in the predicted yield functions were generally small. All three programs predicted that failure was not likely to occur in any layer. As expected, the differences in predicted yield function values tended to increase as the load increased. In the case of the thin pavement, the differences in predicted yield function values were more pronounced. Several instances were noted where one of the three programs predicted failure while the other two programs did not. The non-linear layered elastic program and the finite element program generally predicted very similar yield function values. Only in one instance did these two programs not predict the same outcome (i.e., failure or no failure).

Based on the above observations, it can be concluded that the effects of non-linear material behavior play an important role in predicting pavement response under heavy loads. Even in cases where displacements can be predicted with reasonable accuracy, failure to take material non-linearity into account can lead to significant errors in predicted stresses and yield function values. However, it should be noted that in the absence of information on non-linear material constants, the conventional linear layered elastic approach may still be used with some confidence. This will be especially applicable to thicker pavements.

The non-linear layered elastic program offered a convenient compromise between the linear layered elastic program and the more accurate, but more time consuming, finite element program. The inability of the non-linear layered elastic program to vary the elastic constants in the lateral direction did not seem to have a serious effect on the predicted stress state or yield function values.

CHAPTER VI

ANALYSIS OF THE EFFECTS OF DIFFERENT LOAD CONFIGURATIONS ON THE PREDICTED STRESS STATE

INTRODUCTION

The two main characteristics that differentiate superheavy load vehicles from more typical heavy traffic are the abnormally large gross vehicle weight of superheavy load vehicles and the use of multiple axles and wheels to distribute this load over a larger number of wheels. In routine pavement design, a standard 80 kN axle load having dual wheels is normally modeled with only one side of the axle being included in the modeling process (i.e., one dual wheel load with 20 kN per wheel is used). In the case of superheavy load vehicles, a variety of load configurations are possible. A large number of axles are used, and a variety of wheel spacings can be encountered, depending on the type of vehicle used. It is obvious that an attempt to include all wheels and axles of a superheavy load vehicle in a response model would be a time consuming endeavor. Undoubtedly, the most accurate representation of the actual load and pavement interaction will be obtained when all loads are included as they are encountered in the field. However, an earlier investigation (57) has indicated that stresses and strains attenuate fairly rapidly at increasing offsets from the load center. This indicates that there may be a limited advantage offered by the inclusion of more loads in an analysis if such loads lie relatively far from the point at which stresses are to be evaluated.

In the following, an analysis of the influence of different load configurations on the predicted stress state is described. The general approach was to use a relatively complex load configuration that was representative of load configurations typically encountered in the field. Two simplified variations of this load configuration were then chosen, and the effect of these simplifications on the stress state was studied.

RESULTS FROM PREVIOUS INVESTIGATIONS

A preliminary investigation of the effect that different load configurations have on the stress state was conducted by Jooste and Fernando (57). Although the approach followed in this earlier investigation was slightly different from the one adopted here, several of the findings of this investigation are of interest and are summarized. In the investigation conducted by Jooste and Fernando (57), the behavior of different types of pavements were modeled under a single wheel load. Two pavement types were used, a thin, weak pavement with soft layers and a thicker pavement with relatively stiff layers. Two load magnitudes were also used. Figure 6.1 and Table 6.1 summarize the two pavement structures used in the analysis.

Displacements and strains were calculated at different depths and offsets from the load center, and all observations were noted. Some of the more significant observations of this investigation are summarized below:

1. The strains were found to diminish to less than two percent of the maximum strains (i.e., those measured under the load center) at a distance of 0.61 m in the case of the thin pavement. In the case of the thick pavement, this distance was 1.22 m.
2. Displacements were found to attenuate over a much larger distance than the strains. For the thin pavement, the vertical displacement at the top of the subgrade diminished to 5 percent of the maximum vertical displacement at offsets of between 2.74 m and 5.79 m, depending on the depth at which the evaluation was performed. For the thicker pavement, the corresponding distance was found to be between 6.4 m and 10.79 m.
3. For calculated displacements, the zone of influence was found to be significantly reduced in cases where the subgrade was underlain by a shallow bedrock. However, with respect to strains, the presence of a shallow rigid layer was found to have a negligible influence on the variation of predicted strains with distance from a given wheel load.

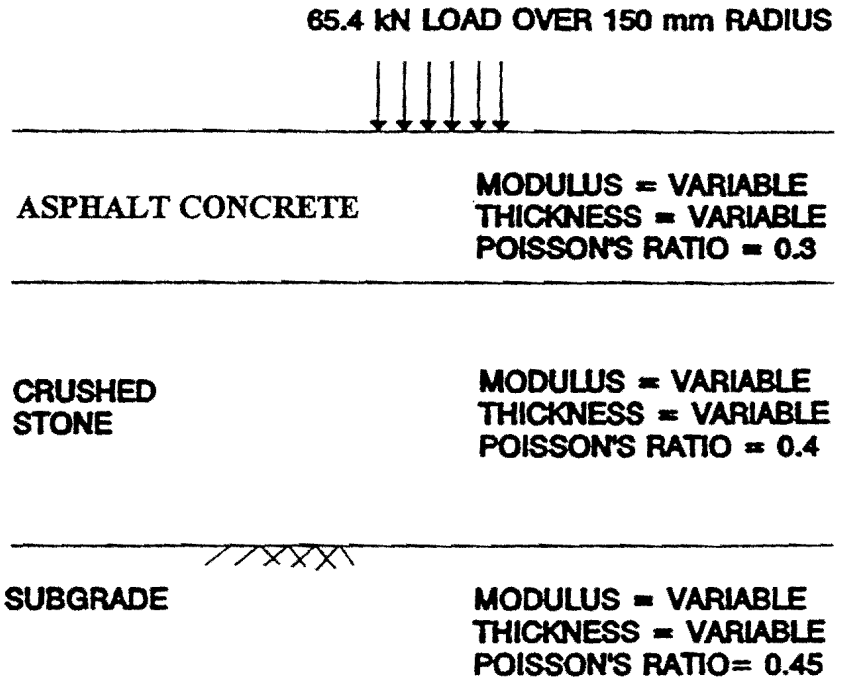

Figure 6.1. Pavement Structure Used in the Study by Jooste and Fernando (57).

Table 6.1. Pavement Layer Moduli and Thicknesses Assumed for Weak and Strong Pavements in Study by Jooste and Fernando (57).

Parameter	Weak Pavement	Strong Pavement
E_1 (MPa)	1725	6900
E_2 (MPa)	103.5	414
E_3 (MPa)	34.5	138
h_1 (mm)	50	150
h_2 (mm)	100	300

Based on the above observations, it can be concluded that the number of wheel loads that need to be included in any investigation will depend on the parameter of interest. Strains attenuate much faster than displacements with increasing distance from the load axis. The attenuation of stresses with increasing distance from the load axis can be expected to follow the same trends as strains. Figures 5.4 through 5.9 in Chapter V also seem to indicate that stresses attenuate relatively rapidly as the distance from the load axis is increased. This is particularly evident in Figure 5.9.

TYPICAL LOAD CONFIGURATIONS USED ON SUPERHEAVY LOAD VEHICLES

During the course of this study, researchers monitored a number of superheavy load moves. They observed that there are three basic configurations used by superheavy load haulers. The first configuration makes use of conventional truck and trailer combinations. Figure 6.2 shows an example of this arrangement, normally used on superheavy loads close to the limits for being classified as superheavy (i.e., 1112 kN). Another arrangement is a tractor-trailer combination shown in Figure 6.3. In this case, a specialized tractor is used with a trailer that can have up to 12 wheels per axle and as many as 20 axles. This configuration has been encountered on most of the heavier superheavy load moves, such as those having more than 8000 kN gross vehicle weight. The third configuration is a specialized vehicle such as the self-propelled multiple axle trailer shown in Figure 6.4.

A study of the load configurations encountered during the course of this study indicated that a variety of axle and wheel spacings are possible on the same type of load moving vehicle. Based on this information, an attempt was made to summarize the axle and wheel spacings encountered on each type of load moving vehicle. Figure 6.5 and Table 6.2 summarize some of the load arrangements encountered during the course of this investigation. Figure 6.5 and Table 6.2 indicate that the highest variation in wheel spacing is typically encountered in the case of specialized tractor-trailer combinations. Axle spacing is fairly constant for most of the other vehicle types. Also, in the case of

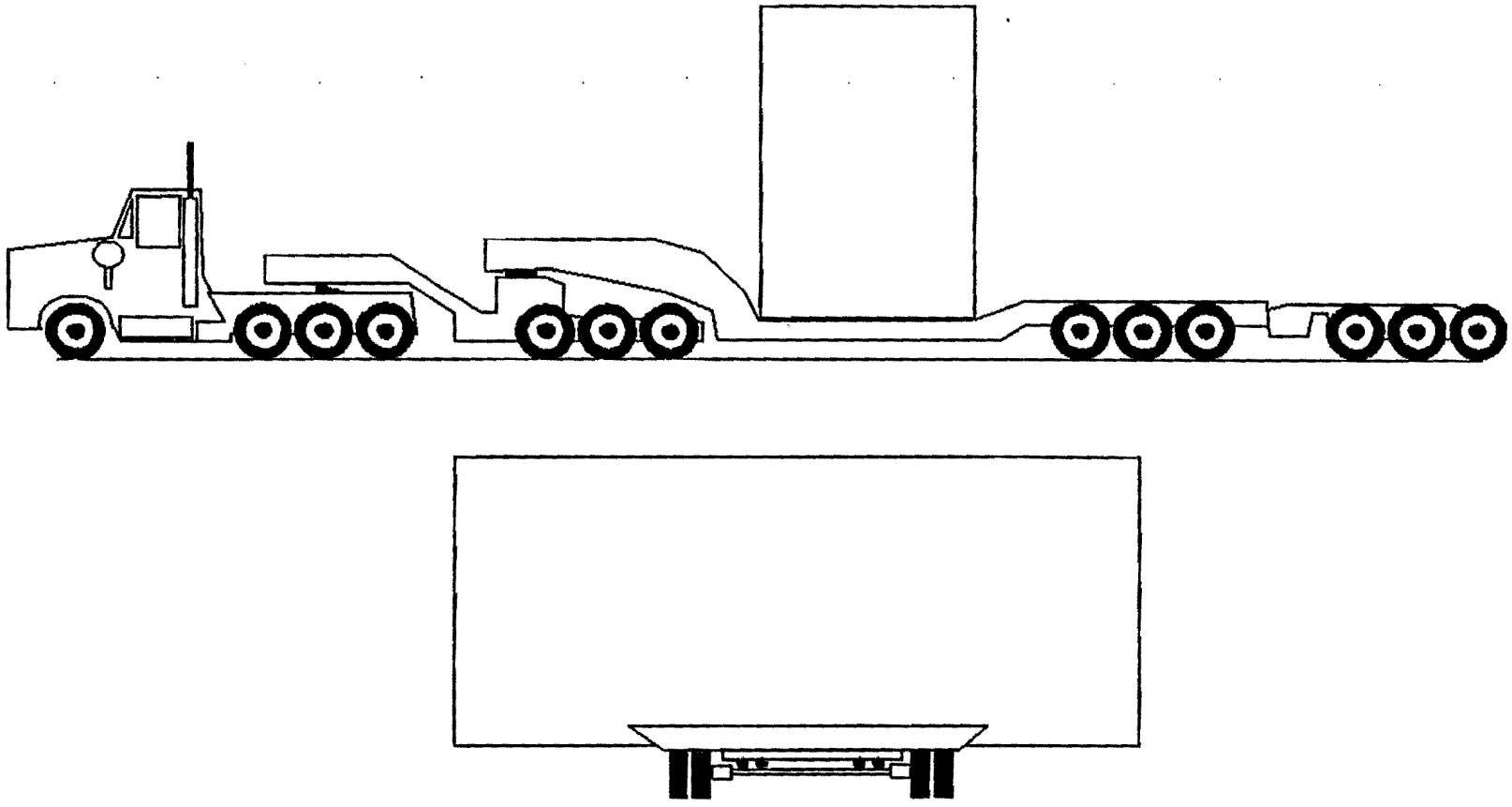

Figure 6.2. Example of a Conventional Truck and Trailer Combination.

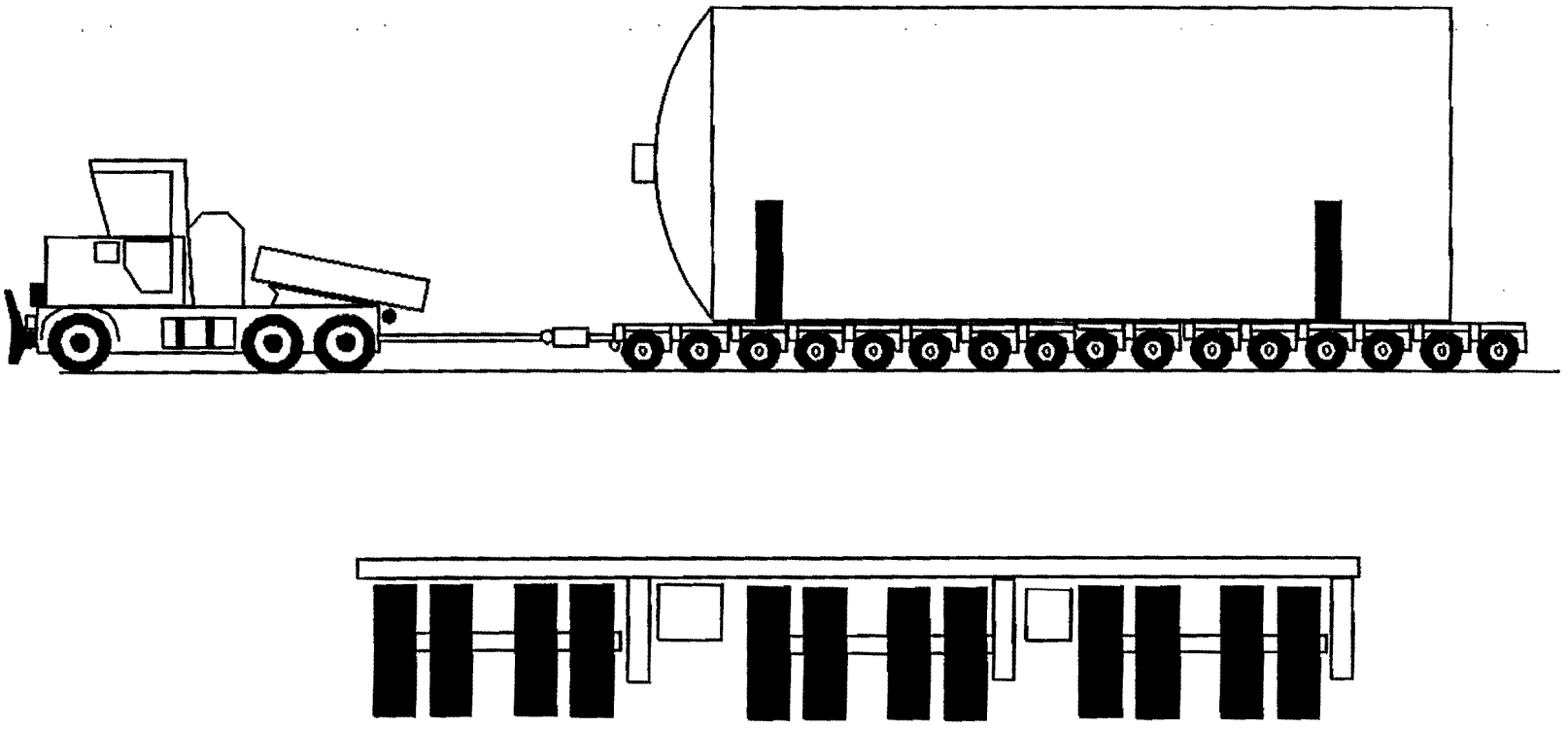

Figure 6.3. Example of a Specialized Tractor-Trailer Combination.

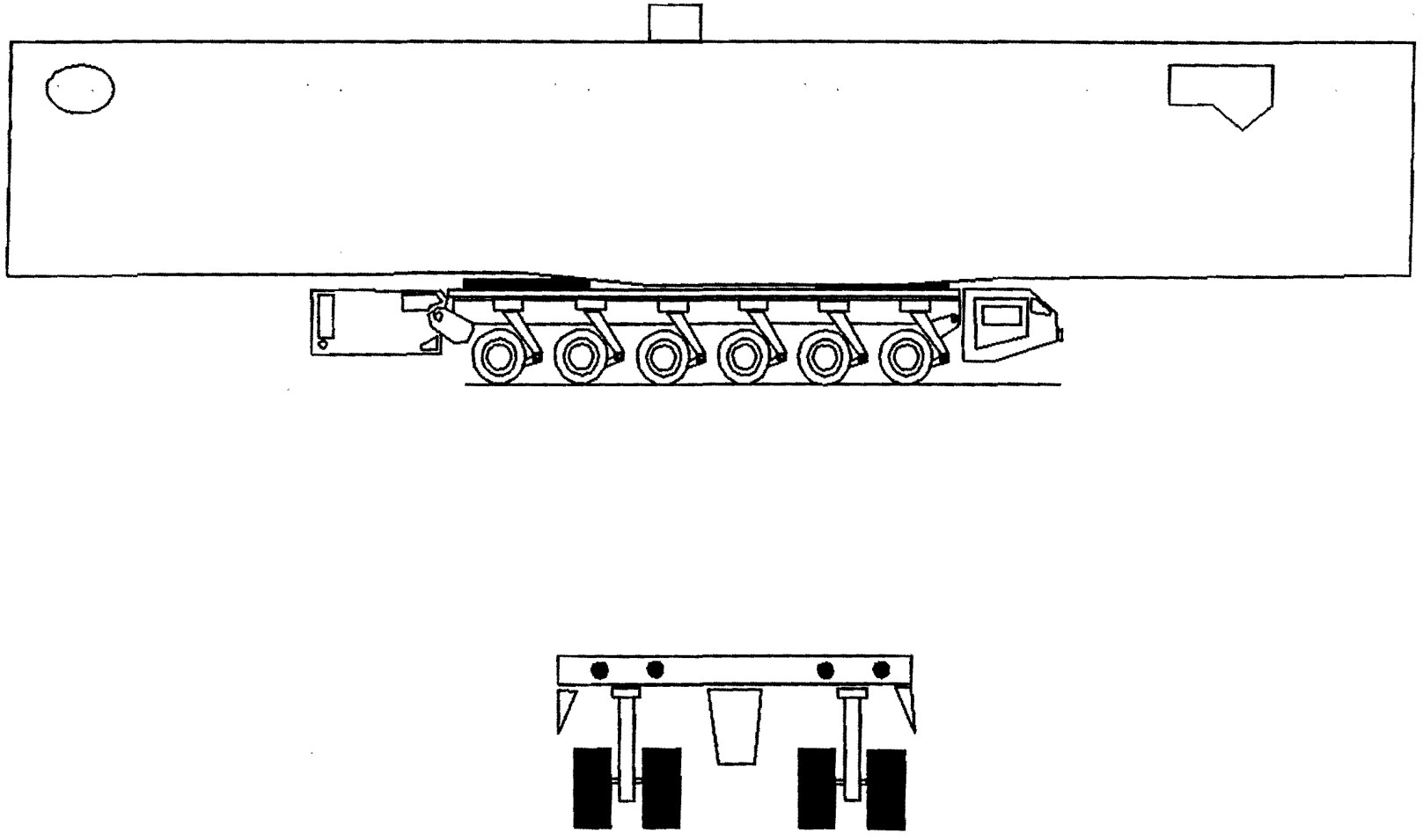

Figure 6.4. Example of a Self-Propelled Multiple Axle Trailer.

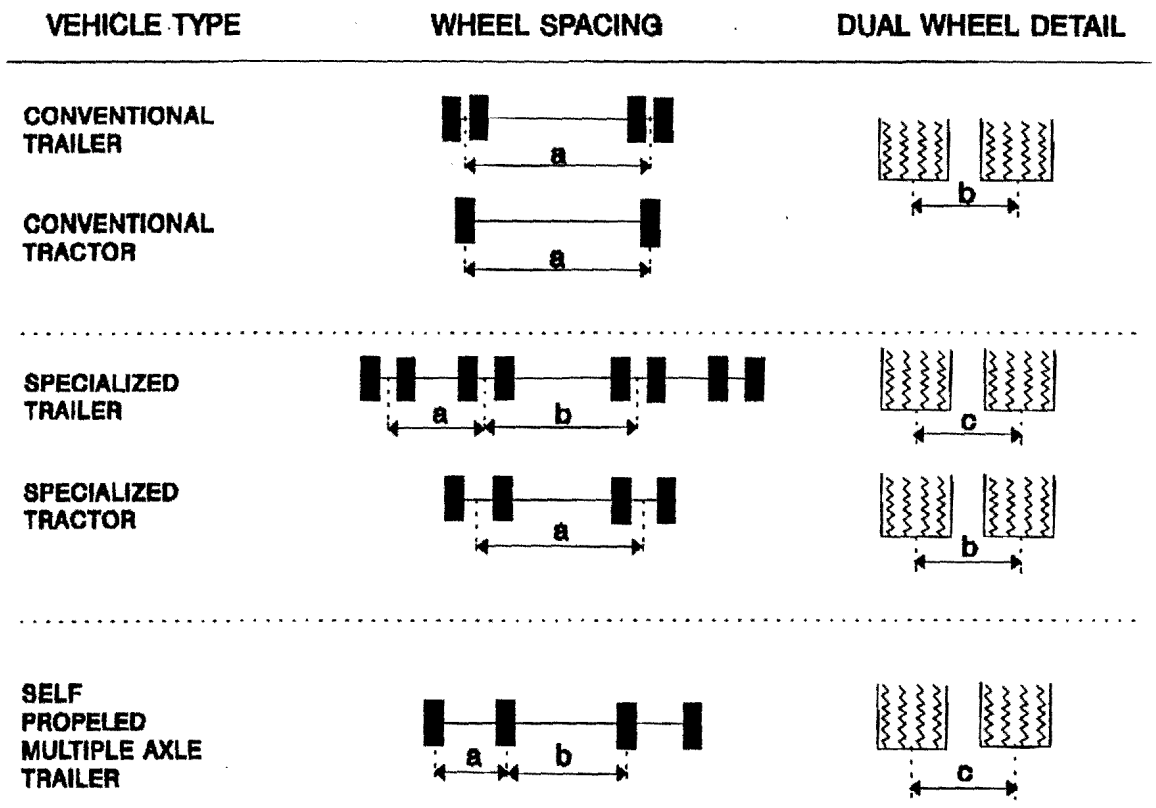

Figure 6.5. Typical Load Configurations Used on Superheavy Load Vehicles.

Table 6.2. Approximate Axle and Wheel Spacings Used on Superheavy Load Vehicles.

Vehicle Type	Approximate Axle Spacing (mm)	Approximate Wheel Spacing		Approximate Wheel Load (kN)
		Reference	Spacing (mm)	
Conventional truck and trailer (rear)	1220	a b	1830 320 to 330	33.4
Conventional truck and trailer (steering)	N/A	a	1960 to 2060	32.0
Specialized Trailer	1370 to 1520	a b c	380 to 1020 1120 to 1220 270 to 325	18.7 to 31.7
Specialized Tractor	1830*	a	2130	34.7
Self-Propelled Multiple Axle Trailer	1400	a b c	620 860 620	40.0

* Spacing refers to rear tandem axle of tractor

the tractor-trailer combinations, a general pattern seems to be that two wheels are spaced close together as in a conventional dual wheel axle.

These groups of two wheels are then spaced at intervals of approximately 380 to 1220 mm. These trailers can normally be connected in a lateral direction so a wider load can be accommodated, if necessary. The typical wheel loads shown in Table 6.2 are only approximate and are based on the wheel loads encountered on superheavy load moves monitored during the course of this study. The wheel loads shown for the conventional truck and trailer combination are based on the maximum equipment limit.

ANALYSIS OF THE EFFECT OF DIFFERENT LOAD CONFIGURATIONS

To study the effects different load configurations have on the predicted stress state and yield function, a typical superheavy load configuration was chosen. The load configuration chosen was approximately that of the special trailer as well as that of the self-propelled multiple axle trailer. Three different models of this load configuration were used to model pavement response. The schematic illustrations of the three load models are shown in Figures 6.6 through 6.8. Figure 6.6 is deemed the most accurate load representation and was used as the standard against which the accuracy of the more simplified load models were evaluated. The numbered dots in the figures represent positions at which the stresses and yield functions were evaluated. The loads shown as dotted ellipses in Figures 6.7 and 6.8 were not included and are shown only to illustrate the relationship between the simplified load configuration and the three-axle configuration shown in Figure 6.6.

The responses of two different pavement types to each of the load configurations were calculated using the non-linear layered elastic program described in Chapter V. This program requires that a single point be chosen within a layer at which stresses are evaluated and stress dependent moduli calculated. For this analysis, point 4 shown in Figure 6.6 was chosen. This point was chosen because it was deemed to be the most representative of the general stress state under the multiple wheels loads. This was deemed to be the case for all three chosen load configurations. For each layer, the depth

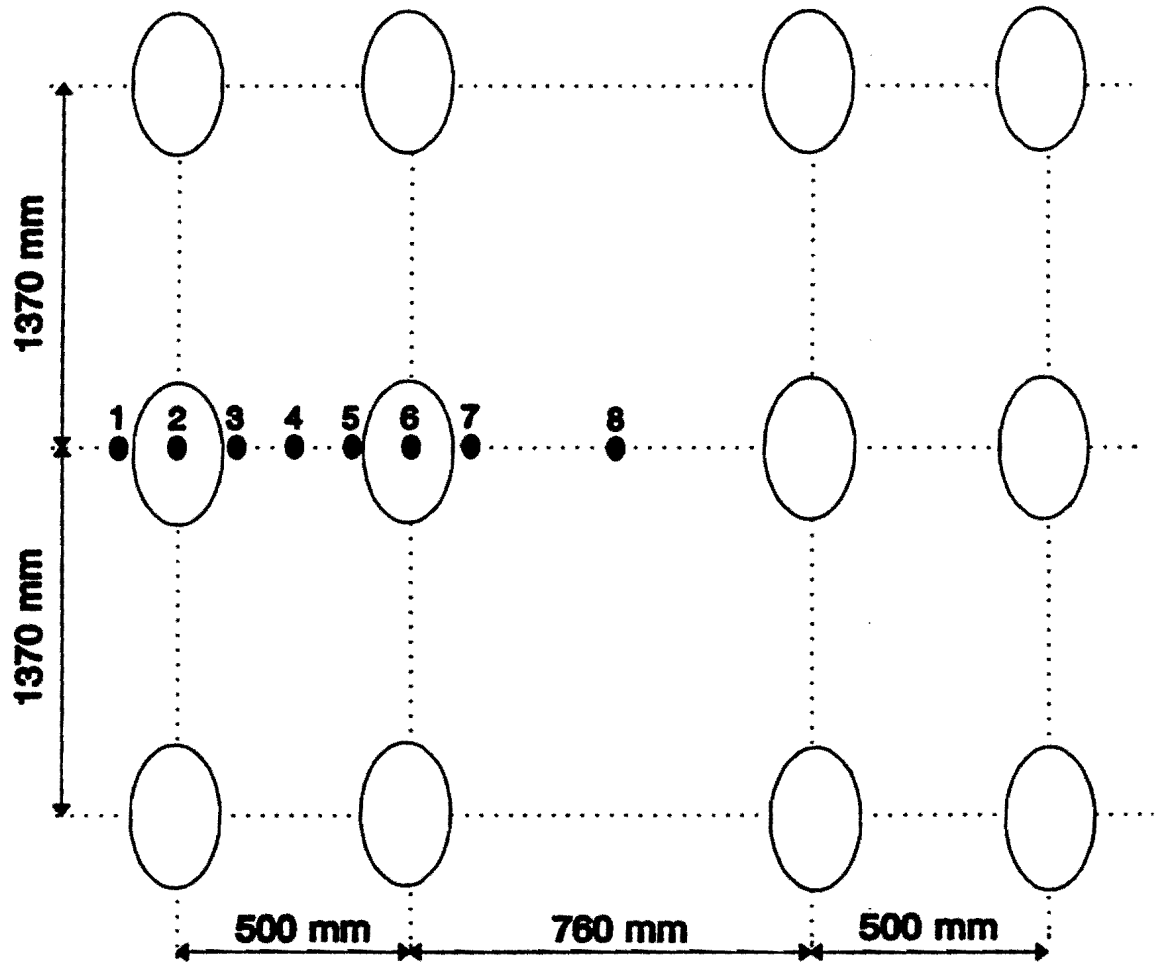

Figure 6.6. Triple Axle Load Used in Analysis.

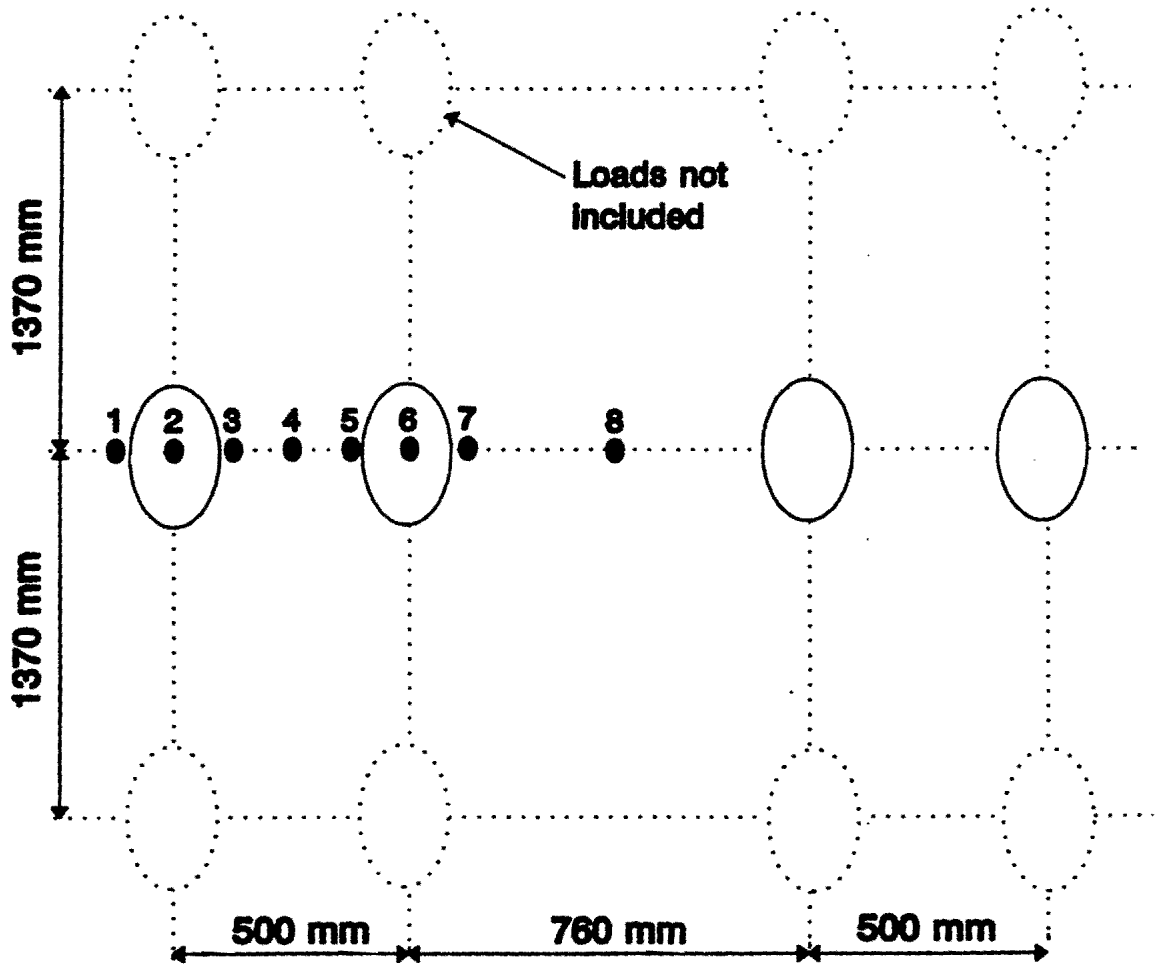

Figure 6.7. Single Axle Load Used in Analysis.

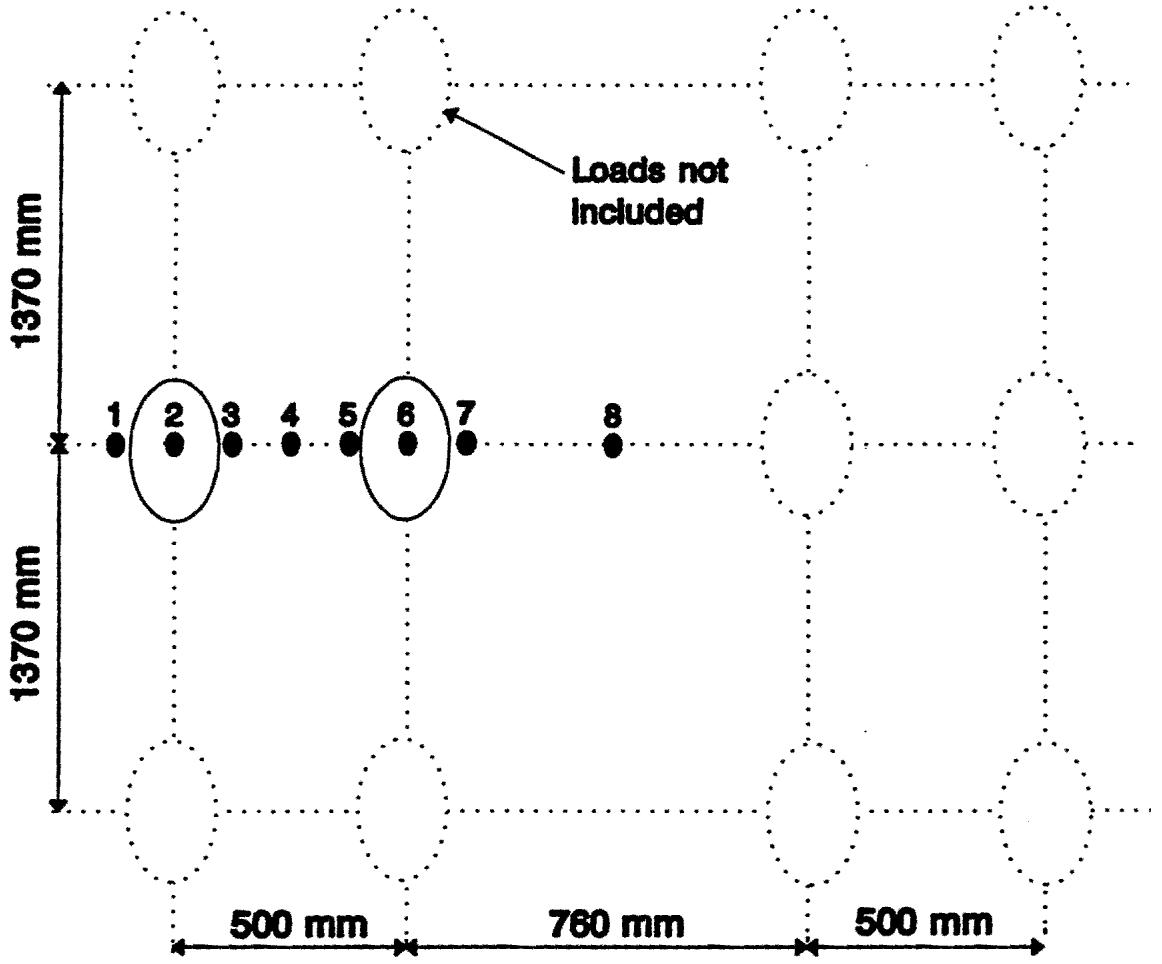

Figure 6.8. Dual Wheel Load Used in Analysis.

at which stress dependent moduli and Poisson's ratios were calculated was in the middle of the layer.

The two pavement types chosen were once again a thin and a thick pavement with typical material properties. Figures 6.9 and 6.10 show the two pavement structures used. For each pavement and load configuration, the stresses and yield functions were evaluated at the numbered positions shown in Figures 6.6 through 6.8. The yield functions were evaluated at the bottom of the asphalt layer, at the top and bottom of the base, and at the top of the subgrade. Figures 6.11 through 6.18 show the resulting yield function values. The numbered positions on the abscissa of these figures refer to the evaluation positions shown in Figures 6.6 through 6.8. The material strength parameters used to calculate the yield function are shown in Table 6.3. These values are deemed to be typical values for the material types assumed in this analysis (37,49).

An immediate observation that can be made from the figures is that similar yield function values are predicted for the three load configurations. In most cases, all three load configurations predict the most critical yield function at similar positions. For instance, in the case of the thick pavement, top of the base position, all three load configurations resulted in the most positive yield function being calculated at position 1 (i.e., the outside edge of the outer wheel). Another general observation is that the differences between the responses under the three load configurations are greater in the case of the thick pavement. In the case of the thin pavement, only minimal changes in the predicted yield functions were noted. This is to be expected, as the zone of influence of a given wheel load extends outward and increases with depth. This finding also corresponds with the earlier study by Jooste and Fernando (57).

Another observation that follows from the figures is that the triple axle load configuration predicts a more negative yield function in the majority of cases. This means that the two simplified load configurations generally result in more conservative predictions. The reason for this seemingly unreasonable result becomes apparent when the stress tensors predicted by each of the load configurations are studied in more detail.

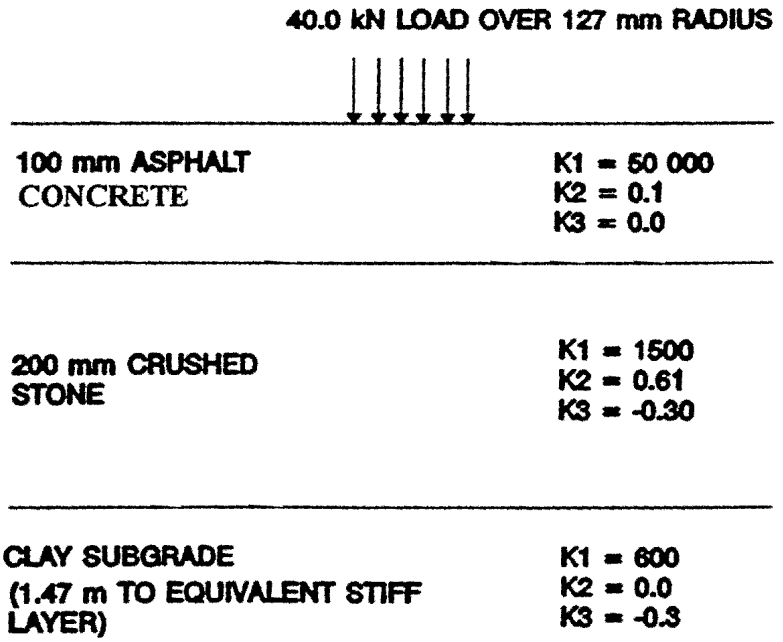

Figure 6.9. Thick Pavement Used in Analysis.

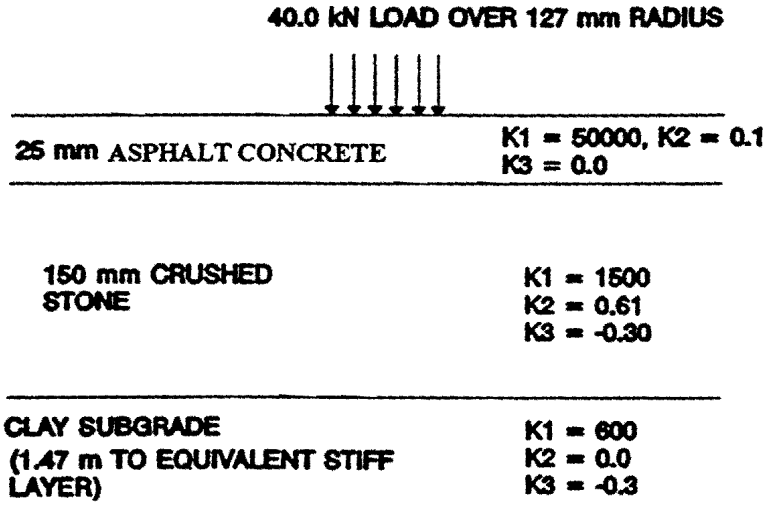

Figure 6.10. Thin Pavement Used in Analysis.

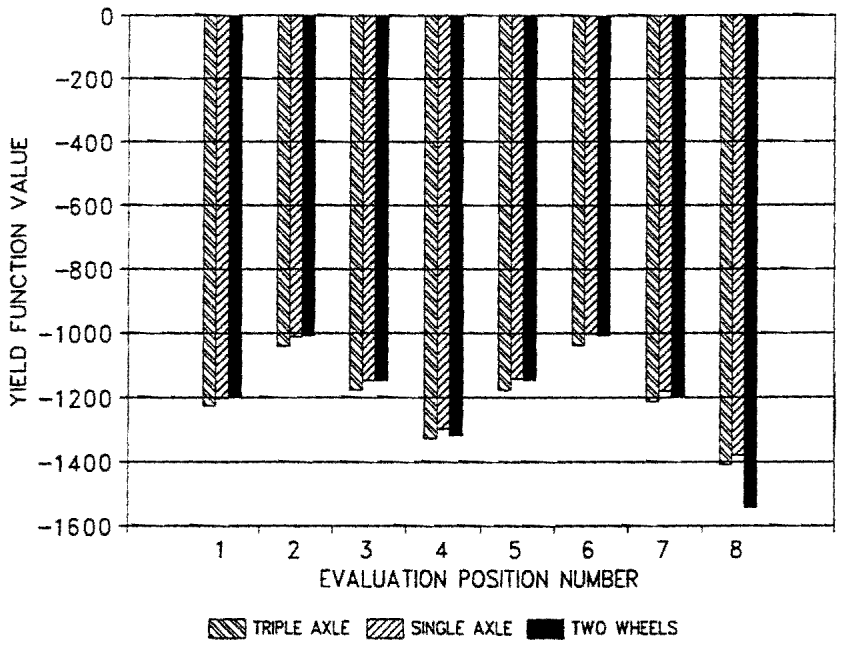

Figure 6.11. Yield Function Values Predicted by the Three Load Configurations - Thick Pavement, Bottom of Asphalt Evaluation Position.

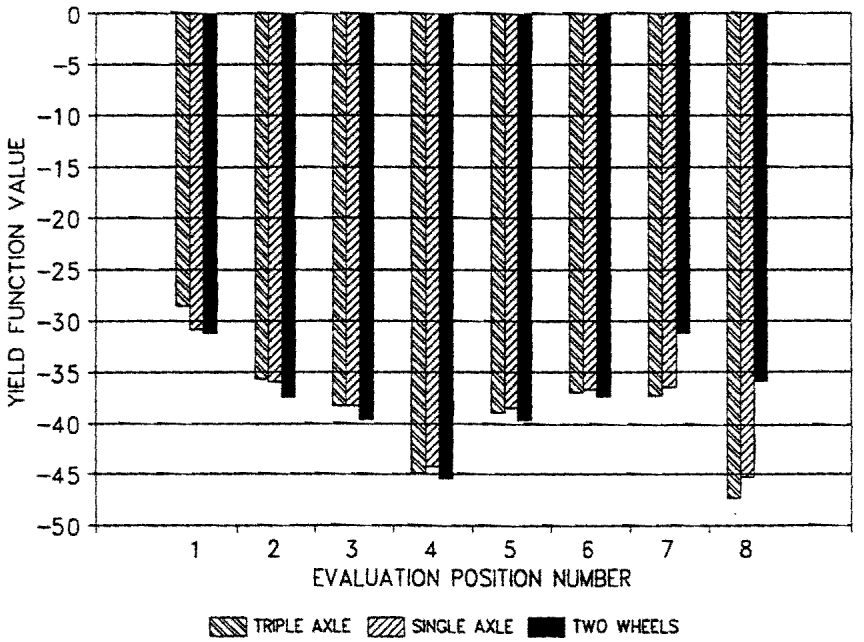

Figure 6.12. Yield Function Values Predicted by the Three Load Configurations - Thick Pavement, Top of Base Evaluation Position.

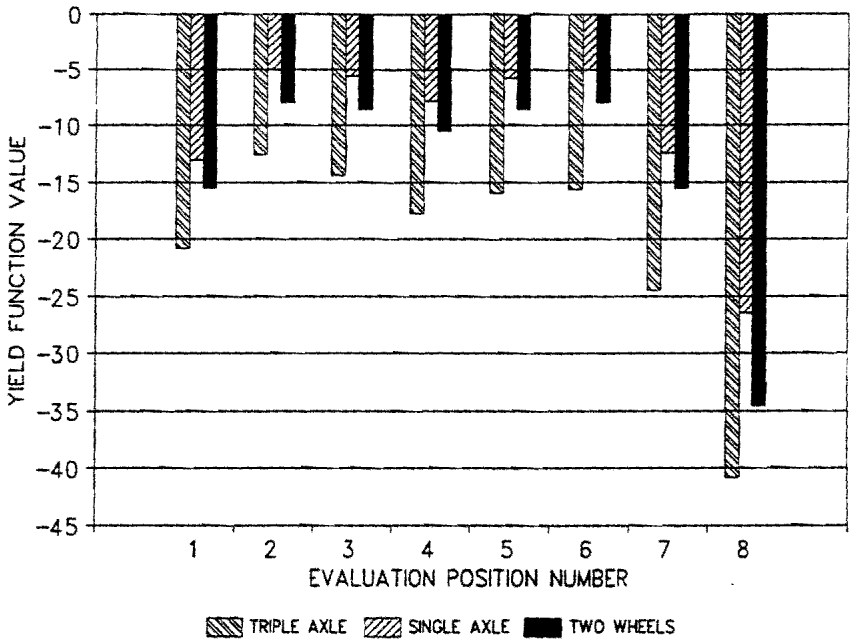

Figure 6.13. Yield Function Values Predicted by the Three Load Configurations - Thick Pavement, Bottom of Base Evaluation Position.

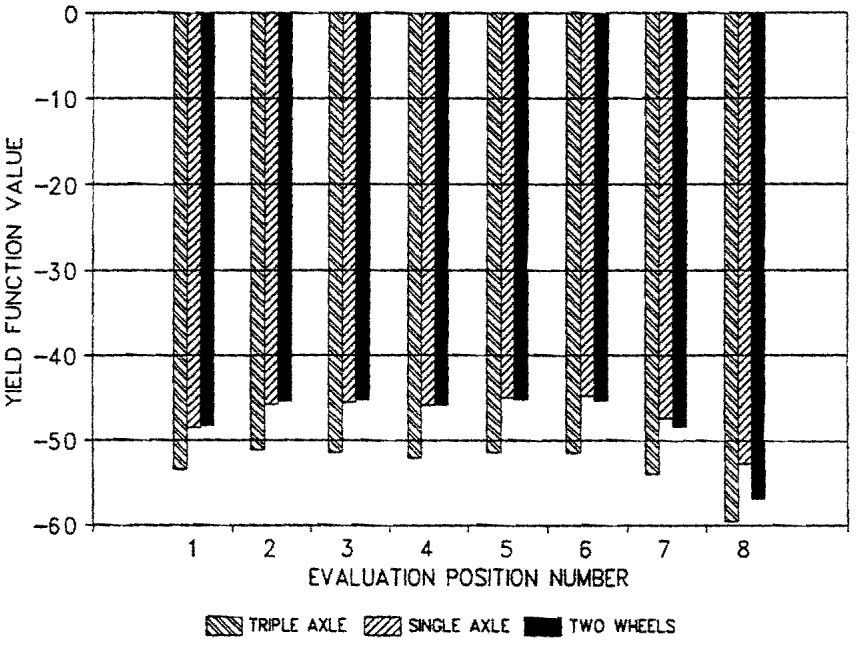

Figure 6.14. Yield Function Values Predicted by the Three Load Configurations - Thick Pavement, Top of Subgrade Evaluation Position.

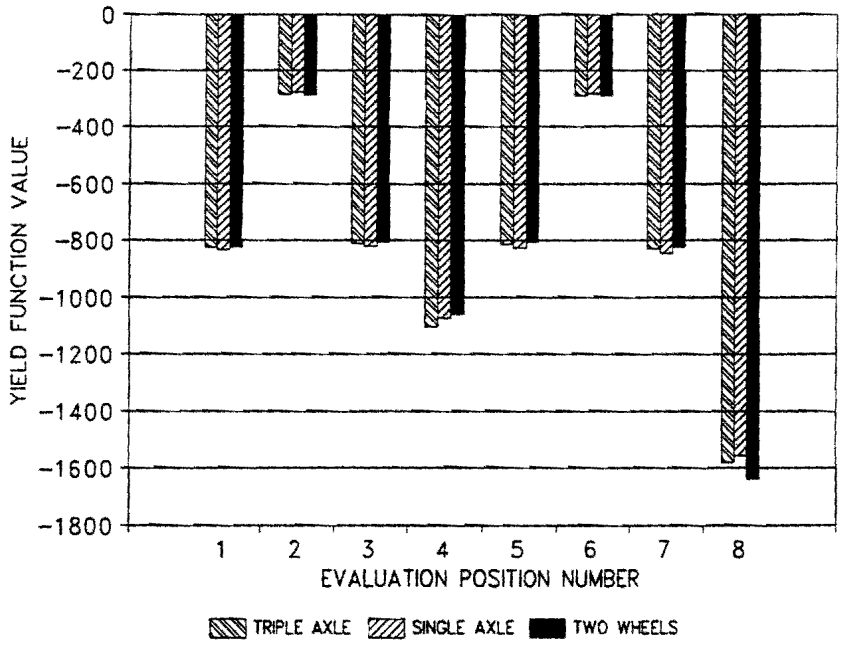

Figure 6.15. Yield Function Values Predicted by the Three Load Configurations - Thin Pavement, Bottom of Asphalt Evaluation Position.

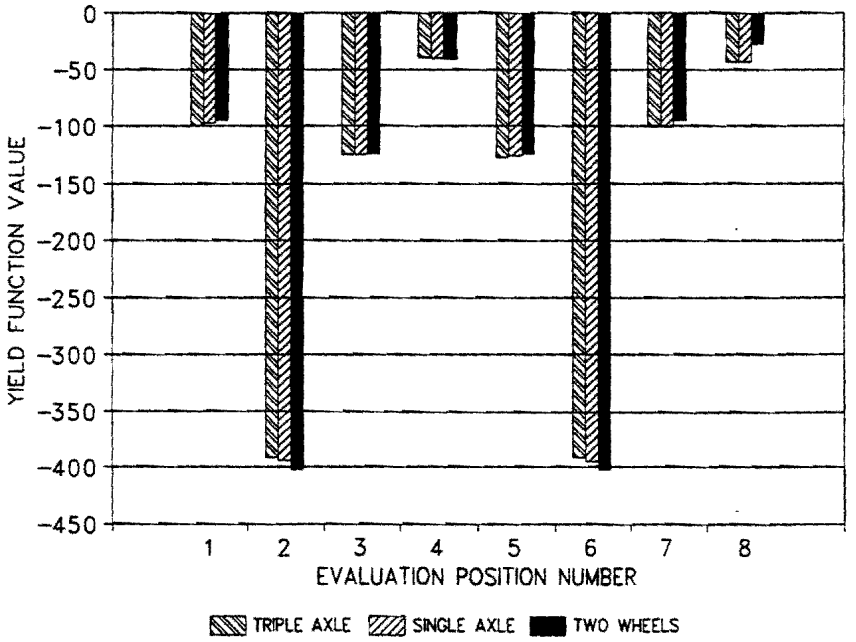

Figure 6.16. Yield Function Values Predicted by the Three Load Configurations - Thin Pavement, Top of Base Evaluation Position.

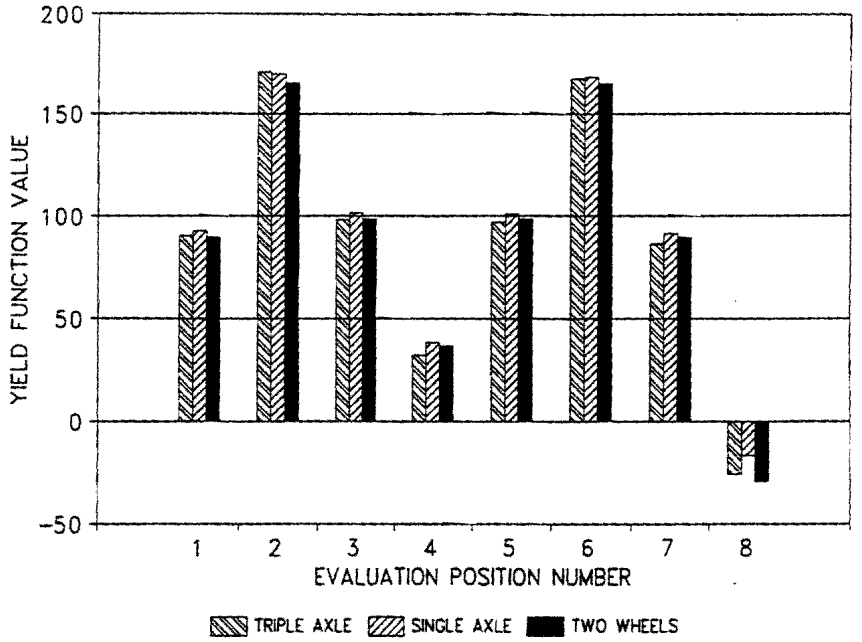

Figure 6.17. Yield Function Values Predicted by the Three Load Configurations - Thin Pavement, Bottom of Base Evaluation Position.

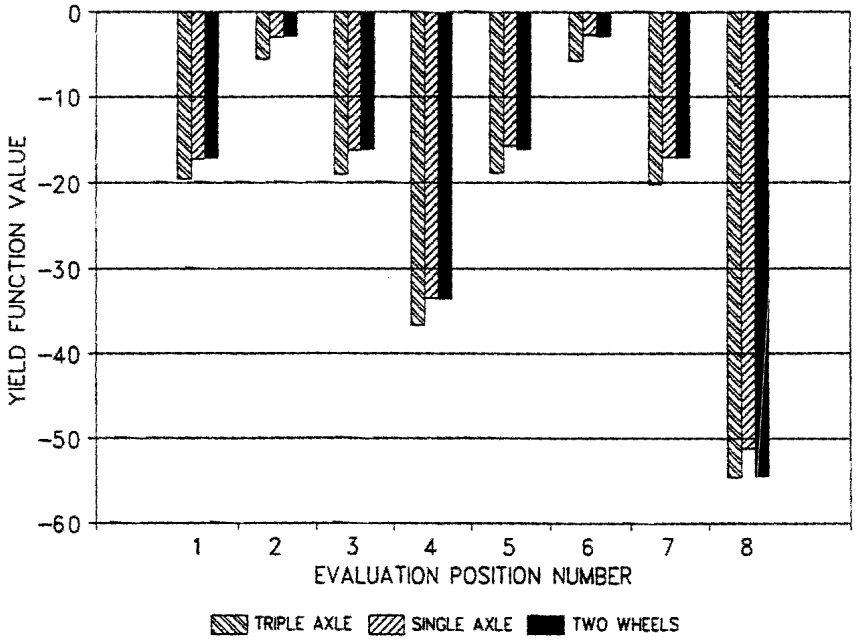

Figure 6.18. Yield Function Values Predicted by the Three Load Configurations - Thin Pavement, Top of Subgrade Evaluation Position.

Table 6.3. Material Strength Parameters Used in Determining Yield Function Values.

Layer and Material Type	Cohesion (kPa)	Angle of Friction
Asphalt Surfacing	1725.0	0° or 24° *
Crushed Stone Base	69.0	50.0°
Clay Subgrade	89.7	30°

* An angle of friction of 0° was used for the bottom of the asphalt evaluation position.

Table 6.4 summarizes the stress states and elastic constants predicted by each of the three load configurations. The stresses shown in Table 6.4 are the principal stresses. σ_1 and σ_2 act approximately in the radial and tangential directions, and σ_3 acts approximately in the vertical direction. Negative stresses denote compression.

Table 6.4 shows that, for the two evaluation positions shown, the stress states predicted for the different load configurations are very similar. This is especially true of the vertical stress component (σ_3). In the case of the two horizontal stress components, it can be seen that the three axle model predicts larger compressive stresses. The effect this has on the yield function value can be seen from resulting values of the first stress invariant (I_1) and the second invariant of the deviatoric stress tensor (J_2). In this respect, it should be noted that, due to the relatively high angle of friction of granular materials, a higher state of compression would lead to a higher resistance to shear. Conversely, a higher J_2 value is indicative of a stress state in which the deviatoric component is high, which means that high shear stresses exist. Table 6.4 shows that in the case of the three-axle load configuration, the magnitude of I_1 is higher than in the case of the other two load configurations. Furthermore, the effect of the two axles adjacent to the central axle is to increase the compressive stresses in the horizontal directions. This results in a lower J_2 value, which in turn results in a more negative yield function value being calculated in the case of the three-axle load configuration.

Table 6.4. Stress States and Yield Functions Predicted by Different Load Configurations.

Position*	Load Type	σ_1 (kPa)	σ_2 (kPa)	σ_3 (kPa)	I_1	J_2	Resilient Modulus (MPa)	Poisson's Ratio	Yield Funct. Value
Bottom of Base	Three Axles	24.7	13.3	-84.7	-46.7	3619.8	197.8	.477	-12.63
	Single Axle	33.4	12.4	-84.0	-38.2	3916.1	178.0	.478	-5.0
	Dual Wheel	30.0	14.6	-83.6	-38.9	3801.0	173.7	.478	-8.0
Top of Subgrade	Three Axles	-1.7	-5.8	-84.1	-91.6	2158.0	84.1	.308	-51.1
	Single Axle	5.6	-4.3	-83.2	-81.9	2369.0	82.5	.304	-45.6
	Dual Wheel	6.1	-1.4	-82.7	-78.0	2426.6	82.3	.294	-45.3

* All evaluations were done at the center of the outer wheel (i.e., position 2 in Figures 6.6 through 6.8).

It would, therefore, seem that simplifying a multiple axle load configuration into a single axle or even a dual wheel load leads to a more conservative yield function prediction. Of the three load configurations analyzed, the single axle generally resulted in the most conservative prediction of failure potential. In those instances where the triple axle or dual wheel loads resulted in a more conservative prediction, the differences between the three predicted yield functions were small. Furthermore, there does not seem to be any advantage to modeling all wheels on an axle as opposed to modeling only the two wheels that are closest together. However, it is conceivable that situations may exist where wheel spacing is so close that this may not be the case. For wheel spacings similar to those shown in Figures 6.6 through 6.9, it seems that the simpler dual wheel offers a very close approximation to the more complex single axle (4 loads). This becomes especially evident when one examines how small the differences are in the I_1 and J_2 values predicted by these two load configurations.

It is also interesting to note the differences in the elastic parameters predicted by the different load configurations. As expected, the three-axle load configuration, because of its higher confinement, results in higher modulus values being calculated. Although the differences in calculated Poisson's ratios are small, they do conform to expected behavior. Table 6.4 shows that, in the case of the stress-stiffening granular base, the higher confinement of the three axle model resulted in a slightly lower Poisson's ratio. For the stress-softening subgrade material, the opposite is observed.

SUMMARY AND CONCLUSIONS

In this chapter, a comparison was made between the stress states predicted by different types of load configurations. Three versions of a load configuration deemed to be fairly representative of the types of load configurations typically encountered on superheavy load moving vehicles were modeled, and the resulting stress states and yield function values were analyzed. Some of the more significant observations made are as follows:

1. The two simplified load configurations generally predicted stress states and yield function values very similar to those of the more complex three axle assembly. The three load configurations generally predicted the same trends and, in the majority of cases, also predicted critical yield functions at the same positions.
2. The differences noted in the yield function values predicted by the different load configurations were greatest in the case of the thick pavement. These differences also seemed to be greater at greater depths. However, the yield function values seem to become less critical as depth increases.
3. In the majority of cases, the two simplified load configurations predicted stress states that were more critical with respect to failure potential. An analysis of the stress states indicated that the three axle assembly predicted higher confinement and lower deviatoric stress components. This results in less critical yield function values being calculated. Thus, the two simplified load configurations generally seem to predict more conservative yield function values.

Based on these observations, it is concluded that, for the load and pavement configurations analyzed, a dual wheel load can be used to satisfactorily simulate the stress conditions under a multiple axle load assembly. This simplified approach is preferred since it will greatly simplify the modeling process and make the modeling of pavement response under superheavy loads easier to perform on a routine basis.

CHAPTER VII
A SUPERHEAVY LOAD ANALYSIS PROCEDURE

OUTLINE OF PROCEDURE

In this chapter, an analysis procedure is presented that will enable engineers to assess the structural adequacy of a pavement prior to a superheavy load being moved over the pavement. It is realized that, due to the relatively large numbers of superheavy load permit applications received by TxDOT every year, the analysis procedure should be as simple and easy to implement as possible. However, this requirement of simplicity stands in direct opposition to the relatively complex behavior of pavements. Therefore, any simplified procedure should of necessity be somewhat conservative in nature. Unfortunately, the adoption of very conservative material parameters can in some instances lead to inaccurate and unrealistic results.

In order to address both the requirements of simplicity and accuracy, a two-stage analysis procedure was developed. This procedure enables engineers to perform an initial analysis with the minimum information and at minimal expenditure of effort, time, and funds. In the first stage procedure, the structural adequacy of the superheavy load route is evaluated by means of charts. In the majority of cases, no testing is required at this stage, and layer properties such as thickness and stiffness are estimated from historical data and from information gained from previous investigations. However, the procedure is structured such that if FWD data and backcalculated moduli are available, it can also be used in the first stage analysis. The availability of FWD data dramatically improves the accuracy of this pavement analysis, and any analysis conducted without the benefit of FWD data is immediately more approximate and open to error.

Figure 7.1 illustrates the methodology adopted in the two-stage analysis procedure. Most of the material parameters assumed in the development of the charts which form the basis of the first stage analysis procedure represent a worst case scenario. Because of this conservative approach, the first stage analysis procedure should be considered a trigger analysis rather than a final analysis. This means the charts used in the first

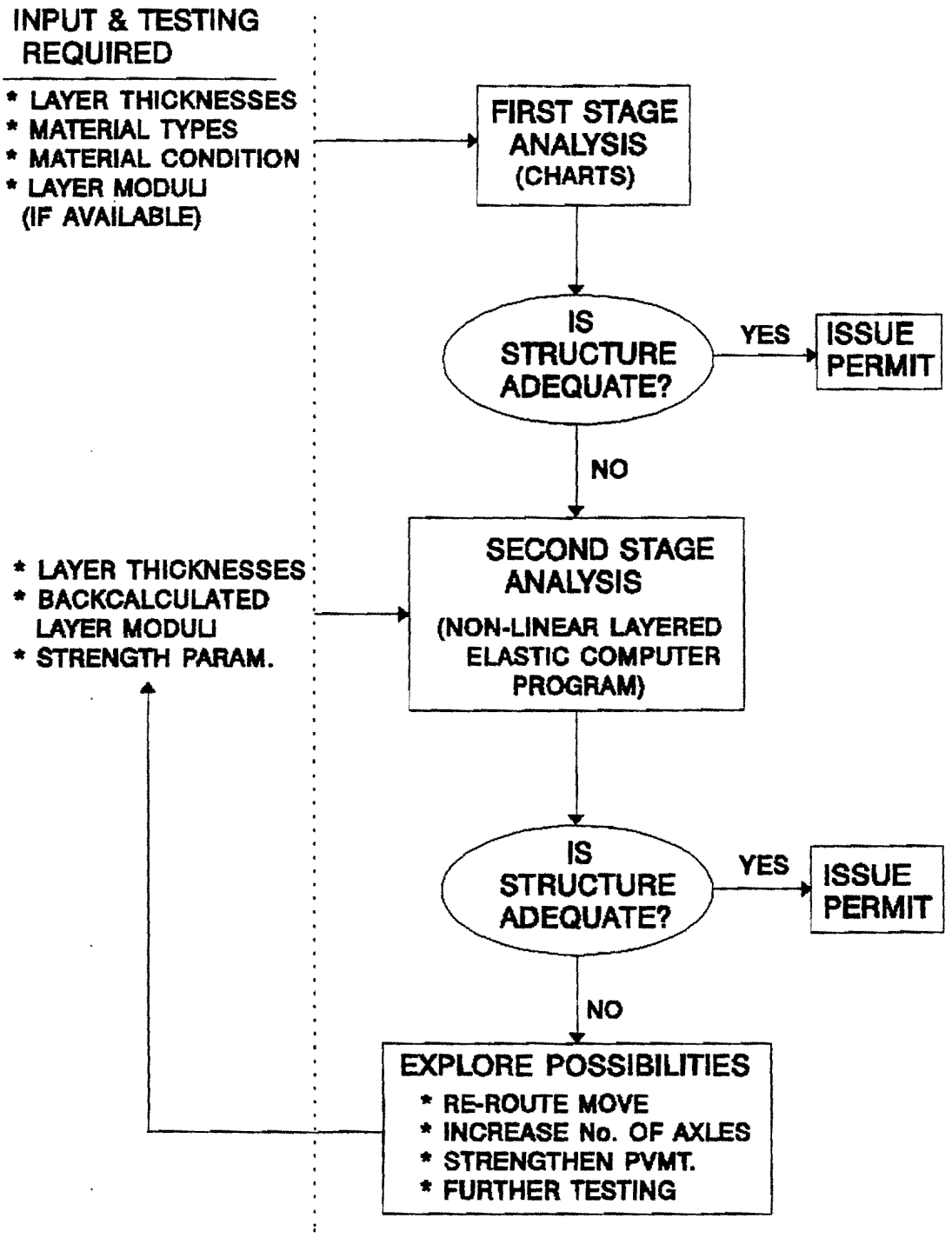

Figure 7.1. Schematic Representation of Superheavy Load Analysis Procedure.

stage analysis procedure are only used to indicate whether further analysis is needed. Should the first stage procedure indicate that the structure is adequate to accommodate the proposed load, then no further analysis is needed. However, should the charts indicate that the structure is inadequate to accommodate the load, then a more detailed investigation should be undertaken.

The second stage analysis requires that FWD data be available. Layer thicknesses can be obtained from historical data. However, cores and/or Ground Penetrating Radar (GPR) measurements are preferred since they provide a more accurate and current record of layer thicknesses. The results from these nondestructive tests are then used in the non-linear version of the BISAR (5) layered elastic program. By making use of an approximate procedure, this program enables the analyst to perform a nonlinear analysis through the use of backcalculated moduli and estimated layer thicknesses. The methodology followed in this program was described in Chapter V and is also outlined in a later section of this chapter. For the second stage procedure, material strength parameters (cohesion and angle of friction) can be obtained from laboratory tests or can be based on typical results from previous testing (49).

If the second stage analysis also indicates that a potential for failure exists, several options are available. The first, and possibly the easiest, is to re-route the load over a stronger pavement structure. Naturally, this requires that a second analysis be undertaken for the new route. If re-routing is not possible, then the possibility of increasing the vehicle's load spreading capabilities by increasing the number of axles should be investigated. Normally this can be achieved by the addition of another trailer unit. If neither of these options are possible, then a strengthening of the pavement through the use of laminated wood sheets or similar devices can be considered. Finally, a more detailed determination of the material strength parameters can be undertaken by sampling and conducting laboratory tests (49).

FIRST STAGE ANALYSIS PROCEDURE

General

The charts used in the first stage analysis procedure were developed through repetitive runs of the non-linear version of the BISAR layered elastic program described in Chapter V. The analysis and synthesis conducted in order to produce the charts were done with due consideration to the results of previous chapters. These considerations included the following:

1. A non-linear layered elastic program that utilizes a multiple-layered structure can closely approximate the results of a more complex finite element model. Any loss in accuracy that results from the use of the more approximate layered elastic theory is likely to result in more conservative estimations of load carrying capability (results from Chapter V).
2. A large majority of multiple wheel load configurations can be modeled with sufficient accuracy if only the two closest wheels are included in the analysis (results from Chapter VI).

For all the pavement structures used, the sublayered system shown in Figure 7.2 was used. Figure 7.2 shows that the asphalt surface was divided into two sublayers while the base and subgrade were divided into three and four sublayers, respectively. For all pavement structures, an equivalent depth to stiff layer of 2.9 m was used. While this depth was chosen to conform more or less with previously observed results, it is recognized that substantial variations in the depth to apparent stiff layer can occur in the field (58). However, as noted in a previous chapter, the depth to apparent stiff layer has a negligible influence in predicted stresses and strains (this is not the case with displacements) (57).

A dual wheel load with a spacing of 380 mm was used for all evaluations. Although this wheel spacing is slightly larger than that used on conventional trailers such as those shown in Figure 6.1, it is considered an acceptable compromise between the closer spacing used on conventional dual-wheel configurations and the larger spacing found on superheavy load trailers such as those shown in Figures 6.2 and 6.3. A tire pressure of 830 kPa was used in all cases. This tire pressure is considered to be representative of

those typically used in the field (57). For all pavements, stresses were evaluated at the bottom of the asphalt and base layers, and at the top of the subgrade. For each layer, evaluations were performed at the outside and inside edge of the wheel as well as at the load center and midway between the two loads.

For each sublayer, stress dependent moduli were evaluated at the mid-depth of the sublayer. All evaluations were performed along the centerline of one of the two loads. This choice of evaluation positions corresponds to the findings of previous researchers who have used layered elastic programs in a non-linear analysis (1,59).

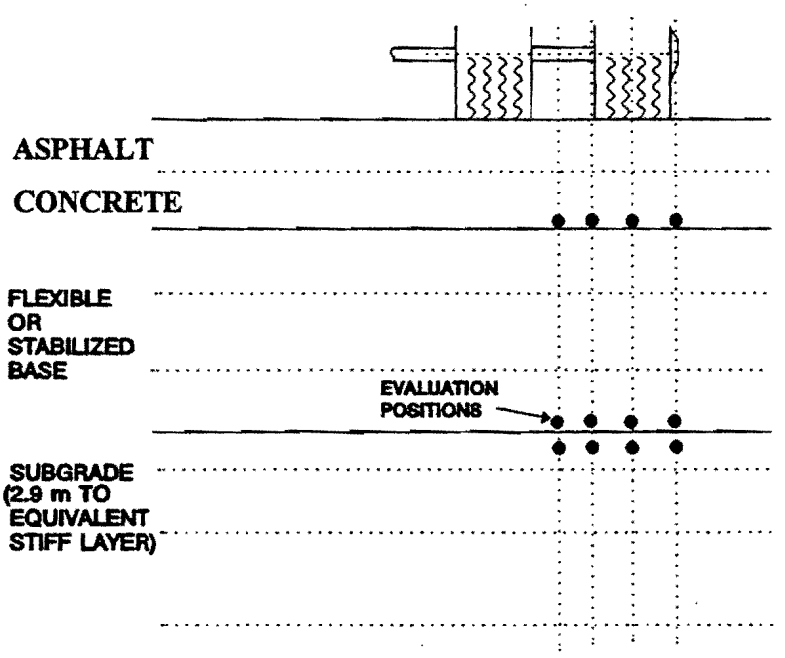

Figure 7.2. Typical Pavement Structure and Load Configuration Used to Develop First Stage Procedure Charts.

Layer Moduli and Strength Parameters Used

In order to accommodate as large a range of pavement situations as possible, different material types and combinations were assumed in developing the charts. However, no distinction was made between different types of materials. Instead, reference is made to the moduli and strength characteristics of each layer. The nomenclature used to distinguish between material types, therefore, consist of rather loose terms such as stiff, weak, or stabilized. Table 7.1 summarizes the material parameters used for each material type. A non-linear formulation was used to obtain the charts. Therefore, the moduli of each layer was not fixed but depended on the load magnitude and the position at which the stress-dependent moduli were evaluated within the layer. In Table 7.1, both the non-linearity constants (k_1 to k_3) and the resulting moduli for the load range are reported. A brief description of the assumptions made with regard to each material follows.

a) Asphalt Surface

As a worst case scenario, the asphalt surface was considered to be soft with low cohesion. As shown in Table 7.1, the asphalt stiffness varied from approximately 830 MPa to 2070 MPa, which is considered to be at the low end of the normal range of moduli for asphalt layers. Although the non-linearity constants for the asphalt were chosen to represent only a slightly non-linear material, the modulus varied significantly over the thickness of the layer due to the relatively large stress state variations.

The cohesion of asphalt material can vary significantly with differences in temperature (1,37). Figure 7.3 shows test results reported by Lytton et al. (37). Also shown in Figure 7.3 is a regression line and equation that was fitted to obtain a relationship between asphalt cohesion and temperature. Table 7.2 was obtained from a study by Perdomo and Button (24) and shows the expected temperature distribution in a 100 mm thick asphalt layer that is divided into 25 mm sublayers. Table 7.2 shows that the lower part of the asphalt, which is considered to be the critical part of the layer, can be expected to have a temperature of above 39°C only 7 percent of the time. Similar

Table 7.1. Material Parameters Used to Derive Charts.

Layer Description	Non-linear Material Constants			Resulting Range of Moduli (MPa)	Cohesion (kPa)	Angle of Friction
	k_1	k_2	k_3			
Asphalt Surface	10000 to 15000	0.1	0.0	790 to 2070	938.0	0.0°
Weak Base	1000	0.6	-0.3	62 to 235	49.0	50.0°
Stabilized Base	20000 to 25000	0.1	0.0	1500 to 3200	621.0	40°
Weak Subgrade	300	0.0	-0.3	48 to 62	41.0	30°
Stiff Subgrade	900	0.0	-0.3	90 to 138	103.0	30°

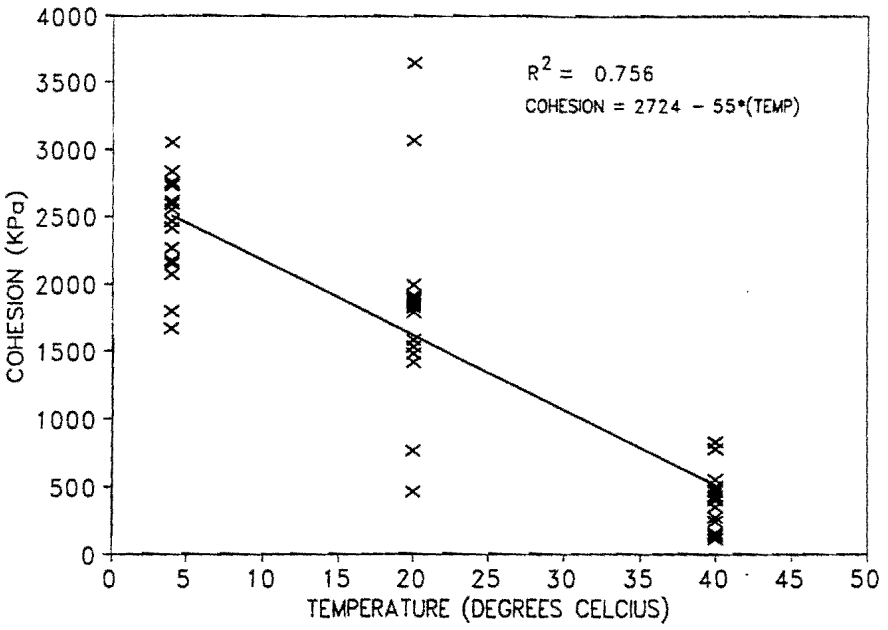

Figure 7.3. Asphalt Cohesion Related to Temperature (Based on Results Reported by Lytton et al. (37)).

Table 7.2. Temperature Distribution in a 100 mm Asphalt Overlay, Dallas Area (From (24)).

Temperature (°C)	Temperature of Sublayer (°C)				% Time
	1	2	3	4	
Less than 24	20	21	22	23	25.58
24 to 29	26	27	28	29	25.58
29 to 35	32	32	31	31	15.05
35 to 41	38	36	34	33	14.58
41 to 46	43	41	38	36	12.15
41 to 52	48	44	42	39	6.83

results indicate that for a 75 mm asphalt layer, the temperature in the lower 25 mm of the layer can be expected to be above 39°C for approximately 19 percent of the time.

Using the preceding information as a guideline, it was decided to use the cohesion estimated at 32°C. By using the relationship shown in Figure 7.3, a cohesion of 938 kPa was calculated and subsequently adopted for evaluation purposes. As explained in Chapter III, the lower part of the asphalt layer is almost always in a state of tension. This means that very little of the interparticle friction is mobilized. Therefore, a friction angle of 0.0° was adopted for the asphalt.

b) Weak Base

The condition described as "weak base" was chosen to represent an unstabilized granular base with a moisture content that is wetter than optimum. This base may consist of crushed limestone, iron ore gravel, shell, or Caliche. The non-linear material constants were chosen such that the modulus of this type of material ranged from 193 MPa for high stresses in the upper sublayer to 67 MPa in the lower sublayer where small tensile stresses may exist. Based on the relationship between Texas Triaxial Class and modulus value, the "weak base" is considered to represent a material with an approximate Texas Triaxial class number of 3.5 to 4.0 and a California Bearing Capacity Ratio (CBR) of between 60 and 15 (1,60).

The cohesion values used for the "weak base" were based on the results of Titus-Glover and Fernando (49). The cohesion value used of 49 kPa was the average cohesion measured for a range of base course materials that were compacted and tested at a moisture content above optimum. A friction angle of 50° was used for this material, which was consistent with results obtained from laboratory testing (49).

c) Stabilized Base

This material was considered to be a good quality material that had been stabilized with lime or cement. The stiffness and cohesion of stabilized materials can vary considerably, depending on the amount of stabilizer used, curing time, and material quality (61,62,63). A relatively low modulus that ranged between approximately 3200 and 1500

MPa was chosen to represent the stabilized base material. While significantly higher modulus values can be encountered in the field, the modulus values used to derive the charts are considered to represent a worst case scenario, such as where the stabilized material has already been broken down by traffic and environmental influences.

By making use of empirical relationships, both the cohesion and the modulus of stabilized material can be related to the Unconfined Compression Strength (UCS) of the material (61,63). Depending on the material type, TxDOT currently specifies a minimum UCS value between 5170 and 3450 kPa for materials stabilized with 3 to 9 percent cement (64). Figure 7.4 shows empirically derived relationships between UCS and cohesion for cement and lime stabilized material, based on the relationships reported by Little et al. (61,63). The cohesion value chosen for evaluation of stabilized materials corresponds

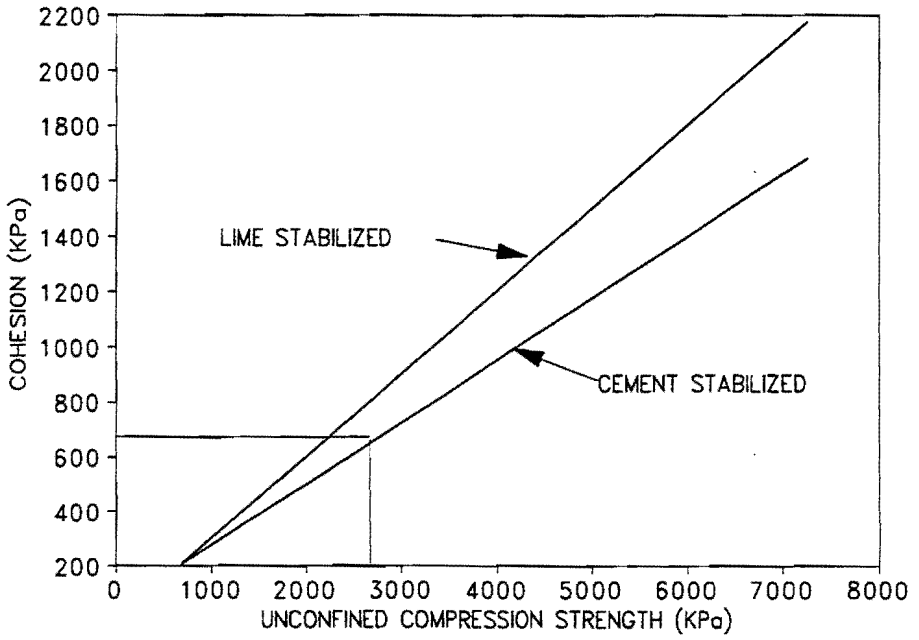

Figure 7.4. Empirical Relationship Between Stabilized Material Cohesion and Unconfined Compression Strength (61,63).

approximately to the minimum specified UCS value of 2760 kPa. While this value is lower than the minimum specified UCS strength, it is deemed to be representative of aged stabilized materials that have experienced some degradation through environmental and traffic effects.

d) Weak Subgrade

The weak subgrade was considered to be a soft, stress softening material that offered poor support to the overlying structure. The non-linear coefficients were chosen so that the modulus under typical stress conditions varied between 48 and 62 MPa. The weak subgrade condition can, therefore, be used to represent a wet clay, a poorly compacted sand, or any other material with high plasticity and relatively high moisture content. The cohesion value used in the evaluation of this material was also based on the results reported by Titus-Glover and Fernando (49) and is typical of clayey materials at a moisture condition wetter than optimum.

e) Stiff Subgrade

The stiff subgrade represents a material that is fairly stiff (modulus values varied between 90 and 138 MPa) and well compacted. The stiff subgrade condition can also represent a lightly stabilized poor quality material. The cohesion value used in the evaluation of this material corresponds to that of a dry clay (49).

Discussion of Results

The charts derived for the conditions noted in the preceding sections are shown in Figures 7.5 through 7.8. These charts can be used to determine the allowable wheel load for a given subgrade support (i.e., weak or stiff), base thickness, and asphalt thickness. Several trends of note were observed in the process of developing the charts. These will be briefly discussed in the following.

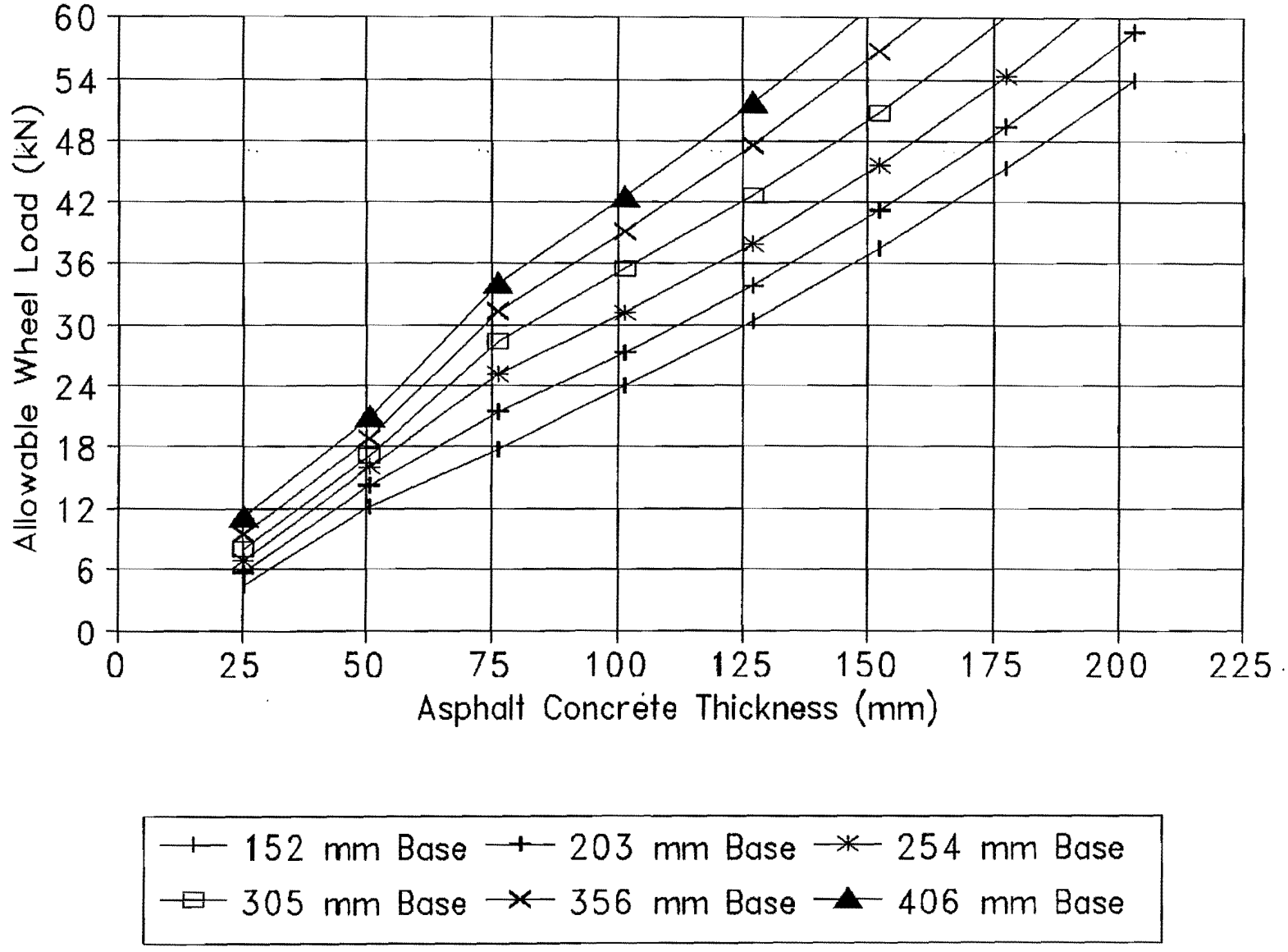

Figure 7.5. Allowable Wheel Load for Weak Subgrade, Weak Base Condition.

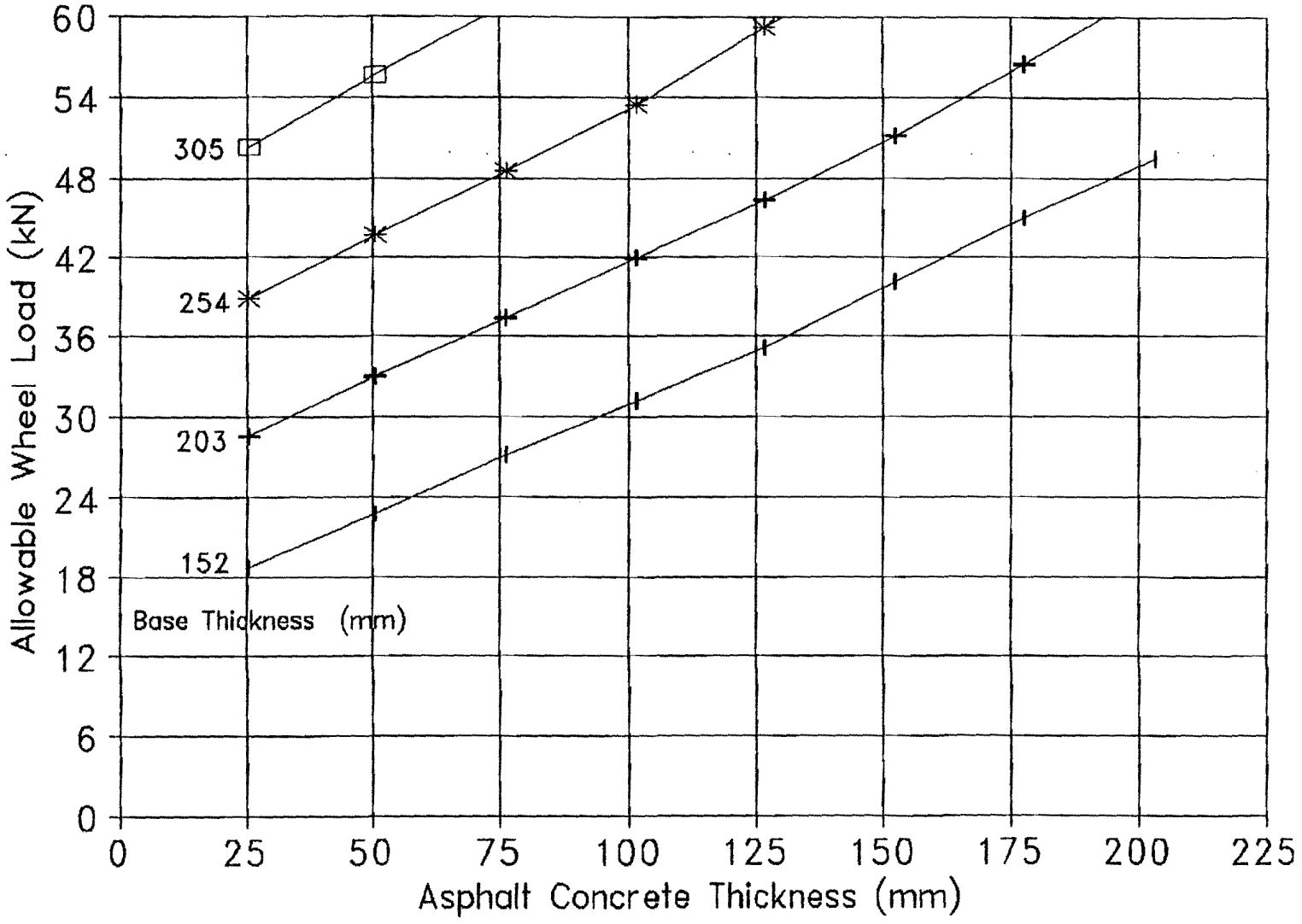

Figure 7.6. Allowable Wheel Load for Weak Subgrade, Stabilized Base Condition.

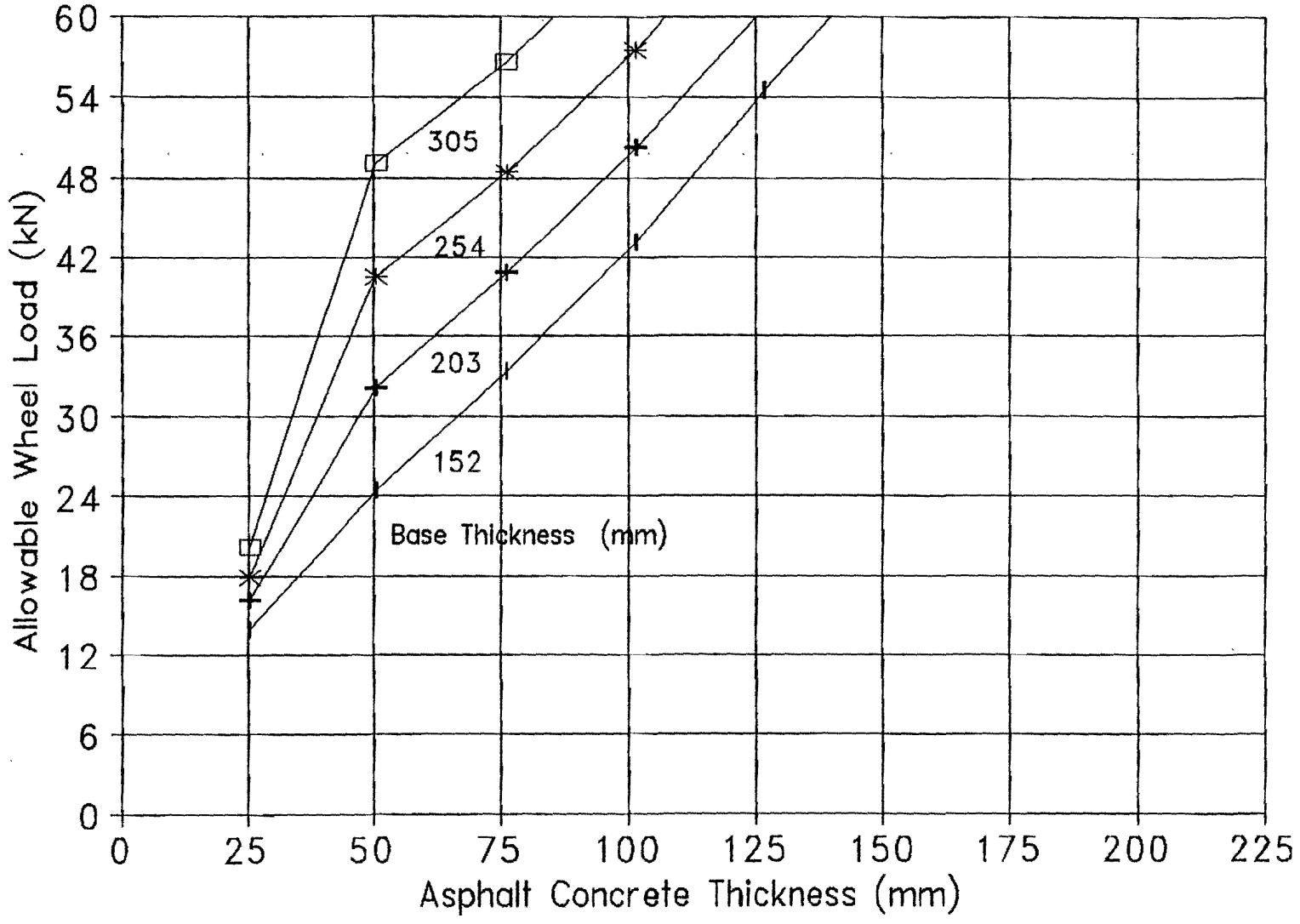

Figure 7.7. Allowable Wheel Load for Stiff Subgrade, Weak Base Condition.

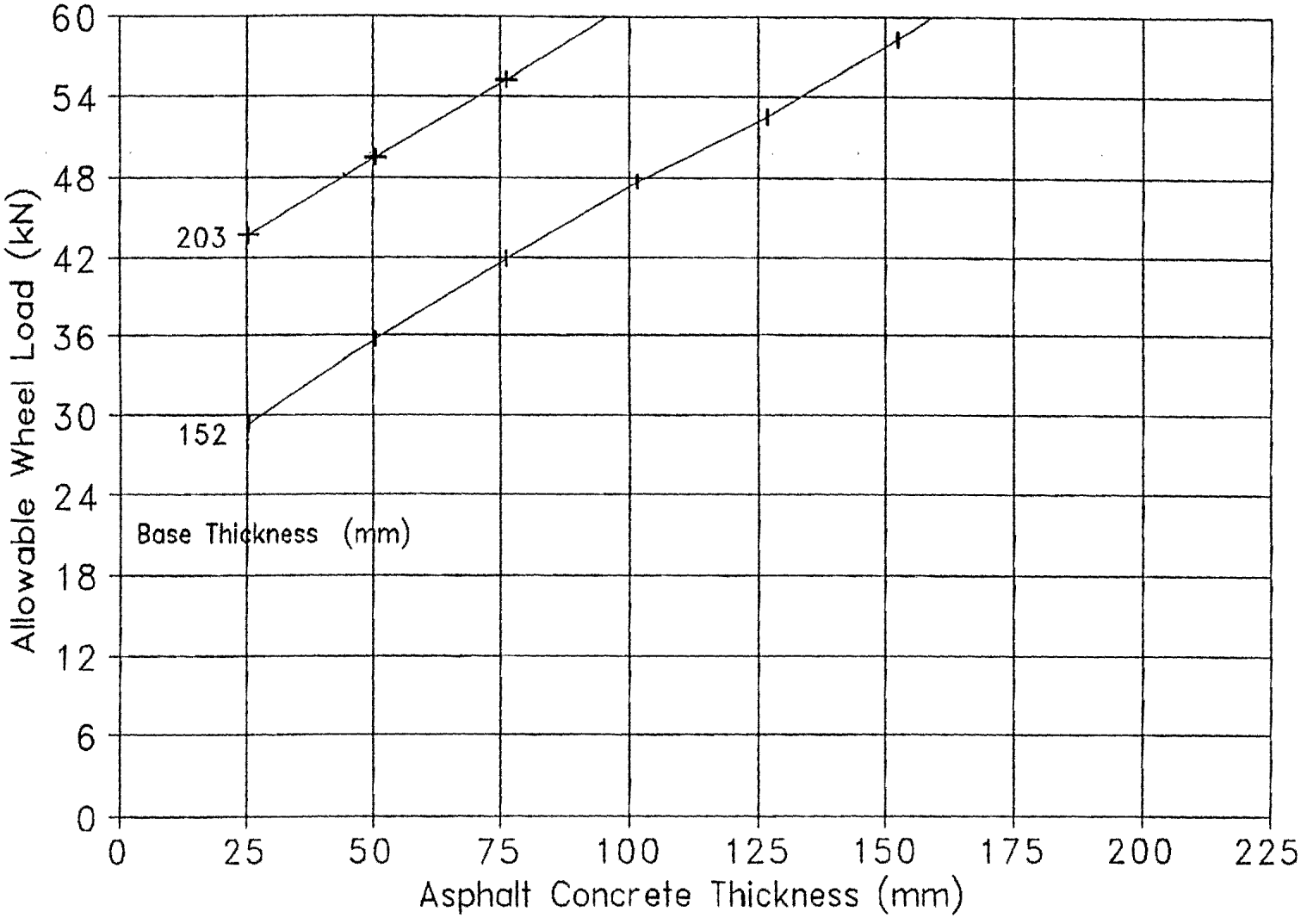

Figure 7.8. Allowable Wheel Load for Stiff Subgrade, Stabilized Base Condition.

In almost all instances, the critical evaluation position was situated in the base. For thin asphalt thicknesses, the outer load edge was the most critical position. However, the most critical position gradually shifted to the inner edge of the load, then to the center of the two loads as the thickness of the asphalt layer increased.

The stiffness of the subgrade had a significant effect on the predicted maximum allowable load. This may be somewhat encouraging, since the stiffness of the subgrade is one of the easier elements to determine in most backcalculation exercises. Thus, even if some uncertainty exists regarding the moduli values of the thinner overlying material, a significant benefit can be derived from FWD data if the subgrade modulus can be estimated. With this information, the analyst can immediately ascertain which charts to use. Based on the assumed moduli values shown in Table 7.1, any subgrade with an estimated modulus in excess of 75 MPa can be classified as a stiff subgrade material.

SECOND STAGE ANALYSIS PROCEDURE

As shown in Figure 7.1, if the charts used in the first stage analysis indicate a potential for failure exists, then a more detailed investigation is warranted. This investigation makes use of the same analysis tools used to derive the charts in the first stage procedure. However, the second stage procedure requires that more detailed information be available. This information can be obtained through FWD testing and backcalculation (14,15). If there is any uncertainty about layer thicknesses and moisture conditions within the pavement structure, then GPR measurements and/or cores may also be needed.

Once this information becomes available, the analyst can proceed to run the non-linear layered elastic program, PALS, that was specifically developed for superheavy load analysis. **PALS** is an acronym for **P**rogram to **A**nalyze **L**oads **S**uperheavy. Input to this program simply requires that the non-linear material constants, material strength parameters, and the maximum expected wheel load be entered into an ASCII input file. A menu-based user interface is incorporated with the program to facilitate data input.

Estimates of material parameters can be found in the study reported by Titus-Glover and Fernando (49) who performed a detailed study to determine typical non-linear and material strength parameters for pavement materials. This study developed relationships for estimating the resilient and strength parameters of base and subgrade materials from results of simple laboratory tests such as those used to determine gradation, Atterberg limits, moisture content, and soil suction. These relationships have been incorporated into the superheavy load analysis program as user options in the absence of test data from actual resilient modulus and triaxial tests.

The program runs on a microcomputer under DOS. Program output simply shows whether the pavement evaluated is adequate for the prescribed superheavy load based on the yield function value. If this value is less than zero, failure is not likely to occur. If the yield function value is larger than zero, a possibility for failure exists, and measures for strengthening the route, increasing the load spreading capabilities of the superheavy load vehicle, or re-routing the superheavy load move need to be considered. More detailed testing to determine the angle of friction and cohesion may also be considered. Such testing may show that the cohesion and angle of friction values previously used were too conservative, and a new analysis may show that failure is not likely to occur.

It should be noted that, as shown in Chapter IV, the material strength parameters play a vital role in determining the Mohr-Coulomb yield function value. Reference is made to the study by Titus-Glover and Fernando (49) in this regard. It should be noted that higher moduli values will lead to higher stresses, and yield will invariably be predicted if the cohesion value used in the analysis is that of a wet, soft material instead of an intact, stiff material. This tendency of the material to have an increased cohesion corresponding to increased moduli can be observed from Figures 7.9 and 7.10 which show cohesion values plotted with the k_1 parameter, which is directly related to the material stiffness. Although Figures 7.9 and 7.10 show a definite relationship between cohesion and resilient modulus, this relationship clearly differs for different materials. The authors recommend a more detailed study of the relationship between modulus and cohesion to provide a

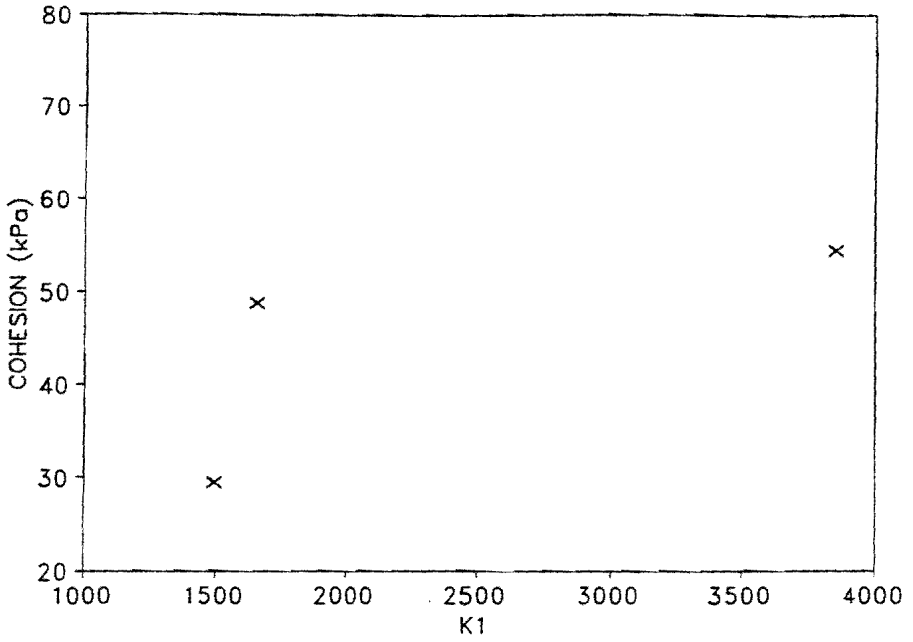

Figure 7.9. Cohesion vs. k_1 Parameter for Crushed Limestone (From (49)).

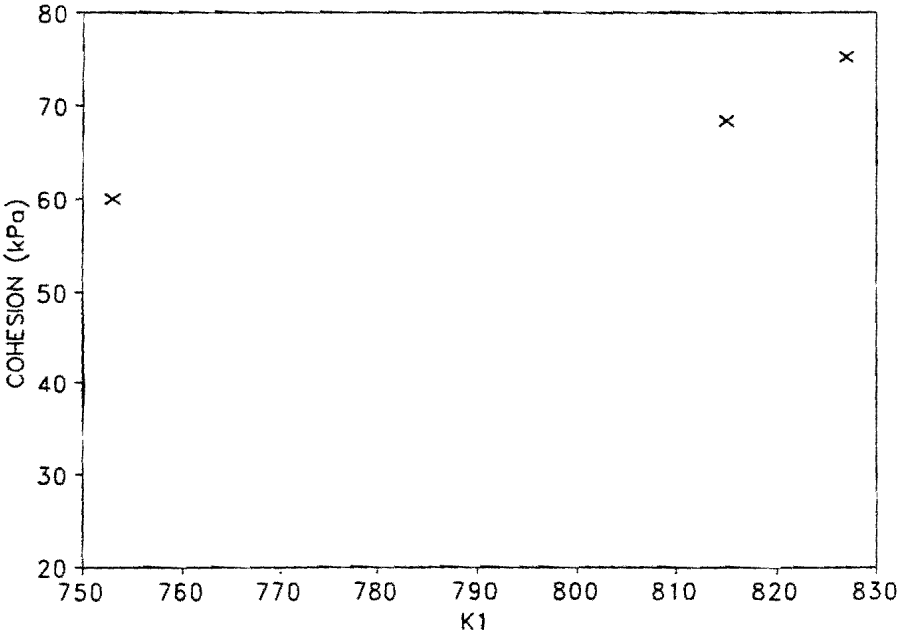

Figure 7.10. Cohesion vs. k_1 Parameter for Shell Base Material (From (49)).

more accurate basis of estimating cohesion changes with changes in layer moduli. Furthermore, research has shown that cohesion can be estimated if the soil suction and moisture content of the soil is known (49,65,66). The moisture content may be estimated non-destructively using GPR or measured from a simple laboratory test conducted on soil samples taken from the proposed superheavy load route. Soil suction, in turn, can be determined if the moisture content versus soil suction relationship for the given material is known. These relationships have been investigated by Titus-Glover and Fernando (49) for a number of base and subgrade materials found in Texas. The data obtained have been used to develop a prediction equation for cohesion that is a function of soil suction and other variables that are determined from simple laboratory tests. This prediction equation provides an alternative method of characterizing cohesion for the structural evaluation of superheavy load routes.

SUMMARY

In this chapter, an analysis procedure was presented for determining the likelihood of failure prior to a superheavy load being moved over a pavement structure. The procedure consists of two stages. In the first stage procedure, use is made of charts. Material parameters used in these charts are conservative and based on previous results from tests performed on pavement materials (37,49). If the charts indicate that the pavement structure can safely accommodate the superheavy load, then no further analysis is needed. However, if the charts indicate that a possibility for failure does exist, then a more detailed analysis is warranted. The second stage procedure uses the same analysis techniques as the first stage procedure. However, in the second stage procedure, use is made of more detailed and site specific information. It is noted that the resilient and strength parameters, in particular k_1, and the cohesion value have a significant influence on the Mohr-Coulomb yield function value. These parameters can vary considerably due to seasonal and moisture condition changes. Because of the variability in material conditions that may exist on a

given route, it becomes important to get accurate and site-specific estimates for these material parameters that are important determinants of the yield function value.

CHAPTER VIII
CONCLUSIONS AND RECOMMENDATIONS

CONCLUSIONS

This study addresses the modeling of flexible pavement response under superheavy load vehicles. In the analysis of superheavy load vehicles, the design parameter is a yield function value which is determined by the stress state and the strength parameters of the material in question. The analysis of pavement response under superheavy load vehicles differs from routine pavement design in that it is the load magnitude rather than the number of loads that are of importance. In this study, an attempt was made to address the major factors that pertain to the modeling of flexible pavement response under abnormally high wheel loads. Several modeling procedures were evaluated and compared. Of these procedures, the finite element model was considered to be the most accurate in its characterization of pavement behavior. A large part of the research effort was devoted to determining the effect of using simplified procedures to model pavement response and predict the likelihood of failure. The following conclusions can be drawn based on this study:

1. The finite element model, which uses stress dependent moduli and Poisson's ratios, provided results that compared well with results measured in the laboratory. Of the two responses monitored in the laboratory, the best comparison between measured and calculated results was obtained for axial strain. While the finite element model correctly predicted trends in radial strain (including dilation), there was a loss in accuracy in predicting absolute values.
2. In studying the sensitivity of the Mohr-Coulomb yield function value to changes in the non-linear constants k_1 to k_3, changes in k_1 were found to have the greatest effect on the yield function. Changes in non-linear material parameters had the greatest effect on the yield function calculated in the base. This was found to be the case

even when parameters of adjacent layers were varied. Yield function values calculated in the subgrade fluctuated very little with changes in the non-linear material parameters.

3. Cohesion was found to be a major determinant in estimating the point of yield for stress conditions that typically exist in pavement layers. The effects of changes in cohesion were found to be most pronounced in the case of the subgrade and the asphalt. The influence of cohesion on the yield function value calculated in the base is still high. However, in this layer, material strength is also highly influenced by the angle of friction.
4. In the majority of cases, the most critical yield function value was calculated in the base. However, because of the yield function's sensitivity to changes in cohesion, situations may exist where the asphalt surface or the subgrade may become the most critical layer. The yield function should, therefore, be calculated in all layers and evaluated by making use of site-specific cohesion values.
5. A comparison of results obtained by a finite element model, a conventional layered elastic model, and a version of the layered elastic model that was adopted to accommodate non-linear material behavior showed that all three models predicted the same trends in stresses and yield function values. Differences in magnitudes of predicted stresses are due to the failure of the simpler models to fully take account of material non-linearity. The version of the layered elastic model that was modified to account for material non-linearity was found to provide a good compromise between traditional layered elastic theory and the more accurate finite element model. This was especially found to be true in the case of thicker pavements. Differences between yield function values predicted by the three response models were greater in the case of thinner pavements.
6. The comparison of response models showed that non-linear material behavior plays an important role in predicting pavement response under heavy loads. Even in cases where displacements can be predicted with reasonable accuracy, failure to take account of material non-linearity and the effects of changing modulus within

pavement layers can lead to significant errors in predicting stresses and yield function values.

7. A comparison of stress states and yield function values calculated under different load configurations showed that a simplified load assembly can predict pavement response with reasonable accuracy. A complex load assembly, where more loads are included, leads to increased vertical stress. However, the larger number of loads also leads to increased confinement, thereby reducing the effect of the larger vertical stress. As a result, the simplified load configurations predicted stress states that were more critical with respect to failure potential. The differences in yield function values predicted under the different load configurations were greatest in the case of thicker pavements. A similar effect can be expected in the case of more rigid pavements. However, in such cases, the yield function values calculated at greater depths, or under more rigid pavements tend to be less critical, and therefore, the differences between yield function values are generally not significant.

RECOMMENDATIONS

This study has developed a methodology for evaluating the structural adequacy of routes for permitting superheavy load moves. Researchers recommend that TxDOT implement the procedure developed for structural evaluation of superheavy load routes. TTI researchers can assist in this implementation effort, particularly in training TxDOT engineers in the use of the procedure developed. The study also has shown the need for additional research in the following areas to facilitate the evaluation of failure potential under superheavy loads:

1. The accuracy of the estimation of the failure potential in pavements under high wheel loads depends on the estimate of the cohesion of the pavement materials at the time the load is moved. Methods do exist whereby the cohesion of pavement materials can be estimated through non-destructive testing techniques such as ground penetrating radar, coupled with information on the moisture-suction curve of the

material in question. Indeed, research efforts made in this TxDOT project have led to the development of an alternative method of estimating cohesion in the absence of triaxial test data (49). It is recommended that additional research be conducted to test and calibrate the method developed in this companion study using a more extensive and up-to-date data base of material strength parameters. This research should also investigate relationships between cohesion and material stiffness.

2. The present research has shown that of the three non-linear material parameters (k_1 to k_3), the yield function value is most significantly affected by k_1. Laboratory tests on various pavement materials have shown that this is also the factor that is the most susceptible to changes in moisture. The k_1 factor seems to be site-specific and varies not only depending on the material type, but also on the prevailing environmental conditions. It is recommended that further research be conducted to investigate the possibility of determining k_1 through routine nondestructive testing such as FWD testing.

REFERENCES

1. Huang, Y.H. *Pavement Analysis and Design*. Prentice Hall, Englewood Cliffs, N.J., 1993.
2. Yoder, E.J. and M.W. Witczak. *Principles of Pavement Design*. 2nd ed., John Wiley and Sons, Inc., N.Y., 1975.
3. *AASHTO Guide for Design of Pavement Structures*. American Association for State Highway and Transportation Officials, Washington, D.C., 1986.
4. Ameri-Gaznon, N. and D.N. Little. *Avoiding Early Failure of Intersection Pavements*. Research Report 1172-1F, Texas Transportation Institute, College Station, Tex., 1989.
5. De Jong, D.L., M.G.F. Peutz, and A.R. Korswagen. *Computer Program Bisar*. Koninklijke/Shell Laboratorium, Rotterdam, Netherlands, 1973.
6. Van Cauwelaert, F.J., D.R. Alexander, T.D. White, and W.R. Barker. Multilayer Elastic Program for Backcalculating Layer Moduli in Pavement Evaluation. In *Nondestructive Testing of Pavements and Backcalculating Moduli*, STP 1026, ASTM, Philadelphia, Pa., 1989.
7. Duncan, J.M., C.L. Monismith, and E.L. Wilson. Finite Element Analysis of Pavements. In *Highway Research Record 228*, HRB, National Research Council, Washington D.C., 1968, pp 18-33.
8. Raad L. and J.L. Figueroa. Load Response of Transportation Support Systems. *Transportation Engineering Journal*, ASCE, Vol. 106, No. TE1, 1980, pp 111-128.
9. Bishop, A.W. Shear Strength Parameters for Undisturbed and Remolded Soil Specimens, Stress-Strain Behavior of Soils, *Proceedings of the Roscoe Memorial Symposium*, Cambridge University, United Kingdom, March, 1971, pp 3 - 58.
10. Harkness, R.M. The Implications of "Mohr-Coulomb" as Failure Criterion, Stress-Strain Behavior of Soils, *Proceedings of the Roscoe Memorial Symposium*, Cambridge University, United Kingdom, March, 1971, pp 212 - 219.

11. Hicks, R.G. and F.N. Finn. Analysis of Results from the Dynamic Measurements Program on the San Diego Test Road. *Proceedings of the Association of Asphalt Paving Technology*, 1970.

12. Thrower, E.N., N.W. Lister and J.F. Potter. Experimental and Theoretical Studies of Pavement Behavior Under Vehicular Loading in Relation to Elastic Theory. *Proceedings, Third International Conference on the Structural Design of Asphalt Pavements*, Ann Arbor, Mich., 1972.

13. Klomp, A.J.G. and T.W. Niesman. Observed and Calculated Strains at Various Depths in Asphalt Pavements. *Proceedings, Second International Conference on the Structural Design of Asphalt Pavements*, Ann Arbor, Mich., 1967.

14. Lytton, R.L. Backcalculation of Pavement Layer Properties. In *Nondestructive Testing of Pavements and Backcalculation of Moduli*, STP 1026, ASTM, Philadelphia, Pa., 1989, pp 7-38.

15. Uzan, J., R.L. Lytton, and F.P. Germann. General Procedure for Backcalculating Layer Moduli. In *Nondestructive Testing of Pavements and Backcalculation of Moduli*, STP 1026, ASTM, Philadelphia, Pa., 1989, pp 217-228.

16. Chen, W.F. and G.Y. Baladi. *Soil Plasticity, Theory and Implementation.* Developments in Geotechnical Engineering Vol. 38, Elsevier, New York, N.Y., 1985.

17. Desai, C.S. and H.J. Siriwardane. *Constitutive Laws for Engineering Materials, With Emphasis on Geologic Materials*. Prentice Hall, Inc., Englewood Cliffs, N.J., 1984.

18. Ullidtz, P. *Pavement Analysis*. Elsevier, New York, N.Y., 1987.

19. Owen, D.R.J. and E. Hinton. *Finite Elements in Plasticity*. Theory and Practice, Pineridge Press, Swansea, United Kingdom, 1980.

20. Roscoe, K.H. and H.B. Pooroshasb. A Theoretical and Experimental Study of Stress-Strain in Triaxial Compression Tests on Normally Consolidated Clays. *Geotechnique*, Vol. 13, 1963, pp 12-28.

21. Schofield, A.N. and C.P Wroth. *Critical State Soil Mechanics*. McGraw Hill, New York, N.Y., 1968.

22. Freeman, T.J. and S.H. Carpenter. Characterizing Permanent Deformation in Asphalt Concrete Placed over Portland Cement Concrete Pavements. In *Transportation Research Record 1070*, TRB, National Research Council, Washington, D.C., 1986, pp 342-387.

23. Ameri-Gaznon, N. and D.N. Little. *Permanent Deformation Potential in Asphalt Concrete Overlay over Portland Cement Concrete Pavements*. FHWA Report No FHWA/TX-88/452-3F, Austin, Tex., 1988.

24. Perdomo, D. and J.W. Button. *Identifying and Correcting Rut-Susceptible Asphalt Mixtures*. Research Report 1121-2F, Texas Transportation Institute, College Station, Tex., 1991.

25. Harichandran, R.S., G.Y. Baladi, and M. Yeh. *Development of a Computer Program for Design of Pavement Systems Consisting of Bound and Unbound Materials*. Department of Civil and Environmental Engineering, Michigan State University, Lansing, Mich., 1989.

26. Zienkiewicz, O.C. *The Finite Element Method*. 3rd ed., McGraw Hill, New York, N.Y., 1977.

27. Desai, C.S. *Elementary Finite Element Method*. Prentice Hall, Inc., Englewood Cliffs, N.J., 1979.

28. Uzan, J. and T. Scullion. Verification of Backcalculation Procedures. *Proceedings, 3rd International Conference on Bearing Capacity of Roads and Airfields*, Trondheim, Norway, July 1990, pp 447-458.

29. Hicks, R.G. *Factors Influencing the Resilient Properties of Granular Materials*, Ph.D. Dissertation. University of California, Berkeley, Calif., 1970.

30. Barksdale, R.D., and R.G. Hicks. *Material Characterization and Layered Theory for Use in Fatigue Analysis*. Special Report 140, Highway Research Board, Washington, D.C., 1973.

31. Thompson, M.R., and Q.L. Robnett. Resilient Properties of Subgrade Soils, *Transportation Engineering Journal*, ASCE, Vol. 105, January 1979, pp 731-739.

32. Witczak, M.W. and J. Uzan. *The Universal Pavement Airport Design System Report I of IV: Granular Material Characterization*, University of Maryland, College Park, Md., September 1988.

33. Hicks, R.G. and C.L Monismith. Factors Influencing the Resilient Response of Granular Materials. *Highway Research Record 345*, HRB, National Research Council, Washington, D.C., 1971, pp 123-131.

34. Allen, J.J. *The Effects of Non-Constant Lateral Pressures on the Resilient Response of Granular Materials*. Ph.D. Dissertation. University of Illinois at Urbana-Champaign, Ill., 1973.

35. Kalcheff, I.V. and R.G. Hicks. A Test Program for Determining the Resilient Properties of Granular Materials. *Journal of Testing and Evaluation*, ASTM, Vol. 1, No. 6, 1976, pp 472-479.

36. Uzan, J. Granular Material Characterization, In *Transportation Research Record* 1022, TRB, National Research Council, Washington, D.C., 1985, pp 52-59.

37. Lytton, R.L., J. Uzan, E.G. Fernando, R. Roque, D. Hiltunten, and S.M. Stoffels. *Development and Validation of Performance Prediction Models and Specifications for Asphalt Binders and Paving Mixes*. Report SHRP-A-357. Strategic Highway Research Program. National Research Council, Washington, D.C., 1993.

38. Crockford, W.W., L.J. Bendaña, W.S. Yang, S.K. Rhee, and S.P. Senadheera, *Modeling Stress and Strain States in Pavement Structures Incorporating Thick Granular Layers*, ESL-TR-89-63, U.S. Air Force, Tyndall Air Force Base, Fla., 1990.

39. Uzan, J. Resilient Characterization of Pavement Materials. *International Journal for Numerical and Analytical Methods in Geomechanics*, Vol. 16, 1992, pp 435-459.

40. Frydman, S. *The Effect of Stress History on the Stress Deformation Behavior of Sand*. M.Sc. Thesis. Technion, Israel, Institute of Technology, 1968.

41. Chen, W.F. and A.F. Saleeb. *Constitutive Equations for Engineering Materials*. Vol 1 - Elasticity and Modeling. Wiley Interscience, Inc., New York, N.Y., 1982.

42. Lade, P.V. and R.D. Nelson. Modeling the Elastic Behavior of Granular Materials. *International Journal for Numerical and Analytical Methods in Geomechanics*, Vol. 13, 1987, pp 521-542.

43. Liu, M. *Numerical Prediction of Pavement Distress with Geotechnical Constitutive Laws*. Ph.D. Dissertation. Texas A&M University, College Station, Tex., 1993.

44. Zagmanoglou, E.C. and D.W. Thoe. *Introduction to Partial Differential Equations with Applications*, Dover, Inc., New York, N.Y., 1976.

45. Botha, J.F. and G.F. Pinder. *Fundamental Concepts in the Numerical Solution of Differential Equations,* Wiley-Interscience Publications, Wiley, New York, N.Y., 1983.

46. Ames, W.F. *Numerical Methods for Partial Differential Equations*, Academic Press, Third Edition, Boston, Mass., 1992.

47. Heulekom, W. and A.J.G. Klomp. Dynamic Testing as a Means of Controlling Pavements During and After Construction. *Proceedings, First International Conference on Structural Design of Asphalt Pavements*, University of Michigan, Ann Arbor, Mich., August 1962, pp 667-679.

48. Billam, J. Aspects of the Behavior of Granular Materials at High Pressures. Stress-Strain Behavior of Soils. *Proceedings of the Roscoe Memorial Symposium*, Cambridge University, United Kingdom, March 1971, pp 69-80.

49. Titus-Glover, L. and E. G. Fernando. *Evaluation of Pavement Base and Subgrade Material Properties and Test Procedures*. Research Report 1335-2, Texas Transportation Institute, Texas A&M University, College Station, Tex., 1995.

50. Jooste, F.J. and E.G. Fernando. Modeling of Pavement Response Under Superheavy Loads. In *Transportation Research Record 1448*, TRB, National Research Council, Washington D.C., 1994, pp 69-74.

51. Yong, R.N. and B.P. Warkentin. *Soil Properties and Behavior*. Developments in Geotechnical Engineering, Vol. 5, Elsevier, New York, N.Y., 1975.

52. Test Method TEX-117-E. *Triaxial Compression Test for Disturbed Soils and Base Material*. Manual of Testing Procedures. Texas Department of Transportation, Austin, Tex., 1993.

53. Basson, J.E.B., O.J. Wijnberger, and J. Skultety. *The Multi-Depth Deflectometer: A Multistage Sensor for the Measurement of Resilient Deflections and Permanent Deformations at Various Depths in Road Pavements*. NITTR Technical Report RP/3/81, Council for Scientific and Industrial Research, Pretoria, South Africa, 1981.

54. Scullion, T., J. Uzan, I. Yazdani, and P. Chan. *Field Evaluation of the Multi-Depth Deflectometer*. Research Report 1123-2. Texas Transportation Institute, College Station, Tex., 1988.

55. Uzan, J., T. Scullion, C.H. Michalek, M. Paredes, and R.L. Lytton. *A Microcomputer-Based Procedure to Backcalculate Layer Moduli from FWD Data*. Research Report 2-18-87-1123-1, Texas Transportation Institute, College Station, Tex., 1988.

56. De Beer, M., E. Horak, and A.T. Visser. *The Multidepth Deflectometer (MDD) System for Determining the Effective Elastic Moduli of Pavement Layers*. Nondestructive Testing of Pavements and Backcalculation of Moduli, STP 1026, ASTM, Philadelphia, Pa., 1989, pp 70-89.

57. Jooste, F.J. and E.G. Fernando. *Victoria Superheavy Load Move: Report on Route Assessment and Pavement Modeling*. Research Report 1335-1, Texas Transportation Institute, College Station, Tex., 1994.

58. Rohde, G.T. and R.E. Smith. *Determining Depth to Apparent Stiff Layer from FWD Data*. Research Report 1159-1, Texas Transportation Institute, College Station, Tex., 1991.

59. Luhr, D.R. and B.F. McCullough. Structural Analysis of AASHO Road Test Flexible Pavements for Performance Evaluation. In *Transportation Research Record 888*, TRB, National Research Council, Washington D.C., 1982, pp 63-69.

60. Van Til, C.J., B.F. McCullough, B.A. Vallerga, and R.G. Hicks. *Evaluation of AASHTO Interim Guides for Design of Pavement Structures*, NCHRP 128, Highway Research Board, 1972.

61. Little, D.N. *Fundamentals of the Stabilization of Soil with Lime*. National Lime Association, Arlington, Va., 1987.

62. Little, D.N. *Handbook for Stabilization of Pavement Subgrades and Base Courses with Lime (Final Draft)*. National Lime Association, Arlington Va., 1994.

63. Van Blerk, P.G.L. and T. Scullion. *Erodability of Cement Stabilized Pavement Materials*. Research Report 2919-1, Texas Transportation Institute, College Station, Tex., 1995.

64. Texas Department of Transportation. *Standard Specifications for Construction and Maintenance of Highways, Streets, and Bridges*. Adopted by the Texas Department of Transportation, Austin, Tex., March 1995.

65. Lamborn, M.J. *A Micromechanical Approach to Modeling Partly Saturated Soils*. M.Sc. Thesis, Texas A&M University, College Station, Tex., 1986.

66. Petersen, R.W. *The Influence of Soil Suction on the Shear Strength of Unsaturated Soil*, Ph.D. Dissertation, Texas A&M University, College Station, Tex., 1990.

67. Chen, W.F. and E. Mizuno. *Nonlinear Analysis in Soil Mechanics*. Developments in Geotechnical Engineering Vol. 53, Elsevier, New York, N.Y., 1985.

68. Hooke, R. *Lectures De Potentia Restitutiva*, The Cutlerian Lectures, No. 6, Printed for John Martyn, London, United Kingdom, 1678.

69. Wolfskill, L.A. *Elastic and Inelastic Strain Relationships of Granular Soils Subjected to Repeated Stressings*. Ph.D. Dissertation. Texas A&M University, College Station, Tex., 1963.

70. Popov, E.P. *Engineering Mechanics of Solids*. Prentice Hall, Englewood Cliffs, N.J., 1990.

71. Mroz, Z. On the Description of Anisotropic Work Hardening. *Journal for Mechanical and Physical Solids*, Vol. 15, 1967, pp 163-175.

72. Iwan, W.D. On a Class of Models for the Yielding Behavior of Continuous and Composite Systems. *Journal for Applied Mechanics*, Trans. ASME, Vol. 34, No. E3, September 1967, pp 195-216.

73. Nadai, A. *Theory of Flow and Fracture in Solids*, McGraw-Hill, New York, N.Y., 1950.

74. Griffith, A.A. The Phenomena of Rupture and Flow of Solids. *Philosophical Transactions of the Royal Society of London*, Series A, Vol. 221, 1920, pp 163-198.

75. Irwin, G.R. Fracture Mechanics. *Proceedings, First Symposium in Naval Structural Mechanics*, Pergamon, New York, N.Y., 1958.

76. Kupfer, H. and K. Gerstle. Behavior of Concrete under Biaxial Stresses. *Journal of the Engineering Mechanics Division*, ASCE, Vol. 99, No. EM4, 1973, pp 863.

77. Bedard, C. and M.D. Kotsovos. Application of NLFEA to Concrete Structures. *Journal of the Structural Division*, ASCE, Vol. 111, No. ST12, 1985, pp 124-154.

78. Bridgeman, P.W. *Studies in Large Plastic Flow and Fracture with Special Emphasis on the Effects of Hydrostatic Pressure*. McGraw-Hill Book Company, New York, N.Y., 1952.

79. Hill, R. *The Mathematical Theory of Plasticity*. Oxford University Press, London, 1950.

80. Roscoe, K.H., A. Schofield and C.P. Wroth. On the Yielding of Soils. *Geotechnique*, Vol. 8, 1958, pp 22-53.

81. DiMaggio, F.L. and I.S. Sandler. Material Modelling for Granular Soils. *Journal of Engineering Mechanics Division*, ASCE, Vol. 97, No. EM3, 1971, pp 935-950.

82. Lade, P.V. and J.M. Duncan. Cubical Triaxial Tests on Cohesionless Soils. *Journal of Soil Mechanics Division*, ASCE, Vol. 99, No. SM10, 1973, pp 793-812.

83. Lade, P.V. and J.M. Duncan. Elastoplastic Stress-Strain Theory for Cohesionless Soil. *Journal of Geotechnical Engineering Division*, ASCE, Vol. 104, No. GT10, 1975, pp 1037-1053.

84. Lade, P.V. Elasto-Plastic Stress-Strain Theory for Cohesionless Soil with Curved Yield Surfaces. *International Journal of Solids and Structures*, Vol. 13, 1977, pp 1014-1035.

85. Lade, P.V. and H.M. Musante. Three-dimensional Behavior of Remolded Clay. *Journal of Geotechnical Engineering Division*, ASCE, Vol. 104, No. GT2, 1978, pp 193-209.

86. Desai, C.S. A General Basis for Yield, Failure and Potential Functions in Plasticity. *International Journal of Numerical Analysis Methods*, Vol. 4, 1980, pp 361-375.

87. Desai, C.S. and H.J. Siriwardane. A Concept of Correction Functions to Account for Non-Associative Characteristics of Geologic Media. *International Journal of Numerical Analysis Methods in Geomechanics*, Vol. 4, 1980, pp 377-387.

88. Baker, R. and C.S. Desai. Induced Anisotropy During Plastic Straining. *International Journal of Numerical Analysis Methods in Geomechanics*, Vol. 10, 1984, pp 1239-1245.

89. Nakai, T. and H. Matsuoka. Deformation of Soil in Three Dimensional Stress. *IUTAM Conference on Deformation and Failure of Granular Materials*, Delft, Netherlands, 1982, pp 275-285.

90. Matsuoka, N. and T. Nakai. Stress-Deformation and Strength Characteristics of Soil Under Three Different Principal Stresses. *Proceedings, Japan Society of Civil Engineers*, No. 232, 1974, pp 59-70.

91. Vermeer, P.A. A Five Constant Model Unifying Well Established Concepts. *International Workshop on Constitutive Relations for Soils*, Grenoble, France, September 1982, pp 175-197.

92. Blazynski, T. Z. *Applied Elasto-Plasticity of Solids*. MacMillan Press, London, 1983.

93. Timoshenko, S. P., and J. N. Goodier. *Theory of Elasticity*. McGraw-Hill Book Company, New York, 1970.

94. Mendelson, A. *Plasticity: Theory and Application*. The MacMillan Company, New York, 1968.

95. Boas, M. L. *Mathematical Methods in the Physical Sciences*. John Wiley, New York, 1983.

96. Chen, W. F. *Plasticity in Reinforced Concrete*. McGraw-Hill Book Company, New York, 1982.

APPENDIX A

LITERATURE SURVEY OF CONSTITUTIVE MODELS AND YIELD CRITERIA

MODELS BASED ON ELASTICITY

LINEAR ELASTICITY AND THE CAUCHY ELASTIC MODEL

Linear elasticity is the oldest and most often used way of modeling material behavior. It assumes that the state of stress at every point of the response is uniquely related to the state of strain (67). Linear elasticity is embodied in Hooke's law, which was based on Hooke's experiments with elastic bodies. In his 1678 paper "*Lectures De Potentia Restitutiva*" (68), Hooke published the results of his experiments with elastic bodies. Wolfskill (69) quoted Hooke's observations as follows:

> "...It is very evident that the Rule or Law of Nature in every springing body is, that the force or power thereof to restore itself to its natural position is always proportionate to the distance or space it is removed therefrom..."
> "... Nor is it observable in these bodies only, but in all other springy bodies whatsoever, whether metal, wood, stones, baked earth, hair, horns, silk, bones, sinews, glass and the like..."

Thus linear elasticity assumes a direct relationship between stress and strain. It also assumes that the material returns to its initial state upon removal of the load (17). For three dimensional bodies, the generalized Hooke's law can be expressed as (17):

$$\sigma_{ij} = C_{ijkl}\epsilon_{kl} \tag{A.1}$$

Where σ_{ij} = the stress tensor,

ϵ_{kl} = the strain tensor,

C_{ijkl} = a fourth order tensor which provides the connecting relationship between stress and strain, and

i,j,k,l = indices ranging from 1 to 3.

The tensor C_{ijkl} in equation (A.1) consists of 36 components. However, if the material is considered as isotropic, then the relationship between stress and strain can be described completely by means of two constants, namely Young's Modulus (E), and Poisson's Ratio (μ) (16) as follows:

$$\sigma_{ij} = \frac{E}{1 + \mu} \epsilon_{ij} + \frac{\mu E}{(1 + \mu)(1 - 2\mu)} \epsilon_{kk} \delta_{ij} \qquad (A.2)$$

Where i,j, and k ranges from 1 to 3, and

δ_{ij} = the Kronecker Delta.

Because of the assumption of complete recovery, linear elasticity has a limited range of application for granular materials (67). However, Chen and Baladi (16) note that soil behavior in the linear elastic range is well understood, and that predictions of acceptable accuracy can be found in many applications. One of the greatest disadvantages of the linear elastic approach is that it assumes a linear relationship between stress and strain. Many granular materials exhibit nonlinear behavior within the elastic range, as illustrated in Figure A.1. One of the ways in which nonlinearity can be accounted for is by replacing the constants C_{ijkl} in equation A.1 by functions of the stress or strain. Materials characterized in this manner are referred to as Cauchy elastic materials. In the Cauchy elastic model, stress is assumed to be a function of strain only.
Thus:

$$\sigma_{ij} = F_{ij}(\epsilon_{kl}) \qquad (A.3)$$

Where F_{ij} is the elastic response function of the material (16). It should be noted that in its lowest form, the Cauchy elastic law is the same as the generalized Hooke's law (17). However, in order to account for the nonlinear relationship between stress and strain, some modifications have been made to the Cauchy function. The simplest of these modifications is to replace the constants F_{ij} with functions of the stress or strain invariants. These

functions are often termed secant moduli. Approaches that use secant moduli together with the Cauchy formulation have been applied with some success to the modeling of soil behavior and have the advantage of being simple to model. However, they have the limitations of path independence and reversibility, which assume that stresses are uniquely determined by the current state of strain (or vice versa), which is an idealization of actual soil behavior. Furthermore, the Cauchy elastic models may generate energy on certain loading-unloading cycles, which is a violation of the laws of thermodynamics (16).

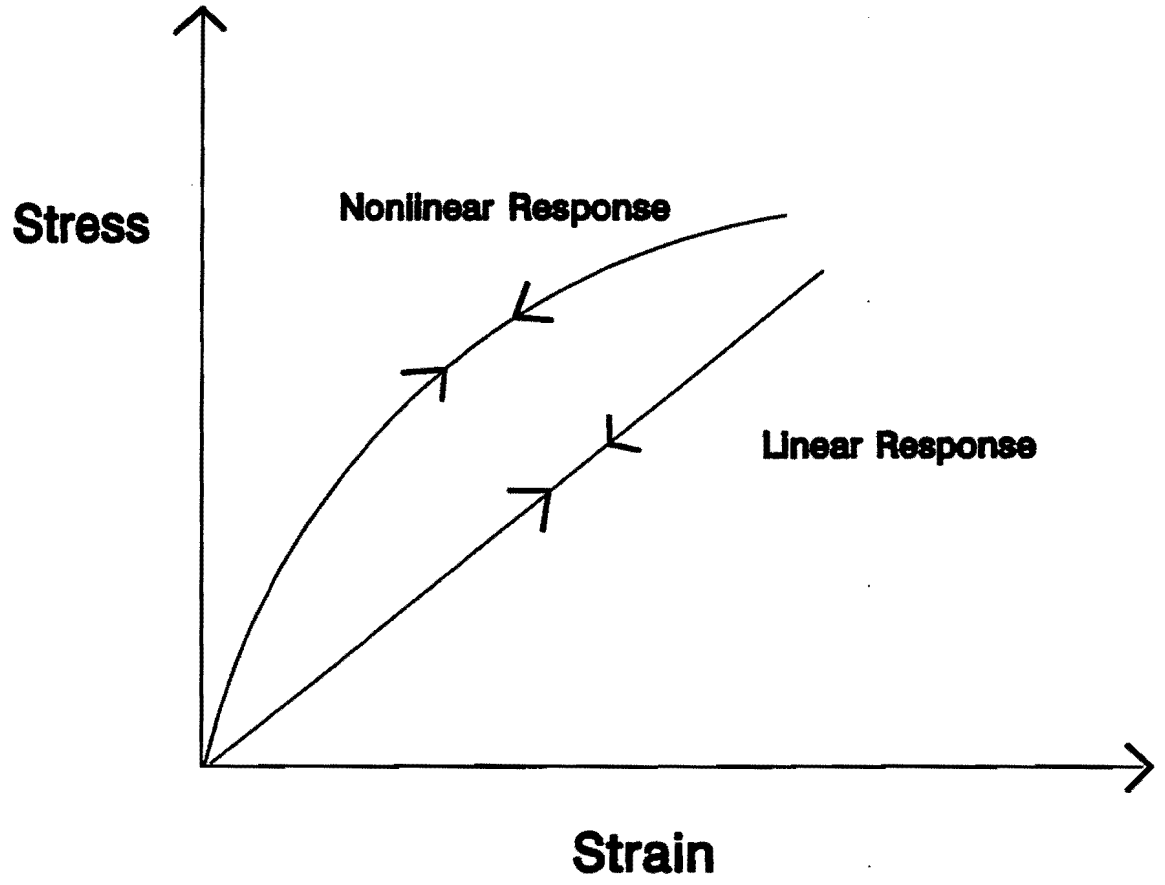

Figure A.1. Linear and Non-Linear Material Behavior.

HYPERELASTIC MODEL

In order to overcome the disadvantages associated with the Cauchy formulation, an alternative method for modeling nonlinear soil behavior, called hyperelastic modeling, was adopted. This model is also known as the Green formulation (67). As in the modifications of the Cauchy formulation, hyperelastic formulations make use of secant moduli. However, the hyperelastic formulation satisfies the first law of thermodynamics and the law of kinetic energy, in that it assumes the existence of a Strain Energy Function, $W(\epsilon_{ij})$, such that (67):

$$\sigma_{ij} = \frac{\partial W}{\partial \epsilon_{ij}} \tag{A.4}$$

The strain energy function, W, is a function of any three independent invariants of the strain tensor. If we choose the invariants:

$$I_1' = \epsilon_{ii} \tag{A.5a}$$

$$I_2' = (1/2)\epsilon_{ij}\epsilon_{ji} \tag{A.5b}$$

$$I_3' = (1/3)\epsilon_{ij}\epsilon_{jk}\epsilon_{ki} \tag{A.5c}$$

Then equation (A.4) can be rewritten as:

$$\sigma_{ij} = \frac{\partial W}{\partial I_1'}\frac{\partial I_1'}{\partial \epsilon_{ij}} + \frac{\partial W}{\partial I_2'}\frac{\partial I_2'}{\partial \epsilon_{ij}} + \frac{\partial W}{\partial I_3'}\frac{\partial I_3'}{\partial \epsilon_{ij}} \tag{A.6a}$$

With

$$\frac{\partial I_1'}{\partial \epsilon_{ij}} = \delta_{ij} \tag{A.6b}$$

$$\frac{\partial I_2'}{\partial \epsilon_{ij}} = \epsilon_{ij} \tag{A.6c}$$

$$\frac{\partial I_3'}{\partial \epsilon_{ij}} = \epsilon_{ik}\,\epsilon_{kj} \tag{A.6d}$$

Equation (A.6a) becomes:

$$\sigma_{ij} = \frac{\partial W}{\partial I_1'} \delta_{ij} + \frac{\partial W}{\partial I_2'} \epsilon_{ij} + \frac{\partial W}{\partial I_3'} \epsilon_{ik} \epsilon_{kj} \qquad (A.7)$$

Equation A.7 has the same form as the Cauchy formulation except the response coefficients in the Cauchy formulation are independent, while those of equation A.7 are dependent on each other under a certain set of integrability conditions, which are given completely in reference 67. Thus, the Green formulation can be seen as a special case of the Cauchy formulation. An example of a third-order hyperelastic formulation is given in reference 43, together with comparisons between model predictions and measured results. An expression similar to equation A.7 can be derived to express strains in terms of stresses by making use of the Energy Density function $\Omega(\sigma_{ij})$.

The hyperelastic model can be accurate for soils under proportional loading (67). It also satisfies the theoretical requirements for stability, uniqueness, continuity, and energy considerations that are required by continuum mechanics. A significant advantage afforded by the hyperelastic model is that it can account for soil behavior that is generally difficult to model, such as dilation, stress induced anisotropy, and strain softening (67).

A disadvantage associated with the hyperelastic model is that it is still a path independent formulation. Furthermore, even when initial isotropy is assumed, the hyperelastic model can contain a large number of response parameters. This requires that a large number of laboratory tests be performed before a particular soil can be modeled with accuracy. The model is also confined to small areas of application (67).

HYPOELASTIC MODEL

All of the models discussed previously can be described as total stress or strain formulations. An improvement on these was obtained through the hypoelastic model, which is an incremental formulation. This model has the advantage that it can model soil behavior that is path-dependent (67). This means that, for the hypoelastic formulation, a different stress or strain will be obtained for different stress paths, whereas for the

previous formulations, the stress path followed would have no influence on the state of stress at any particular point along the load cycle.

In the hypoelastic formulation, the stress is represented by a material response that is a function of the current state of stress, as well as the current rate of strain. Thus, the general form of the hypoelastic formulation is (67):

$$\dot{\sigma}_{ij} = F_{ij} (\sigma_{mn} , \dot{\epsilon}_{kl}) \tag{A.8}$$

Where the dot indicates a rate of stress or strain. For isotropic, time-independent materials, it can be shown (67) that:

$$d\sigma_{ij} = C_{ijkl}(\sigma_{mn})\, d\epsilon_{kl} \tag{A.9}$$

Where C_{ijkl} is called the tangential stiffness tensor. In its most general form, the tangential stiffness tensor contains 12 material coefficients that all depend only on the invariants of the stress tensor.

From equation A.9 we can see that the stress-strain relationship for a single increment is reversible. The term *hypo*elastic (meaning "lower", or "minimum" elastic) arises because the reversibility requirement applies only in the incremental sense. An integration of equation A.9 yields:

$$\sigma_{ij} = \int C_{ijkl}(\sigma_{mn})\, d\epsilon_{kl} + \sigma^{0}_{ij} \tag{A.10}$$

Where σ_{ij}^{0} is the initial stress state. Equation A.10 shows that the hypoelastic model assures a path-dependent process. It should be noted that, for the linear case in which C_{ijkl} is constant, the hypoelastic model reduces to the Cauchy model. For the hypoelastic model, failure of the material occurs when:

$$\det\left|C_{ijkl}(\sigma_{mn})\right| = 0 \tag{A.11}$$

Equation A.11 leads to an eigenvalue problem for which the eigenvectors span a failure surface in stress space (17,67).

The two main problems associated with the hypoelastic formulation are that, for multiaxial stress conditions, it is not always clear whether the material is being loaded or unloaded. Thus, it is conceivable that the shear stress may increase while the normal stress may decrease. Additional assumptions are, therefore, needed in order to define loading and unloading (16,67). Secondly, in the non-linear range, the hypoelastic model exhibits stress-induced anisotropy. Thus, the principal stress and principal strain axes do not coincide. This introduces a coupling effect between normal and shear strains which results in having to define 21 different material constants at every point of the loading path. Thus, the hypoelastic model can be difficult to implement in practice (67).

One of the simplest applications of the hypoelastic formulation uses the incremental stress-strain equations as a simple extension of the isotropic linear elastic model, where the constants of elasticity are replaced by tangential moduli that are functions of the stress or strain invariants. This type of model has been applied to finite element programs that have yielded successful results (67). As with the hyperelastic formulation, the hypoelastic model is often limited by the relatively large amount of tests required to determine the response parameters.

ELASTO-PLASTIC MODELS

All the models discussed thus far have presupposed that the material will return to its initial state upon load removal. However, if a material is loaded beyond a certain level of stress, irrecoverable deformation will take place in many materials. Thus, beyond this point of loading, not all strains will be elastic. A material in such a state is said to behave elasto-plastically. In the elasto-plastic formulation, the total strain increment that develops during a load increment is assumed to be the sum of the elastic and plastic strain increments (67):

$$d\epsilon_{ij} = d\epsilon_{ij}^{e} + d\epsilon_{ij}^{p} \tag{A.12}$$

Where $d\epsilon_{ij}^{e}$ is the elastic portion of the strain increment, and $d\epsilon_{ij}^{p}$ is the plastic part of the total strain increment.

The elastic strain increment is assumed to be described totally by Hooke's law (67). In this elastic formulation, the constants can be either constant (leading to a linear-elasto-plastic formulation), or they can be functions of the stress or strain invariants (leading to a nonlinear-elasto-plastic formulation). Plasticity models are generally more complex than elasticity models, but they have been shown to accurately model complex soil behavior such as dilatancy, dependence of strength on stress or strain history, and nonlinear hysteretic behavior (67).

There are two basic approaches that can be used to model the plastic part of the total strain increment. The first is known as the Incremental Theory of Plasticity. The second is known as the Flow Theory of Plasticity. The incremental theory of plasticity, although easier to model, does not satisfy rigorous theoretical requirements such as continuity (67). The flow theory is regarded as being more theoretically sound and is commonly used in finite element applications (67).

The flow theory of plasticity is based on two fundamental assumptions (67):

1) there exists a yield surface that delineates the onset of plastic behavior; and

2) the stress-strain relationship in the plastic domain is described by a flow rule.

These two assumptions will briefly be discussed in the following.

THE YIELD SURFACE

In order to separate the zone where purely elastic behavior takes place from the zone where elasto-plastic behavior takes place, yield criteria are needed. Furthermore, in the elasto-plastic range, yield criteria can be used to define the stress conditions under which plastic deformation will take place (67). The point at which the material starts to yield can easily be visualized for a uniaxial loading condition, where the yield point can be determined by means of methods such as the tangent, or off-set method (67,70). However, for more general three dimensional tests, the yield "point" needs to be described by a surface in three dimensional stress space. The general form of the yield criterion is (67):

$$f(\sigma_{ij}) = f_c = 0 \tag{A.13a}$$

For any state of stress, σ_{ij}, the value of the yield function can be calculated as (67):

$$f = f(\sigma_{ij}) \tag{A.13b}$$

When f equals zero, we also have $f = f_c$, and the material will be in a state of yield. For all values of σ_{ij} such that $f < 0$, the material will behave elastically. The yield function can also be used to define loading or unloading. For example, if $df > 0$, the material is normally said to be loading, and vice versa. The yield function is a mathematical relationship which describes a surface in stress space. A distinction needs to be made between the yield function and the yield criteria. A yield criterion is a condition, which is or is not satisfied by the yield function. Most yield criteria and yield functions are set up as described above, that is, the criterion for yield is satisfied when $f = 0$.

Different yield functions are used for different materials. Well known yield functions are those proposed by Tresca, Von Mises, and (for soil and rocks), Mohr-Coulomb (16,17,67). Some of these functions form the main subject of this study and will be discussed in detail in a later section.

THE FLOW RULE

For a material at a state of stress such that yielding has occurred (i.e., $f_c = 0$), the flow rule provides a mathematical relationship between the present state of stress and the next increment of plastic strain, ϵ_{ij}^p. The flow rule has the following form (67):

$$d\epsilon_{ij}^p = d\lambda \frac{\partial g}{\partial \sigma_{ij}} \tag{A.14}$$

Where g is a function known as the plastic potential, or plastic potential function, and $d\lambda$ is a positive scalar of proportionality. Equation A.14 indicates that the plastic strain is normal to the plastic potential surface, as shown in Figure A.2 (67).

Some flow rules assume that the plastic potential, g, and the yield function, f, coincide. Such a flow rule is known as an associative flow rule. Flow rules for which f and g do not coincide are called non-associative flow rules. It has been found that non-associative flow rules are more suited to modeling the behavior of geological materials such as soil, rock, and concrete (17,67).

An important aspect of plasticity theory is the assumptions made regarding the post-yield behavior of the material. Post yield behavior is generally assumed to be either elastic-perfectly plastic or elastic-work hardening (16,67). The difference between these types of plasticity is illustrated schematically in Figures A.3a and A.3b.

In the case of an elastic-perfectly plastic material, the initial yield criterion, f_c, is assumed to remain fixed and unchanged for all stress increments, $d\sigma_{ij}$, beyond the point of yield. Figure A.4 shows this situation. For a state of stress such that $f(\sigma_{ij}) = f_c$, plastic deformation will occur for any increment of stress, $d\sigma_{ij}$, unless $f(\sigma_{ij}) < f_c$. As long as $f(\sigma_{ij})$is not less than f_c, any stress point, σ_{ij}, will move along the boundary of the yield surface for any increment of stress, thereby causing further plastic deformation to take

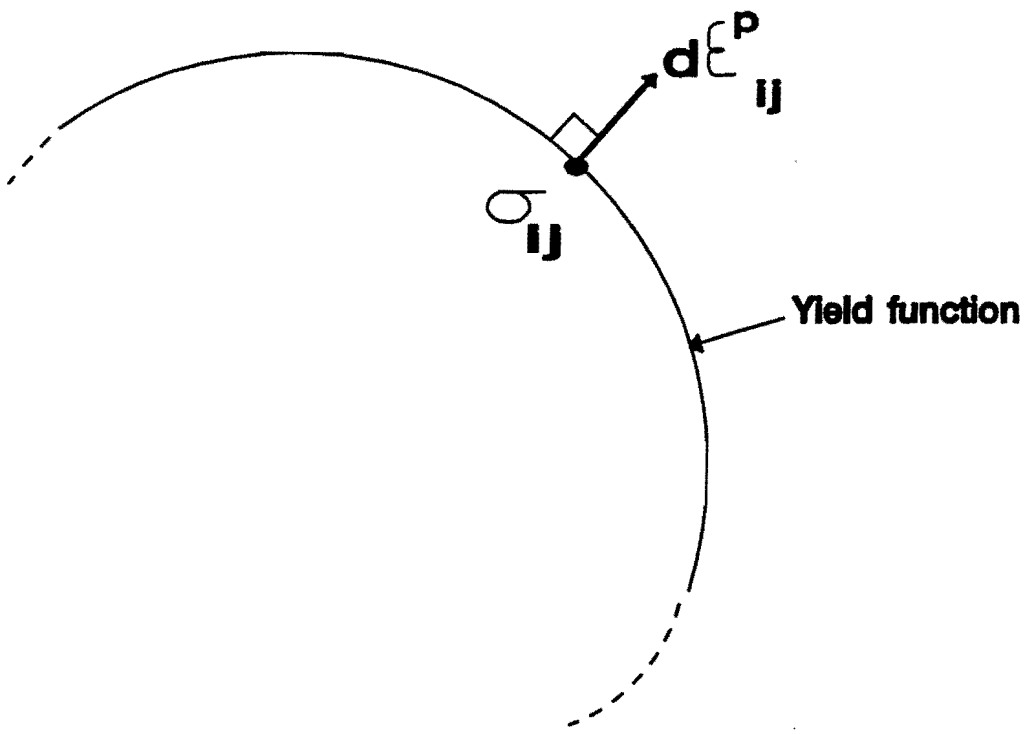

Figure A.2. Schematic Representation of the Flow Rule (From (67)).

place. Perfect plasticity, however, assumes that the stress state cannot move outside of the yield surface, thus the condition $f(\sigma_{ij}) > f_c$ is not possible, so that (67):

$$\frac{df}{d\sigma_{ij}} = \frac{\partial f}{\partial \sigma_{ij}} = 0 \qquad \text{(A.15)}$$

If, however, any stress increment leads to a new state of stress such that $f(\sigma_{ij}) < f_c$, the material will behave elastically, and no further plastic deformation will take place.

Although the perfectly plastic model has been used successfully in predicting the collapse or limit state of geological materials (67), it fails to take into account the possible increase in the strength of soils with increasing effective normal stress. In order to model the post yield behavior of most soil types, a work hardening theory of plasticity is needed. This modification to the plasticity model allows the material to harden or soften after

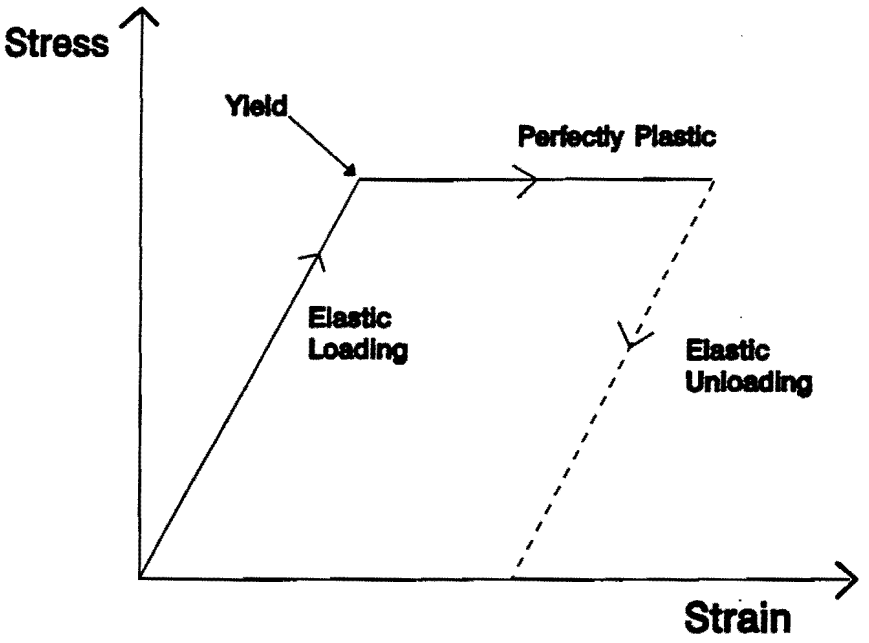

Figure A.3a. Perfectly Plastic Response.

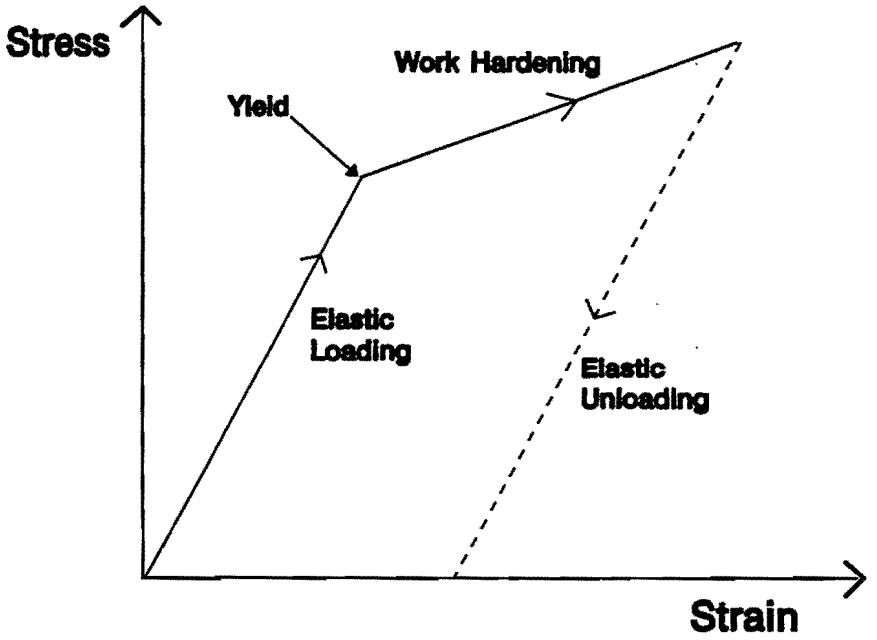

Figure A.3b. Work Hardening Plasticity.

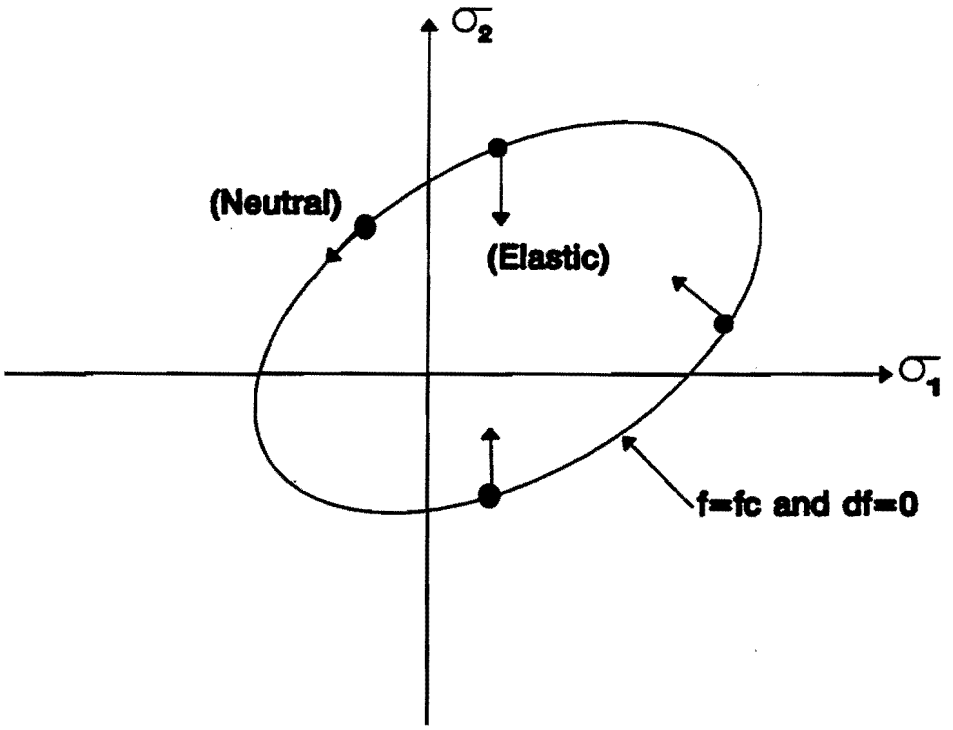

Figure A.4. Elastic-Perfectly Plastic Material Response (From (67)).

initial yielding (67). Figure A.5 shows the work hardening behavior in a schematic form. For work hardening behavior, a subsequent yield surface (also called a loading surface) is assumed to exist beyond the initial yield surface described by f_c. Physically, this means the material can offer resistance beyond the point of initial yield, that is more or less than the resistance offered at yield. Thus, the loading function is not fixed after yielding. The loading function is generally expressed in terms of (67):

1. the state of stress;
2. the plastic strain developed; and
3. a hardening parameter, k.

Thus, the loading function has the form (67):

$$f_{loading} = f(\sigma_{ij}, \epsilon_{ij}^{p}, k)$$

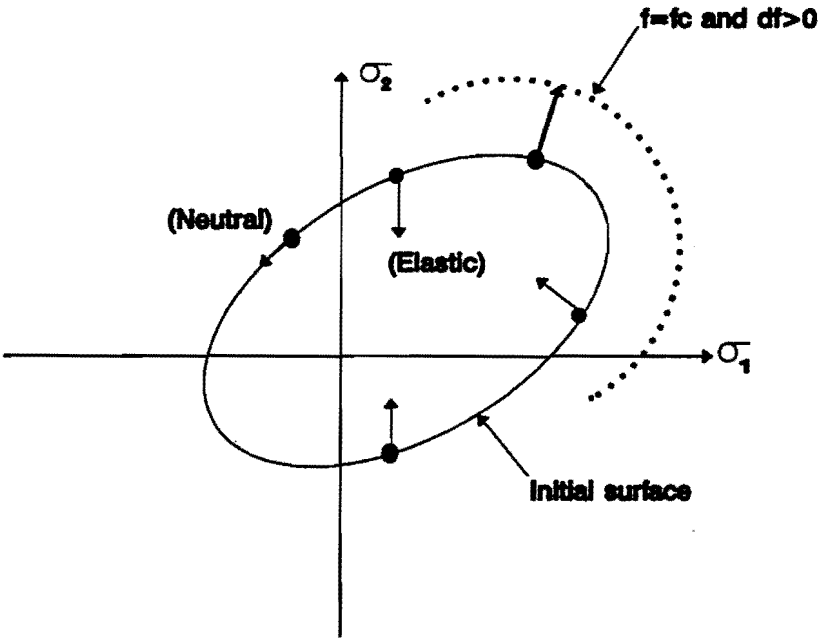

Figure A.5. Work Hardening Material Behavior (From (67)).

Figure A.5 shows that for any stress increment, σ_{ij}, the yield surface (now called the loading function) will move beyond its present boundary, so that (67):

$$\frac{df}{d\sigma_{ij}} = \frac{\partial f}{\partial \sigma_{ij}} > 0 \qquad \text{(A.16)}$$

In order to describe the shape of the subsequent yield surfaces, a hardening rule needs to be defined. At the point of initial yielding, the loading surface and the yield surface coincides. Upon further loading, the yield function will change value and/or form. The hardening rule describes the way this function changes. The three types of hardening rules identified by Chen and Mizuno (67), are:

1. Isotropic hardening, which assumes the subsequent yield function expands or contracts uniformly from its initial position without any distortion;
2. Kinematic hardening, which assumes that the loading surface translates in stress space without any rotation or change in size; and
3. Mixed hardening, which is a combination of the isotropic and kinematic hardening rules.

Chen and Mizuno (67) stated that the mixed hardening rule is specifically well suited to modeling the behavior of soils under cyclic and reversed types of loading. An example of this type of hardening can be found in the nested surface models of Mroz (71) and Iwan (72).

YIELD CRITERIA

BACKGROUND AND INTRODUCTION

In the previous section, it was noted that the onset of plastic deformations can be predicted by evaluating a yield function, or yield criterion, which depends on the state of stress and certain material parameters. Different yield criteria have been developed to predict the onset of plastic deformations in different types of materials. Some of the earliest yield criteria were used to predict failure in metals. Most of these criteria date back to the previous century. One of the first criterion was proposed by Tresca in 1868 (70). This theory is widely known as the maximum shear stress theory and may have been formulated by Coulomb as early as 1773 (70). The Tresca criterion has been applied with success to ductile material such as metals. The Tresca criterion can also be used to construct a surface in three dimensional stress space. A schematic representation of the Tresca criterion is shown in two and three dimensions in Figures A.6a and A.6b. Figure A.6a shows that the Tresca criterion compares the maximum shear stress developed during loading to a predetermined and constant value, which is known as the yield strength.

A second yield theory that has often been applied to metals is the maximum distortion energy theory, also known as the Von Mises criterion (16). This criterion is often used in plasticity applications due to its smooth and continuous shape, which reduces computational difficulties. The Von Mises criterion was originally proposed by M.T. Huber in 1904 and subsequently developed by R. Von Mises and H. Hencky (70). Figure A.7 is a schematical representation of the Von Mises yield surface in three-dimensional stress space. Figures A.6a, A.6b, and A.7 show that both the Tresca and Von Mises criteria represent a hexagonal or cylindrical shape of uniform diameter in stress space.

Both the Tresca and Von Mises criteria assume the material has the same strength in tension and compression. This is clearly not the case with many materials, and in 1885 Dugeut attempted to adapt the maximum stress theory of Tresca to improve the correlation

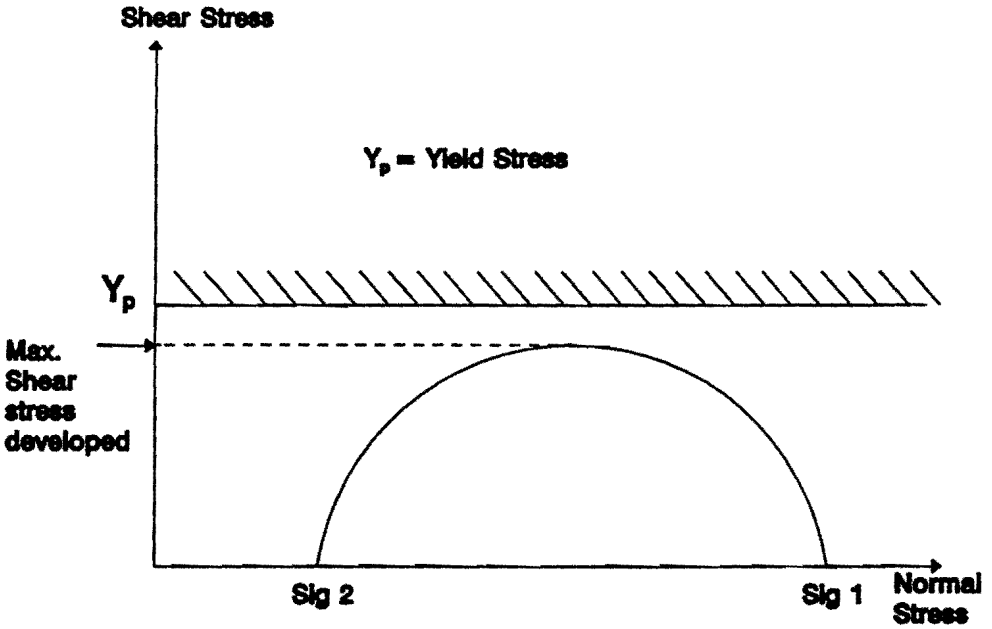

Figure A.6a. Tresca Criterion in Two Dimensional Stress Space.

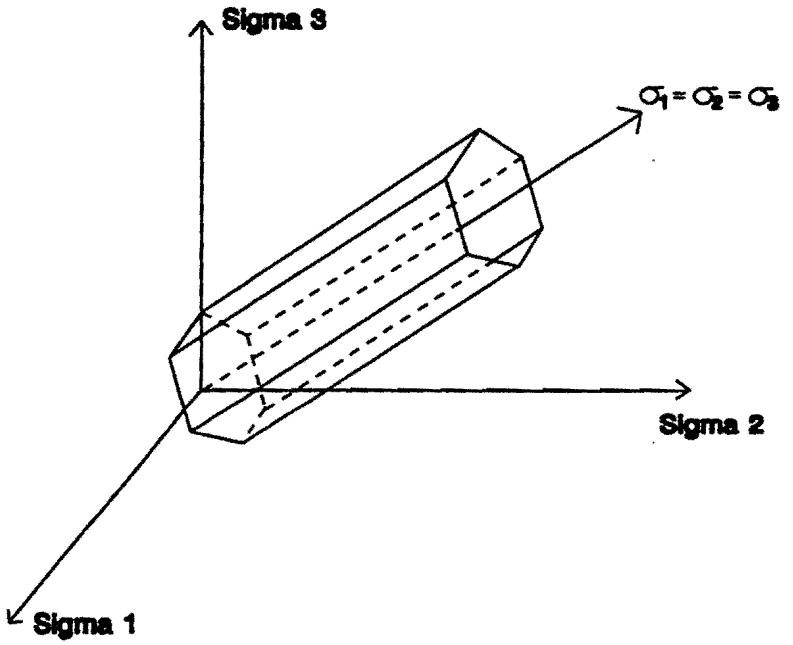

Figure A.6b. Tresca Yield Surface in Principal Stress Space.

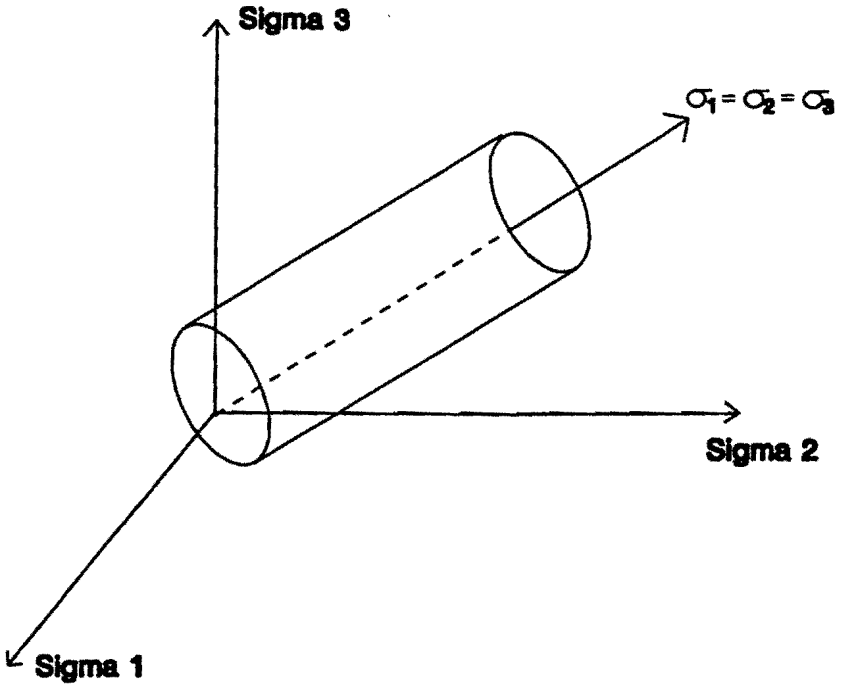

Figure A.7. Von Mises Failure Surface in Three Dimensional Stress Space.

between measured and predicted point of failure (70,73). A.A Griffith refined Dugeut's explanations by introducing the idea of microscopic cracks (70,74). Griffith's approach was later expanded and improved by Irwin (75) and was subsequently applied with success to prediction of failure in concrete specimens of different strengths (76,77).

A further limitation of the Tresca and Von Mises criteria is their failure to take into account the effect that stress magnitude has on material strength. In continuum mechanics, the total stress tensor is often decomposed into a deviatoric and a volumetric component. This can be represented by the following equation (67):

$$\sigma_{ij} = S_{ij} + \frac{\sigma_{nn}}{3} \delta_{ij} \qquad \text{(A.17)}$$

Where σ_{ij} = the total stress tensor,

σ_{nn} = the hydrostatic, or volumetric stress tensor,

S_{ij} = the deviatoric stress tensor, and

δ_{ij} = the Kronecker delta.

By definition, the volumetric stress component will always act along the hydrostatic axis. The deviatoric stress component will always act in a plane that is perpendicular to the hydrostatic axis. This plane is normally known as the π-plane. Figure A.8 shows the hydrostatic and volumetric components in principal stress space.

If we apply the concepts of deviatoric and volumetric stress components to the Tresca and Von Mises criteria, it becomes clear that the point of failure is purely dependent on the deviatoric component. That is, due to the constant diameter of the hexagonal and cylindrical shapes of the Tresca and Von Mises criteria, the point at

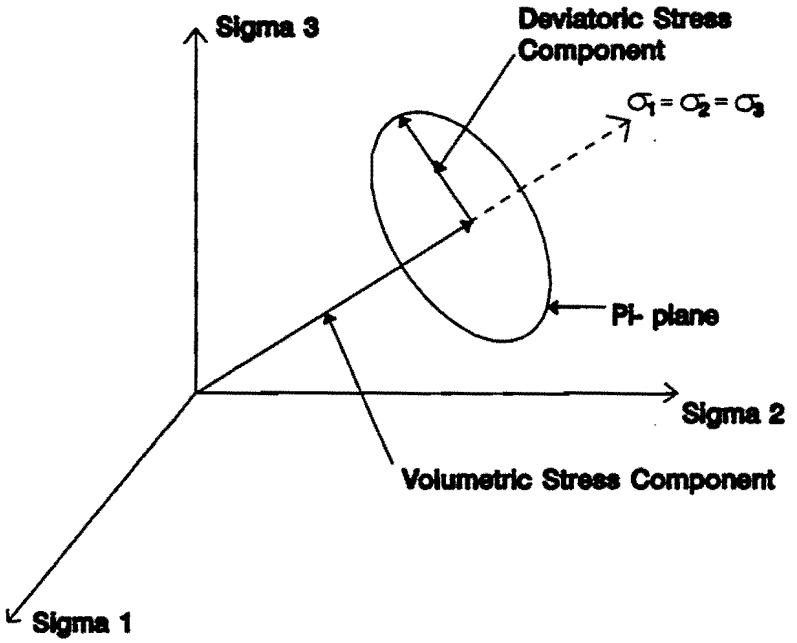

Figure A.8. Deviatoric and Volumetric Stress Components.

which failure will be predicted is independent of the magnitude of the volumetric component.

Experiments by Bridgeman (78) have shown that the influence of the hydrostatic stress component was negligible for many materials. Also, theoretical and experimental work performed by Hill pointed out that the yield criterion for metals depends only on the deviatoric stress (79). This means the yield function can be expressed solely in terms of the deviatoric stress component. For instance, the Von Mises criterion is given by (17,67):

$$J_2 - k^2 = 0 \qquad \text{(A.18)}$$

Where J_2 = the second deviatoric stress invariant, and

k^2 = a yield strength determined through testing.

Thus, the Von Mises criterion states that the material will behave elastic as long as the left hand side of equation A.18 is less than zero.

Experience gained from strength tests conducted on soils and other granular materials shows that the point at which yield will start in granular media is dependent not only on the deviatoric stress component, but also the hydrostatic stress component (17). This is because of the frictional nature of granular media. When a hydrostatic stress is applied to soil, the particles, which are angular, are pressed together, and the number of contact points as well as the intensity of contact is increased. This leads to increased friction which offers more resistance to sliding of particles over one another. Thus, in soils and rocks, the strength of the material is dependent on the hydrostatic component of stress (17).

The Mohr-Coulomb failure theory takes account of the volumetric stress component and is one of the most widely applied and successful theories used to predict failure in frictional media (16,17). Figure A.9 shows a comparison of the Mohr-Coulomb and Tresca criteria. Figure A.9 shows that the Mohr-Coulomb failure surface opens up as the hydrostatic stress component is increased. Effectively, this means that, for the same

material, the Tresca criterion will predict failure at higher volumetric stresses, whereas the Mohr-Coulomb criterion will still indicate that the material is behaving elastically.

In recent years, a number of yield criteria were developed which are in some way or another based on the Mohr-Coulomb yield criterion. In the following, the Mohr-Coulomb criterion will be discussed together with three of the more recently developed yield criteria. All of these criteria have been used to predict yield in geological media, but all differ with respect to complexity and in the types of parameters required to characterize the yield function.

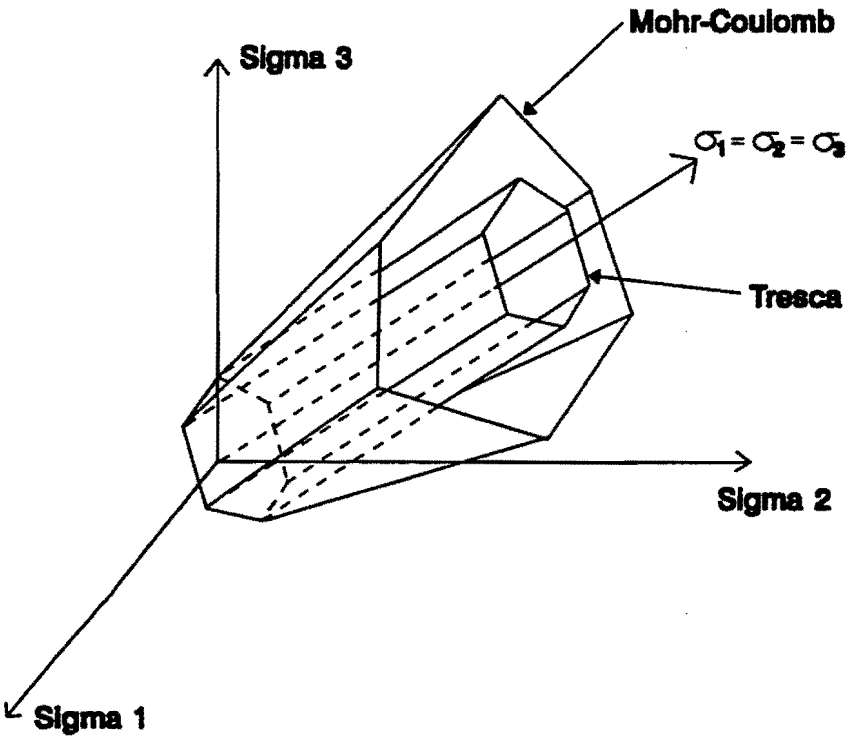

Figure A.9. Mohr-Coulomb and Tresca Yield Criteria.

THE MOHR-COULOMB YIELD CRITERION

The Mohr-Coulomb failure theory is a generalization of the failure theory proposed by Coulomb in 1773 (67). According to the Coulomb friction law, the magnitude of shearing stress (τ) is a function of the normal stress (σ_n), the cohesion (c), and the internal angle of friction (ϕ) of the material (17):

$$\tau = c + \sigma_n \tan\phi \tag{A.19}$$

This failure law can easily be visualized by means of a Mohr circle representation, as shown in Figure A.10. The straight line shown in Figure A.10 represents equation A.19 and is a limiting function, or failure envelope, in that all states of stress for which the Mohr circle plots below this line are elastic. Failure will occur when the Mohr circle touches the envelope.

By using the Mohr circle construction, the Mohr-Coulomb failure criterion can be written in terms of the principal stresses (17):

$$f = \left(\frac{\sigma_1 + \sigma_3}{2}\right) \sin(\phi) - \left(\frac{\sigma_1 - \sigma_3}{2}\right) + c\cos(\phi) \tag{A.20}$$

Where σ_1 = major principal stress,

σ_3 = minor principal stress,

ϕ = internal angle of friction, and

c = cohesion.

Equation A.20 represents an irregular hexagonal pyramid in stress space (Figure A.11). The irregularity of the hexagonal pyramid can be attributed to the fact that materials which obey the Mohr-Coulomb failure law generally have a much lower tensile strength than compressive strength.

Equation A.20 shows that the Mohr-Coulomb failure criterion is independent of the intermediate principal stress. Therefore, there is some difficulty involved in expressing

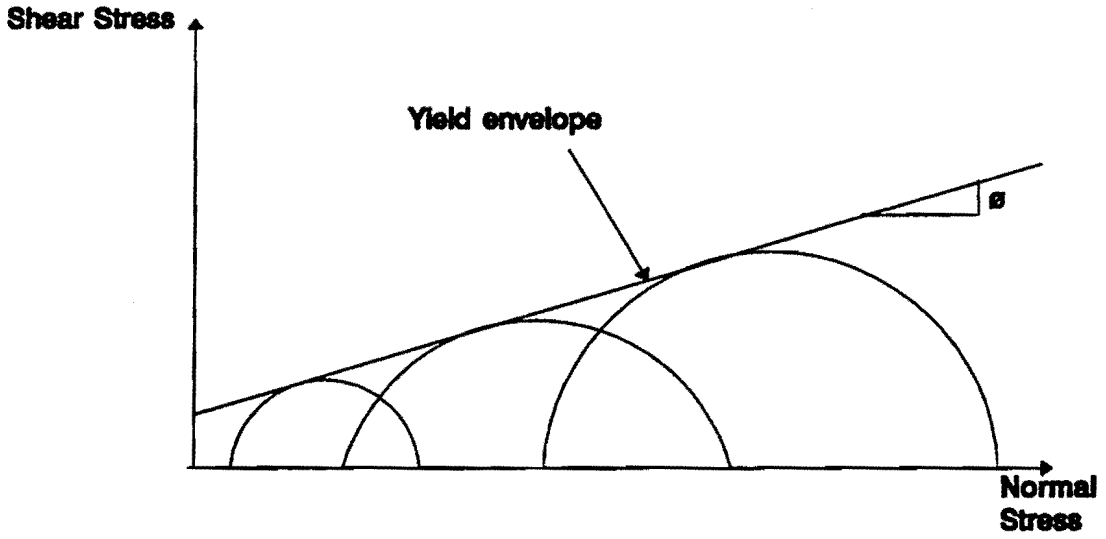

Figure A.10. Mohr-Coulomb Failure Envelope.

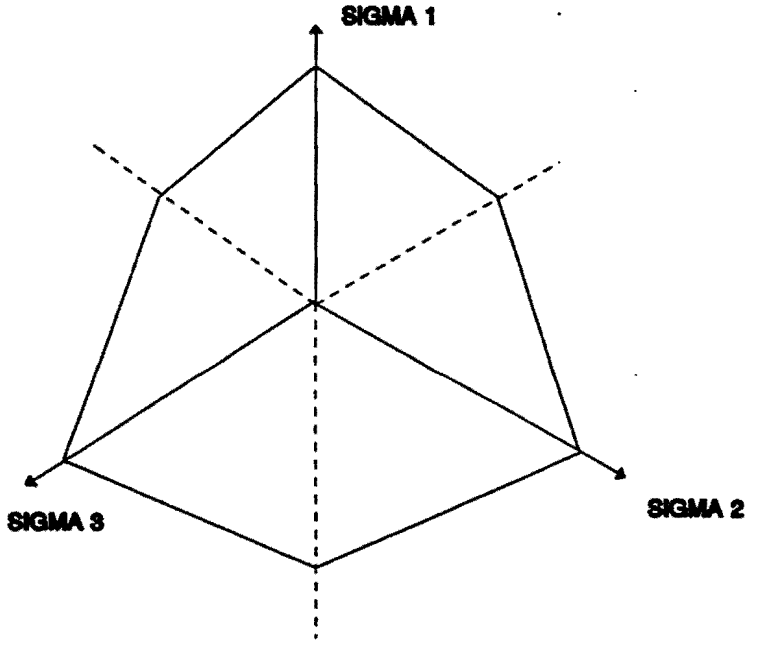

Figure A.11. Mohr-Coulomb Failure Surface on the π-Plane.

the failure criterion in terms of a general three-dimensional stress state. For this reason, an alternative set of invariants are used, which make use of the quantity known as the Lode Angle (Θ), defined by (16):

$$\theta = (1/3)\cos^{-1}\left(\frac{3\sqrt{3}}{2}\frac{J_3}{(J_2)^{(3/2)}}\right) \tag{A.21}$$

Where: J_2 and J_3 are the second and third deviatoric stress invariants, respectively.

By making further use of the first stress invariant I_1, the Mohr-Coulomb criterion in three dimensional stress space can be expressed by (16):

$$f = \frac{I_1}{3}\sin(\phi) + \sqrt{J_2}\sin\left(\Theta + \frac{\pi}{3}\right) + \frac{\sqrt{J_2}}{\sqrt{3}}\cos\left(\Theta + \frac{\pi}{3}\right)\sin(\phi) - c\cos(\phi) = 0 \tag{A.22}$$

It is interesting to note that for $\phi = 0$, equation A.22 reduces to the Tresca criterion. Equation A.22 indicates that, in addition to knowing the state of stress, two other parameters are needed in order to predict failure. They are the cohesion (c) and the internal angle of friction (ϕ). Both these parameters can be determined through conventional triaxial laboratory testing.

DEFICIENCIES IN THE MOHR-COULOMB CRITERION

The Mohr-Coulomb yield theory, as traditionally applied to bearing capacity problems, assumes that the soil behaves as a purely elastic medium until a stress state is reached such that yield function attains a value of zero. It is assumed that plastic deformation will take place only after this point. While this may be the case with highly compacted geological media such as densely compacted pavement layers, this simplified view of soil behavior does not apply to more loosely packed soils in which plastic deformations take place from an early stage in the loading process. As such, the material

passes through a number of successive yield points until it reaches an ultimate yield point. This ultimate yield point is considered to lie on the ultimate yield surface (17). As the material passes through the series of successive yield points, it hardens, so that the yield surface is changed after each successive yield.

Although the Mohr-Coulomb criterion does make use of the hydrostatic stress component to determine the resistance to yielding, the volumetric component in itself is not assumed to affect yielding. That is, the Mohr-Coulomb criterion will not predict failure as long as the deviatoric component is close to zero, regardless of the size of the volumetric stress component. However, experience shows that soils often experience plastic deformations under a purely hydrostatic stress condition (17). Thus, there should also be a restriction placed on the magnitude of the hydrostatic stress component.

In effect, this means that the Mohr-Coulomb criterion should not be open-ended, as shown in Figure A.10, but should have a boundary, or cap, on the end. This is a deficiency in the Mohr-Coulomb criterion which has led to the subsequent development of "Cap-Models" for which most of the pioneering work was done at Cambridge University under Roscoe (80,20), Schofield (21), and Di Maggio and Sandler (81). The concept of the Cap model is illustrated in Figure A.12.

In the Cap model as applied by Di Maggio and Sandler (81), the conventional yield surface is assumed to be fixed and defined by the Drucker-Prager criterion, which was smoothed into the Von Mises criterion for higher stresses (17). This part of the total yield function stays fixed. The cap portion is called a yield cap and does not stay fixed but moves as the material passes through successive stages of yielding. The position of this yield cap was assumed to depend on the volumetric plastic strain.

A third disadvantage associated with the Mohr-Coulomb criterion is the existence of corners at certain points of the yield surface (Figure A.11). In order for the plastic strains to be determined, there is a need to obtain the derivative of the yield function (as shown in equations A.14 and A.15). This places a limitation on the Mohr-Coulomb surface, which, due to its angular shape, can lead to singularities and computational difficulties when calculating the derivative of the yield function. For this reason, many of the more advanced yield criteria use smoothed approximations of the Mohr-Coulomb yield function.

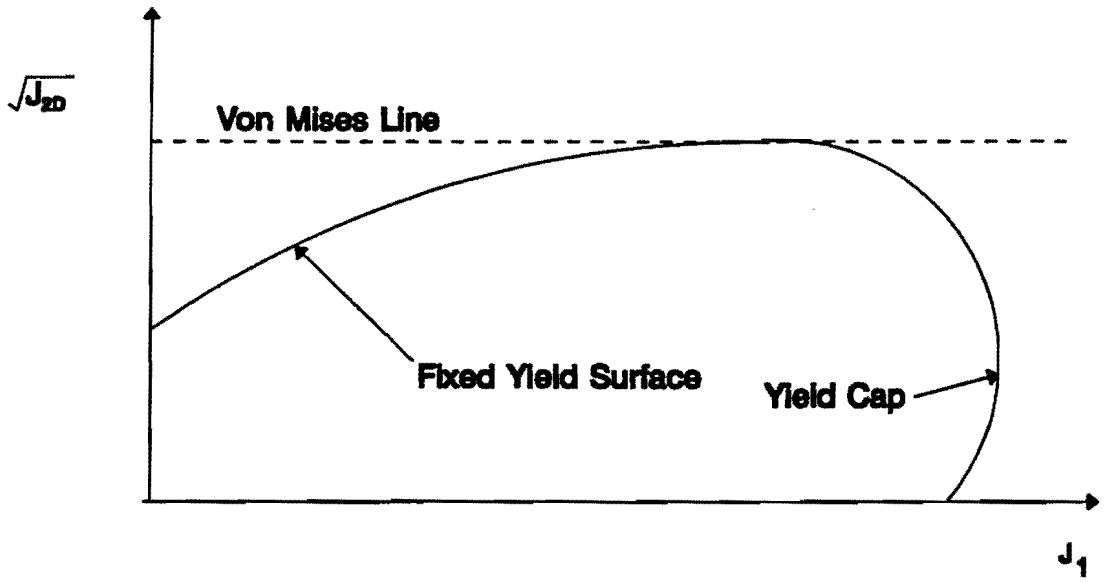

Figure A.12. Yield Surface with End Cap.

To summarize, it can be seen that the traditional application of the Mohr-Coulomb criterion is deficient in two respects:

1. The traditional Mohr-Coulomb yield surface is fixed. Thus, it does not take into account any transition that may exist between states of purely elastic and purely plastic behavior. This simplified approach cannot be used to predict the behavior of loose materials under loading.
2. The Mohr-Coulomb criterion does not take into account that there may be a limiting point at which the volumetric stress component alone can lead to plastic strains taking place.

It should be noted that these deficiencies do not render the Mohr-Coulomb criterion obsolete. In fact, almost all of the modern yield criteria are in some way derived from the Mohr-Coulomb criterion and make use of the basic principles expressed by the Mohr-Coulomb yield theory, i.e., that of dependence of shear strength on the hydrostatic stress component and different yield strengths in tension and compression. In the following sections, three of these more recently developed yield criteria applied to the prediction of yield in geological media will be discussed.

LADE YIELD CRITERION

During 1973, Lade and Duncan performed a series of cubical triaxial tests on Monterey No. 0 sand (82). Some of the results from these tests are shown in Figure A.13. This figure also shows the Mohr-Coulomb failure surfaces that correspond to the yield strengths from triaxial tests. It is clear that although the comparison between the Mohr-Coulomb failure surface and the experimental results are good, the experimentally obtained failure surfaces have a smoother shape than the angular Mohr-Coulomb surface.

Subsequent to this study, Lade and Duncan proposed a failure criterion in 1973 that can be expressed as a simple combination of stress invariants (83).

$$f_f = I_1^3 - \kappa_1 I_3 \tag{A.23}$$

Where I_1 and I_3 are the first and third stress invariants, respectively, and κ_1 is a value of stress level at failure which depends on the density of the sand.

Lade and Duncan also developed an isotropic elasto-plastic work hardening model (83). In this model, the form of the failure surface is the same as that of equation A.23. The loading surfaces have an identical form, but the constant, κ_1, is replaced by K, which is dependent on the current level of stress. Figure A.14 shows the loading surfaces to lie within the ultimate yield surface. Thus, when K takes on a value of κ_1, the loading surface and the ultimate yield surface will coincide. Lade at a later stage modified this failure criterion to include curved yield and loading surfaces, instead of having straight meridian lines (84). The modified criterion also included a cap type of yield surface, which is controlled by the plastic collapse strains which occur during isotropic compression (17,84).

In order to make use of a curved yield surface, the angle of friction was assumed to decrease as the hydrostatic pressure increases. This modification led to the following yield criterion (17):

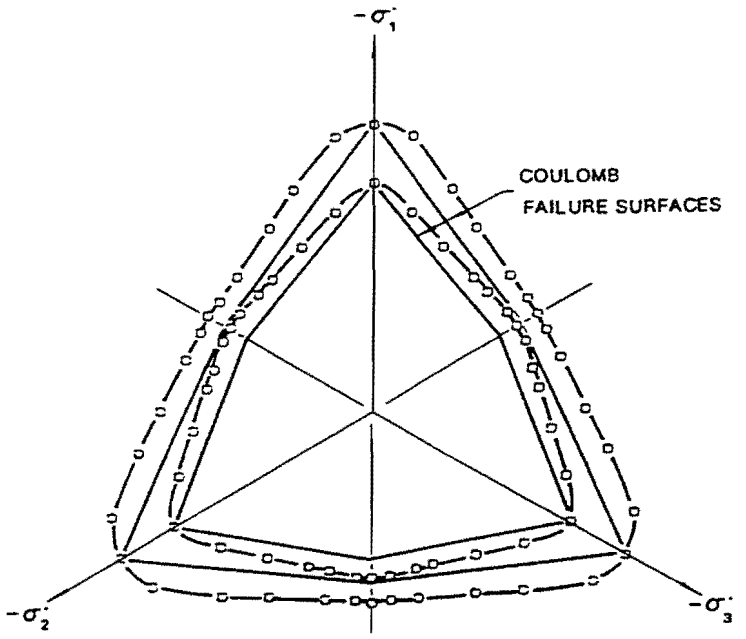

Figure A.13. Tests Results Reported by Lade (From (82)).

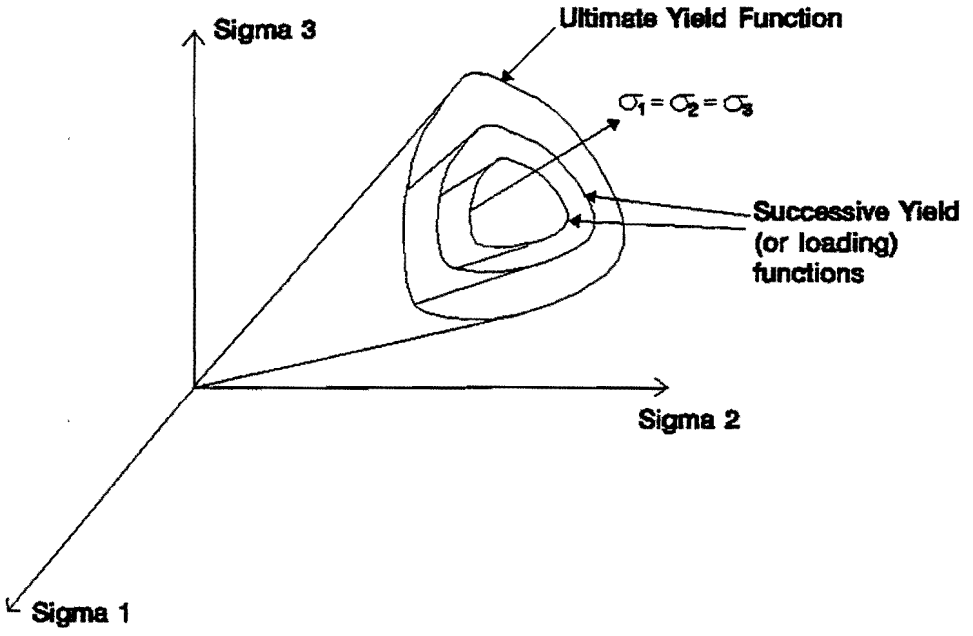

Figure A.14. Lade-Duncan Yield Surfaces (From (83)).

$$f_f = \left(\frac{I_1^3}{I_3} - 27 \right) \left(\frac{I_1}{P_a} \right)^m \qquad \text{(A.24)}$$

Where f_f has a value of η_1 at failure. P_a is the atmospheric pressure. The values of η_1 and m in equation A.24 are obtained by plotting $(I_1^3/I_3 - 27)$ versus P_a/I_1 at failure on a log-log diagram (17). The value of m controls the curvature of the failure surface. For m = 0, the failure surface becomes identical to the Lade-Duncan criterion defined by equation A.23. The cap type of yield surface is defined by (17,84):

$$f_c = I_1^2 - 2I_2 \qquad \text{(A.25)}$$

The cap surface is defined to expand isotropically as f_c increases. Figure A.15 illustrates the conical yield surface and the spherical yield cap in the triaxial plane (67). A flow rule was also set up using the above yield surfaces. A detailed description of these yield surfaces can be found in references 17 and 84, and they will not be described in detail here.

The Lade criterion has been examined by Lade for the prediction of soil and pore pressure behavior in saturated triaxial compression tests (17,85). The model has the advantages of having smooth, curved surfaces, being simple in application, and applying to a relatively wide range of pressures (17).

DESAI YIELD CRITERION

Desai and Siriwardane have stated that a general form for yield surfaces can be expressed by the following (17):

$$f = f(\sigma_{ij}, \epsilon_{ij}^p, W^p) \qquad \text{(A.26)}$$

Where σ_{ij} is the stress state,

ϵ_{ij}^p is the plastic strain, and

W^p is the plastic work.

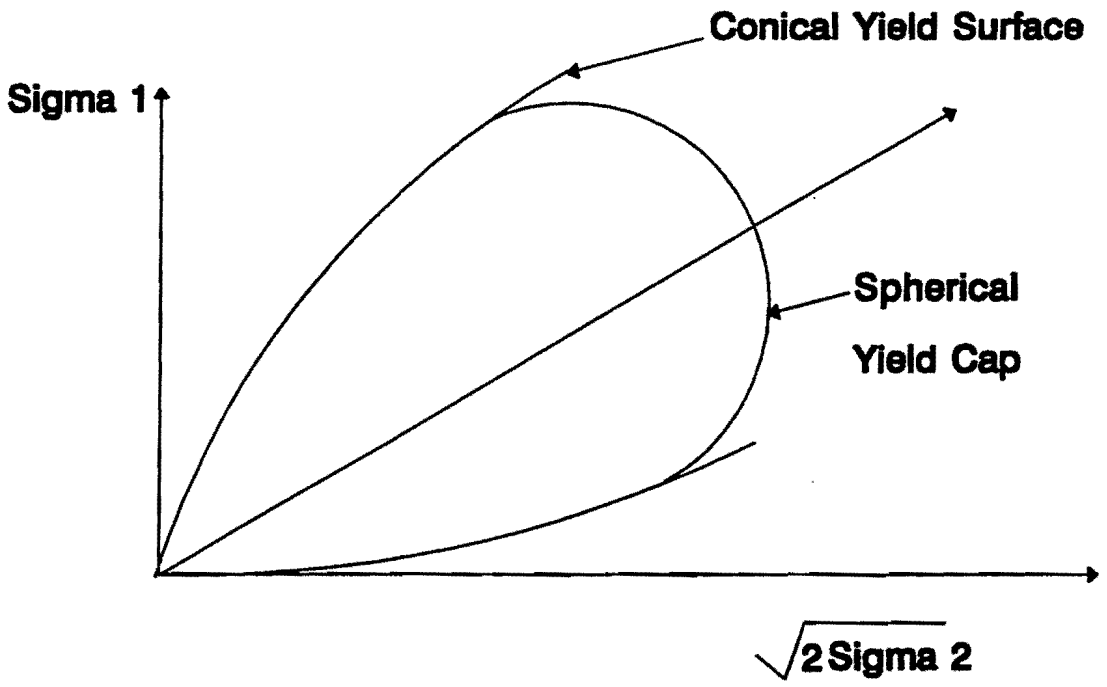

Figure A.15. Conical Yield Surface and Yield Cap (From (67)).

Desai (86), Desai and Siriwardane (87), and Baker and Desai (88) have studied a number of special forms of equation A.26. Desai studied a special case of equation A.26 in which f is expressed in terms of I_1, J_2, and I_3 as (17):

$$\bar{f}_f = J_2 + \alpha I_1 - \beta I_1 I_3^{1/3} - \gamma I_1 - k^2 \qquad \text{(A.27)}$$

Where α, ß, γ and k are material parameters. The factor, k, is a measure of cohesion, and ß is the hardening function (17). Figure A.16 shows plots of the Desai criterion for different values of β. Figure A.17 shows a schematic representation of the Desai criterion in the π-plane. As can be seen from Figure A.16, the Desai criterion combines the ultimate yield and cap functions, a significant simplification over conventional cap models. The values of the parameters α, ß, γ, and k are calculated from the ultimate yield envelope that can be obtained from laboratory test data (17).

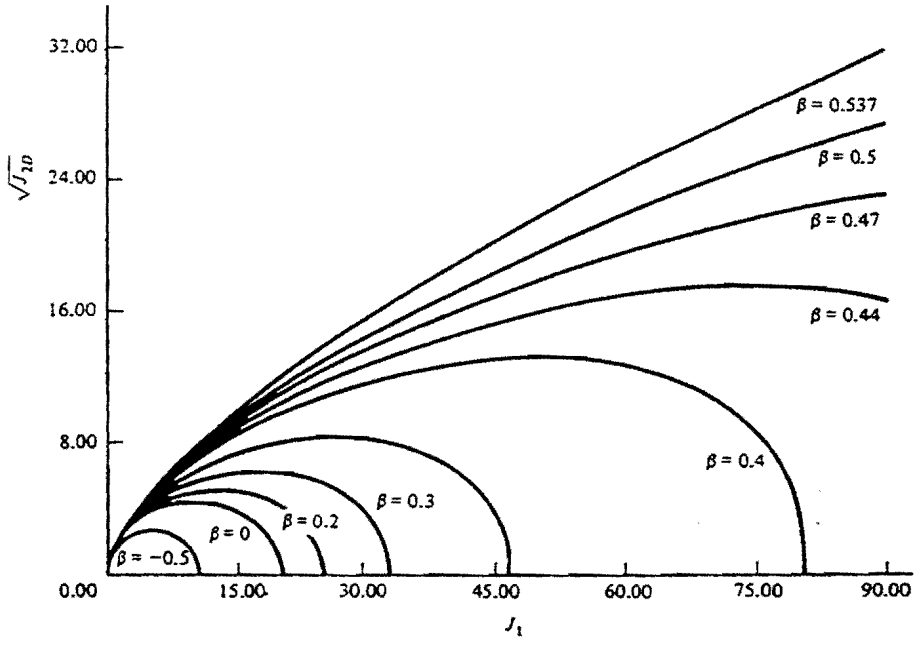

Figure A.16. Desai Criteria for Different β Values (From (17)).

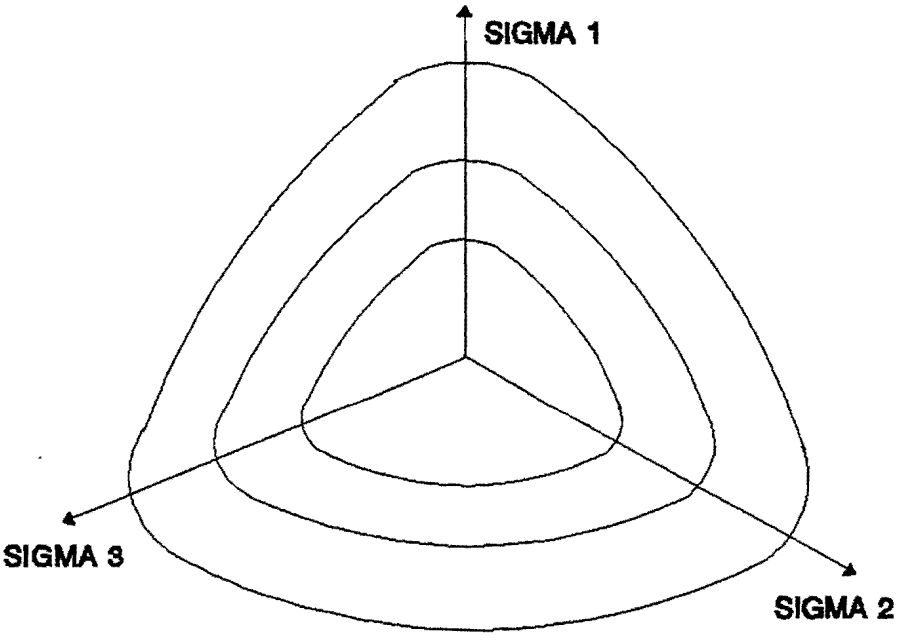

Figure A.17. Desai Failure Surfaces (From (17)).

MODIFIED VERMEER YIELD CRITERION

The Vermeer Failure Law is one of the more recent developments in the field of limit analysis and has been used with success in a number of plasticity applications. The Vermeer model makes use of the failure criterion developed by Matsuoka and Nakai (43,89,90). The Matsuoka-Nakai failure law can be expressed in terms of the first, second, and third stress invariants as (43):

$$f_p = -I_1 I_2 + \frac{9 - \sin^2(\phi_p)}{\cos^2(\phi_p)} I_3 \qquad \text{(A.28)}$$

Where ϕ_p is the peak friction angle and I_1, I_2, and I_3 are the first, second, and third stress invariants, respectively. Compression is considered to be negative. Comparisons between the Matsuoka-Nakai failure law and the stress measured at failure for Toyova sand showed that measured and predicted values compared quite well (91).

The failure surface described by equation A.28 is the limiting position of an expanding yield surface. In order to obtain the loading functions that will eventually lead to the limiting yield function, the peak friction angle ϕ_p in equation A.28 is replaced by the mobilized friction angle, ϕ_m. The mobilized friction angle is dependent on the plastic distortion and the level of stress.

The appearance of the Matsuoka-Nakai failure surface in three dimensional stress space is similar to that of the Lade and Desai criteria (Figure A.17). As such, it can be described as a smooth hexagonal curve circumscribing the hexagonal Mohr-Coulomb yield surface. Vermeer derived a relation between the plastic distortional strain and stress which is expressed through a factor known as the normalized plastic distortion which is used to define the hardening behavior of the material. The validity of this hardening law was checked by Vermeer (43,91).

The Vermeer model was intended for use with cohesionless materials only. In order to include the influence of cohesion (particularly important in asphalt and clay materials), the yield surface developed for cohesionless materials is adapted for cohesive materials by translating the principal stress along the hydrostatic axis by addition of a constant stress to the normal stress. This modification can be expressed as (43):

$$\sigma'_{ij} = \sigma_{ij} - c \cot(\phi_p)\ \delta_{ij} \quad \text{(A.29)}$$

Where σ'_{ij} = the transformed stress tensor,

σ_{ij} = the actual stress tensor,

c = cohesion, and

δ_{ij} = the Kronecker delta.

This translation is applied only to stresses used in conjunction with yield and the plastic potential surfaces (43).

SUITABILITY OF MOHR-COULOMB YIELD CRITERION FOR USE IN PAVEMENT ANALYSIS

In an earlier discussion, the deficiencies in the Mohr-Coulomb yield criteria were noted as (1) having a fixed yield surface; and (2) not placing a cap on the volumetric stress component. In the analysis of pavement response under superheavy load vehicles, the purpose of the analysis is to prevent yield (and, therefore, plastic deformations). The first deficiency in the Mohr-Coulomb yield criteria noted above is not considered to apply to this study, where the purpose is to analyze stresses invoked when the material is still in an elastic state.

The second deficiency noted above is also not considered to be critical in the case of this study. Researchers conducted a comparison between the Mohr-Coulomb yield criterion and the three more recently developed criteria discussed in the preceding sections. This analysis showed that, for the stress levels typically induced in pavements, failure occurs due to excessive shear in the low stress range where cohesion is a critical component of the overall shear strength. This indicates that, for pavements, the likelihood of failure due to excessive volumetric stresses is very small. Also, the results of analyses reported in this study support this observation.

A major advantage of the Mohr-Coulomb yield criterion is its relative simplicity. Engineers are well acquainted with the terms cohesion and angle of friction. Also, most engineers are acquainted with the tests required to determine cohesion and angle of

friction. This is considered to be a critical factor in the choice of a failure criterion to be used in this study, since it is important that the analysis methodology developed makes use of test methods currently employed by the Texas Department of Transportation. For these reasons, the Mohr-Coulomb yield criterion was chosen to be used in the evaluation of the potential for pavement damage under superheavy loads.

APPENDIX B

DERIVATION OF RELATIONSHIP BETWEEN POISSON'S RATIO AND STRESS STATE

The following derivation was obtained from the dissertation of Liu (43). Further discussions of the relationship between the resilient modulus and Poisson's ratio under thermodynamic constraints can be found in Chen et al. (41) and Lade et al. (42). Figure B.1 shows a schematic representation of the loading and unloading path followed when a material is subjected to a state of stress. The stress at a given point is initially at point A. For a loading that follows path ACB, the elastic work per unit volume can be expressed as:

$$W_{ACB} = \int_{ACB} dW = \int_{ACB} (\sigma)^T (d\epsilon) \tag{B.1}$$

Equation B.1 can be written in terms of the stress invariants as:

$$W_{ACB} = \int_{ACB} (\frac{I_1}{9K} dI_1 + \frac{dJ_2}{2G}) \tag{B.2}$$

Where I_1 is the first stress invariant and J_2 is the second invariant of the deviatoric stress tensor. K and G are the bulk and shear moduli, respectively. The total elastic work along the stress path ACBDA is:

$$W_{ACB} + W_{BDA} = \int_{ACBDA} (\frac{I_1}{9K} dI_1 + \frac{dJ_2}{2G}) \tag{B.3}$$

Assuming that K and G can be expressed as a function of I_1 and J_2:

$$K = K(I_1, J_2) \tag{B.4}$$

and

$$G = G(I_1, J_2) \tag{B.5}$$

The law of energy conservation requires that the total work along the cycle ACBDA must be zero. The integral in equation B.3 will be zero provided it can be written in the following form:

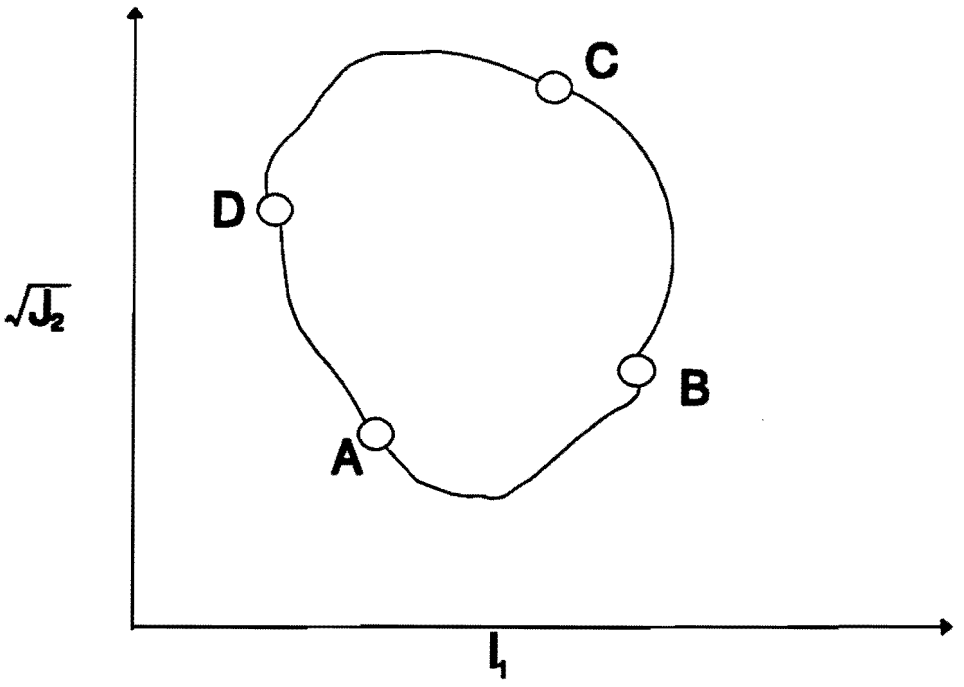

Figure B.1. Stress Path Diagram.

$$\oint(P\,dx + Q\,dy) = \iint_A \left(\frac{\partial Q}{\partial x} - \frac{\partial P}{\partial y}\right)dA \tag{B.6}$$

where $P = \partial W/\partial x, Q = \partial W/\partial y$. Equation B.6 states that if P and Q can be derived from a potential function, W, then the line integral vanishes and no net work is done on the closed stress path. If the work is path independent, then the quantity, dW, can be written in the following form:

$$dW = \frac{I_1}{9K}dI_1 + \frac{dJ_2}{2G} = \frac{\partial W}{\partial I_1}dI_1 + \frac{\partial W}{\partial J_2}dJ_2 \tag{B.7}$$

Equation B.7 shows that the following identities are satisfied:

$$\frac{I_1}{9K} = \frac{\partial W}{\partial I_1} \tag{B.8}$$

$$\frac{1}{2G} = \frac{\partial W}{\partial J_2} \tag{B.9}$$

The potential function can be expressed as:

$$\frac{\partial^2 W}{\partial I_1 \partial J_2} = \frac{\partial^2 W}{\partial J_2 \partial I_1} \tag{B.10}$$

Substituting equations B.8 and B.9 into equation B.10 results in the following constraint on the expression for K and G:

$$\frac{I_1}{9K^2}\frac{\partial K}{\partial J_2} = \frac{1}{2G^2}\frac{\partial G}{\partial I_1} \tag{B.11}$$

Since

$$K = \frac{E}{3(1-2\nu)} \tag{B.12}$$

and,

$$G = \frac{E}{2(1+2\nu)} \tag{B.13}$$

equation B.11 can be rewritten as:

$$\frac{2}{3}\cdot\frac{\partial \nu}{\partial J_2} + \frac{1}{I_1}\cdot\frac{\partial \nu}{\partial I_1} = -\frac{(1-2\nu)}{3}\cdot\frac{\partial \ln E}{\partial J_2} + \frac{(1+\nu)}{I_1}\cdot\frac{\partial \ln E}{\partial I_1} \tag{B.14}$$

By making use of the stress dependent resilient modulus equation developed by Uzan (36), the resilient modulus can be written as:

$$E_r = (k_1 \cdot p_a)\left(\frac{I_1}{p_a}\right)^{k_2}\left(\frac{\tau_{oct}}{p_a}\right)^{k_3} \tag{B.15}$$

Where:

p_a	=	atmospheric pressure
τ_{oct}	=	octahedral shear stress
k_i	=	material constants (i = 1,2,3)

Equation B.15 can be rewritten in terms of I_1 and J_2 as:

$$\ln E = \ln k_1' + k_2 \ln I_1 + k_3' \ln J_2 \tag{B.16}$$

where:

$$k_1' = k_1 \cdot pa^{1-k_2-k_3} \cdot \left(\frac{2}{3}\right)^{\frac{k_3}{2}} \tag{B.17}$$

and,

$$k_3' = \frac{k_3}{2} \tag{B.18}$$

Finally, substitution of equation B.16 into equation B.14 yields:

$$\frac{2}{3}\cdot\frac{\partial v}{\partial J_2} + \frac{1}{I_1}\cdot\frac{\partial v}{\partial I_1} = v\left(\frac{2}{3}\cdot\frac{k_3'}{J_2} + \frac{k_2}{I_1^2}\right) + \left(-\frac{1}{3}\cdot\frac{k_3'}{J_2} + \frac{k_2}{I_1^2}\right) \tag{B.19}$$

APPENDIX C

PHOTOGRAPHS OF LABORATORY TESTS

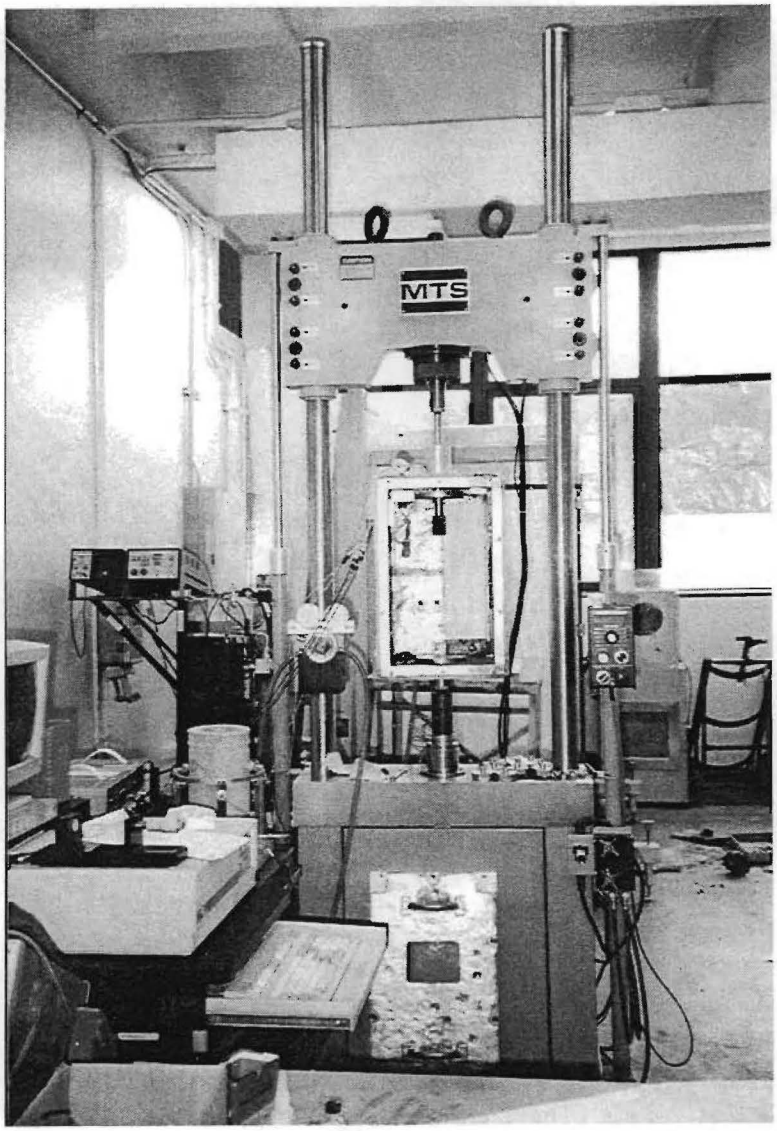

Figure C.1. Test Apparatus with Mounted Air Pressure Chamber.

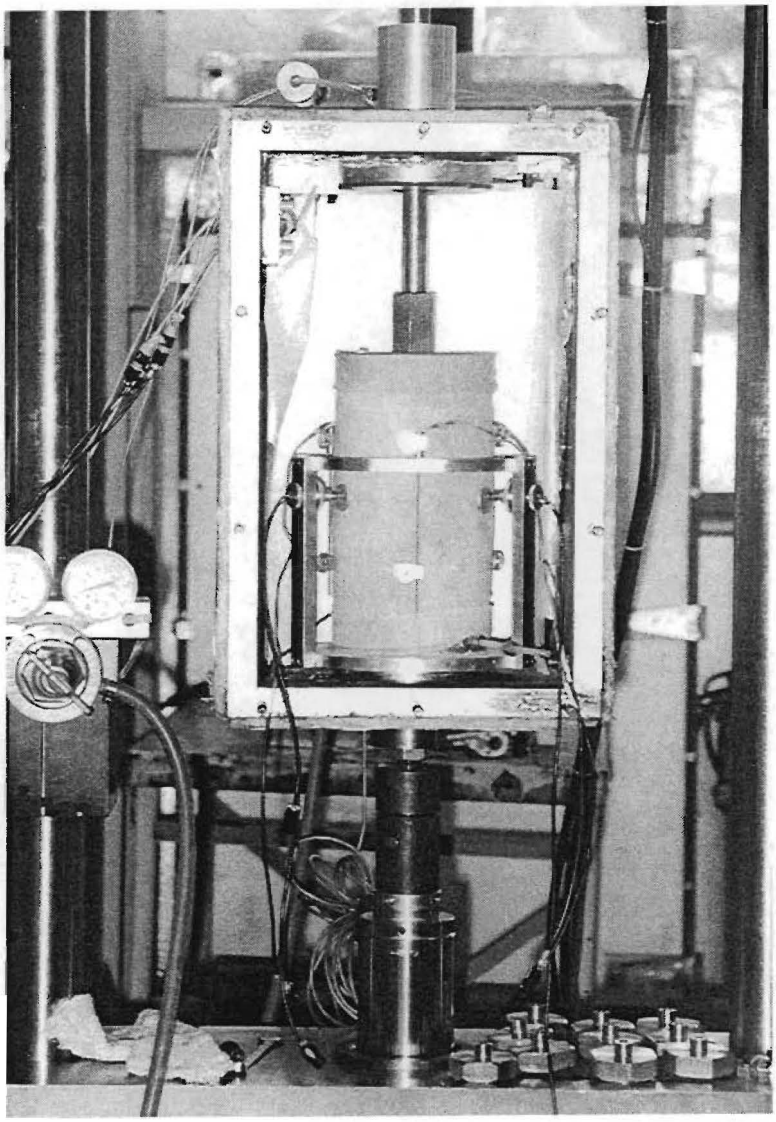

Figure C.2. Air Pressure Chamber with Test Sample in Place.

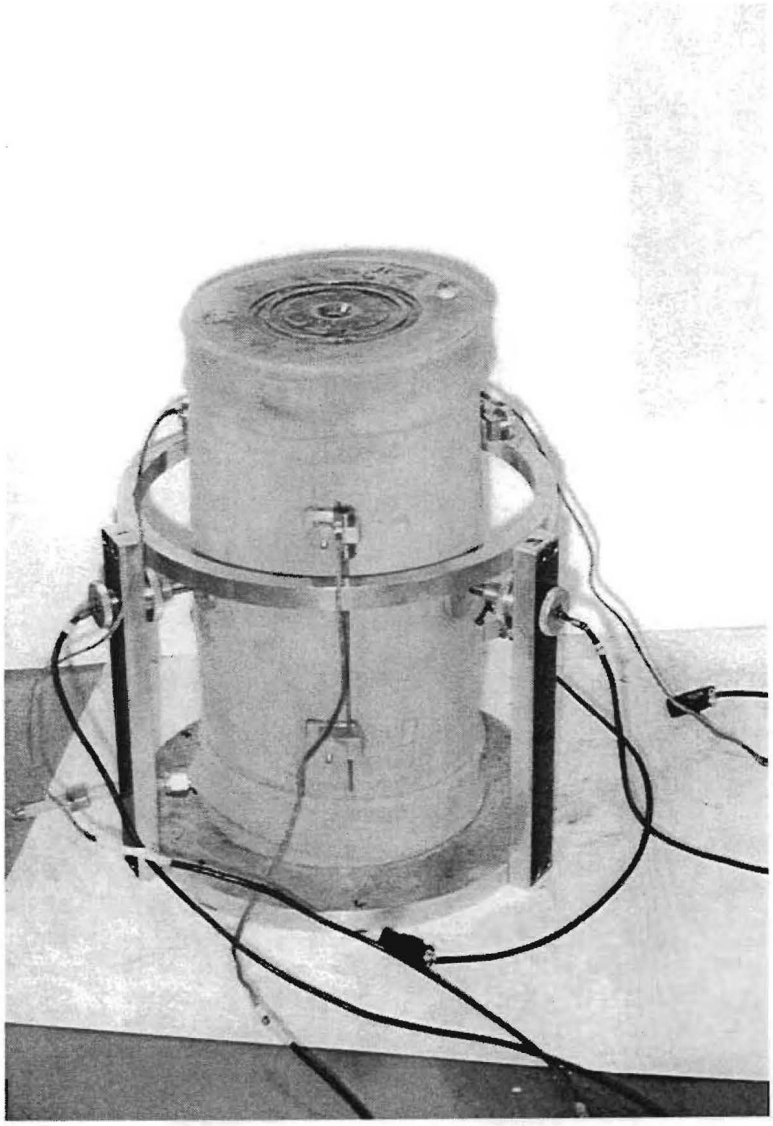

Figure C.3. Details of Test Sample Showing Positions of Sensors Used for Measurement of Axial and Radial Deformations.

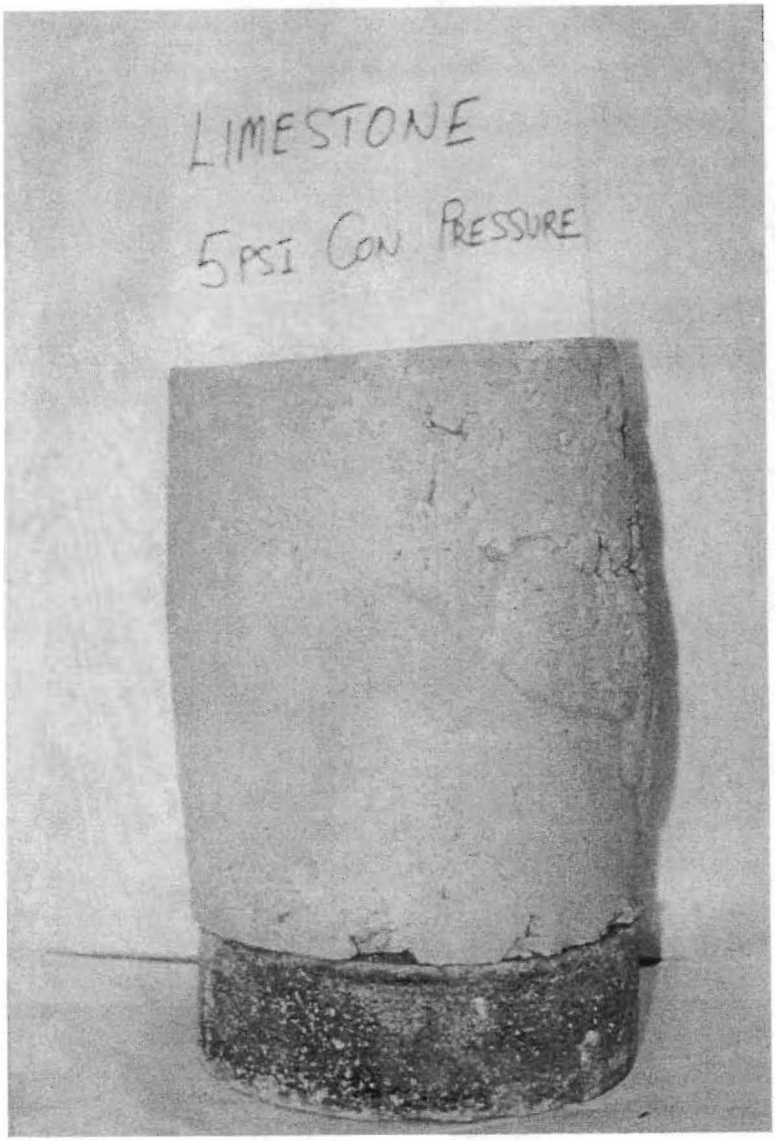

Figure C.4. Failed Specimen with Marked Failure Plane (Crushed Limestone at 34.5 kPa Confining Pressure).

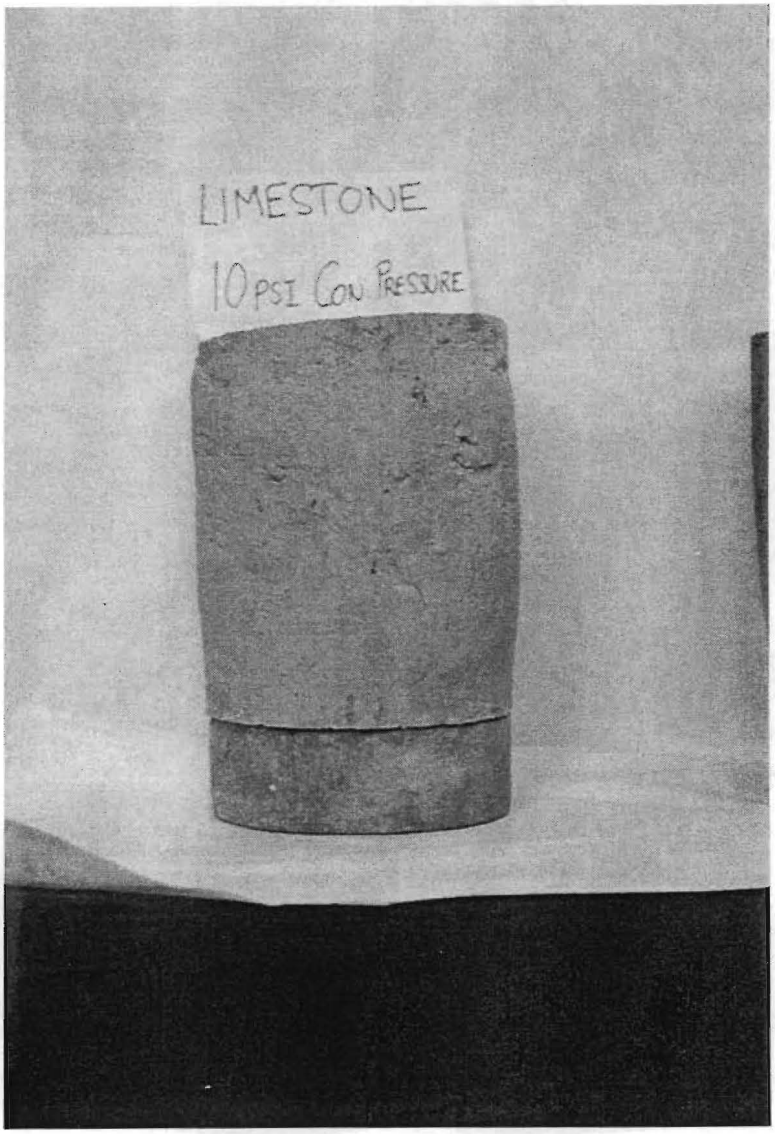

Figure C.5. Failed Specimen with Marked Failure Plane (Crushed Limestone at 69.0 kPa Confining Pressure).

APPENDIX D

RESULTS OF SENSITIVITY ANALYSIS

Figures D.1 through D.12 contain the results of the analysis of the sensitivity of the Mohr-Coulomb yield function to changes in the resilient modulus and Poisson's ratio parameters. Due to the large amount of output data that was obtained from this analysis, the graphs are presented in compact form and, thus, a large amount of information is contained in each graph.

Each graph documents the percentage change in the yield function that was calculated in each different layer when one of the k_1 to k_3 parameters for a single layer was varied. In the graphs, the boxed text states the layer and the parameter that was varied. Other text which accompanies the bars state in which layer the yield function was evaluated. For each evaluation position, there are two bars. The bar on the left hand side (filled with light crosshatching) represents the percentage change in the yield function when the given parameter was varied to 30 percent **below** its assumed average value. The bar on the right hand side (filled with dark crosshatching) represents the change in the yield function value when the given parameter was changed to 30 percent **above** its assumed average. The average values assumed for each coefficient and each layer are discussed in detail in Chapter IV.

As an example, in Figure D.1, the left-most bar indicates that changing the k_1 value for the surface layer to 30 percent below its assumed average resulted in approximately a 190 percent drop in the yield function value. The darkly crosshatched bar second from the left indicates that, when the k_1 value for the asphalt was raised to 30 percent above its assumed average, the yield function calculated in the surface was raised by about 170 percent. The same change (i.e., increasing k_1 for the surface by 30 percent) resulted in a drop of approximately 26 percent in the yield function calculated for the base while the yield function calculated in the subgrade remained virtually unchanged.

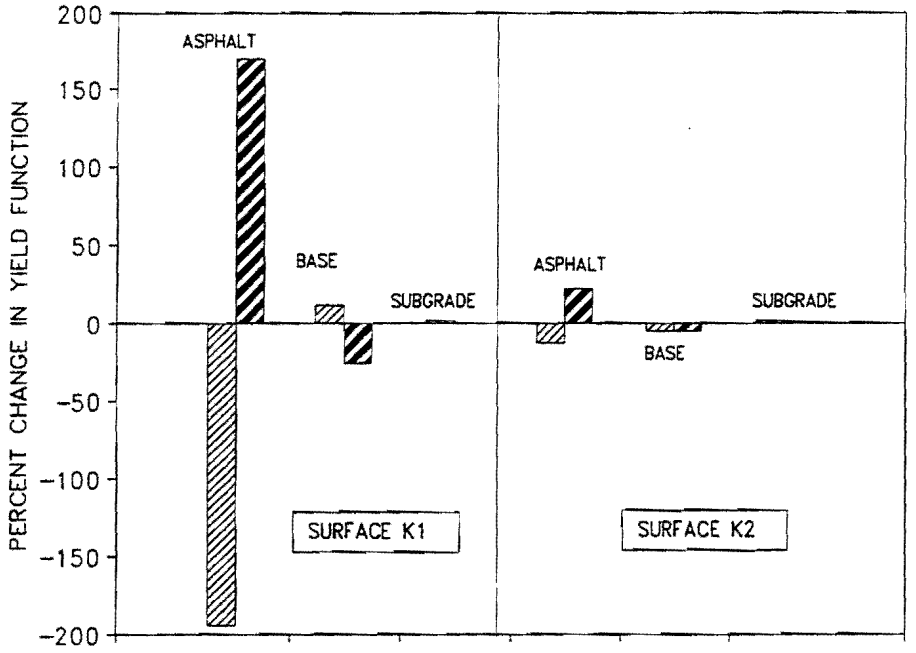

Figure D.1. Sensitivity of the Yield Function to Changes in the k_1 to k_3 Parameters of the Asphalt Surface (Thin Pavement, Center of Load Evaluation Position).

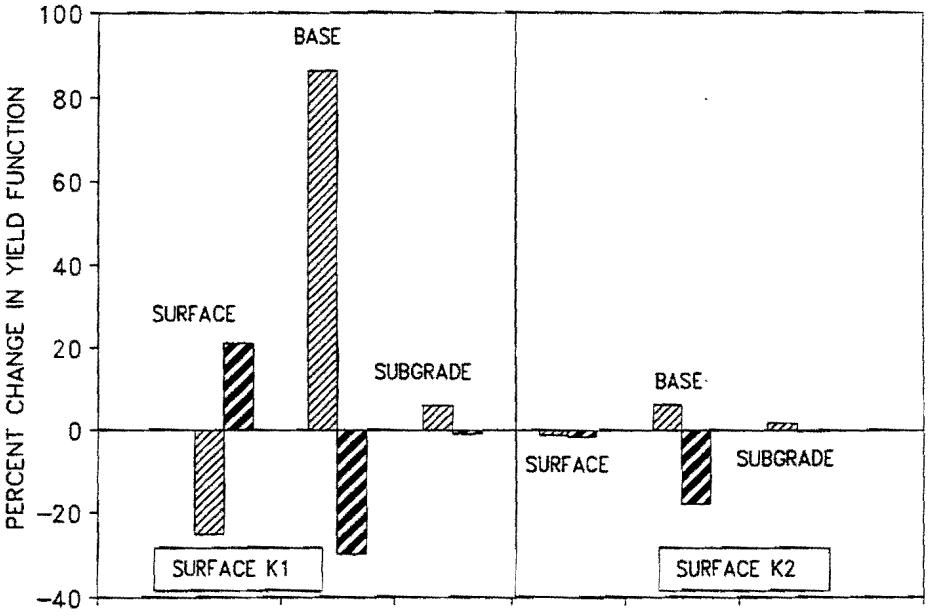

Figure D.2. Sensitivity of the Yield Function to Changes in the k_1 to k_3 Parameters of the Asphalt Surface (Thin Pavement, Edge of Load Evaluation Position).

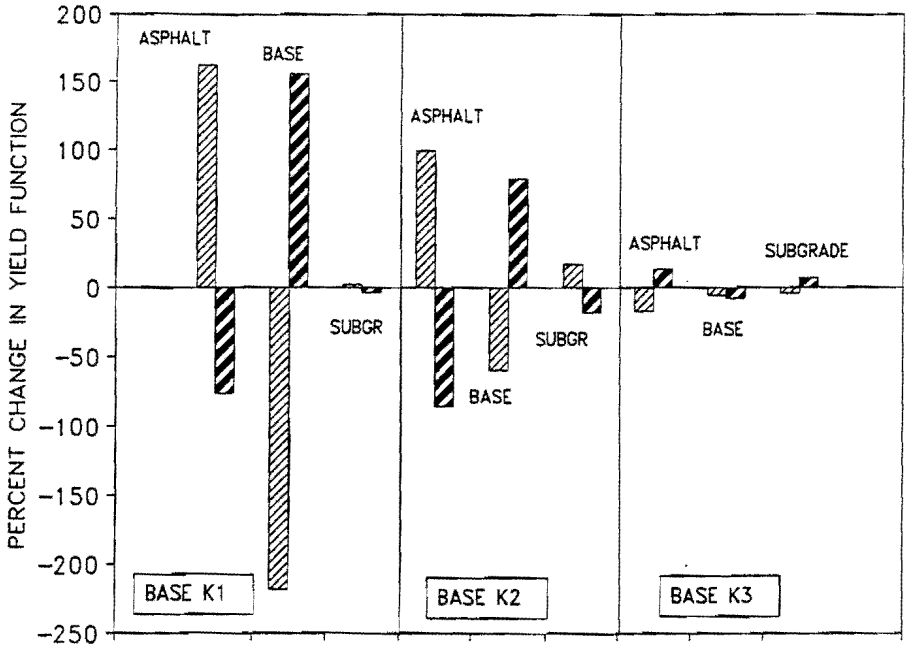

Figure D.3. Sensitivity of the Yield Function to Changes in the k_1 to k_3 Parameters of the Base (Thin Pavement, Center of Load Evaluation Position).

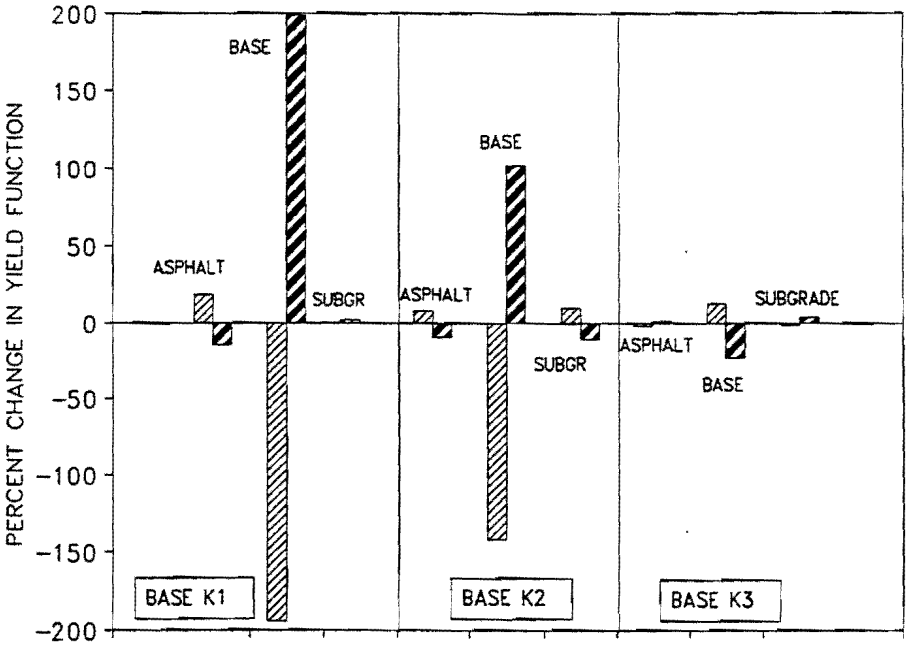

Figure D.4. Sensitivity of the Yield Function to Changes in the k_1 to k_3 Parameters of the Base (Thin Pavement, Edge of Load Evaluation Position).

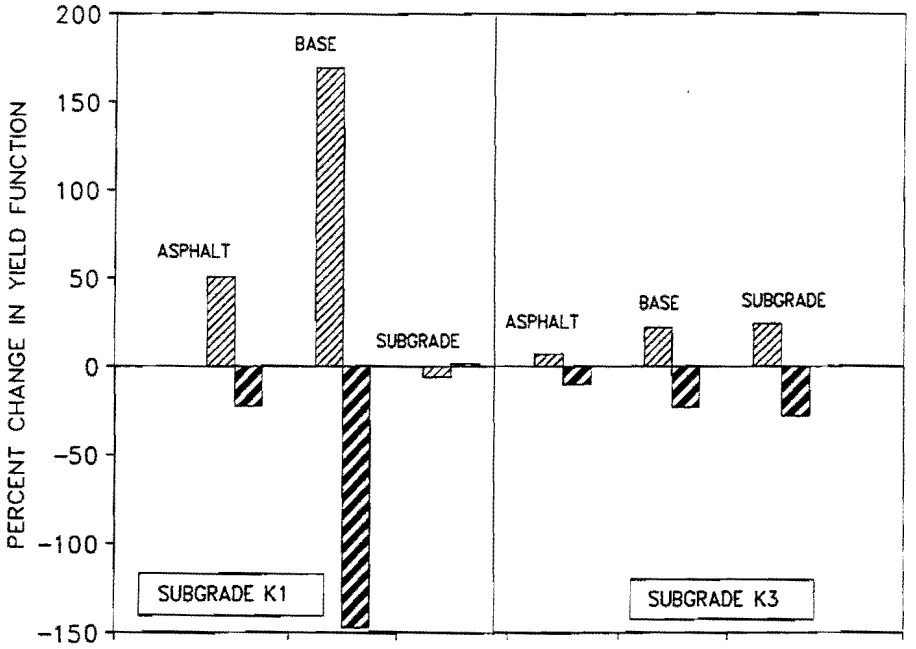

Figure D.5. Sensitivity of the Yield Function to Changes in the k_1 to k_3 Parameters of the Subgrade (Thin Pavement, Center of Load Evaluation Position).

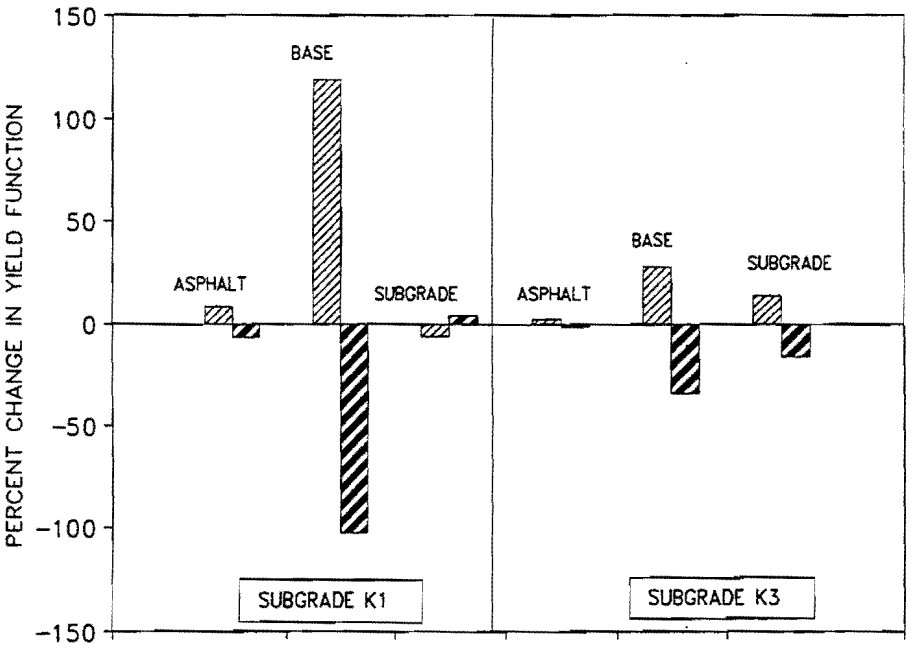

Figure D.6. Sensitivity of the Yield Function to Changes in the k_1 to k_3 Parameters of the Subgrade (Thin Pavement, Edge of Load Evaluation Position).

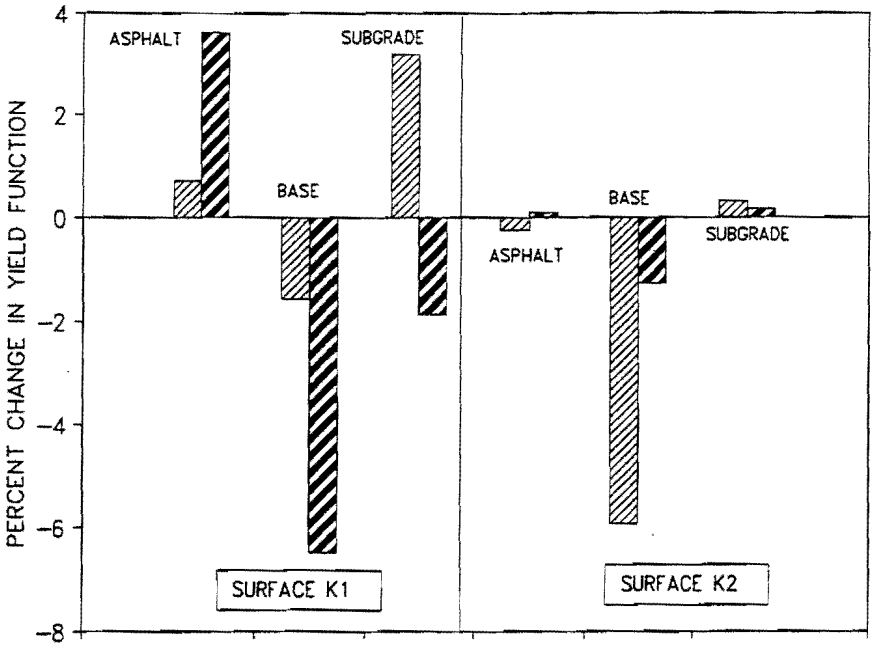

Figure D.7. Sensitivity of the Yield Function to Changes in the k_1 to k_3 Parameters of the Asphalt Surface (Thick Pavement, Center of Load Evaluation Position).

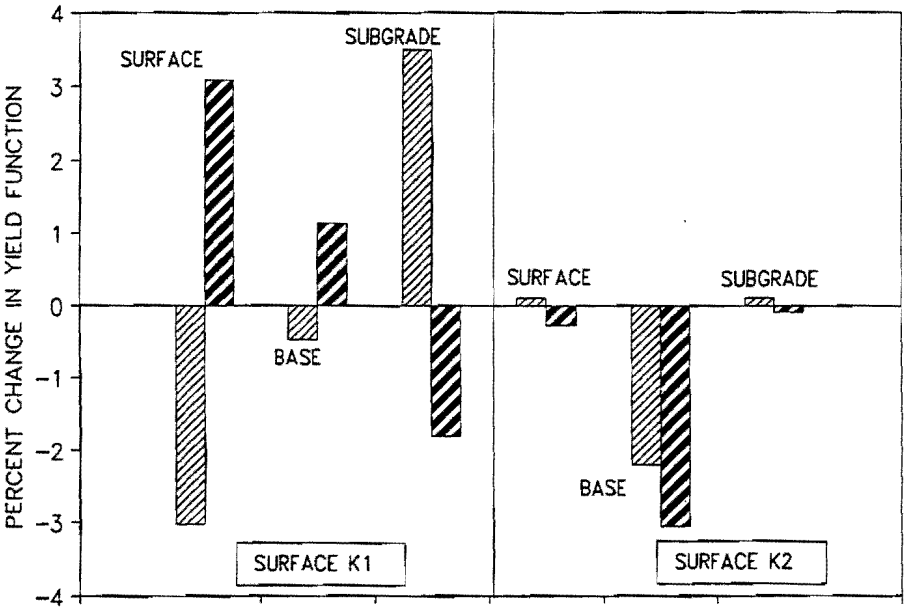

Figure D.8. Sensitivity of the Yield Function to Changes in the k_1 to k_3 Parameters of the Asphalt Surface (Thick Pavement, Edge of Load Evaluation Position).

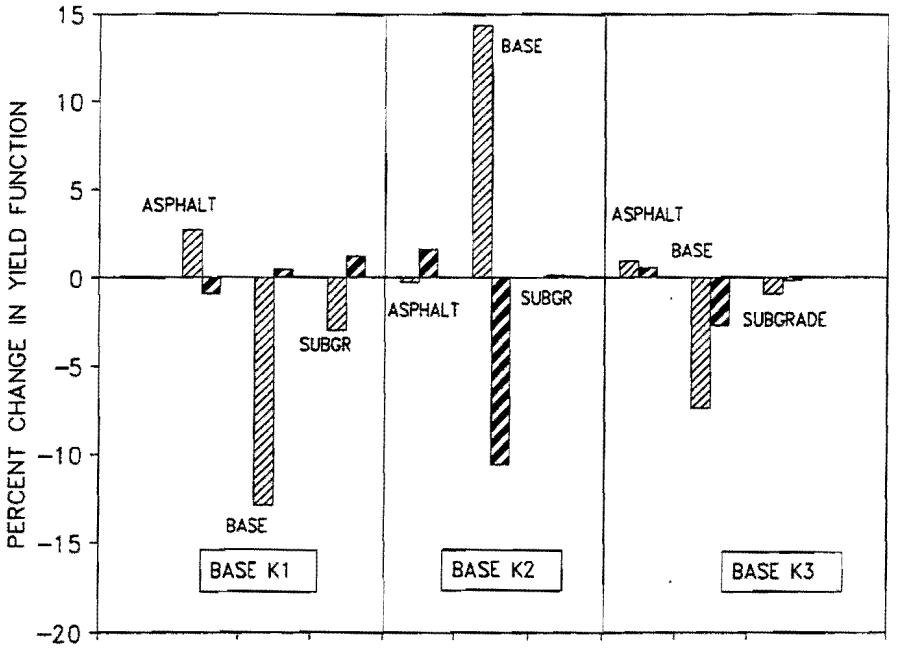

Figure D.9. Sensitivity of the Yield Function to Changes in the k_1 to k_3 Parameters of the Base (Thick Pavement, Center of Load Evaluation Position).

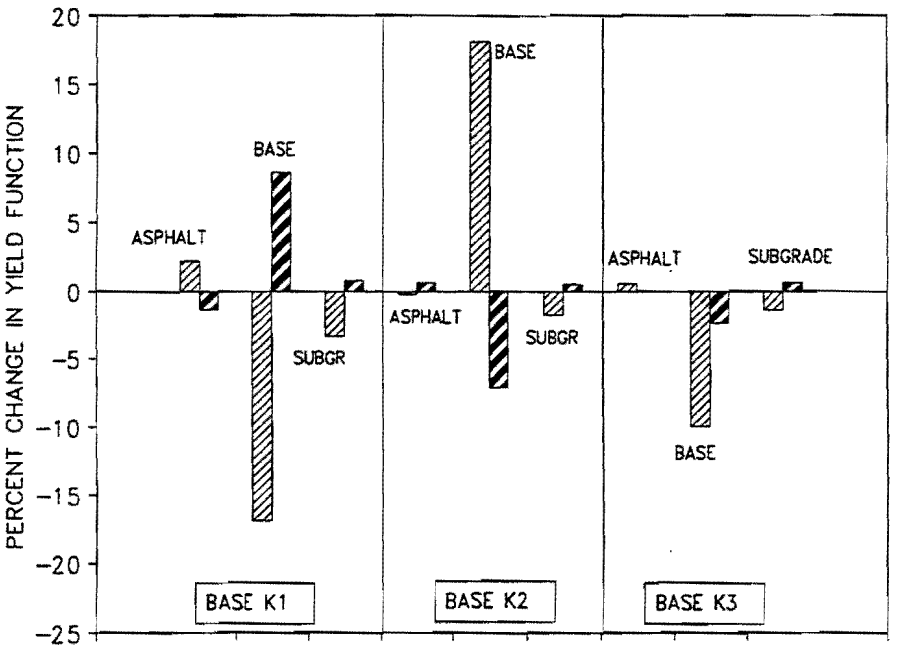

Figure D.10. Sensitivity of the Yield Function to Changes in the k_1 to k_3 Parameters of the Base (Thick Pavement, Edge of Load Evaluation Position).

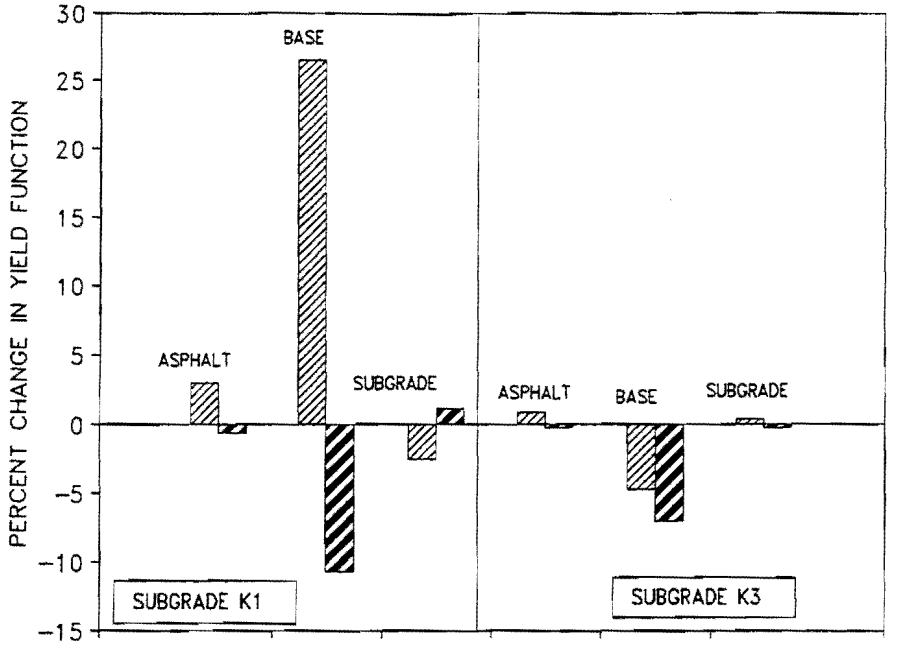

Figure D.11. Sensitivity of the Yield Function to Changes in the k_1 to k_3 Parameters of the Subgrade (Thick Pavement, Center of Load Evaluation Position).

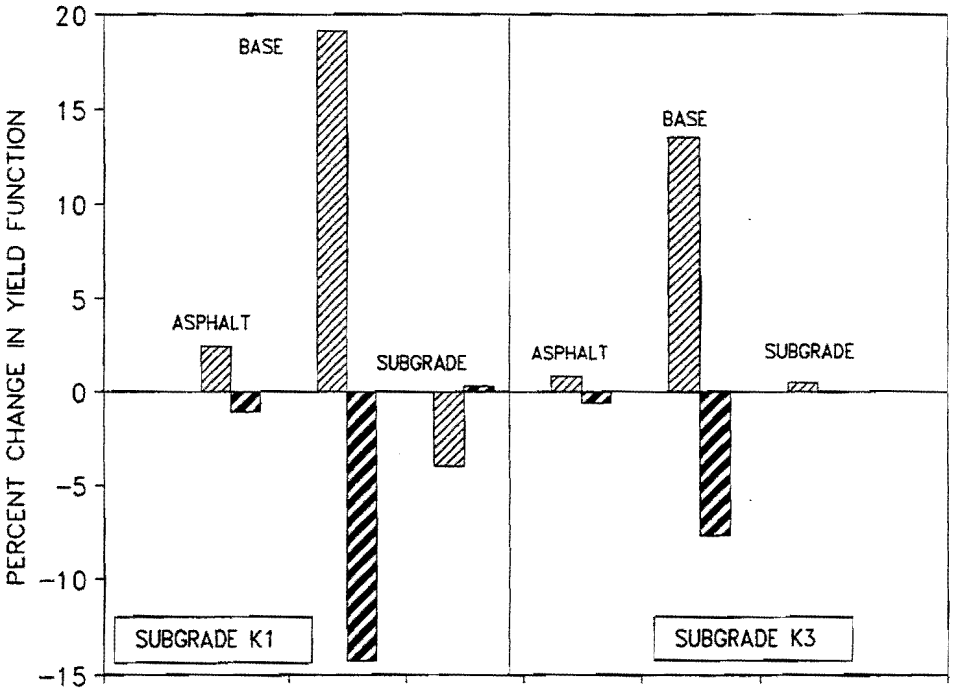

Figure D.12. Sensitivity of the Yield Function to Changes in the k_1 to k_3 Parameters of the Subgrade (Thick Pavement, Edge of Load Evaluation Position).

Figures D.13 through D.24 contain the results of the analysis of the sensitivity of the Mohr-Coulomb yield function to changes in the cohesion and angle of friction of the different pavement materials. Details of the averages assumed, and the method in which the graphs were derived can be found in Chapter IV. For each case, the stresses were kept constant while only the cohesion and angle of friction were varied. The stresses are those stresses which were calculated using the assumed average values for the k_1 to k_3 parameters. The cohesion and angle of friction values were changed to thirty percent above and below the assumed average value for the type of material under consideration. The yield function values are those calculated within the layer under consideration.

As an example, Figure D.13 documents the changes that can be expected in the yield function which is calculated in the asphalt surface if the asphalt cohesion is varied by thirty percent. For each layer, the stresses calculated at the edge and at the center of the load were used so the influence of the change in cohesion or angle of friction could be calculated at each of these evaluation positions.

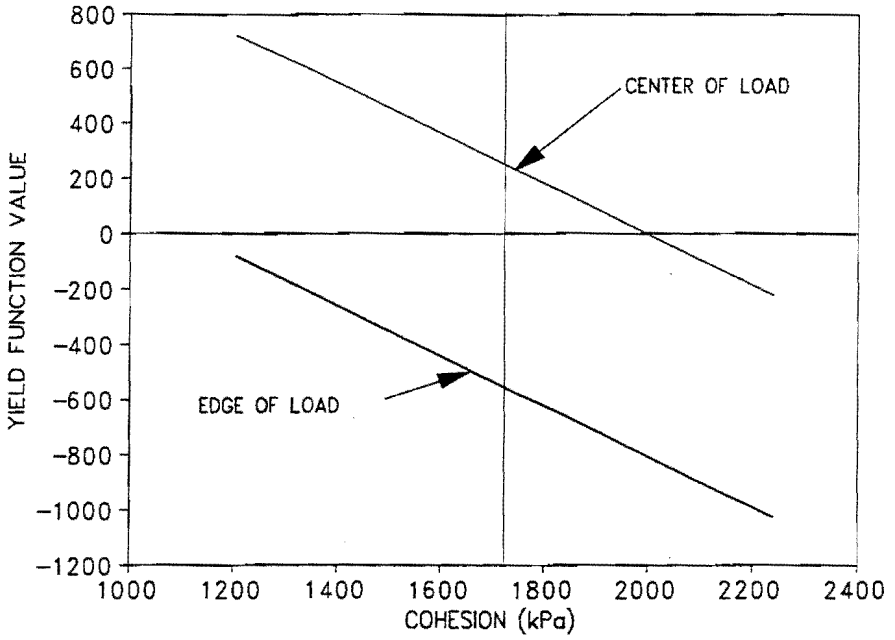

Figure D.13. Sensitivity of the Yield Function to Changes in the Asphalt Cohesion (Thin Pavement).

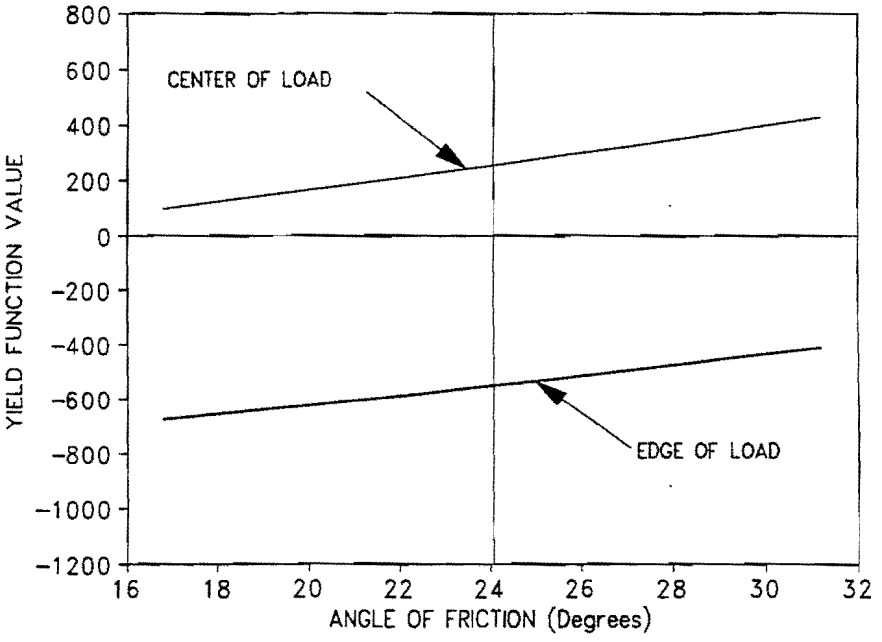

Figure D.14. Sensitivity of the Yield Function to Changes in the Asphalt Angle of Friction (Thin Pavement).

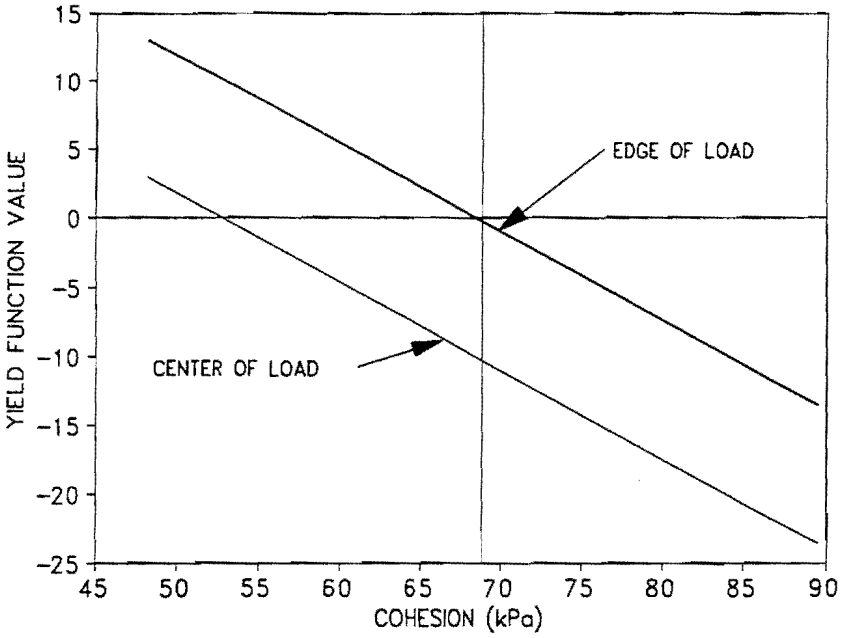

Figure D.15. Sensitivity of the Yield Function to Changes in the Base Course Cohesion (Thin Pavement).

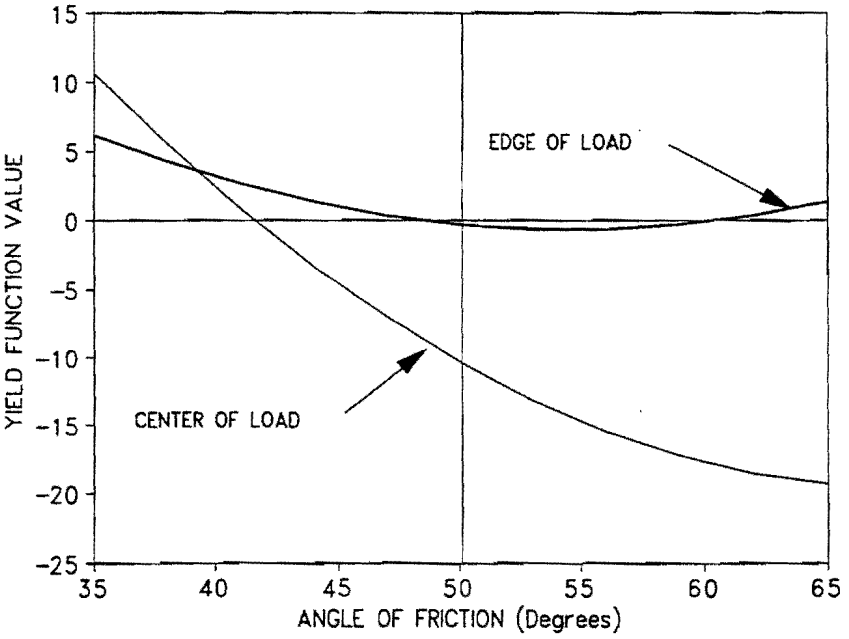

Figure D.16. Sensitivity of the Yield Function to Changes in the Base Course Angle of Friction (Thin Pavement).

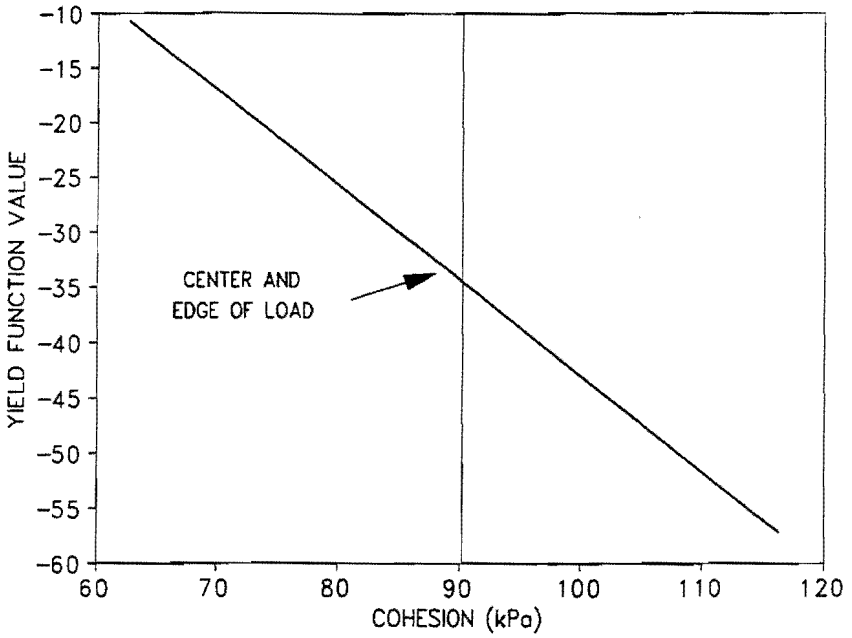

Figure D.17. Sensitivity of the Yield Function to Changes in the Subgrade Cohesion (Thin Pavement).

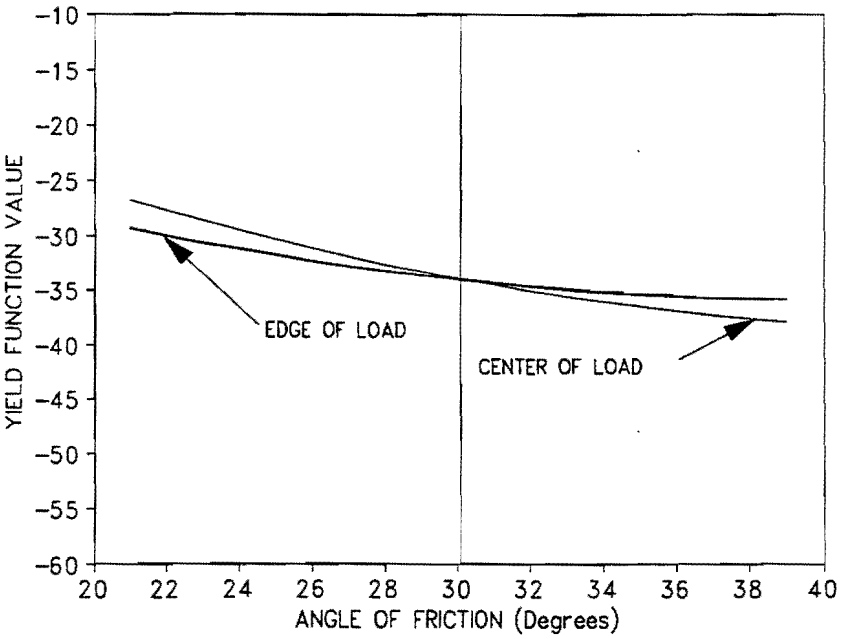

Figure D.18. Sensitivity of the Yield Function to Changes in the Subgrade Angle of Friction (Thin Pavement).

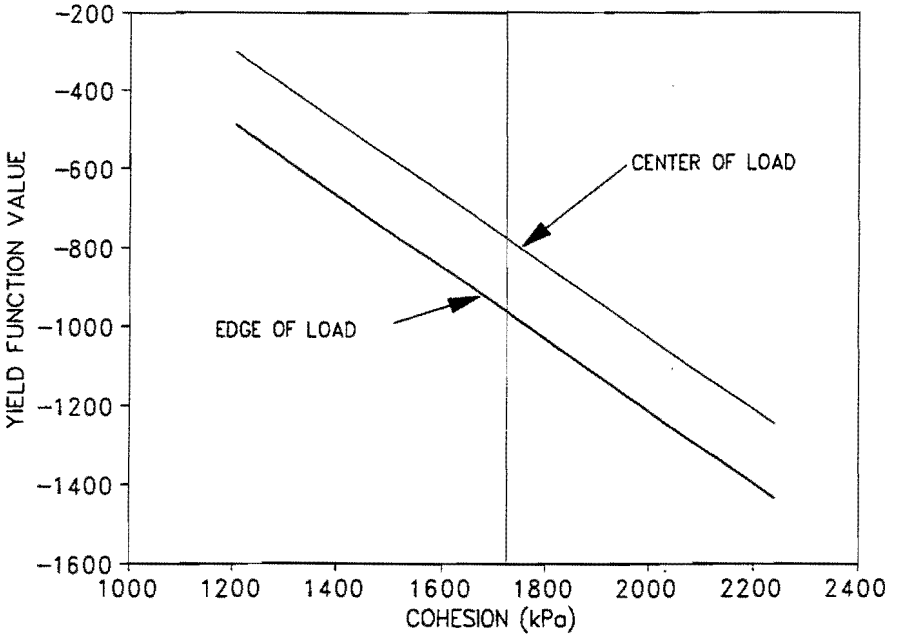

Figure D.19. Sensitivity of the Yield Function to Changes in the Asphalt Cohesion (Thick Pavement).

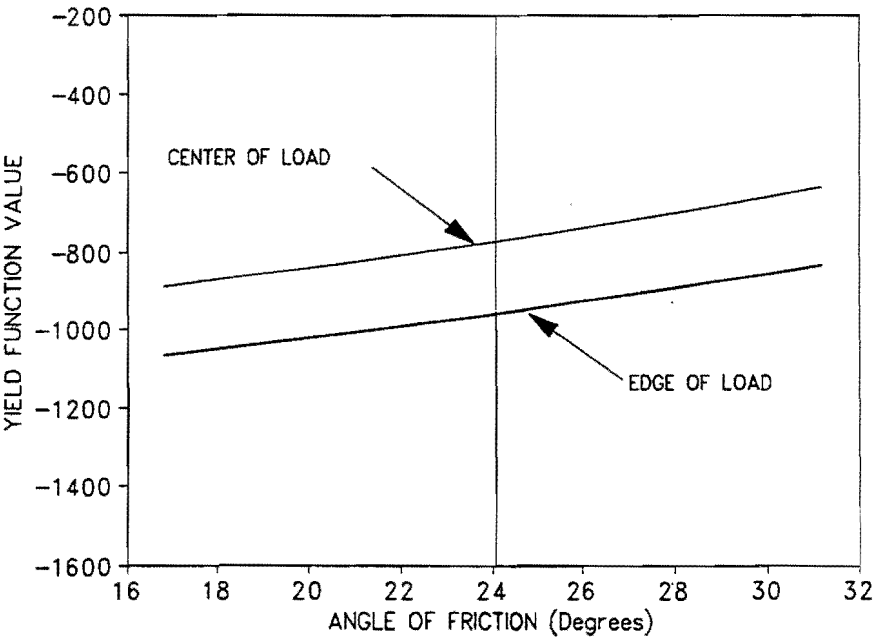

Figure D.20. Sensitivity of the Yield Function to Changes in the Asphalt Angle of Friction (Thick Pavement).

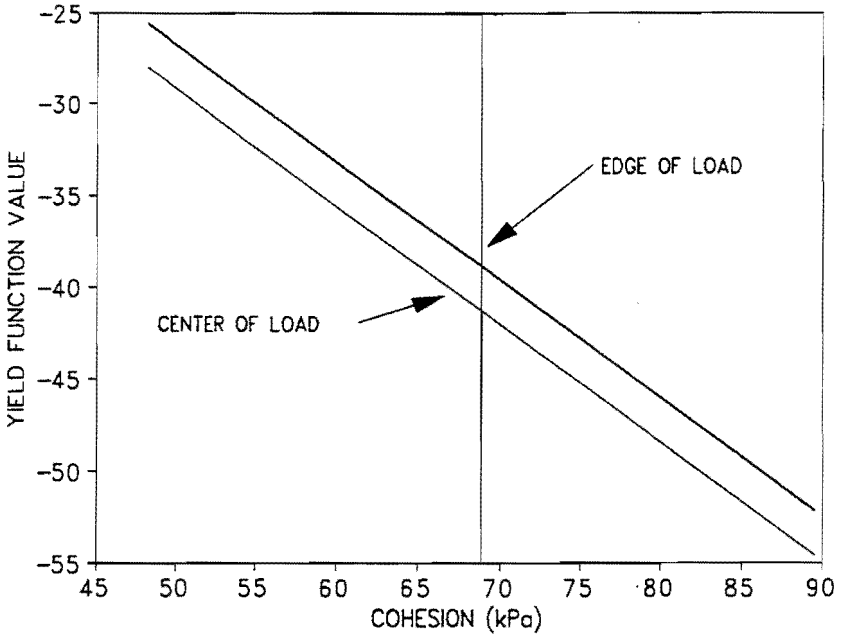

Figure D.21. Sensitivity of the Yield Function to Changes in the Base Course Cohesion (Thick Pavement).

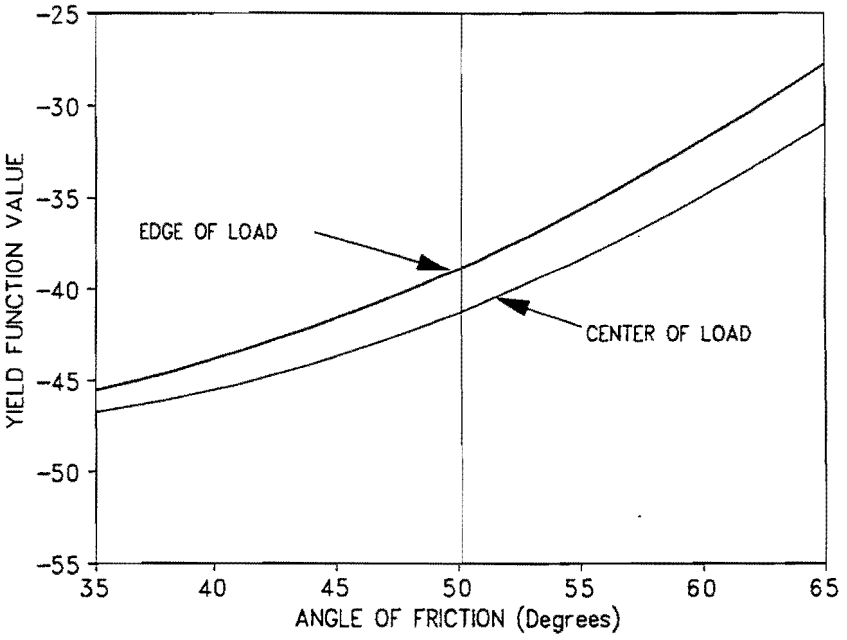

Figure D.22. Sensitivity of the Yield Function to Changes in the Base Course Angle of Friction (Thick Pavement).

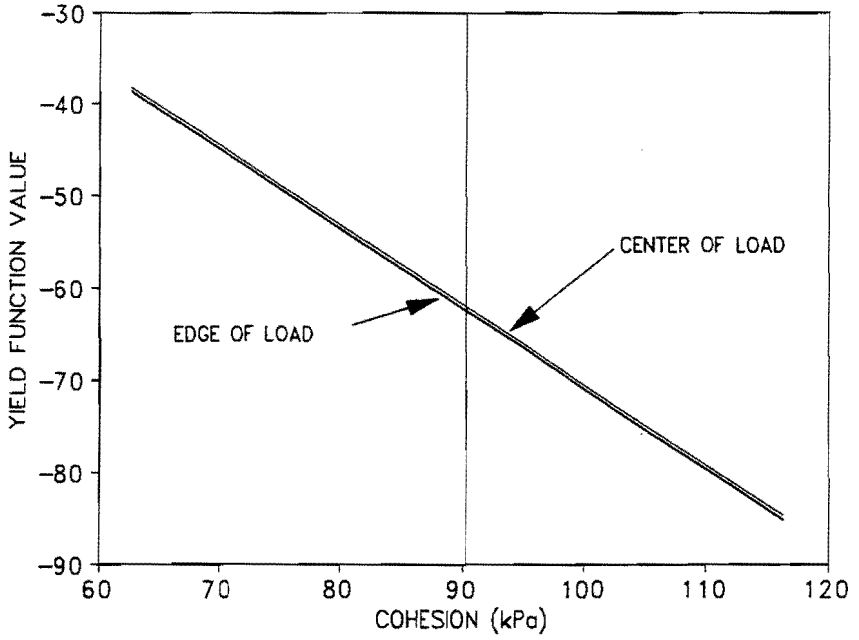

Figure D.23. Sensitivity of the Yield Function to Changes in the Subgrade Cohesion (Thick Pavement).

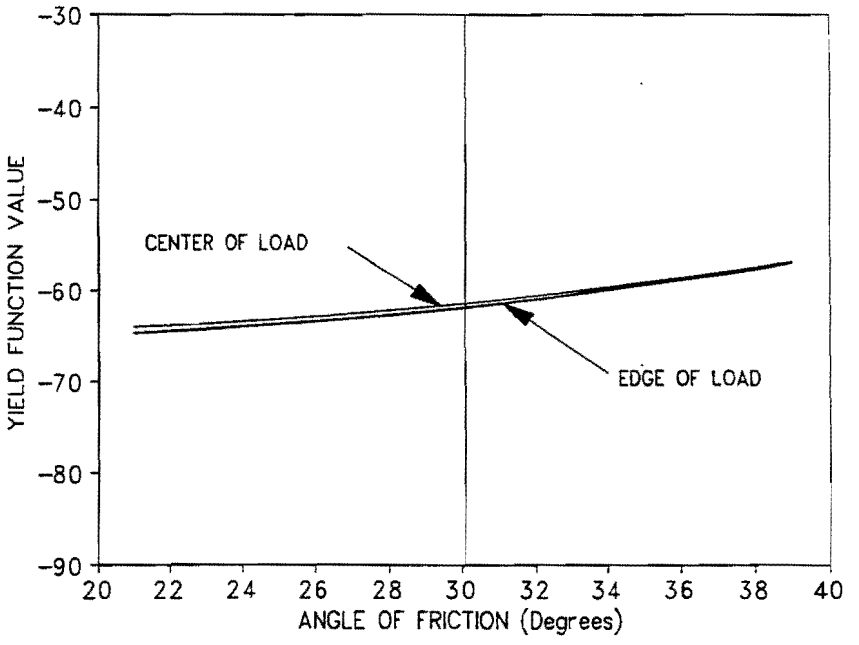

Figure D.24. Sensitivity of the Yield Function to Changes in the Subgrade Angle of Friction (Thick Pavement).

APPENDIX E

A REVIEW OF STRESS CONCEPTS

INTRODUCTION

While the word, *stress*, is commonly used in engineering disciplines, it is often forgotten that the word refers to an abstract concept. Stress is a quantity that cannot be measured directly, but is calculated from knowledge of two physical parameters, force and geometry, that are directly measurable. Thus, stress is a mathematical rather than a physical quantity (*92*). However, it is a very useful engineering quantity in explaining how bodies subjected to external forces will respond or behave, principally because it is usually the distribution of an applied or induced force, i.e., the force intensity over a unit area, that directly influences the material response.

The concept of stress is explained in simplistic terms with the aid of Figure E.1, which shows a prismatic bar subjected to an applied force, P, at the ends. Due to these applied forces, an internal force distribution will develop at any cross-section, *ll*, of the bar in opposition to the applied external force, according to Newton's third law of motion. It is the intensity of the induced internal forces, i.e., the force per unit area, that is referred to as *stress*. For the example shown in Figure E.1, the internal forces are uniformly distributed over any cross-section, *ll*, and the intensity of the force distribution is obtained by simply dividing the applied load, P, by the cross-sectional area, A, at *ll*.

In the general case, the stress distribution is non-uniform and may be oriented in any direction. If a very small area, δA, is cut-out at a given point in a material, and if the resultant force acting on this area is, δP, then the stress, p, acting at the point is calculated as:

$$p = \lim_{\delta A \to 0} \left(\frac{\delta P}{\delta A} \right) \tag{E.1}$$

Thus, the stress at a point may be viewed as the limiting value of, $\delta P/\delta A$, as the elemental area, δA, is continuously contracted, i.e., $\delta A \to 0$. In general, the unit stress, p, need not be perpendicular to the plane on which it acts. However, any force or stress, can be decomposed into two perpendicular components, one acting normal to the plane of

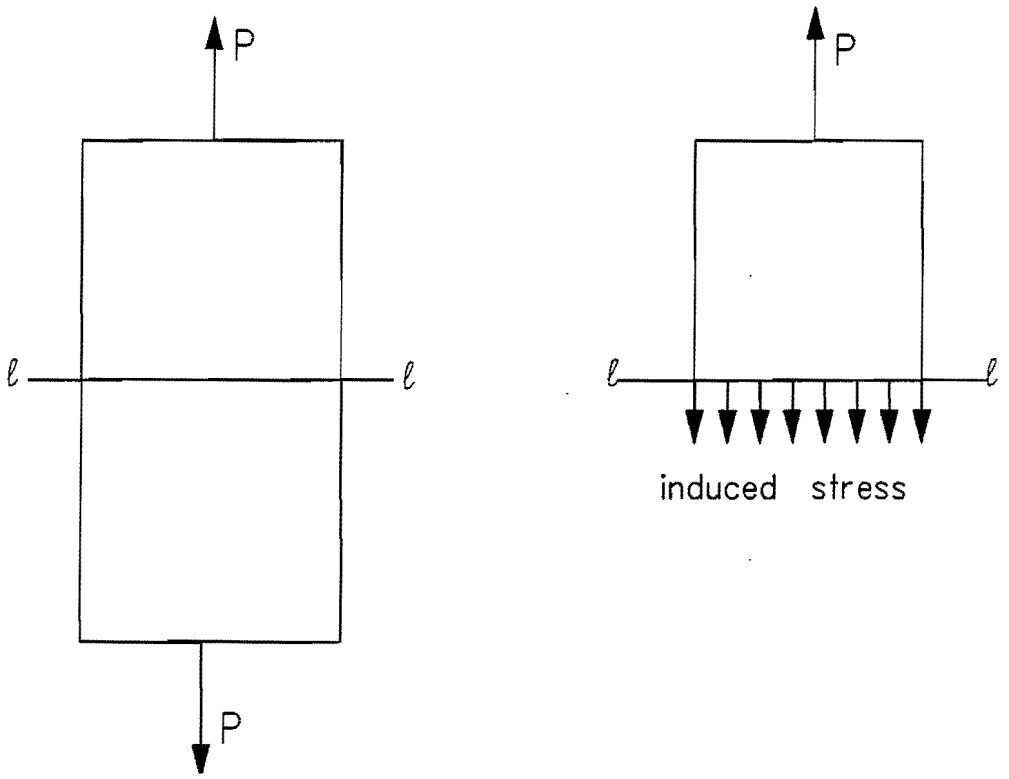

Figure E.1. Prismatic Bar Subjected To End Forces.

reference, and the other acting parallel to the plane, i.e., the shear component. This is illustrated in Figure E.2. The normal component of stress is usually designated with the symbol, σ, while the shear component is designated with the symbol, τ.

To completely establish the state of stress at a point, it is necessary to specify components on three orthogonal planes passing through the point. Let these three orthogonal planes be the planes perpendicular to the x, y, and z coordinate axes. If we take a very small cubic element at a point, the stresses acting on the sides of the cubic element are as illustrated in Figure E.3. The subscript used in conjunction with a normal component of stress denotes the direction of the stress. Thus, σ_x, denotes the normal stress acting in the direction of the x-axis. For shear stresses, two subscripts are used. The first subscript denotes the direction of the normal to the plane on which the stress acts, while

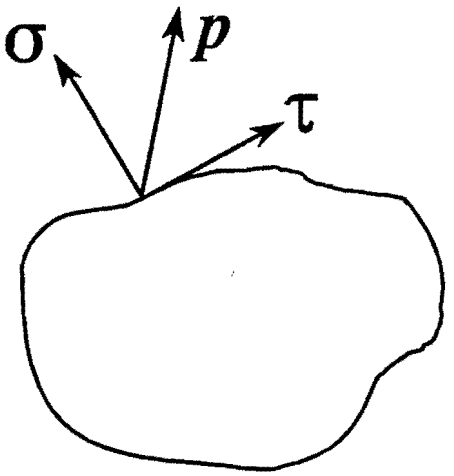

Figure E.2. Horizontal (τ) and Normal (σ) Components of Stress, *p*.

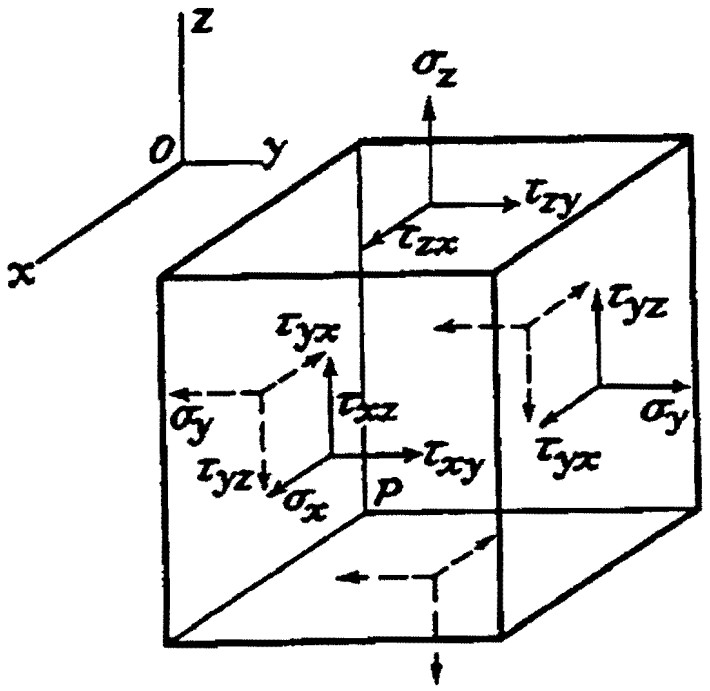

Figure E.3. Components of the Stress Matrix (from *93*).

the second subscript denotes the direction of the stress (*94*). Consider, for example, the shear stress component, τ_{xy}. The first subscript says that this shear stress acts on the plane whose normal is in the x-direction. Further, the second subscript shows that the shear stress acts in the y-direction. It is noted that double subscripts have also been used with normal stresses. Thus, the symbol, σ_{xx}, has been used to denote the normal stress component acting in the x-direction on the plane whose normal is also in the x-direction. However, for this discussion, we drop one of the subscripts and denote this normal stress simply as, σ_x. Similarly, we denote the normal stresses acting in the y- and z-directions as σ_y, and σ_z, respectively.

The stresses illustrated in Figure E.3 are all positive. Herein, a normal stress is positive if it produces tension and negative when it produces compression. For a shear stress component acting on a face of the cubic element, the positive direction is taken as the positive direction of the coordinate axis if a tensile stress on the same face would have the positive direction of the corresponding axis. If the tensile stress has a direction opposite to the positive, the positive direction of the shear stress component is reversed (*93*).

It is seen from Figure E.3 that the stress at a point is completely specified by nine quantities which can be represented in an array as:

$$[s] = \begin{bmatrix} \sigma_x & \tau_{xy} & \tau_{xz} \\ \tau_{yx} & \sigma_y & \tau_{yz} \\ \tau_{zx} & \tau_{zy} & \sigma_z \end{bmatrix} \tag{E.2}$$

In most cases, surface and body couples are not significant and may be ignored. Consequently, by equilibrium, $\tau_{xy} = \tau_{yx}$, $\tau_{yz} = \tau_{zy}$, and $\tau_{xz} = \tau_{zx}$, and the number of independent stress components reduces from nine to six.

PRINCIPAL STRESSES AND STRESS INVARIANTS

If the six independent components of stress at a point are known, the stresses acting on any inclined plane through the point can be evaluated by static equilibrium. Consider the infinitesimal tetrahedron, *OABC*, illustrated in Figure E.4a, that is formed by the intersection of the coordinate planes with a plane inclined at an arbitrary angle. (This tetrahedron may also be viewed as the intersection of an inclined plane within the cubical element shown in Figure E.3.) It is assumed that the stresses acting on the coordinate planes in Figure E.4a are known. To remain in equilibrium, there must be a resultant force acting on the surface, *ABC*, of the tetrahedron that counteracts the stresses on the coordinate planes. This resultant force, denoted as *S* in Figure E.4b, will in general be inclined at a certain angle from the surface, *ABC*. The resultant force, *S*, can be decomposed into normal, S_n, and shear, S_s, components. Clearly, the magnitude of the resultant force on the surface, *ABC*, will vary depending on the inclination of the surface. Further, as the resultant force varies, the magnitudes of the normal and shear components will also vary. If we imagine the surface, *ABC*, in Figure E.4a as being hinged at *B*, and assume that the stresses on the coordinate planes remain constant, we can swing the surface, *ABC*, in such a way that the normal force component, S_n, increases, while the shear component, S_s, decreases. Eventually, we will reach a position wherein the shear component vanishes and only the normal component remains. When this happens, the resultant force, *S*, equals the normal component, S_n. The stress determined when S_n is divided by the area of the surface, *ABC*, is referred to as the *principal stress*, and the plane on which it acts is called the *principal plane* (*92*). The orientation of this plane is specified by the direction of the normal to the plane relative to the coordinate axes.

The resultant force, *S*, in Figure E.4b can also be decomposed into components, S_x, S_y, and S_z, relative to the *x*, *y*, and *z* coordinate axes. Considering the equilibrium of forces along the x-direction for the infinitesimal tetrahedron shown in Figure E.4a and E.4b, the magnitude of S_x, is determined as:

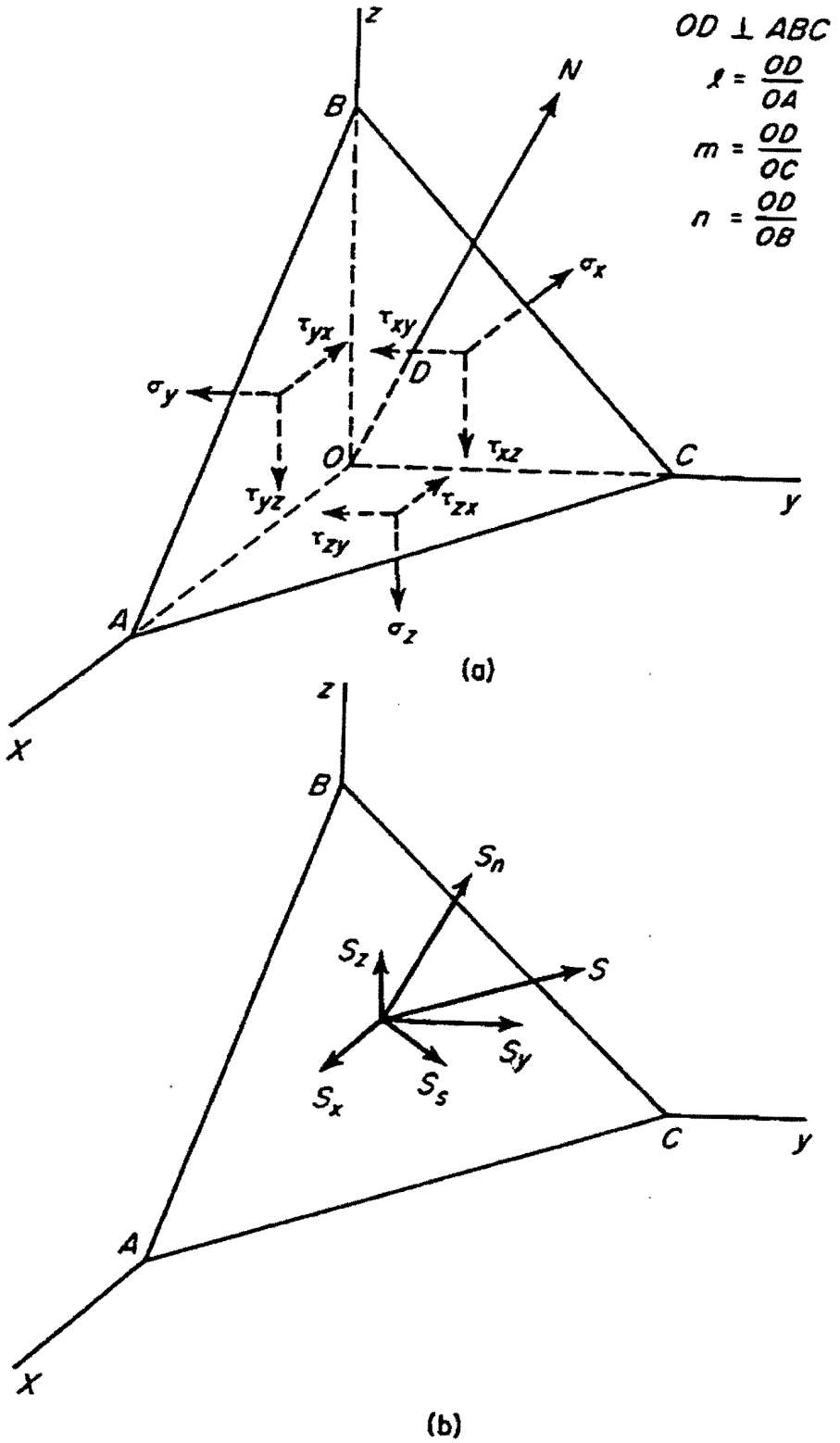

Figure E.4. Forces on an Infinitesimal Tetrahedron (from *94*).

$$S_x = \sigma_x A_x + \tau_{yx} A_y + \tau_{zx} A_z \qquad \text{(E.3)}$$

where,

A_x = area of the face, *BOC*, on which the stress, σ_x, acts

A_y = area of the face, *BOA*, on which the stress, τ_{yx}, acts

A_z = area of the face, *OAC*, on which the stress, τ_{zx}, acts

If we let A_w be the area of the face, *ABC*, of the tetrahedron, relationships between A_w and the areas of the other faces may be determined by equivalence of the volume of the tetrahedron. Thus,

$$A_w\, OD = A_x\, OA$$
$$A_w\, OD = A_y\, OC$$
$$A_w\, OD = A_z\, OB$$

where,

OD is the length of the normal to side, *ABC*

OA is the length of the normal to side, *BOC*

OC is the length of the normal to side, *BOA*

OB is the length of the normal to side, *OAC*

From the above expressions, we get the ratios of the areas as:

$$\frac{A_x}{A_w} = \frac{OD}{OA} = l$$

$$\frac{A_y}{A_w} = \frac{OD}{OC} = m$$

$$\frac{A_z}{A_w} = \frac{OD}{OB} = n$$

where, l, m, and n are referred to as the direction cosines of the normal to the side, *ABC*. If we divide both sides of Eq. E.3 by, A_w, we get the following expression for the stress, s_x, acting on side, *ABC*:

$$s_x = \sigma_x l + \tau_{yx} m + \tau_{zx} n \tag{E.4}$$

Similarly,

$$s_y = \tau_{xy} l + \sigma_y m + \tau_{zy} n \tag{E.5}$$

$$s_z = \tau_{xz} l + \tau_{yz} m + \sigma_z n \tag{E.6}$$

If the side, *ABC*, is a principal plane, the shear force component of the resultant force, S, in Figure E.4b is zero, so that the resultant force is equal to the normal force, S_n. In this case, the components, S_x, S_y, and S_z, are given by the equations:

$$S_x = lS \tag{E.7}$$

$$S_y = mS \tag{E.8}$$

$$S_z = nS \tag{E.9}$$

If we designate the resultant principal stress on side, *ABC*, with a lower case, s, Eqs. E.4 to E.6 can be written as:

$$l(\sigma_x - s) + m\tau_{yx} + n\tau_{zx} = 0 \tag{E.10}$$

$$l\tau_{xy} + m(\sigma_y - s) + n\tau_{zy} = 0 \tag{E.11}$$

$$l\tau_{xz} + m\tau_{yz} + n(\sigma_z - s) = 0 \tag{E.12}$$

The above are three homogeneous linear equations in l, m, and n. Solutions different from zero can be obtained only if the determinant of these equations is zero. Expanding the determinant gives the following cubic equation for, s (*94*):

$$s^3 - I_1 s^2 - I_2 s - I_3 = 0 \tag{E.13}$$

where,

$$I_1 = \sigma_x + \sigma_y + \sigma_z \tag{E.14}$$

$$I_2 = \tau^2_{xy} + \tau^2_{yz} + \tau^2_{zx} - (\sigma_x\sigma_y + \sigma_y\sigma_z + \sigma_z\sigma_x) \tag{E.15}$$

$$I_3 = \sigma_x\sigma_y\sigma_z + 2\tau_{xy}\tau_{yz}\tau_{zx} - (\sigma_x\tau^2_{yz} + \sigma_y\tau^2_{zx} + \sigma_z\tau^2_{xy}) \tag{E.16}$$

Solving for the roots of Eq. E.13 gives the three principal stresses, σ_1, σ_2, and σ_3. Now, the stresses, σ_x, σ_y, σ_z, τ_{xy}, τ_{yz}, and τ_{zx}, in Eqs. E.14 to E.16 may be given in any coordinate system. However, Eq. E.13 must always give the same roots, no matter what coordinate system is used. This means that the coefficients, I_1, I_2, and I_3, must remain constant and independent of the coordinate system used. For this reason, I_1, I_2, and I_3, are called *stress invariants*, and are referred to respectively, as the first, second, and third stress invariants (*93*). Also, since Eq. E.13 must always give the same roots, the principal stresses are also invariant.

Eqs. E.14 to E.16 may also be specified in terms of the principal stresses. In this case, the stress invariants reduce to:

$$I_1 = \sigma_1 + \sigma_2 + \sigma_3 \tag{E.17}$$

$$I_2 = -(\sigma_1\sigma_2 + \sigma_2\sigma_3 + \sigma_3\sigma_1) \tag{E.18}$$

$$I_3 = \sigma_1\sigma_2\sigma_3 \tag{E.19}$$

Whether Eqs. E.14 to E.16 or Eqs. E.17 to E.19 are used to compute the stress invariants, the values determined will be the same.

OCTAHEDRAL STRESSES

If the normal stresses acting on sides, *BOC*, *BOA*, and *OAC* in Figure E.4a are assumed to be principal stresses, the stresses, s_x, s_y, and s_z, are simply determined as:

$$s_x = \sigma_x l = \sigma_1 l$$
$$s_y = \sigma_y m = \sigma_2 m$$
$$s_z = \sigma_z n = \sigma_3 n$$

from Eqs. E.4 to E.6. The normal stress, s_n, on side, *ABC*, will then be:

$$s_n = l s_x + m s_y + n s_z = l^2\sigma_1 + m^2\sigma_2 + n^2\sigma_3 \tag{E.20}$$

and the shear stress, s_s, is determined from the relation:

$$s^2 = s^2_n + s^2_s = s^2_x + s^2_y + s^2_z \tag{E.21}$$

where, s, is the resultant shear stress on side, *ABC*. Solving for the shear stress, we get:

$$s^2_s = s^2 - s^2_n = \sigma^2_1 l^2 + \sigma^2_2 m^2 + \sigma^2_3 n^2 - (l^2\sigma_1 + m^2\sigma_2 + n^2\sigma_3)^2 \tag{E.22}$$

If the plane, *ABC*, in Figure E.4b is oriented such that $OA = OB = OC$, the normal to the plane will make equal angles with the coordinate axes. In this case, the direction cosines are given by:

$$l = m = n = \pm\frac{1}{\sqrt{3}} \tag{E.23}$$

Substituting the values of the direction cosines in Eqs. E.20 and E.22, we get the following expressions for the normal stress, s_n, and the shear stress, s_s, on side, *ABC*:

$$s_n = \frac{1}{3}(\sigma_1 + \sigma_2 + \sigma_3) = \sigma_m \tag{E.24}$$

$$s_s^2 = \frac{1}{2}(\sigma_1^2 + \sigma_2^2 + \sigma_3^2) - \frac{1}{9}(\sigma_1 + \sigma_2 + \sigma_3)^2 \qquad \text{(E.25)}$$

The normal stress, s_n, in Eq. E.24 is an average of the three principal stresses, and is also referred to as the mean stress, σ_m. The expression for shear stress in Eq. E.25 is simplified further as follows:

$$s_s = \frac{1}{3}\left[(\sigma_1 - \sigma_2)^2 + (\sigma_2 - \sigma_3)^2 + (\sigma_3 - \sigma_1)^2\right]^{\frac{1}{2}} \qquad \text{(E.26)}$$

Referring again to Figure E.4a, the tetrahedron with plane, *ABC*, as one side, can be constructed in each of the four quadrants above the *xy* plane, and in each of the four quadrants below this plane. For each tetrahedron, the direction cosines will be as given in Eq. E.23, although the signs attached to *l*, *m*, and *n*, will differ among the eight tetrahedra which, together, form an octahedron. On the faces of this octahedron, the normal and shear stresses will be as given by Eqs. E.24 and E.26, respectively. These stresses acting on the faces of the octahedron are referred to as the octahedral normal stress, and the octahedral shear stress, and the planes where these stresses act are called the octahedral planes (*94*). The octahedral normal stress is, thus, equal to the mean stress, σ_m. From Eqs. E.24 and E.17, it is seen that the octahedral normal stress is one-third of the first stress invariant. The octahedral shear stress is also designated in the literature as, τ_{oct}, and can be expressed in terms of the stress invariants as (*94*):

$$\tau_{oct} = \frac{\sqrt{2}}{3}\left(I_1^2 + 3I_2\right)^{\frac{1}{2}} \qquad \text{(E.27)}$$

From the preceding, it is obvious that the octahedral normal stress, and the octahedral shear stress are also invariant or independent of the coordinate system used to determine the stresses.

DEVIATORIC STRESSES

The stress matrix can be decomposed into a hydrostatic and a deviatoric component. The hydrostatic component, [*h*], is associated with the mean stress, σ_m, and is defined as (*94*):

$$[h] = \begin{bmatrix} \sigma_m & 0 & 0 \\ 0 & \sigma_m & 0 \\ 0 & 0 & \sigma_m \end{bmatrix} \tag{E.28}$$

Note that σ_m is invariant, i.e., its magnitude is constant irrespective of orientation. Thus, the term, *hydrostatic*. The deviatoric component is determined by deducting the hydrostatic component, [*h*], from the total stress, [*s*], given by Eq. E.2:

$$[s] - [h] = [d] = \begin{bmatrix} \sigma_x & \tau_{xy} & \tau_{xz} \\ \tau_{yx} & \sigma_y & \tau_{yz} \\ \tau_{zx} & \tau_{zy} & \sigma_z \end{bmatrix} - \begin{bmatrix} \sigma_m & 0 & 0 \\ 0 & \sigma_m & 0 \\ 0 & 0 & \sigma_m \end{bmatrix}$$

Carrying out the matrix subtraction, we get:

$$[d] = \begin{bmatrix} (\sigma_x - \sigma_m) & \tau_{xy} & \tau_{xz} \\ \tau_{yx} & (\sigma_y - \sigma_m) & \tau_{yz} \\ \tau_{zx} & \tau_{zy} & (\sigma_z - \sigma_m) \end{bmatrix} \tag{E.29}$$

Physically, the hydrostatic component is responsible for volume change in a material. Experiments have shown that this component has negligible effect on yielding and plastic flow. On the other hand, the deviatoric component is responsible for dimensional change and consequently, for plastic flow (*92,94*). It plays a significant role in plasticity theory.

Just as there are invariants associated with the total stress matrix, invariants corresponding to the deviatoric stress matrix may be determined. To do this, we note that the total stress is made up of a deviatoric component, d, and a hydrostatic component that is equal to $I_1/3$. Thus, we simply replace, s, in Eq. E.13, by $(d + I_1/3)$, to get (*94*):

$$d^3 - J_1 d^2 - J_2 d - J_3 = 0 \tag{E.30}$$

where,

$$J_1 = 0 \tag{E.31}$$

$$J_2 = \frac{1}{3}\,(I_1^2 + 3\,I_2) \tag{E.32}$$

$$J_3 = \frac{1}{27}\,(2\,I_1^3 + 9\,I_1\,I_2 + 27\,I_3) \tag{E.33}$$

The deviatoric stress invariants, J_2 and J_3, can also be expressed in terms of principal stresses (*94*):

$$J_2 = \frac{1}{6}\left[(\sigma_1 - \sigma_2)^2 + (\sigma_2 - \sigma_3)^2 + (\sigma_3 - \sigma_1)^2\right] \tag{E.34}$$

$$J_3 = (\sigma_1 - \sigma_m)\,(\sigma_2 - \sigma_m)\,(\sigma_3 - \sigma_m) \tag{E.35}$$

The second deviatoric stress invariant, J_2, is also related to the octahedral shear stress, τ_{oct}, through the relation (*94*):

$$J_2 = \frac{3}{2} \tau_{oct}^2 \tag{E.36}$$

Finally, the deviatoric stress invariants may be expressed in terms of the principal stress deviators, d_1, d_2, and d_3, through the equations (*94*):

$$J_2 = -(d_1 d_2 + d_2 d_3 + d_3 d_1) \tag{E.37}$$

$$J_3 = d_1 d_2 d_3 \tag{E.38}$$

where,

$$d_1 = \sigma_1 - \sigma_m \tag{E.39}$$

$$d_2 = \sigma_2 - \sigma_m \tag{E.40}$$

$$d_3 = \sigma_3 - \sigma_m \tag{E.41}$$

APPENDIX F

GLOSSARY OF SELECTED TECHNICAL TERMS

Axial Strain

When a state of stress ($\sigma_1 > \sigma_2 = \sigma_3$) in a cylindrical sample is considered, the axial strain is the change in length in the direction of σ_1 expressed as a percentage of the original sample length. The *radial strain* is the corresponding change in length in the lateral direction.

Behavior

The manner in which a particular material responds under loading, as determined from its stress-strain curve, is referred to as material behavior for the applied loading conditions. If there is a straight line relationship between stress and strain, the material is said to exhibit *linear behavior* for the range of loads considered. Otherwise, if the relationship is a curve, the behavior is referred to as *nonlinear*.

Boundary Conditions

In the solution of differential equations, the given conditions which are to be satisfied by the particular solution are called the boundary conditions (*95*).

Constitutive Equation

Chen and Mizuno (*67*) define a *constitutive equation* as the stress-strain relationship for a material under general loading and environmental conditions. A number of mathematical models relating stress and strain have been used to predict the behavior of materials under load. These models vary in complexity, the simplest being Hooke's law, which assumes linear elastic behavior, i.e., materials are assumed to return to their original undeformed condition upon removal of load. The constitutive equation for a particular material is typically determined experimentally to quantify the coefficients in the mathematical model. For many pavement materials, the constitutive equation depends on many factors that include homogeneity, isotropy, rate and magnitude of loading, temperature, stress history, and other factors.

Dilation

Dilation denotes a volume change characterized by expansion of a material under loading. The tendency of dense granular materials to dilate under loading has been observed experimentally (see, for example, Figure 3.2 in this report). This is attributed to the motion of particles that tend to roll over one another under the action of shear stresses induced in the material by applied loads.

Elastic Half-Space

An elastic half-space is a semi-infinite elastic body with a surface boundary. The surface boundary is typically taken as the *xy* plane and is infinite in the lateral direction. The *z*-axis is typically assumed to be positive toward the interior of the half-space which has infinite depth from the surface boundary.

Elastic Modulus

When a cylindrical specimen is loaded monotonically in uniaxial tension or compression, axial strain increases with increase in load. The ratio of stress, σ, to strain, ϵ, is a measure of the material stiffness and is referred to as the elastic modulus (assuming that the material response is still within the elastic range). In Figure F.1a, the stress-strain curve is linear for the range of the applied loads. In this case, the elastic modulus is a constant equal to the slope of the line. In Figure F.1b, the slope of the stress-strain relation varies with the applied load, i.e., it is nonlinear. In this case, there are two ways of determining the elastic modulus for a given point on the stress-strain curve. For example, if the elastic modulus is desired at point *C*, the slope of the tangent to the curve at *C* may be used. This is referred to as the *tangent modulus*. The other way is to determine the slope of the line connecting the point *C* with the origin, *O*. This slope is referred to as the *secant modulus*.

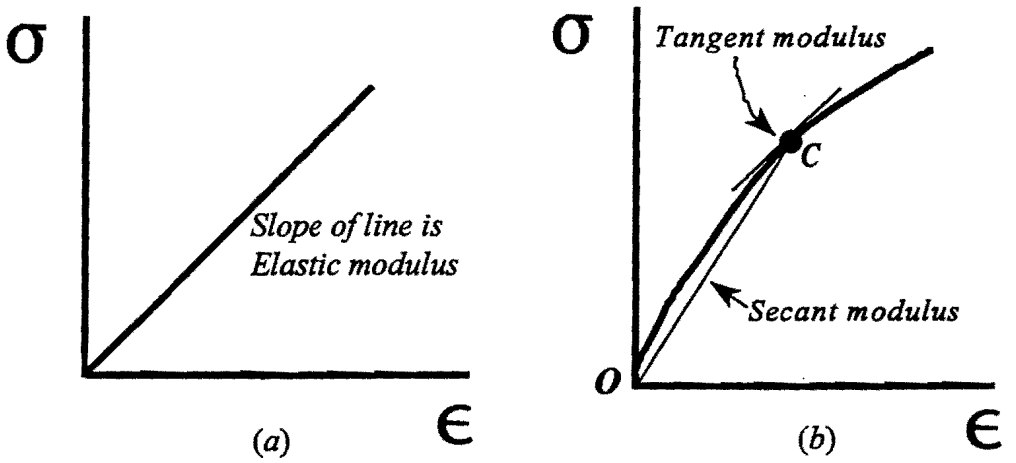

Figure F.1. Elastic Modulus for (a) Linear Stress-Strain Relation; and (b) Nonlinear Stress-Strain Curve.

Isotropic

A material is characterized as isotropic if its physical properties at a given point are the same in all directions.

Lode Angle

A vector of stress state can be decomposed into hydrostatic and deviatoric components as illustrated in Figure F.2. In this figure, the stress state is given in the principal stress coordinate system. The hydrostatic axis is the diagonal from the origin, *O*, of the coordinate system where $\sigma_1 = \sigma_2 = \sigma_3$. The segment *OB* along this diagonal represents the hydrostatic component of vector *OA*, while the segment *BA* perpendicular to the hydrostatic axis represents the deviatoric component. The deviatoric component lies on a plane perpendicular to the hydrostatic axis, called the *deviatoric* or the *octahedral plane*. The angle between the deviatoric component and the projection of the largest principal stress axis onto the deviatoric

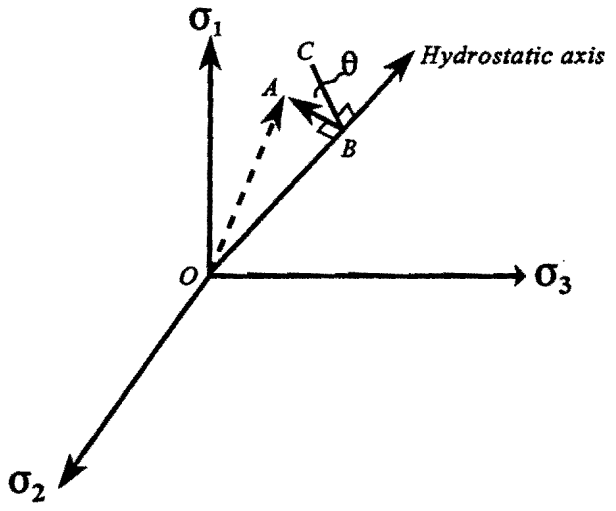

Figure F.2. Stress State in Principal Stress Coordinate System (from *67*).

plane is referred to as the lode angle, θ, in Figure F.2 (*67*). This angle varies from 0 to 60 degrees. In Figure F.2, it is assumed that $\sigma_1 > \sigma_2 > \sigma_3$, so that the lode angle is referred to the projection of the σ_1 axis onto the deviatoric plane, represented by *BC* in the figure. If the stress state is such that $\sigma_3 > \sigma_2 > \sigma_1$, the lode angle must then be measured from the projection of the σ_3 axis onto the deviatoric plane. Other stress conditions are handled in a similar fashion. From Figure F.2, it is seen that the lode angle helps to locate a stress point in the principal stress space. In the example shown, the location of point *A* is determined by the distance along the hydrostatic axis *OB*, the lode angle θ, and the distance *BA*. From mechanics, these quantities are determined from the following relations (*67*):

$$|OB| = \frac{1}{\sqrt{3}} I_1$$

$$|BA| = \sqrt{2\ J_2} = \sqrt{3}\ \tau_{oct}$$

$$\theta = \frac{1}{3}\cos^{-1}\left[\frac{3\sqrt{3}}{2}\frac{J_3}{J_2^{3/2}}\right]$$

where,

$\|OB\|$	=	the magnitude of the hydrostatic component of stress vector, *OA*
I_1	=	the first stress invariant
J_2	=	the second deviatoric stress invariant
J_3	=	the third deviatoric stress invariant
$\|BA\|$	=	the magnitude of the deviatoric component of stress vector, *OA*
τ_{oct}	=	the octahedral shear stress

It is thus seen from the above expressions that the hydrostatic component of stress is related to the first stress invariant, while the deviatoric component is related to the second deviatoric stress invariant or to the octahedral shear stress.

Multi-Depth Deflectometer (MDD)

The Multi-Depth Deflectometer is an assembly of linear variable differential transducers (LVDTs) installed inside a cylindrical vertical cavity within the pavement to measure vertical displacements at selected depths under moving wheel loads. Both recoverable and permanent displacements can be measured with the MDD.

Poisson's Ratio

When a material specimen is subjected to uniaxial tension or compression, the axial strain in the direction of the applied load is accompanied by a lateral strain in the transverse direction. The ratio of the lateral strain to the axial strain is referred to as the Poisson's ratio, ν.

Resilient Modulus

When a cylindrical sample of a pavement material is tested under repeated loading in the laboratory, the total deformation at a given number of load applications is observed to consist of a resilient or recoverable component, and a non-recoverable component (see Figure 3.1). From the test data, the *resilient modulus* of the material is calculated as the ratio of the repeated deviatoric stress to the recoverable axial strain (*I*). Since the stiffness of pavement materials are dependent on the rate of loading and applied stress, laboratory tests are usually conducted at a range of frequencies and deviatoric stresses that correspond to the expected traffic loadings in the field. A number of models have been proposed to characterize the stress-dependency of the resilient modulus of pavement materials, in particular, granular and fine-grained soils. For the superheavy load evaluation procedure, the Universal Soil Model (*32,36,37*) is used in evaluating the structural capacity of superheavy load routes. This model is given by:

$$E_r = (k_1\ Pa)\left(\frac{I_1}{Pa}\right)^{k_2}\left(\frac{\tau_{oct}}{Pa}\right)^{k_3}$$

where,

I_1	=	first stress invariant
τ_{oct}	=	octahedral shear stress
Pa	=	atmospheric pressure
E_r	=	resilient modulus

The coefficients, k_1, k_2, and k_3, are determined from resilient modulus tests. Since the calculated stresses are normalized with respect to the atmospheric pressure, these coefficients are dimensionless. From results of sensitivity analyses, the coefficient k_1 was found to have the most influence on the predicted resilient modulus. In general, the higher the k_1, the higher the predicted resilient modulus. This is illustrated in Figure F.3 which shows predicted resilient moduli for a granular base material at three different values of k_1. The data shown were calculated assuming a pavement with a 100-mm thick asphalt concrete surface layer and a 200-mm thick granular base layer. Values of 0.6 and -0.3 were assumed for the parameters

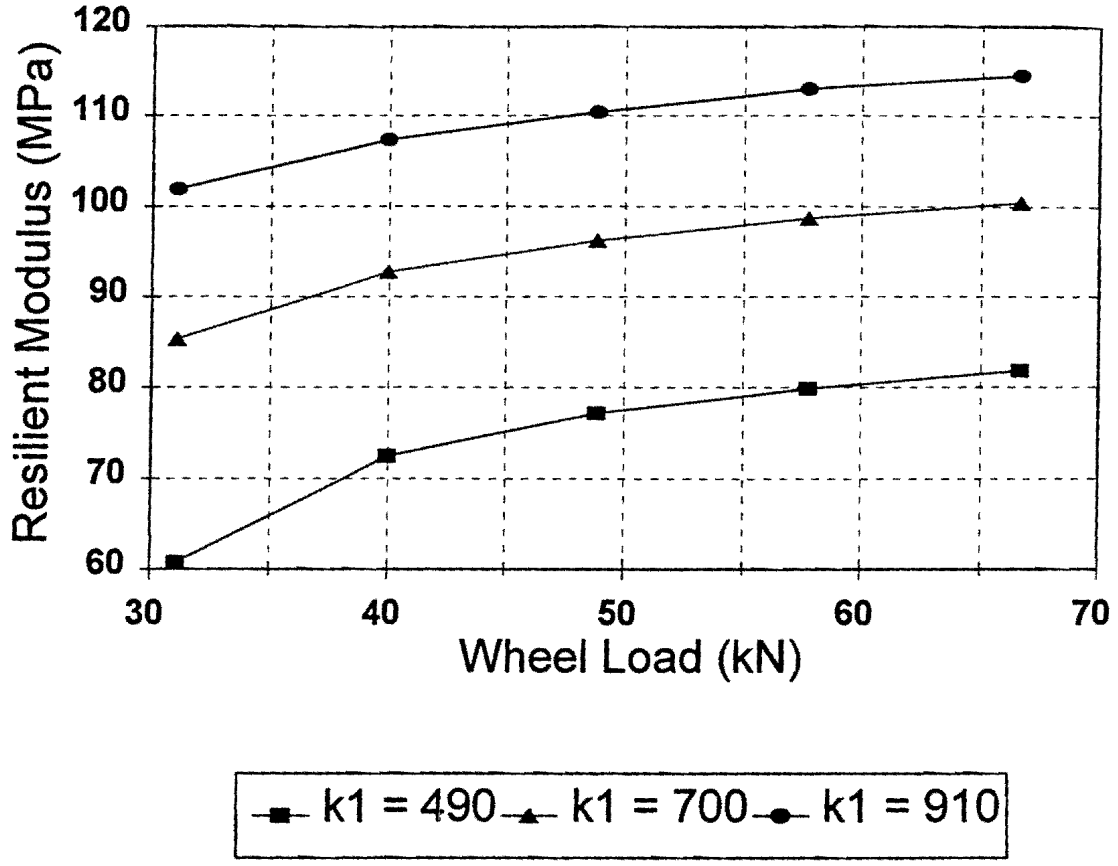

Figure F.3. Variation in Resilient Modulus With Parameter, k_1.

k_2 and k_3, respectively, for the base layer. For a given curve, it is observed that the resilient modulus increases with increasing wheel load, illustrating the hardening effect of increasing confinement on the predicted resilient modulus. This hardening effect is associated with the k_2 term,

$$k_2 \ term = \left(\frac{I_1}{Pa} \right)^{k_2}$$

As the wheel load increases, the confining pressures also increase resulting in higher predicted values for the resilient modulus. It is noted that the octahedral shear stress also increases with increasing wheel load, which will tend to decrease the resilient modulus.

However, for the pavement and range of wheel loads considered in Figure F.3, the increase in confinement with higher wheel loads more than compensates for the softening effect of the octahedral shear stress. Thus, the resilient modulus is predicted to increase with higher wheel loads in the figure shown. However, the opposite trend may be obtained for other pavements (such as thin pavements), where the softening effect of the octahedral shear stress may be more pronounced. The hardening effect of higher confinement and the softening effect of higher octahedral shear stress can be discerned from Figure F.4. The k_3 term in the figure is equal to,

$$k_3 \ term = \left(\frac{\tau_{oct}}{Pa} \right)^{k_3}$$

Note that, as the wheel load increases, the k_2 term increases because of higher confinement. However, the octahedral shear stress also increases so that the k_3 term diminishes with higher wheel loads. Consequently, while the effect of higher k_1 is generally to increase the predicted resilient modulus, the effects of k_2 and k_3 depend on the interactions between these coefficients, the applied loads, and the pavement geometry. The tendency of a material to stiffen with increasing confinement (I_1) is related to k_2. However, this tendency is counteracted by the softening effect under increasing shear, as controlled by the coefficient k_3. The greater the tendency of a material to stiffen under increasing confinement, the higher the effect of k_2. Similarly, the greater the tendency of a material to soften under shear, the higher the effect of k_3. The effects of these coefficients on the resilient modulus are also affected by the applied loads and pavement geometry due to the effects of these latter factors on the induced stresses. The coefficients k_1, k_2, and k_3 are also used in evaluating the stress-dependency of the Poisson's ratio based on the relationship developed by Uzan (39) [see Eq. 3.3 and Appendix B].

Response Model

The model for predicting the induced displacements, strains and stresses under loading is referred to as the *response model*.

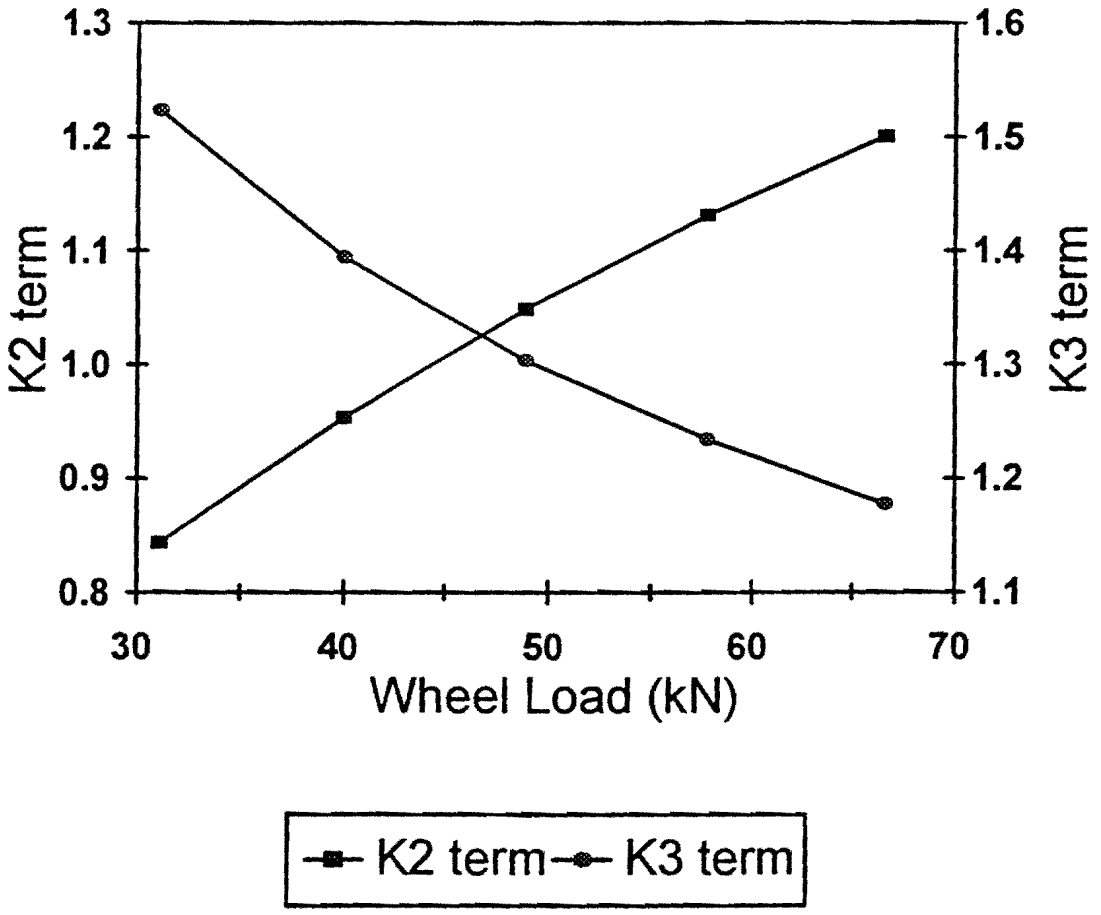

Figure F.4. Variation in k_2 and k_3 Terms With Wheel Load Magnitude.

Stress Invariant

Stress parameters (e.g, I_1, I_2, I_3) which are independent of the choice of coordinate axes are known as stress invariants. Stress invariants are scalar quantities, examples of which include the principal stresses, the mean stress, σ_m, the octahedral shear stress, τ_{oct}, the invariants associated with the total stress tensor, designated as I_1, I_2, and I_3, and the deviatoric stress invariants, J_2 and J_3. Obviously, quantities that are determined by combining any number of these stress invariants will also be invariant. Definitions of stress invariants used in various failure criteria are given in the following.

Principal Stresses

The normal stresses acting on a planes where the shear stresses are zero are called the principal stresses. The set of three orthogonal planes on which the principal stresses act are referred to as the *principal planes.*

First Stress Invariant

The sum of the three principal stresses, designated as I_1, is the first stress invariant (*94*):

$$I_1 = \sigma_1 + \sigma_2 + \sigma_3$$

where σ_1 = the major principal stress,

σ_2 = the intermediate principal stress, and

σ_3 = the minor principal stress.

The first stress invariant is associated with the hydrostatic component of the stress tensor which is responsible for volume change in a material subjected to loading. Specifically, the hydrostatic component is defined by $I_1/3$, which is also known as the mean stress, σ_m.

Octahedral Shear Stress

The shear stress acting on a plane whose normal makes equal angles with the principal stress directions is called the octahedral shear stress, τ_{oct}. In terms of principal stresses, the octahedral shear stress is given by (*94*):

$$\tau_{oct} = \frac{1}{3}\left[(\sigma_1 - \sigma_2)^2 + (\sigma_2 - \sigma_3)^2 + (\sigma_3 - \sigma_1)^2 \right]^{\frac{1}{2}}$$

The plane on which the octahedral shear stress acts is called the *octahedral plane*. By definition, this plane is perpendicular to the hydrostatic axis, defined by the line where $\sigma_1 = \sigma_2 = \sigma_3$, in the principal stress coordinate system. The octahedral plane that passes through the origin of this coordinate system is called the π *plane*. The normal stress acting on the

octahedral plane is called the *octahedral normal stress*, also known as the mean stress, σ_m. The octahedral shear stress is related to the second deviatoric stress invariant, J_2, by the relation (*16*):

$$\tau_{oct} = \sqrt{\frac{2}{3} J_2}$$

The octahedral shear stress (and the second deviatoric stress invariant) is responsible for distortion of a material under loading.

Second Deviatoric Stress Invariant

In terms of principal stresses, the second deviatoric stress invariant, J_2, is given by (*94*):

$$J_2 = \frac{1}{6} [(\sigma_1 - \sigma_2)^2 + (\sigma_2 - \sigma_3)^2 + (\sigma_3 - \sigma_1)^2]$$

From mechanics, J_2 can also be interpreted as twice the value of the mean square of the *principal shear stresses*. Just as there are planes where shear stresses are at a minimum (the principal planes), there exist planes where the shear stresses are at a maximum, referred to as the principal shear stresses. These stresses are given by:

$$\tau_1 = \pm\frac{1}{2} (\sigma_2 - \sigma_3)$$

$$\tau_2 = \pm\frac{1}{2}(\sigma_1 - \sigma_3)$$

$$\tau_3 = \pm\frac{1}{2}(\sigma_1 - \sigma_2)$$

It can be shown that the above maximum shear stresses act on planes that bisect each pair of principal planes. Using the above relations, the expression for, J_2, can be re-written as:

$$J_2 = 2\left[\frac{\tau_1^2 + \tau_2^2 + \tau_3^2}{3}\right]$$

which shows that, J_2, is twice the mean square of the three principal shear stresses. Because of this link with the principal shear stresses, the second deviatoric stress invariant is associated with distortion or dimensional changes in a material under loading.

Third Deviatoric Stress Invariant

In terms of principal stresses, the third deviatoric stress invariant, J_3, is given by (*94*):

$$J_3 = (\sigma_1 - \sigma_m)(\sigma_2 - \sigma_m)(\sigma_3 - \sigma_m)$$

The third deviatoric stress invariant is used in determining the lode angle, θ, to locate a stress point on the octahedral plane.

Stress Path

A stress path is a plot of a theoretical or experimental relationship between two stress parameters. Both total stress and effective stress paths can be plotted. Most pavement materials exhibit path-dependency, i.e., the response depends on the load history or the stress path followed.

Yield Function

When a material is stressed beyond the elastic limit, permanent deformation or yielding takes place. The function that is used to determine the onset of yielding or inelastic deformations is referred to as the *yield function*, which is a mathematical relationship that is typically expressed in terms of the principal stresses; the stress invariants, I_1, J_2 (or τ_{oct}), and J_3; the lode angle, θ; or combinations of these invariants. The yield function value that corresponds to the onset of yielding or inelastic deformations is called the *yield criterion*. Note that the yield criterion may, or may not, be satisfied by the yield function. When the yield criterion for a given material is plotted, the *yield surface* is obtained. Thus, the yield surface is the graphical representation of the yield criterion. Generally, a yield surface is founded by experimental observations which are used to formulate the mathematical expression (*17*). In plasticity theory, a material undergoes yielding or permanent deformations when the stress state is on the yield surface. After initial yielding, subsequent yield surfaces develop for a work-hardening material. These may develop by expansion of the initial yield surface, by translation of the initial surface, or by a combination of expansion and translation. For an elastic-perfectly plastic material, subsequent yield surfaces all approach the initial yield surface and coincide with it (*96*). A number of yield criteria are used to evaluate the inelastic or plastic behavior of pavement materials. Some of these criteria are defined in the following.

Tresca Yield Surface

The Tresca yield surface is based on the premise that yielding of a material begins when the maximum shearing stress at a point reaches a critical value, Y_p, determined from a simple

tension test for a ductile material, or a compression test for a brittle material. Mathematically, the yield criterion may be written as (*96*):

$$\max\left(\frac{1}{2}|\sigma_1 - \sigma_2|, \frac{1}{2}|\sigma_2 - \sigma_3|, \frac{1}{2}|\sigma_3 - \sigma_1| \right) = Y_p$$

where, Y_p, corresponds to the shear strength of the material. The Tresca yield criterion may also be expressed in terms of stress invariants as follows (*96*):

$$f(J_2, \theta) = \sqrt{J_2}\sin\left(\theta + \frac{\pi}{3}\right) - Y_p = 0$$

Note that the effect of hydrostatic pressure is not considered in this criterion. The Tresca yield surface is a cylinder with a hexagonal cross-section (see Figure A.6b). Because the yield criterion does not consider the hydrostatic component of stress, the cross-sectional area of the cylindrical surface is a constant that does not vary with distance along the hydrostatic axis. Also, the cross-section of a deviatoric or octahedral plane is a regular hexagon.

Mohr-Coulomb Yield Criterion

Experience gained from strength tests conducted on soils and other granular materials shows that the point at which yield will start in granular media is dependent not only on the deviatoric stress component, but also on the hydrostatic stress component (*17*). This is because of the frictional nature of granular media. When a hydrostatic stress is applied to soil, the particles, which are angular, are pressed together, and the number of contact points as well as the intensity of contact are increased. This leads to increased friction which offers more resistance to sliding of particles over one another. Thus, in soils and rocks, the strength of the material is dependent on the hydrostatic component of stress (*17*). The Mohr-Coulomb yield criterion is given by the following equation:

$$f = \frac{I_1}{3}\sin(\phi) + \sqrt{J_2}\sin\left(\theta + \frac{\pi}{3}\right) + \frac{\sqrt{J_2}}{\sqrt{3}}\cos\left(\theta + \frac{\pi}{3}\right)\sin(\phi) - c\cos(\phi) = 0$$

where c and ϕ are the cohesion and friction angle of the material, respectively. The Mohr-Coulomb yield surface is illustrated in Figure A.9. The shape of the deviatoric or octahedral plane is an irregular hexagonal pyramid. Because of the dependence on the hydrostatic stress component represented by the mean stress, $I_1/3$, in the above equation, the cross-sectional area of the yield surface increases with increasing distance along the hydrostatic axis, reflecting the contribution of the hydrostatic stress component to the strength of the material. It is also observed that if the friction angle, ϕ, is zero, the Mohr-Coulomb yield criterion reduces to the Tresca criterion, with the cohesion, c, corresponding to the shear strength of the material, Y_p.

Lade-Duncan Yield Surface

This yield surface is based on triaxial test data for cohesionless soils (sands) by Lade and Duncan, and is expressed in terms of the first (I_1) and third (I_3) stress invariants. The general shape of the yield surface is conical with the apex of the cone at the origin of the principal stress axes (*67*). The mathematical form of the yield criterion is given by:

$$f = I_1^3 - \kappa_1 I_3 = 0$$

The Lade-Duncan model consists of nested yield surfaces and an ultimate failure surface as illustrated in Figure A.14. The failure surface is defined by a particular value of the parameter, κ_1, which is the stress level at failure that depends on the density of sand. The yield surface has a smooth cross-section unlike the Tresca and Mohr-Coulomb yield criteria. Similar to the Mohr-Coulomb yield criterion, the yield surface expands about the hydrostatic axis with increasing hydrostatic pressures. The subsequent yield surfaces and the ultimate failure surface of the Lade-Duncan model all have the same form of the yield function except that, for the subsequent yield surfaces enclosed by the failure surface, the parameter, κ_1, is replaced by κ, whose value depends on the current stress level. As κ approaches κ_1, the yield surface approaches the failure surface. The Lade-Duncan model accounts for factors such as hydrostatic pressure sensitivity, effect of the intermediate principal stress, shear dilatancy effects, and stress-path effects.

Desai Yield Criterion

The Desai yield criterion is given by the equation:

$$f = J_2 + \alpha I_1 + \beta I_1 I_3^{1/3} - \gamma I_1 - k^2 = 0$$

where α, β, γ, and k, are material parameters determined from laboratory tests. The factor k is a measure of cohesion, and β is the hardening function (*17*). Figure A.16 shows plots of the Desai criterion for different values of β. Figure A.17 shows a schematic representation of the Desai criterion on the π plane. The cross-section of the yield surfaces have smooth edges like the Lade-Duncan model. The nested yield surfaces correspond to different values of I_1. Higher values of I_1 lead to yield surfaces of larger cross-sections, implying higher strength with greater confinement or hydrostatic pressures.